



Room 14-0551
77 Massachusetts Avenue
Cambridge, MA 02139
Ph: 617.253.5668 Fax: 617.253.1690
Email: docs@mit.edu
<http://libraries.mit.edu/docs>

DISCLAIMER OF QUALITY

Due to the condition of the original material, there are unavoidable flaws in this reproduction. We have made every effort possible to provide you with the best copy available. If you are dissatisfied with this product and find it unusable, please contact Document Services as soon as possible.

Thank you.

Some pages in the original document contain color pictures or graphics that will not scan or reproduce well.

ENERGY TRANSFER PROCESSES IN METHANE AND
TRIDEUTEROMETHANE

by

Jody J. Klaassen

B.A. Augustana College 1988

Submitted to the Department of Chemistry
in Partial Fulfillment of the Requirements for the Degree of

DOCTOR OF PHILOSOPHY IN CHEMISTRY

at the Massachusetts Institute of Technology

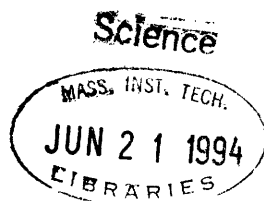
May 20, 1994

© Massachusetts Institute of Technology 1994

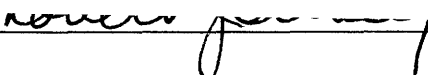
Signature of Author _____ Department of Chemistry
May 1994

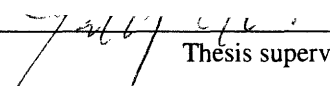
Certified by _____ Jeffrey I. Steinfeld
Thesis supervisor

Accepted by _____ Glenn A. Berchtold
Chairman, Departmental Committee on Graduate Students



This doctoral thesis has been examined by a committee of the Department of Chemistry as follows:

Professor Robert Silbey _____  Chairman

Professor Jeffrey I. Steinfeld _____  Thesis supervisor

Professor Robert W. Field _____

ENERGY TRANSFER PROCESSES IN METHANE AND TRIDEUTEROMETHANE

by

Jody J. Klaassen

Submitted to the Department of Chemistry on May, 20 1994
in partial fulfillment of the requirements for the degree of
Doctor of Philosophy in Chemistry

Abstract

A time-resolved CO₂/diode laser double resonance technique is used to study energy transfer processes in CHD₃. Both the rates of ground state recovery (GSR) and total depopulation (TD) from a single rovibrational level are measured. Comparison of these rates to pressure broadening measurements indicates that inelastic collisions underestimate the broadening coefficient by 30%-40%. GSR and TD rates with other collision partners (H₂, He, Ar, CH₄, NH₃, and CHF₃) are 0.5 to 1.0 times Lennard-Jones collision rates. Vibration-vibration (V→V) energy transfer between the Coriolis coupled ν_3/ν_6 vibrational levels is measured at $\sim 0.8 \mu\text{sec}^{-1} \text{ torr}^{-1}$ with no indication of rotational state specificity. Vibrational swap between a ν_3 vibrationally excited molecule and a ground state molecule is observed as an apparent symmetry changing process (A↔E) at $0.17 \mu\text{sec}^{-1} \text{ torr}^{-1}$. A Förster type mechanism quantitatively explains this effect. State-resolved rotational energy transfer (R.E.T.) in the ν_3 vibrational level is studied for two different initially prepared rotational levels, $\nu_3 J' = 12, K' = 7, "E"$ and $\nu_3 J' = 12, K' = 9, "A"$. R.E.T. is analyzed using a kinetic master equation model. A strong propensity rule, $\Delta K = \pm 3n$, similar to that found previously in polar C_{3v} molecules also applies to CHD₃.

A Raman-shifted Ti:sapphire I.R. source is described and characterized. This source provides completely tunable pump radiation from 3.3 μm to 740 nm. This source is suitable as a pump laser for double resonance studies, both spectroscopic and energy transfer, of numerous molecular systems which have previously been inaccessible. We describe initial experiments of fluorescence-detected I.R./U.V. double resonance in HCCH.

Raman-shifted Ti:sapphire/diode laser double resonance is used to study energy transfer processes in CH₄. The 2nd Stokes in H₂ of the Ti:sapphire laser is used to directly pump the CH₄ $\nu_3+\nu_4$ combination band at 2.3 μm . Transient gain on $\nu_3+\nu_4-\nu_4$ hotband transitions at 3.3 μm is measured with a liquid nitrogen cooled diode laser. A model of vibrational energy transfer among the CH₄ octad, pentad, and dyad levels is described. This model is used as a basis for analysis of R.E.T. in $\nu_3+\nu_4$. The $\Delta(R-J) = 0$ propensity rule found in earlier experiments on high J levels of spherical top molecules also applies for the low J levels measured in these experiments. A strong propensity for parity preserving collisions is also observed. State-to-state R.E.T. rates in the ground vibrational state for $J'' = 0 A_1 \rightarrow J'' = 3 A_2$, $J'' = 0 A_1 \rightarrow J'' = 4 A_1$, and $J'' = 3 A_2 \rightarrow J'' = 4 A_1$ are directly determined from a least squares fit to the kinetic data. A propensity for parity conserving collisions is observed. The polarization dependence of GSR and TD rates is measured. The large difference ($\sim 35\%$) in GSR rates between the cases when the probe laser samples an m_j distribution similar or dissimilar to that created by the pump laser illustrates the significance of elastic reorientation.

Thesis supervisor: Jeffrey I. Steinfeld
Title: Professor

Acknowledgments

During my years as a graduate student, there have been many people who provided me with help, guidance, and friendship. I am deeply grateful to all. I would like to convey particular thanks to some of them here.

First, many thanks to my advisor, Jeff Steinfeld, for having me as a graduate student and for giving me my start in science. Thanks also for introducing me to some of the great restaurants in Dijon, France.

Several foreign visitors to our lab have been a great help to me both for their scientific expertise and their friendship. Yoshiro Mizugai helped get me started in the very beginning and has been encouraging and supporting me ever since. He and Osamu Suto made up the Japanese contingent of our lab in the early days of my graduate work. A hearty BANZAI!! for them both. Bernd Abel was the German addition to the lab. He always has an infectious enthusiasm for our work that makes me want to do even more. Many thanks to you, Bernd. Thanks for the science and thanks for the friendship (and also thanks for all the beer and pizza). I would not have made it if not for you. Christine Roche, from Dijon, France, worked out the CHD₃ overtone and hotband spectroscopy so essential for the energy transfer experiments. Thanks, Christine and good luck. Alexander Golger and I have had many very interesting lunchtime conversations about politics and the differences between Russian and American life. I've learned a great deal from you, Alex, and I value your friendship deeply.

Charlotte Flannery was my classmate, coworker, and good friend. Thanks for always being there for me Charlotte.

Stephani Solina and I put together the plan for I.R./U.V. double resonance in acetylene one night while having a few beers and griping over our respective projects. Our collaborations have been a success ever since. I hope we get the opportunity to work together again in the future, and also to have a few more beers.

Steve Coy has always been a great person to talk with, to bounce ideas off, and to extract bits of knowledge from. Thanks for everything, Steve.

There has never been a shortage of friendship and goodwill in the basement of Building 2. Whether it was the loan of some piece of equipment, help with some problem, or just a break from work for some

food or beer, there was always someone to turn to. Many thanks to George Adamson, Chris Gittens, Nicole Harris, Jon O'Brien, and Zygmunt Jakubek.

Thanks also to my good friends from college, Peter Hanson and Dayton Meyer, who would always drop in on me just when I needed an infusion of friendship and happiness the most.

For the new guys in the lab, James Janni, Ilia Dubinsky, and Jason Clark, I wish the best of luck in your graduate work.

And finally, loving thanks to my parents and family for their never-ending, never-failing love and support.

Table of Contents

Abstract	3
Acknowledgements	4
Table of Contents	6
List of Figures	8
List of Tables	10
1. Introduction	11
2. CHD₃ Spectroscopy	14
2.1 Introduction	14
2.2 Energy Level Structure of ν_3/ν_6 Dyad	14
2.3 $2\{\nu_3, \nu_6\}$ Overtone and Combination Bands	15
3. CHD₃ Energy Transfer	17
3.1 Introduction	17
3.2 Previous Experimental Studies	17
3.3 Experimental Arrangement for Time-resolved CO ₂ -Infrared Diode Laser Double Resonance	18
3.4 Pump-Probe Double Resonance Scheme	23
3.5 Upper State Total Depopulation and Ground State Recovery Measurements	30
3.6 Connection Between Inelastic Collisions and Pressure Broadening	47
3.7 Vibrational Energy Transfer in the Coriolis-coupled ν_3/ν_6 Dyad	48
3.8 Symmetry Changing Collisions: A Simple Förster Mechanism	50
3.9 Master Equation Kinetics	51
3.10 State-to-state R.E.T. in ν_3 "A" and "E" Rotational Levels	54
4. Raman-shifted Ti:sapphire I.R. Source	55
4.1 Incentive for Broadly Tunable I.R. Laser Source	55
4.2 Basic Principles of Stimulated Raman Scattering	55
4.3 Experimental Arrangement	62
4.4 Characterization and Capabilities Raman-shifted Ti:sapphire I.R. Source	63
4.5 Fluorescence-detected double resonance in HCCH	68
5. CH₄ Energy Transfer	70
5.1 Introduction	70
5.2 Overview of CH ₄ Spectroscopy	70
5.3 Experimental Arrangement for Time-resolved Raman-shifted Ti:sapphire- Infrared Diode Laser Double Resonance	74
5.4 Vibrational Energy Transfer from the Octad	78
5.5 Rotational Energy Transfer in $\nu_3+\nu_4$	84
5.6 Rotational Energy Transfer in the CH ₄ Ground State	91
5.7 Reorientation Measurements	102
6. Conclusions and Future Work	107

References	109
Appendix 1. "State-to-state rotational energy-transfer measurements in the $\nu_2 = 1$ state of ammonia by infrared-infrared double resonance", <i>J. Chem. Phys.</i> 96 , 8236 (1992).	113
Appendix 2. "Overtone and hotband assignments in the $2\{\nu_3, \nu_6\}$ levels of CHD_3 ", <i>J. Chem. Phys.</i> 100 , 5508 (1994).	129
Appendix 3. "State-to-state rotational energy transfer measurements in methane (CHD_3) by infrared double resonance with a tunable diode laser", <i>J. Chem. Phys.</i> 100 , 5519 (1994).	141
Appendix 4. Program for converting LeCroy 9400A "*.tra" files to ASCII files	156
Appendix 5. Timing circuit for synchronization of Continuum NY61-20 Nd:YAG laser and Lambda Physik LPX-200 Excimer laser	163
Afterword	164

List of Figures

Figure	Title	Page
2.1	Reduced energy level diagram for the CHD ₃ ν_3/ν_6 dyad	15
2.2	Stick spectrum of CHD ₃ $2\nu_3$ overtone	16
3.1	Experimental setup for CO ₂ /diode laser double resonance	19
3.2	Combiner for perpendicularly polarized CO ₂ /diode laser beams	20
3.3	Temporal profile of LSI PRF 150S CO ₂ laser at 10R(24)	22
3.4	Saturation curve for CHD ₃ ν_3 ^Q Q(12,9) "A" transition	28
3.5	Pump/probe scheme used for studying energy transfer in CHD ₃	30
3.6	Ground state recovery transient for CHD ₃ self-relaxation at 50 mtorr	32
3.7	Total depopulation transient for CHD ₃ self-relaxation at 50 mtorr	33
3.8	$\rho\tau$ plot for CHD ₃ g.s. J" = 9, K" = 3 "A" for self-relaxation	37
3.9	$\rho\tau$ plot for CHD ₃ ν_6 J' = 8, K' = 4, l = +1 "A" for self-relaxation	37
3.10	$\rho\tau$ plot for CHD ₃ g.s. J" = 12, K" = 7 "E" for self-relaxation	38
3.11	$\rho\tau$ plot for CHD ₃ ν_3 J' = 12, K' = 7 "E" for self-relaxation	38
3.12	$\rho\tau$ plot for CHD ₃ g.s. J" = 12, K" = 9 "A" for self-relaxation	39
3.13	$\rho\tau$ plot for CHD ₃ ν_3 J' = 12, K' = 9 "A" for self-relaxation	39
3.14	$\rho\tau$ plot for CHD ₃ ν_3 J' = 16 K' = 14 "E" for self-relaxation	40
3.15	$\rho\tau$ plot for CHD ₃ ν_3 J' = 12, K' = 9 "A" with H ₂ as collision partner	41
3.16	$\rho\tau$ plot for CHD ₃ ν_3 J' = 12, K' = 9 "A" with He as collision partner	42
3.17	$\rho\tau$ plot for CHD ₃ ν_3 J' = 12, K' = 9 "A" with Ar as collision partner	42
3.18	$\rho\tau$ plot for CHD ₃ ν_3 J' = 12, K' = 9 "A" with CH ₄ as collision partner	43
3.19	$\rho\tau$ plot for CHD ₃ ν_3 J' = 12, K' = 9 "A" with CHF ₃ as collision partner	43
3.20	$\rho\tau$ plot for CHD ₃ ν_6 J' = 8, K' = 4, l = +1 "A" with H ₂ as collision partner	44
3.21	$\rho\tau$ plot for CHD ₃ ν_6 J' = 8, K' = 4, l = +1 "A" with NH ₃ as collision partner	44
3.22	Schematic for ν_3/ν_6 vibrational energy transfer model	49
3.23	Experimental signal and model simulation for A \leftrightarrow E vibrational swap in CHD ₃	50
3.24	$\rho\tau$ plot for A \leftrightarrow E swap in CHD ₃ ν_3	51
4.1	Energy level diagram for stimulated Raman scattering	56
4.2	Photograph of 1 st anti-Stokes and rotational Raman in H ₂	59
4.3	Schematic of the 2 m internal lens Raman shifter	63
4.4	Spectrum of Raman-shifted output near the Ti:sapphire fundamental	64
4.5	Spectrum of 1 st anti-Stokes and rotational Raman	64
4.6	Output pulse energy vs. input pulse energy of the Raman-shifted Ti:sapphire	65
4.7	Temporal profile of the 532 nm Nd:YAG and the Ti:sapphire at 835 nm	66
4.8	Pulse widths and delays of the Raman-shifted Ti:sapphire	67
4.9	2 nd Stokes bandwidth measured at the CH ₄ $2\nu_3$ R(0) transition	67
4.10	I.R./U.V. double resonance spectrum in HCCH	69

5.1	Vibrational energy level diagram for CH ₄	72
5.2	Experimental setup for Raman-shifted Ti:sapphire/diode laser double resonance	75
5.3	Schematic of diode laser lock electronics	77
5.4	Pump/probe scheme for overtone pump/transient gain double resonance	79
5.5	Example of 3-level transient gain signal	80
5.6	Vibrational relaxation transient for $\nu_1+\nu_4$	82
5.7	Rotational energy level diagram for the CH ₄ $\nu_3+\nu_4$ combination band	86
5.8	Experimental signals and model calculations for CH ₄ $\nu_3+\nu_4$ R.E.T.	88
5.9	Pump/probe scheme for CH ₄ ground state energy transfer	92
5.10	Rotational energy level diagram for CH ₄ g.s.	96
5.11	Experimental signals and model simulations for CH ₄ g.s. R.E.T.	101
5.12	Rel. population deviations in J" = 2 E	102
5.13	Allowed m _J transitions for parallel polarization of pump and probe	103
5.14	Allowed m _J transitions for perpendicular polarization of pump and probe	104
5.15	Transient signals for ground state recovery of the CH ₄ J" = 2 "E" level recorded with parallel and perpendicular polarizations	105
5.16	Scaled transient signals for ground state recovery of the CH ₄ J" = 2 "E" level	106

List of Tables

Table	Title	Page
3.1	CO ₂ laser/CHD ₃ coincidence table	25
3.2	Comparison of σ_{eff} with σ_{LJ} for several C _{3v} type molecules.	47
3.3	CHD ₃ pressure-broadening coefficients with CH ₄ as collision partner	48
4.1	Stimulated Raman scattering parameters for H ₂ and D ₂	62
5.1	Vibrational relaxation rates for CH ₄	83
5.2	Total depopulation rates in the CH ₄ $\nu_3+\nu_4$ vibrational level	85
5.3	Initial estimates of R.E.T. rates in $\nu_3+\nu_4$	89
5.4	State-to-state R.E.T. rates in the CH ₄ $\nu_3+\nu_4$ vibrational level	90
5.5	Ground state recovery rates for CH ₄	95
5.6	Pump/probe transitions used for studying CH ₄ g.s. R.E.T.	97
5.7	State-to-state rates connecting levels not directly measured	98
5.8	State-to-state rates for CH ₄ g.s. "A" levels	100

Chapter 1. Introduction

Experimental results for energy transfer studies in two isotopes of methane, CHD_3 and CH_4 , are presented in this thesis. The motivation for the present work originates in earlier studies of rotational energy transfer (R.E.T.) in the spherical top molecules $^{13}\text{CD}_4$ [FOY88] and SiH_4 [HETZLER89]. These highly symmetric molecules lack permanent dipole moments and have very complex rotational energy level structure. R.E.T. in these molecules proceeds by highly selective "principal pathways" in which only a few of the possible final states receive significant population from the parent level.

There is also much interest in methane because of its importance as a greenhouse gas in the Earth's atmosphere [SLANINA94] and as an important constituent of the atmospheres of the giant gas planets and many of their moons [ATREYA89]. Laboratory studies of the spectral parameters, transition frequency, intensity, and pressure broadening coefficient, are essential to interpreting remote sensing data [STRONG93]. Studies of rotational energy transfer have bearing on this applied field as the experimental measurements of state-to-state inelastic R.E.T. rates provide an excellent check on the theories which are used in the calculation of pressure broadening [FLANNERY93].

The isotope of methane that is of interest in terrestrial and extraterrestrial atmospheres is, of course, the most abundant, $^{12}\text{CH}_4$. That this isotope of methane has not been studied previously is not due to the lack of recognition of its importance, but rather because the experimental techniques necessary to investigate this molecule were previously nonexistent. The $^{13}\text{CD}_4$ and CHD_3 isotopes of methane could be studied by double resonance techniques because lines in their absorption bands happen to be in coincidence with fixed frequency CO_2 laser transitions. In this thesis, we describe the use of a Raman-shifted Titanium-doped sapphire laser as a source of continuously tunable laser radiation in the mid and near I.R. As a first application of this I.R. source, we have studied energy transfer processes in $^{12}\text{CH}_4$. This is exciting new work which is relevant both for the more fundamental aspect of investigating the effect of molecular symmetry on R.E.T. and for providing important spectral data.

As a large part of this thesis deals with rotational energy transfer, it is important to recognize the significant contribution made to this field more than twenty years ago when Oka wrote his seminal review of collision induced transitions between the rotational levels of small molecules [OKA73A]. In this work, Oka addressed the issue of the disparity in understanding of the fundamental selection rules for collision induced rotational transitions as compared to those for radiative transitions. He developed a set of approximate selection rules, or propensity rules, on ΔJ , Δk , and parity for rotational state changing collisions. These propensity rules were based on consideration of the leading terms in a multipole expansion of the intermolecular potential and also on consideration of the symmetry of the collision

process. The propensity rules for ΔJ changing collisions follow from the nonvanishing terms in an electric multipole expansion of the interaction potential. For a dipole interaction, the ΔJ propensity rule is $\Delta J = \pm 1, 0$, and the parity propensity rule is $+\leftrightarrow-$. For quadrupole interaction the ΔJ and parity propensity rules are $\Delta J = \pm 2, \pm 1, 0$ and $+\leftrightarrow+ / -\leftrightarrow-$. For octupole interaction there is the addition of $\Delta J = \pm 3$ processes and the parity propensity rule is $+\leftrightarrow-$. The propensity rule for Δk changing collisions follows from the symmetry of the molecule. For a molecule with an p -fold rotation axis, the propensity rule on Δk is $\Delta k = pn$, where n is an integer.

These propensity rules are in good agreement with many experimental studies, particularly for polar, symmetric top molecules. Oka cautions in his paper that the collisional propensity rules are really only applicable for weak collisions, the classic example being $\text{NH}_3\text{-NH}_3$ collisions at room temperature. In Appendix 1 we present the results of energy transfer experiments that were carried out in this laboratory on NH_3 . These results are included here as an example of rotational energy transfer in a highly polar, C_{3v} molecule where weak collisions dominate. The results of the kinetic analysis for R.E.T. in the $v_2 = 1$ state of NH_3 showed that the primary R.E.T. pathways were those that follow dipole-like propensity rules, $\Delta J = \pm 1, 0$ and $+\leftrightarrow-$ and the only k -changing collisions observed were $\Delta k = 3n$, as predicted by Oka's theory. The rates for the dipole-like pathways accounted for ~50% of the total rate. In addition to these processes following dipole-like propensity rules, smaller but significant rates were also observed for nondipole-like processes. This indicates that even for this prototypical case of a weak collision interaction, higher order terms in the interaction potential are significant.

Unlike NH_3 , both CHD_3 and CH_4 are closer to the strong collision limit. Propensity rules based on the multipole expansion of the intermolecular potential are not likely to be applicable for either, but propensity rules based on the overall symmetry of the collision process will still apply. In Oka's work the overall symmetry propensity rule is expressed by the $\Delta k = pn$ rule. The application of this rule to symmetric top molecules is straightforward, but for spherical top molecules it is not clear how this rule applies since k is not at all a good quantum number for these. Parson [PARSON90, PARSON91] has tackled this problem with a synthesis of the $\Delta k = pn$ propensity rule with the Harter-Patterson theory of spectral clustering [HARTER78]. Harter-Patterson theory describes the clustering seen in high rotational states of spherical top molecules as a distortion of the molecule along one of its symmetry axes. In this distorted form it is like a symmetric top. A "cluster quantum number", k_R , which represents the projection of the total angular momentum on the unique symmetry axis created by the distortion, can be assigned to these clusters. Parson's argument was that for impulsive collisions the $\Delta k = pn$ propensity rule should apply to k_R . He applied this analysis to the $^{13}\text{CD}_4$ and SiH_4 data and was extremely successful in describing the fine structure selectivity seen for both.

Parson's analysis illustrated that because vibration-rotation interaction causes distortion about their symmetry axes, spherical top molecules behave like symmetric tops during collisions. The study of R.E.T. in CHD_3 presented here was done to further expose the role of molecular symmetry on energy transfer processes. CHD_3 is a symmetric top molecule, like NH_3 , but with essentially no dipole moment ($\mu \sim 0.006 \text{ D}$) [DÜBAL89, MEERTS81]. In terms of its intermolecular potential it resembles a spherical top. However, its rotational energy level structure is that of an oblate symmetric top. Because of these properties, CHD_3 is an ideal test case for separating the effect of molecular symmetry from the dynamics of the collision process.

The complete tunability of our Raman-shifted Ti:sapphire I.R. source allows us to examine any rotational state we choose. For the R.E.T. studies in CH_4 presented here, we have concentrated on low J states. This is particularly interesting because the other studies of R.E.T. in spherical tops were done with relatively high J, $J > 10$. The prediction of Parson's theory for low J states is not at all clear, since spectral clustering is a high J property. These studies of R.E.T. for low J provide still more insight into the role of molecular symmetry on the energy transfer process.

Chapter 2. CHD₃ Spectroscopy

2.1 Introduction

A necessary prerequisite for the study of collisional energy transfer on a detailed state-to-state basis is knowledge of the spectroscopy of the system to be studied. Spectroscopy is the blueprint which allows us to effectively use our lasers as tools for the study of collisional interactions. Practical limitations based on the availability of suitable laser sources dictate which vibrational levels may be studied. The experimental technique used for the energy transfer experiments in CHD₃, which will be described in Chapter 3, is CO₂/infrared diode laser double resonance. The vibrational levels of interest in these experiments are those near 1000 cm⁻¹ which can be efficiently pumped with a CO₂ laser. These are the ν_3 and ν_6 fundamentals. A necessity for double resonance experiments are probe transitions which can be used to monitor energy transfer. For CHD₃ these are the hot bands originating from ν_3 and ν_6 . Often the systems which are the most amenable for kinetic studies are not the same as those which have been subject to extensive spectroscopic work. Fortunately, the ν_3 and ν_6 vibrational bands have been well studied and accurate spectroscopic assignments are known [DUPRE-MAQUAIRE82, ROCHE92]. While there has been extensive work on many of the overtone and combination bands of CHD₃, [LEWERENZ88], previous to this work there had been no spectroscopic studies of the hotbands of ν_3 and ν_6 nor of the binary overtone and combination bands of these two low-lying fundamentals. As the spectroscopy of these levels was essential for the initially proposed energy transfer studies, we partially analyzed the 2{ ν_3 , ν_6 } overtone and combination bands at 2000 cm⁻¹. This analysis* was extremely valuable for predicting hot band transitions which were vital to the success of the energy transfer experiments presented in Chapter 3. The results of this analysis have been published in the *Journal of Chemical Physics* **100**, 5508 (1994) and are reproduced here as Appendix 2.

2.2 Energy Level Structure of ν_3/ν_6 Dyad

CHD₃ is a symmetric top molecule belonging to the C_{3v} point group. It has six normal modes, three nondegenerate (A) and three doubly degenerate (E). The two lowest energy vibrations are the Coriolis-coupled ν_3/ν_6 dyad at ~1000 cm⁻¹. These levels are correlated to the triply degenerate ν_4 vibration of CD₄ [HERZBERG45, GRAY79]. Replacing a deuterium atom of CD₄ with a hydrogen atom reduces the T_d symmetry of CD₄ to the C_{3v} symmetry of CHD₃. The triply degenerate ν_4 vibration of CD₄ splits into a nondegenerate (A₁) and a doubly degenerate (E) vibration in CHD₃. These are, respectively, ν_3 and ν_6 . A reduced energy level diagram for ν_3 and ν_6 is shown in Figure 2.1. It can be seen from this figure that the splitting in the vibrational structure caused by the reduction in symmetry is not large. The band centers of ν_3 and ν_6 are only separated by 31.3 cm⁻¹ [DUPRE-MAQUAIRE82].

* Dr. Christine Roche is gratefully acknowledged for her substantial work on this analysis.

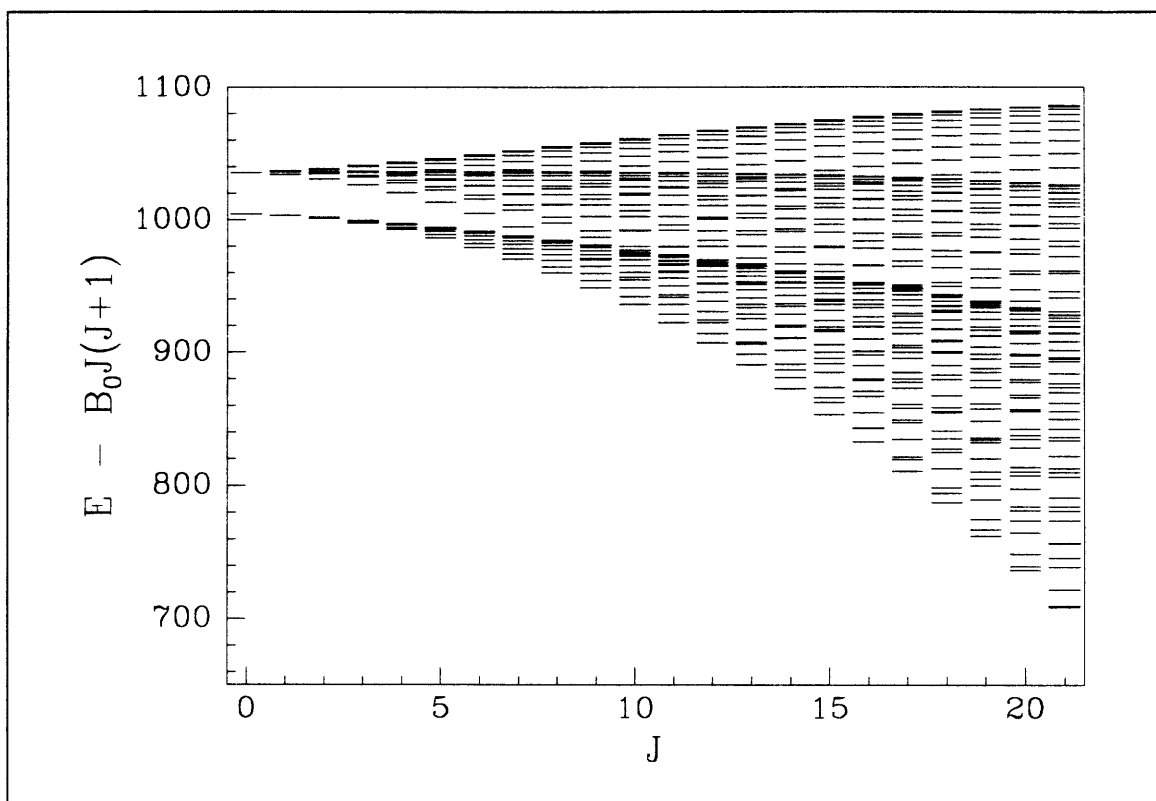


Figure 2.1
Reduced energy level diagram for the CHD₃ ν_3/ν_6 dyad

While the splitting in the vibrational structure caused by the change in symmetry in going from CD₄ to CHD₃ is not large, the effect on the rotational structure is pronounced. CHD₃ is an oblate symmetric top and its rotational level structure is completely consistent with this. Since CHD₃ belongs to the point group C_{3v}, the species of its total wavefunction is either A or E with respect to the rotational subgroup C₃. This is quite different from CD₄ which has its wavefunctions classified in T_d as either A, E or F. There can be no spectroscopic transitions linking the A and E levels of CHD₃, nor can they interact through collisions, though in Chapter 3 we describe a vibrational swap process which causes an apparent exchange between A and E levels. The species of a rovibrational level is determined by $|K-l|$. Only levels which have $|K-l| \equiv (0 \pmod{3n})$ are of A type symmetry. All others are of E symmetry.

2.3 2{ ν_3, ν_6 } Overtone and Combination Bands

CHD₃ spectra were recorded in the range of 1850-2150 cm⁻¹. The bands falling within this range consist of the 2 ν_3 , $\nu_3+\nu_6$, and 2 ν_6 overtone and combination bands and the QP and QQ branches of the ν_2 fundamental. These spectra were obtained on the modified BOMEM DA3.002 at the Herzberg Institute for Astrophysics, NRCC, Ottawa, Canada. A temperature adjustable, multipass cell with a base pathlength of 2 m was used. Two high quality spectra were obtained. Both covered the same frequency

range but were recorded at different pressure paths and temperatures. A low temperature, 103 °K, spectrum was recorded at a pressure of 330 mtorr and a total pathlength of 24 m. A warmer temperature spectrum, 264 °K, was taken at 360 mtorr with a 48 m pathlength. Absolute calibration of the spectra was made by reference to CO transitions [HITRAN92], CO being a trace impurity in the CHD₃ sample.

The overtone spectra are quite complicated. The same Coriolis interaction that affects the ν_3 and ν_6 fundamentals is even more pronounced in the overtones and combination band. The majority of transitions are not assignable simply by inspection. Through the use of combination differences and the relative intensities of the two different temperature spectra, which allows an estimate of the ground state energy to be made, assignments and isolated band fits have been made for the $2\nu_3$ and partial assignments for $2\nu_6$ (E), $2\nu_6$ (A), and $\nu_3+\nu_6$ $l = +1$. The P-branch of $2\nu_3$ was the only part of the spectra that could easily be assigned by inspection alone. A stick spectrum of the $2\nu_3$ band is shown in Figure 3.3. Fortunately, assignment of this band was sufficient to allow us to make enough hotband assignments to do a substantial amount of energy transfer work in the ν_3/ν_6 dyad. Using the assignments for $2\nu_3$ and the well known parameters for the ground state [ROCHE93] and the ν_3/ν_6 dyad [ROCHE92] we were able to calculate $2\nu_3$ - ν_3 hotband transitions with great accuracy. A high resolution FTIR spectrum of CHD₃ in the 10 μm region was very useful in identifying these hotbands as was the diode laser spectroscopy we did in our own lab.

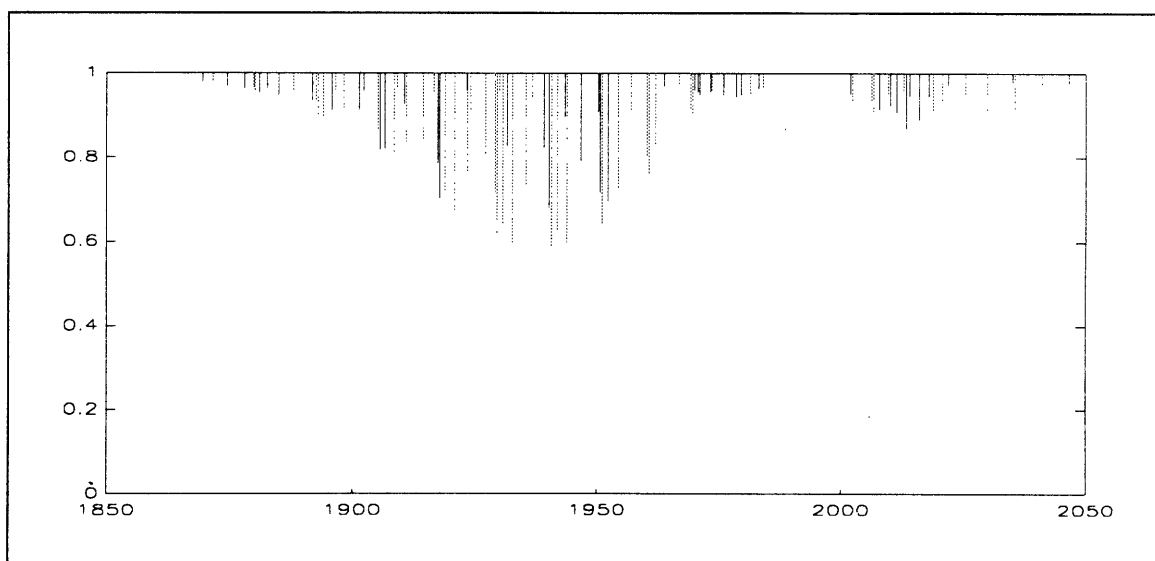


Figure 2.2

Stick spectrum of the CHD₃ $2\nu_3$ overtone. The intensities and line positions have been taken from the 103 °K spectrum. The P-branch is strong and regular, but the Q- and R-branches are weak and have many missing lines.

Chapter 3. CHD₃ Energy Transfer

3.1 Introduction

This chapter presents the description and results of all the energy transfer experiments that were carried out with CHD₃. Measurements of total depopulation rates from a single rotational level in a vibrationally excited state have been carried out for three different initial states for both self collisions and collisions with noble gases and simple polyatomic partners. The corresponding process of the total rate of population refilling a depleted level in the vibrational ground state has also been measured. The fast process of vibrational energy transfer between two nearly degenerate and strongly Coriolis coupled vibrations has been measured, as has also the slower rate of vibrational excitation exchange between a vibrationally excited molecule and a ground state molecule as evidenced by an apparent nuclear spin changing process. This latter process is neatly explained by invoking a very simple, zero-adjustable-parameter Förster mechanism. Finally, we present the results of a detailed master equation analysis of rotational energy transfer in a vibrationally excited state for two initially excited levels having different nuclear spin symmetry.

The results of this work have been published in the *Journal of Chemical Physics* **100**, 5519 (1994). A preprint of this article is included as Appendix 3. The reader is directed to this Appendix for the conclusions of this work which will only be summarized here. This chapter will focus more on the details of the experimental setup and data reduction techniques than were presented in the paper in Appendix 3.

3.2 Previous Experimental Studies

Previous studies of energy transfer in CHD₃ complement the work presented here. Two early studies of V→T,R and V→V processes used a Q-switched CO₂ laser to populate the ν₃/ν₆ vibrational levels and time-resolved I.R. fluorescence to monitor energy transfer [DROZDOSKI77] and [DROZDOSKI78]. In this work the V→T,R rate for CHD₃ self collisions was measured as $8.4 \times 10^{-4} \mu\text{sec}^{-1} \text{ torr}^{-1}$. The rates for V→T,R for CHD₃ with other collision partners was found to scale exponentially with the square root of the reduced mass of the collision partners. V→V rates were measured for the ν₃/ν₆ vibrational levels to other vibrational levels. From the rise time of the I.R. fluorescence the V→V energy transfer rates from ν₃/ν₆ to ν₅ and ν₂/ν₄ were determined as $0.18 \pm 0.03 \mu\text{sec}^{-1} \text{ torr}^{-1}$ and $0.30 \pm 0.05 \mu\text{sec}^{-1} \text{ torr}^{-1}$, respectively. The rate to the ν₁ fundamental could not be determined although a lower bound was set at $0.25 \mu\text{sec}^{-1} \text{ torr}^{-1}$.

In more recent experiments [MENNARD-BOURCIN88] time resolved infrared double resonance (TRIRD) was used to investigate V→T,R, V→V, and A←E vibrational swap processes. Menard-Bourcin and Doyennette used two CO₂ lasers, Q-switched and c.w., to pump and probe coincident

transitions in the ν_3/ν_6 dyad. Their determination of $V \rightarrow T,R$ of $1.16 \pm 0.35 \times 10^{-3} \mu\text{sec}^{-1} \text{ torr}^{-1}$ is in good agreement with the work of Drozdowski *et. al* [DROZDOSKI77]. An apparent $A \leftarrow E$ symmetry changing rate of $0.23 \pm 0.02 \mu\text{sec}^{-1} \text{ torr}^{-1}$ was found. A $V \rightarrow V$ rate between the coriolis coupled ν_3 and ν_6 vibrations could not be determined. It was estimated that the process is very fast, on the order of $10 \mu\text{sec}^{-1} \text{ torr}^{-1}$.

In the work presented here, the availability of a high power, short pulse length TEA CO_2 laser and narrow bandwidth, tunable diode lasers along with the new spectroscopic information about the overtone, combination bands, and particularly hot bands of ν_3 and ν_6 allowed a detailed study of rotational energy transfer in the ν_3/ν_6 dyad of CHD_3 which was not possible in these earlier studies.

3.3 Experimental Arrangement for Time-resolved CO_2 -Infrared Diode Laser Double Resonance

For the energy transfer experiments in CHD_3 , the CO_2 /diode laser double resonance technique that is well developed in this laboratory was used with great success. The experimental apparatus has been described a number of times [FOY88] and [HETZLER89]. The cumulative experience of several generations now of graduate students has made this system, although not trivial to use, very reliable and extremely fruitful. We review here the basic components of the experimental setup and the minor enhancements that were used to advantage in the CHD_3 work. A schematic diagram of the experimental setup is shown in Figure 3.1.

In its earlier configuration, the pump and probe beams in this double resonance setup were counterpropagated and spatially crossed at a small angle in order to combine and separate the two. As the setup was used for most of the measurements described here, slight modifications were made in order to achieve better beam overlap and hence improve the signal amplitude. The pump and probe beams were linearly polarized and perpendicular to one another. This crossed polarization was advantageous both for combining the beams and for discriminating against the much more intense CO_2 laser radiation which wreaks havoc when it falls on the sensitive diode laser source and detection equipment. The perpendicular relative polarization of the pump and probe was also used to good advantage to achieve completely collinear overlap of the two beams. Dichroic mirrors cannot be advantageously used as beam combiners when both sources are nearly the same wavelength. However, the difference in reflectivity and transmission for s- and p-polarized light on a substrate of high refractive index at large incident angles can be used effectively to combine beams of the same wavelength, see Fig. 3.2. A ZnSe plate ($n_{10\mu\text{m}} = 2.41$) was placed in the diode laser beam plane at an angle of 75° . At this angle, transmission of the diode laser beam, which was p-polarized with respect to the ZnSe plate, was high, $\sim 96\%$. However, the CO_2 laser beam, which was s-polarized with respect to the ZnSe plate was highly reflective at this angle, $\sim 60\%$. With 20-30 mJ of CO_2 laser pulse energy available, the loss in pump power was more than offset

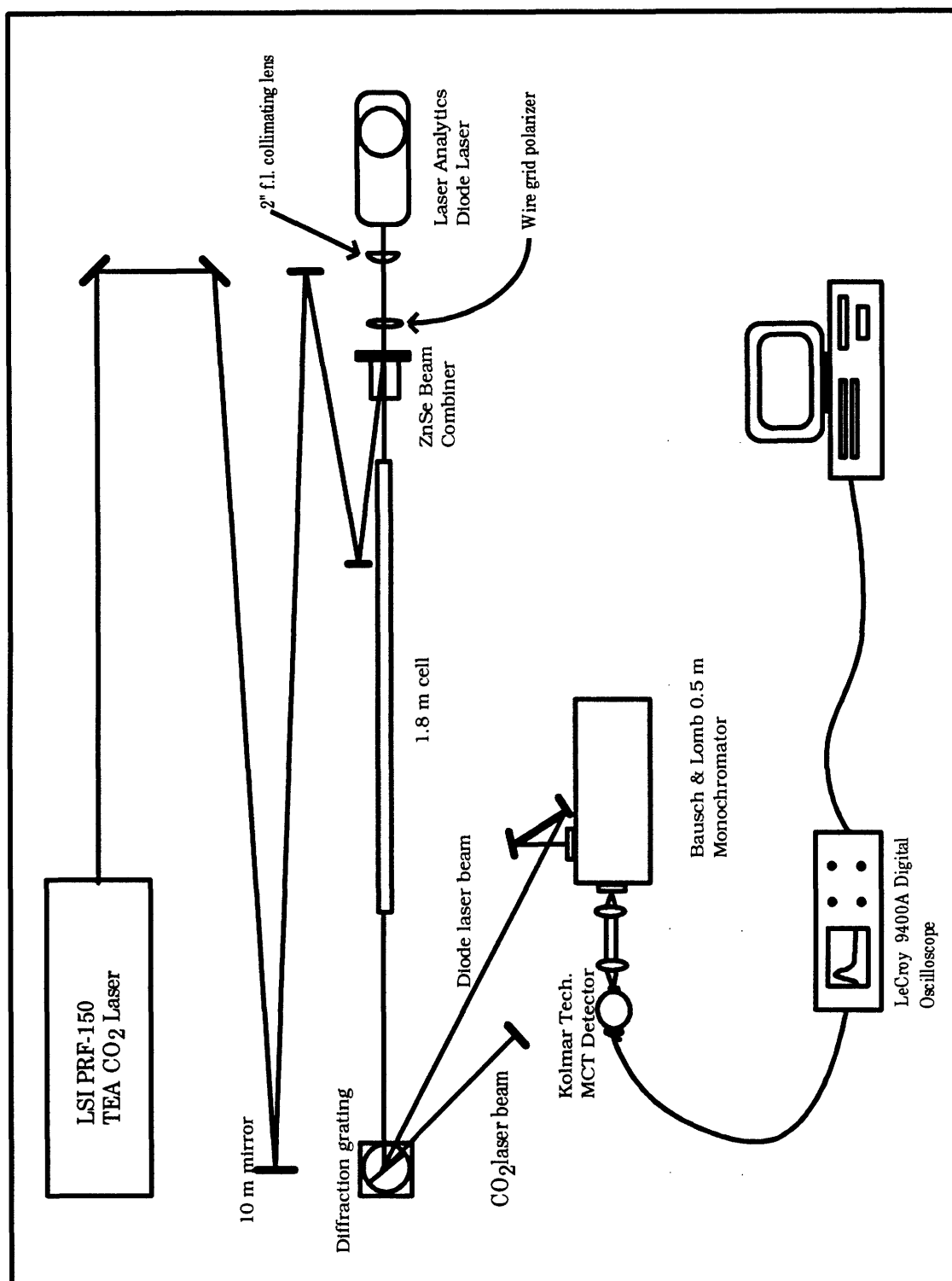


Figure 3.1

Experimental arrangement for CO₂-diode laser time-resolved double resonance as it was used for state-to-state R.E.T. measurements in CHD₃

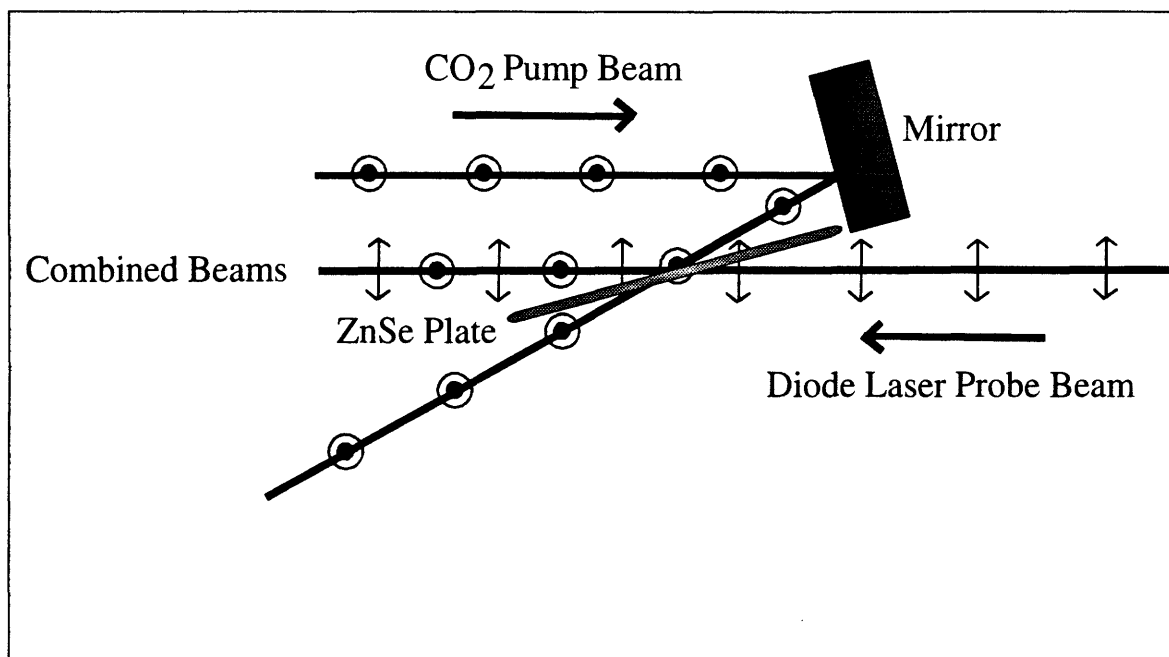


Figure 3.2

Schematic of optics used to combine perpendicularly polarized CO₂ pump and diode laser probe.

by the increase in interaction length from having the beams completely collinear over the entire length of the cell.

After the beams were combined, they were copropagated through a 1.8 m double resonance cell. The cell was constructed from pieces of stainless steel tubing fitted with 3.5" Conflat flanges which were sealed with Viton o-rings. This construction made the cell very easy to assemble and disassemble and allowed use to be made of many high quality pieces of standard UHV plumbing. It also proved to be a very vacuum-tight arrangement. Leak rates of 1 mtorr/hr or less were achieved with careful assembly. The windows on the cell were BaF₂ which has fairly good transmission characteristics, ~90%, at 9.5-10 μm . These were mounted onto conflat blanks which had o-ring grooves machined onto the outside and were held in place with a retaining ring. Sample pressures inside the cell were measured with a 1.0 torr capacitance manometers (MKS baratron Model 127).

Exiting the double resonance cell, the pump and probe beams were separated by a diffraction grating. The CO₂ laser beam was sent to a beam dump and the diode laser beam was directed through a monochromator (Bausch & Lomb, 0.5 m). This served both to further isolate the weak diode laser probe from scattered light due to the CO₂ laser and to allow only one mode of the diode laser to reach the detector. The detector used was a liquid nitrogen cooled photoconductive MCT (Kolmar Technologies).

This was a high sensitivity (0.77 quantum efficiency at 10 μm , 7.27 amp/watt responsivity), low noise ($D^* = 1.94 \times 10^{10}$ at 10.6 μm), and fast response (rise time 18 nsec) detector/amplifier combination. The transient diode laser absorption signals monitored with this detector were recorded and averaged on a digital oscilloscope (LeCroy 9400A). Depending on the signal-to-noise ratio, several hundred to several thousand transients were averaged on the scope. These averaged signals were then transferred to a PC for storage and analysis. A software package (MASP) was provided by LeCroy to interface its 9400A oscilloscope via GPIB to a PC. The code for a C program (SIGNAL) which converts the LeCroy .tra formatted data files to an ASCII format that can be read directly into MATLAB is given in Appendix 4.

The pump laser used in the double resonance experiments was an LSI PRF 150S TEA CO_2 laser. The laser was operated on a 8:3 mix of helium and CO_2 with essentially no N_2 in the mix. In practice the N_2 flow into the laser cavity was adjusted so that the ball in the flow meter just barely lifted out of its seat. This low percentage of N_2 in the gas mix was done to prevent the long after pulse or "nitrogen tail" which was present with higher percentages of N_2 . The presence of the after pulse would have made interpretation of time resolved kinetic data difficult. The pulse width under the conditions used for these experiments was 120 nsec. Displayed in Figure 3.3 is the time profile of the CO_2 pulse recorded when the laser was operating on the 10R(24) transition. Curve a is the pulse recorded with a fast response (~ 1 nsec) photon drag detector (Rofin Optics and Electronics). Axial mode beating is clearly evident in curve a. Axial mode beating occurs when there is lasing action on two or more of the longitudinal cavity modes at the same time [SIEGMAN86]. These modes are separated in frequency by the amount $c/2L$. Multimode operation broadens the spectral width of the laser pulse and causes complications in some double resonance cases since more than one transition may be effectively pumped by the broad bandwidth pulse. The laser bandwidth can be reduced by running on a single longitudinal mode (SLM). This is conveniently accomplished for a TEA CO_2 laser by introducing a low-pressure, narrow bandwidth gain cell within the laser cavity. For the LSI PRF 150S this was a short (~ 25 cm) discharge cell through which a CO_2 gas mix was run at a pressure of approximately 10 torr. There was no lasing action in this cell. Instead it provided a region of narrowband preferential gain. Curve b in Fig. 3.2 shows the pulse profile when the laser was run with the gain cell on. The laser pulse was recorded with the same photon drag detector used to observe the mode beating shown in curve a. The smooth temporal profile in curve b indicates that the laser was operating on a single longitudinal mode. Curve c shows the multimode pulse as detected by the same fast MCT detector (Kolmar Technologies) used in the energy transfer experiments to monitor the diode laser transient absorption. This detector followed the overall temporal profile of the laser pulse, but was not fast enough to resolve the mode beating.

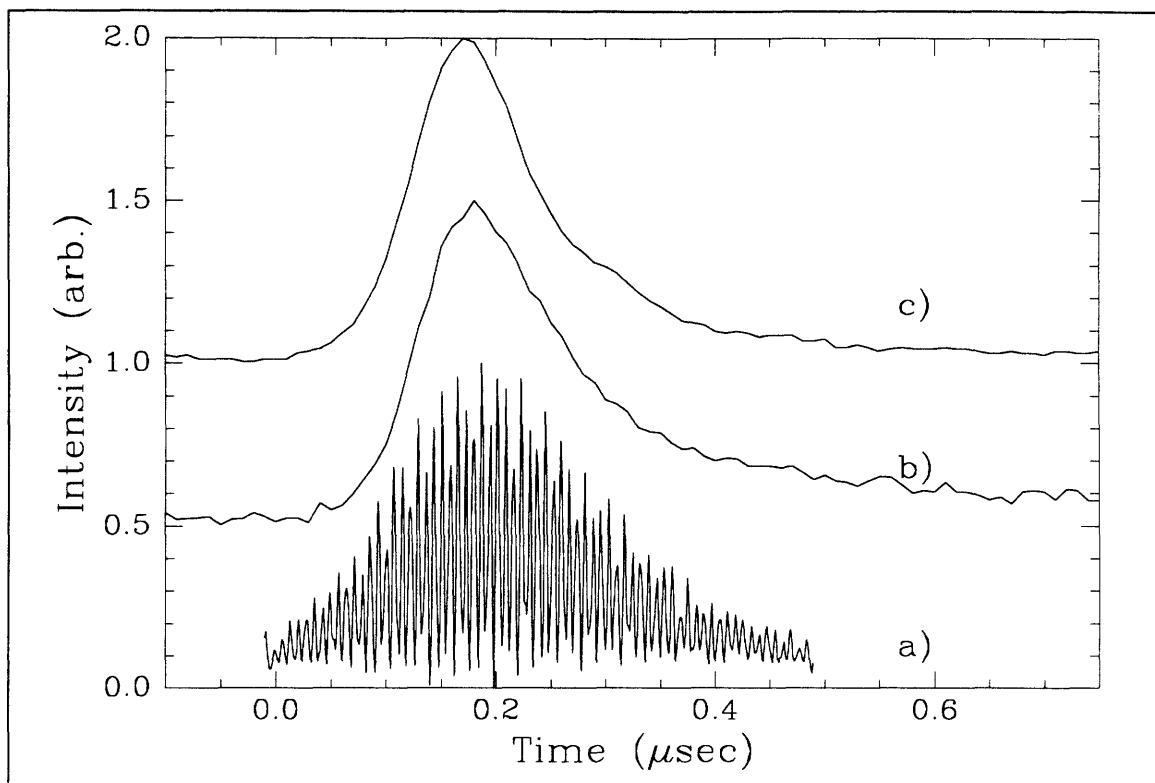


Figure 3.3

Temporal profile of LSI PRF 150S CO₂ laser at 10R(24). a) multimode operation recorded with photon drag detector; b) single longitudinal mode operation recorded with photon drag detector; c) multimode operation recorded with fast MCT.

The probe lasers used in these double resonance experiments were lead salt tunable diode lasers (Laser Photonics, Analytics Division 10 μm diodes: S/N 9081-16 and 9094-05; 7.8 μm diode: 270-03). The diodes operating near 10 μm were specifically selected to have good lasing characteristics at 1020 cm⁻¹. This is the center of the region containing the best probe transitions for CHD₃ double resonance with a CO₂ pump laser. The diode lasers output frequency could be adjusted from about ~950 cm⁻¹ to ~1060 cm⁻¹ with more than 50% of this range being covered by good modes. The diode 9081-16 was an exceptionally good performer. The output of these diodes was always multimode. Typically 5-6 modes lase simultaneously each being separated in frequency from its nearest neighboring mode by a few cm⁻¹. The relative power in the mode of interest could be maximized by adjusting the diode laser temperature. Shorter wavelengths required warmer temperatures; longer, cooler. Single modes were easily isolated with a monochromator. Isolated, single, diode laser modes have very narrow bandwidth, on the order of 5 x 10⁻⁴ cm⁻¹, and output powers of 10-100 μW.

Infrared diode lasers systems exhibit some quirky behavior which makes them different from other laser systems. First, they have extremely divergent output. A 2" f.l. Irtran lens mounted on an XYZ stage was

used to collimate the beam and to provide some steering of it down the optical table. A wire grid polarizer was placed after this lens. The diode laser beam was already linearly polarized. The polarizer was used to prevent scattered CO₂ light from reaching and transiently warming the diode. Such slight heating would change the diode laser frequency sufficiently to cause the laser to go off resonance. The beam profile of the diode lasers was far from gaussian, having instead an elliptical shape. A pair of irises, one immediately in front of the laser and another some 40-50 cm down the table, was used to select only the central portion of this elliptical beam. This not only created a more gaussian beam profile, it also was essential for beam stability. The outer portions of the beam were much more sensitive to minor temperature and mechanical fluctuations. These lasers operated at cryogenic temperatures, ~20-60 °K, and so they were mounted in a closed-cycle helium refrigeration unit, a cold head. A mechanical piston delivered a charge of cold helium to the tip of the refrigeration unit which is in thermal contact with the brass heat sink on which the diode lasers were mounted. Unfortunately, this mechanical cooling system also adversely affected the power and pointing stability of the diode lasers. In the worst case mechanical vibrations transmitted to the diode lasers by the cooling system would cause power fluctuations of 100%, complete on/off behavior at three Hz, making any time resolved experiment hopeless. Under such conditions the only solution is to replace the cold head motor. Cold head motors last for approximately one year of continuous service before needing to be reconditioned.

The trideuteromethane (CHD₃) gas samples used in all experiments was obtained from MSD Isotopes. These samples were 98 atom % deuterium. Trace quantities of other gases (CO and NO) from the synthesis process were also present. These trace gases were not easily removed and so the samples were used as delivered. Methane does not completely freeze out in liquid nitrogen; it has a sublimation pressure of ~ 13 torr at 77 °K [CRC93]. Extensive use of freeze/pump/thaw cycles was not practical. In daily use, such quantities of CHD₃ gas as were possible were frozen out in liquid nitrogen. The gas bulb was then briefly opened to vacuum to remove air that may have entered. Before resuming experiments after extended periods of nonuse, new samples of CHD₃ were purchased.

3.4 Pump-Probe Double Resonance Scheme

A double resonance experiment which uses a CO₂ laser as a pump source necessitates a coincidence between the strong CO₂ laser transitions and molecular rovibration transitions. For CHD₃ this means that the vibrational states that can be populated belong to the ν_3/ν_6 dyad near 1000 cm⁻¹. There are a number of possible coincidences which are listed in Table 3.1. For rotationally resolved energy transfer experiments the pump transition should be a strong CO₂ laser line, be closely coincident with a strong molecular transition, and should populate only a single rovibrational level. The CO₂ 10R(22), 10R(24), and 10R(34) transitions most closely meet these criteria.

In Table 3.1 the intensity is given as molecular line strengths, S , with units of cm molecule^{-1} , or equivalently $\text{cm}^{-1} \text{cm}^2 \text{molecule}^{-1}$ [SMITH88, PUGH76]. From dimensional analysis, it can be seen that S has units of molecular cross section ($\text{cm}^2 \text{molecule}^{-1}$) times frequency (cm^{-1}). S is just the absorption cross section integrated over the molecular lineshape. It is related to the more familiar extinction coefficient in the Beer-Lambert law, $\alpha(\bar{\nu})$.

$$\alpha(\bar{\nu}) = S g(\bar{\nu} - \bar{\nu}_0) N \quad \text{Eq. 3.1}$$

In Eq. 3.1, $g(\bar{\nu} - \bar{\nu}_0)$ is the normalized line shape function having units of cm and N is the number density of the absorbing gas per atmosphere ($\text{molecule cm}^{-3} \text{atm}^{-1}$). Under the experimental conditions employed for the work presented here, $g(\bar{\nu} - \bar{\nu}_0)$ can always be accurately estimated as a Doppler or Gaussian line profile.

The molecular line strength is an important indicator of the effectiveness with which a transition can be pumped, and so it is also an indication of how successful an experiment may be. Knowing the molecular line strength and the pulse energy and bandwidth of the pump laser, it is possible to estimate the amount of population which will be moved by the pump laser. This is important information for the experimentalist. The double resonance signals observed for the experiments described here all depend on changing the equilibrium population of some particular state with the pump laser. Once a transition is saturated, no further enhancement of the signal would be achieved by increasing the pump laser power. Any improvement in the signal must then come from the probe side of the double resonance scheme. On the other hand, if the amount of population moved is less than that detectable by the probe technique, no amount of perseverance in the lab will produce data. In either case, it is to the experimenter's advantage to have some *a priori* knowledge of the effectiveness of the pump laser/molecular transition combination.

The amount of population moved by the pump laser can be successfully modeled using a simple, two-level rate equation kinetic model [STEINFELD74]. The rate equation model provides an intuitive picture of the dynamics occurring between molecules and high power, pulsed laser radiation, and within the limits of its validity, it can also provide quantitatively correct results of the degree of saturation which can be achieved with a particular pump transition. In the two-level rate equation model, induced transitions from the lower level of the pump transition, $|1\rangle$, to the upper level, $|2\rangle$, occur at a rate k_{12} , and stimulated emission from $|2\rangle$ to $|1\rangle$ occurs at a rate given by $k_{21} = (g_1/g_2)k_{12}$, where g_1 and g_2 are the degeneracies of $|1\rangle$ and $|2\rangle$ respectively. Level $|2\rangle$ can also return to $|1\rangle$ through spontaneous emission at a rate given by the Einstein A_{21} coefficient. Using these constants, the kinetic equations for the population in levels $|1\rangle$ and $|2\rangle$ are given in Eqs. 3.2 and 3.3.

CO ₂ line	Frequency cm ⁻¹	Transition	Sym.	Frequency cm ⁻¹	Intensity cm molecule ⁻¹	Detuning cm ⁻¹
10P(4)	957.8005	R _P (12,3)	A	957.8051	8.83x10 ⁻²³	-0.0046
10R(6)	966.2504	R _P (18,3)	A ₂	966.2633	1.62x10 ⁻²²	-0.0129
10R(8)	967.7072	P _P (11,10)	E	967.7381	4.70x10 ⁻²¹	-0.0309
10R(10)	969.1395	R _P (10,7)	E	969.1588	6.36x10 ⁻²²	-0.0193
10R(12)	970.5472	R _P (17,0)	A ₂	970.5282	2.64x10 ⁻²²	0.0190
		P _P (16,5)	E	970.5411	6.33x10 ⁻²²	0.0061
10R(16)	973.2885	P _P (16,2)	E	973.2656	6.17x10 ⁻²²	0.0229
10R(18)	974.6219	Q _Q (20,17)	E	974.6324	1.02x10 ⁻²²	-0.0105
10R(22)*	977.2139	R _P (9,3)	A	977.2236	2.91x10 ⁻²²	-0.0097
10R(24)*	978.4723	Q _Q (12,7)	E	978.4702	9.56x10 ⁻²²	0.0021
		Q _Q (11,5)	E	978.4365	7.23x10 ⁻²²	0.0358
10R(30)	982.0955	P _P (13,3)	A ₁	982.0689	1.39x10 ⁻²¹	0.0266
		Q _Q (9,2)	E	982.0980	2.66x10 ⁻²²	-0.0025
10R(34)*	984.3832	Q _Q (12,9)	A	984.3804	2.55x10 ⁻²¹	0.0028
		Q _Q (16,14)	E	984.3969	7.56x10 ⁻²²	-0.0137
9P(36)	1031.4774	R _Q (18,13)	E	1031.4824	2.24x10 ⁻²²	0.0050
9P(32)	1035.4736	R _Q (14,6)	A	1035.4729	1.85x10 ⁻²¹	0.0007
		R _Q (16,6)	A	1035.4786	8.50x10 ⁻²²	0.0050
9P(22)	1045.0217	P _Q (5,2)	E	1045.0440	4.86x10 ⁻²³	-0.0223
9P(8)	1057.3002	P _Q (16,13)	E	1057.2865	1.82x10 ⁻²²	0.0137
9P(6)	1058.9487	Q _R (14,3)	A	1058.9392	2.53x10 ⁻²¹	0.0095
9R(12)	1073.2785	R _Q (18,11)	E	1073.2614	4.70x10 ⁻²³	0.0171
9R(26)	1082.2962	Q _R (17,12)	A	1082.2767	7.81x10 ⁻²²	0.0195
9R(28)	1083.4788	Q _R (20,10)	E	1083.4910	1.17x10 ⁻²²	-0.0122

Table 3.1

CO₂ laser/CHD₃ absorption coincidence table. CO₂ laser frequencies are from the Handbook of Infrared Standards [GUELACHVILI86] and the CHD₃ assignments and intensities are from the analysis by Dupre-Maquaire and Tarrago [DUPRE-MAQUAIRE82]. The transitions marked with an asterisk are the ones used in energy transfer experiments.

$$dN_1 / dt = -k_{12}N_1 + (k_{21} + A_{21})N_2 \quad \text{Eq. 3.2}$$

$$dN_2 / dt = -(k_{21} + A_{21})N_2 + k_{12}N_1 \quad \text{Eq. 3.3}$$

These two coupled differential equations can be solved to yield expressions for the time evolution of the population in levels $|1\rangle$ and $|2\rangle$ subject to the initial conditions that $N_1(0) = 1$ and $N_2(0) = 0$.

$$N_1(t) = \frac{k_{21} + A_{21}}{k_{12} + k_{21} + A_{21}} + \left[1 - \frac{k_{21} + A_{21}}{k_{12} + k_{21} + A_{21}} \right] e^{-(k_{12} + k_{21} + A_{21})t} \quad \text{Eq. 3.4}$$

$$N_2(t) = \frac{k_{12}}{k_{12} + k_{21} + A_{21}} \left[1 - e^{-(k_{12} + k_{21} + A_{21})t} \right] \quad \text{Eq. 3.5}$$

From these equations it is possible to estimate the amount of population moved by the pump laser pulse once the rate constants k_{12} , k_{21} , and A_{21} are derived from molecular and experimental parameters. The rate constants are all related to the molecular line strength. A very nice discussion of the conversion between the various measures of molecular absorption strength is given in the paper by Hilborn [HILBORN82]. The spontaneous emission rate, A_{21} , is found from S (in units of $\text{cm}^2 \text{cm}^{-1} \text{molecule}^{-1}$) by the relationship

$$A_{21} = \frac{g_1}{g_2} 8\pi c \tilde{\nu}^2 S. \quad \text{Eq. 3.6.}$$

The rate constants for induced absorption, k_{12} , and stimulated emission, k_{21} , are the product of the Einstein B coefficients and the pump laser spectral irradiance (power per unit area per unit frequency interval),

$$k_{12} = B_{12} I(\tilde{\nu}). \quad \text{Eq. 3.7}$$

The conversion between the B_{12} and S depends on how one describes the "intensity" of the pump laser. Using spectral irradiance, units of $\text{W}/(\text{cm}^2 \text{cm}^{-1})$, as the measure of "intensity", B_{12} in terms of S is given in Eq 3.8.

$$B_{12}^{\bar{\nu}} = \frac{S}{h c \bar{\nu}} \quad \text{Eq. 3.8}$$

Using the CHD_3 ν_3 QQ(12,9) "A" transition at 984.3804 cm^{-1} as an example, the Einstein A and B coefficients can be calculated from Eqs. 3.6 and 3.8 using the measured line strength of $2.55 \times 10^{-21} \text{ cm molecule}^{-1}$, and the relative population of the upper and lower levels can be predicted from Eqs. 3.4 and 3.5 as a function of the pump laser energy. The degeneracies of the upper and lower levels of the ν_3 QQ(12,9) "A" transition are the same, so $g_1/g_2 = 1$ and $k_{12} = k_{21}$. From Eq. 3.6, the spontaneous emission rate at this transition is $1.86 \times 10^3 \text{ sec}^{-1}$. From Eq. 3.8, $B_{12}^{\bar{\nu}}$ is $0.130 \text{ cm}^2/\text{J}$. The induced absorption and stimulated emission rate, $k_{12} = k_{21}$, can be found from Eq. 3.7 after evaluation of the pump laser's spectral irradiance. This is estimated by assuming that the pulse profile in both the time and frequency domains is rectangular. Assuming a rectangular laser bandwidth is a fair assumption as long as it is much larger than the molecular linewidth. The spectral irradiance is then estimated as

$$I = \frac{E_{\text{pulse}}}{\Delta t \phi \Delta \bar{\nu}} \quad \text{Eq. 3.9}$$

E_{pulse} is the laser pulse energy in Joules, Δt is the temporal FWHM of the pulse in seconds, ϕ is the beam cross section in cm^2 , and $\Delta \bar{\nu}$ is the laser bandwidth (FWHM) in cm^{-1} . Using some typical parameters, $E_{\text{pulse}} = 0.015 \text{ J}$, $\Delta t = 120 \text{ ns}$, $\phi = \pi(d/2)^2 = 0.071 \text{ cm}^2$ ($d = 0.3 \text{ cm}$), and $\Delta \bar{\nu} = 1 \text{ GHz} = 0.033 \text{ cm}^{-1}$, the induced absorption and stimulated emission rates, k_{12} and k_{21} , are $7.0 \times 10^6 \text{ s}^{-1}$. The contribution of these two rate constants to the time evolution of the population in levels $|1\rangle$ and $|2\rangle$ as given in Eqs. 3.4 and 3.5 is ~ 4 orders of magnitude greater than the effect of A_{21} . Because it is so much smaller than the induced absorption and stimulated emission rates, the spontaneous emission rate can be ignored for calculating the extent of saturation.

The predicted relative population in the upper level of the ν_3 QQ(12,9) "A" transition plotted as a function of the CO_2 laser pulse energy is shown as the solid curve in Figure 3.4. Since the degeneracies of the upper and lower levels are the same, the upper state population at saturation approaches 50% of the initial population in the lower level. The individual points are experimental measurements of the relative upper state population. They are the increase in diode laser absorption immediately following the laser pulse when the diode laser was tuned to a transition originating in the upper level of the pump transition. The experimental points have been adjusted by an overall scale factor to fall onto the predicted curve, but the predicted curve has not been in any way fit to the experimental data. The predicted curve is derived entirely from the measured line strength and the laser pulse parameters as given in the example above.

The good agreement between the relative variations in the measured and calculated values is justification for the validity of the rate equation model in this double resonance scheme. Also, this calculation informs us that at the pulse energy typical for the measurements reported here, ~ 15 mJ/pulse, the ν_3 $Q_Q(12,9)$ "A" transition is about 60% saturated.

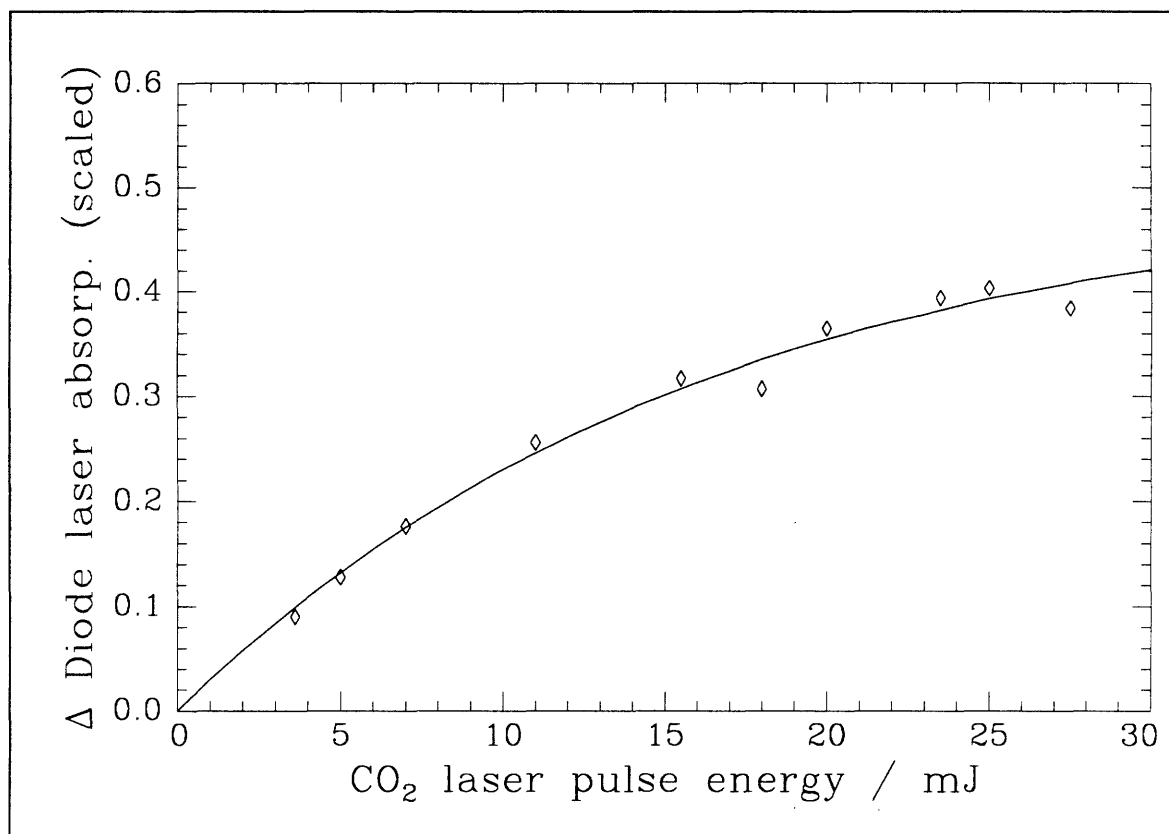


Figure 3.4

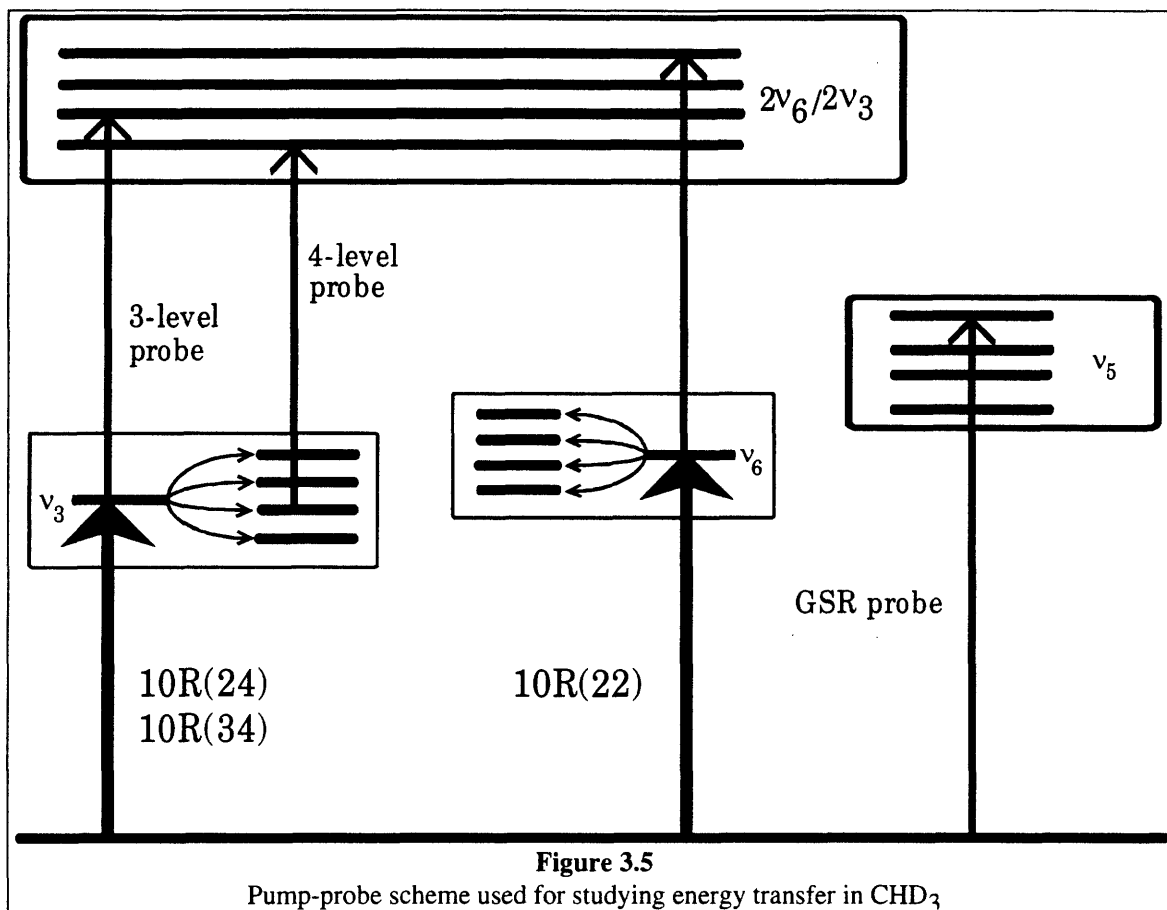
The solid curve is the amount of population transferred to the upper level of the ν_3 $Q_Q(12,9)$ "A" transition relative to the lower level predicted from Eq. 3.5 using the molecular and laser parameters described in the text. The symbols are scaled values of the measured change in diode laser absorption on a 3-level transition at various CO₂ laser pulse energies.

The line strengths of the CHD₃ transitions used for double resonance are fairly weak when compared with those of some other molecules studied in this lab. For example, the ozone ν_3 $17_{4,13} \leftarrow 16_{4,12}$ and ν_3 $10_{5,6} \leftarrow 9_{5,5}$ transitions, which were used as pump transitions for state-resolved energy transfer [FLANNERY93], have line strengths of 3.11×10^{-20} cm molecule⁻¹ and 1.86×10^{-20} cm molecule⁻¹, respectively. These are about an order of magnitude stronger than the CHD₃ pump transitions. The ammonia transition used for double resonance [APPENDIX1], ν_2 $Q_a(5,3)$, is another order of magnitude

stronger. Its very impressive line strength is 1.36×10^{-19} cm molecule $^{-1}$. The much weaker pump and probe transitions for CHD₃ necessitated optimizing the experimental setup to have state-to-state energy transfer measurements of the similar quality to those obtained in previous work.

Figure 3.5 shows schematically the pump/probe combinations that were used in the energy transfer experiments. Because most of the hotband assignments known for the ν_3/ν_6 dyad originate in ν_3 , extensive use was made of the 10R(24) and 10R(34) CO₂ laser lines, both of which populated rotational levels in $\nu_3 = 1$. Both of these transitions were used for studying rotational energy transfer in ν_3 . The 10R(34) pump transition populated the $\nu_3(12,9)$ "A" rovibrational level and also, within the laser's multimode bandwidth, the $\nu_3(16,14)$ "E" level, although this level was not as greatly populated as the $\nu_3(12,9)$ "A" due to the coincidence mismatch. This did not cause any problems in the analysis of rotational energy transfer since the "A" and "E" levels do not interconvert on the time scale of RET, as will be shown later. The 10R(24) pump is in near perfect coincidence with the $\nu_3(12,7)$ "E" transition, $\Delta\nu = 2.1 \times 10^{-4}$ cm $^{-1}$. Just barely within the CO₂ laser multimode bandwidth, the 10R(24) transition also populated the $\nu_3(11,5)$ "E" level, $\Delta\nu = 0.033$ cm $^{-1}$. These two levels are both the same nuclear spin species and are very close in energy. Simultaneously populating both of these levels would have made the interpretation of rotational energy transfer very difficult. Fortunately, running the CO₂ laser on a single longitudinal mode sufficiently narrowed the laser bandwidth so that only the very near coincident $\nu_3(12,7)$ "E" level was pumped. SLM operation was used for all rotationally resolved energy transfer experiments with the 10R(24) pump. The 10R(22) laser line populated the $\nu_6(8,4,1)$ "A" rotational level. This transition was used for measurement of the total depopulation rate in ν_6 and also for V \rightarrow V measurements between ν_3 and ν_6 .

The probe transitions used for total depopulation measurements and rotational and vibrational energy transfer experiments are listed in Table I.B.i. of Appendix 3 for transitions which access levels of "A" symmetry and in Table I.B.ii. of the same for levels of "E" symmetry. With one exception, all the hotband probe transitions belong to the QR branch of the $2\nu_3-\nu_3$ hotband. For the total depopulation measurement of the $\nu_6(8,4,1)$ "A" level (10R(22) pump), the $2\nu_6^0-\nu_6^1$ PQ(8,4) transition at 1027.762 cm $^{-1}$ was used. This transition was initially identified by double resonance as originating in the $\nu_6(8,4,1)$ "A" level. Later analysis of the CHD₃ overtone and hot-band spectra [Appendix 2] confirmed the identity of the transition and produced the assignment. Ground state recovery measurements were made by monitoring fundamental transitions in the ν_5 band centered at 1292.5 cm $^{-1}$.



3.5 Upper State Total Depopulation and Ground State Recovery Measurements

An important first step in the study of state-to-state rotational energy transfer is the measurement of the total rate at which population is removed from an initially pumped level. The 3-level double resonance scheme used for this measurement is shown in Fig. 3.5. This is both a conceptually and experimentally simple measurement. Population is moved from a ground vibrational level by the pulsed pump laser to a single rotational level in the $v = 1$ state. The c.w. probe laser monitors a hot band transition between $v = 1$ and $v = 2$ which originates in the same $v = 1$ rotational level that is populated by the pump laser. The ground state, $v = 1$, and $v = 2$ energy levels are linked by the pump and probe lasers, thus the designation "3-level" double resonance. Spectroscopic assignment of the pump transition defines the initial vibrational, rotational, and nuclear spin quantum labels of the prepared state. Because of the very much larger room temperature equilibrium population in the ground state, a large increase in the population of the $v = 1$ rotational level is created, particularly when the pump transition is saturated. By fixing the probe laser to a hot band transition originating from this initially populated rovibrational level, the excess population can be monitored as an increase in probe laser absorption. The absorption of the probe laser is proportional to the difference in population between the $v = 2$ and $v = 1$ levels, viz.:

$$\alpha_{\text{probe}}(t) = [N(v=1, J'', K'')] - [N(v=2, J', K')] \quad \text{Eq. 3.10.}$$

The $v = 2$ level of the probe transition is $\sim 1000 \text{ cm}^{-1}$ higher than the $v = 1$ level, or about 5 kT endothermic. Collisions will not transfer any significant population up to this third level so that transient absorption of the hot band transition is a measure of only the total rate at which collisions remove population from the pumped level. Inelastic collisions cause molecules initially prepared in this one state to change to other states. The fastest state changing process is energy transfer to other rotational levels in $v = 1$. The total depopulation rate is dominated by rotational equilibration in $v = 1$. Note that these experiments are only sensitive to state changing collisions. Elastic collisions, which reorient the space fixed projection of J or the translational velocity of the molecule or the phase of the wavefunction, but do not change the molecular rovibrational state, are not detectable in this experimental scheme.

Ground state recovery (GSR) rates provide information similar to total depopulation rates about the collisional dynamics occurring in the ground vibrational state. The pump laser that moves population into the vibrationally excited state creates a "hole", or less than equilibrium Boltzmann distribution in the ground state rotational level of the pump transition. Collisions will "fill in" this "hole" and return the population to its equilibrium value. The rate for this process can be measured by monitoring the decrease in population of another transition which originates in the pumped level. For CHD_3 , transitions in the ν_5 band were used. The ν_5 vibrational level is $\sim 300 \text{ cm}^{-1}$ higher than ν_3/ν_6 dyad. Because the probe transitions belonged to a different vibrational band more than $k_B T$ endothermic than those being pumped, complications from population arriving in the upper level of the probe transitions were minimized.

The GSR measurements were made before the other work on CHD_3 energy transfer. There were a few minor differences in the experimental setup that are worth noting. Both the pump and probe beams were copropagated through the cell, but instead of being collinearly combined on the ZnSe plate, the beams were spatially separated in front of the cell and were crossed within it. The diffraction grating after the cell was not used for separating the beams. Instead a MgF_2 plate which was 75% transmissive for the 7.8 μm diode laser and completely absorptive for the CO_2 laser was used as a very effective filter. Also, the MCT detector in use at this time was an older unit (Santa Barbara, Model 40742). This MCT was similar, though not as fast or sensitive, to the Kolmar unit described previously.

TD and GSR rates were both measured for three CHD_3 pump transitions: ν_6 $\text{RP}(9,3)$ "A", ν_3 $\text{QQ}(12,7)$ "E", and ν_3 $\text{QQ}(12,9)$ "A". In addition, the GSR rate for the ν_3 $\text{QQ}(16,14)$ "E" was also measured. Shown in Fig. 3.6 and 3.7 are examples of the transient curves obtained as raw data in these experiments and the fit of the decaying portion of the signal to a single exponential.

For both of these figures the CO₂ laser pump transition was the 10R(34). The CHD₃ ν_3 Q_Q(12,9) "A" transition is coincident with this laser line. Fig 3.6 shows the decrease in absorption caused by population being moved from the ground state by the CO₂ pump and transient recovery as collisions return the

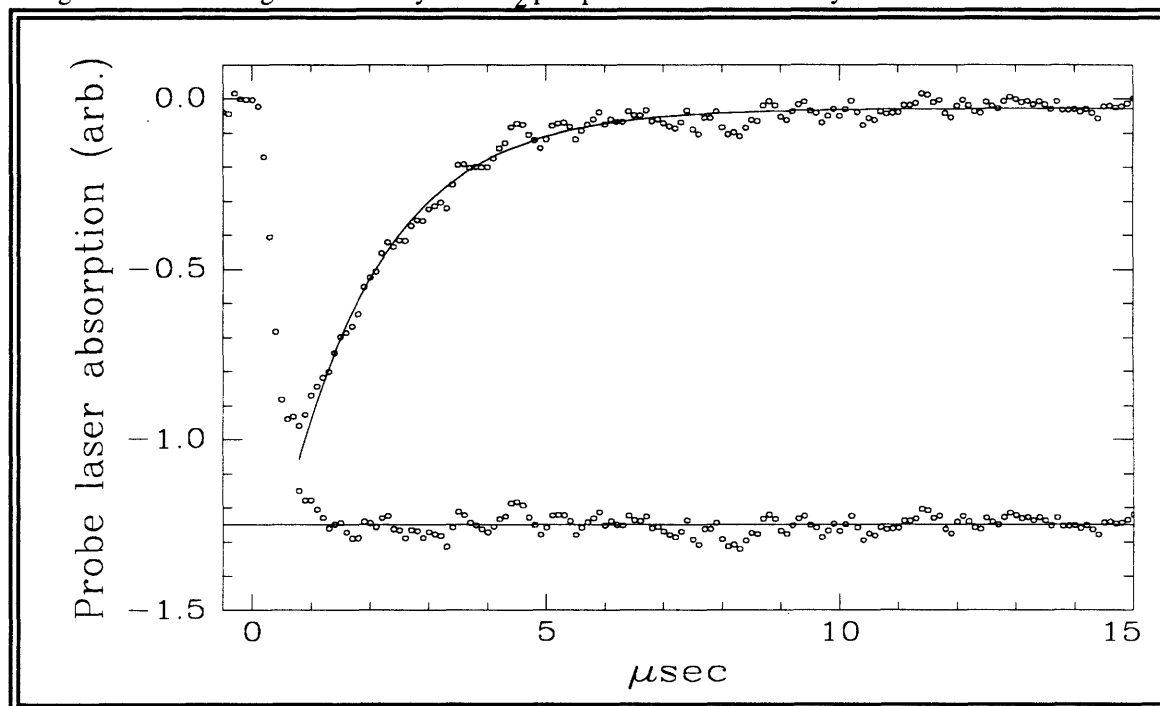


Figure 3.6

Ground state recovery transient decay curve for CHD₃ self-relaxation at 50 mtorr. The pump transition was ν_3 Q_Q(12,9) "A" and the probe was ν_5 R_R(12,9) "A". The solid line through the data points is a fit of the transient decay to a single exponential. The residuals between the fit and the data are offset at the bottom of the plot.

population to the Boltzmann equilibrium. The probe laser was fixed to the center of the ν_5 R_R(12,9) ground state transition for this measurement. In Fig. 3.7 the increase in population in the ν_3 (12,9) "A" level caused by the CO₂ pump was monitored by the increase in absorption of the hotband transition $2\nu_3$ - ν_3 Q_R(12,9). The pressure for both of these curves was 50 mtorr CHD₃.

The physical process being monitored by 3-level double resonance, such as the total depopulation shown in Fig. 3.7 is the evolution of population in a particular level which is initially perturbed from its Boltzmann equilibrium by the action of the pump laser. The rate at which population initially moves into this level is proportional to the intensity/time profile of the pump laser pulse, $I(t)$. (This is strictly true only in the limit of linear absorption, i.e., when the pump transition is not being saturated.) The population moved by the pump laser into the upper level of the pumped transition, N_i , can be transferred by inelastic collisions to a set of all other accessible levels, N_f . The rate at which population in N_i is

transferred to each of these levels is quantified by a set of first order rate constants, $k_{f \leftarrow i}$. Similarly, population in each of the levels N_f can be transferred by collisions back to N_i at a set of rates $k_{i \leftarrow f}$. The pairs of rates, $k_{f \leftarrow i} / k_{i \leftarrow f}$, are related to one another by detailed balance which will

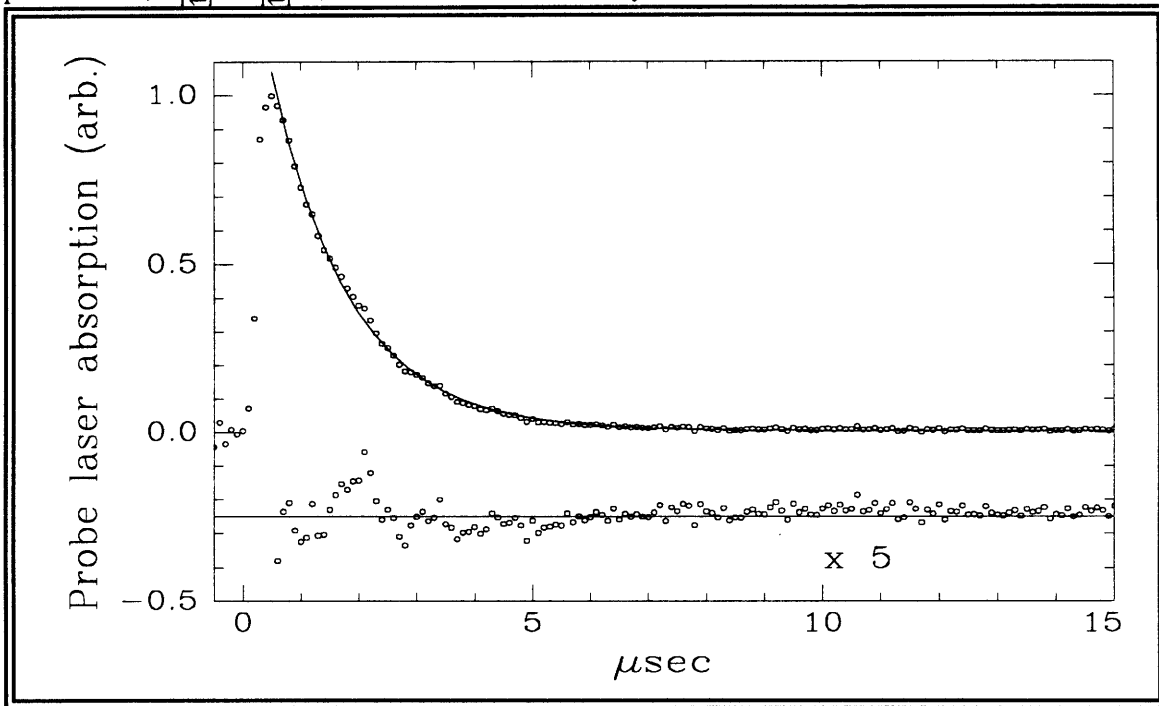


Figure 3.7

Total depopulation transient decay curve for CHD_3 self-relaxation at 50 mtorr. The pump transition was v_3 $Q(12,9)$ "A" and the probe was $2v_3-v_3$ $Q(12,9)$ "A". The solid line through the data points is the best fit of the transient decay to a single exponential. The residuals are shown in a magnified scale at the bottom of the plot.

be described in the section dealing with state-to-state rotational energy transfer. Here it is important to note that the time evolution of the initial level, N_i , is described by the rate equation

$$dN_i / dt = - \sum_f k_{f \leftarrow i} N_i + \sum_f k_{i \leftarrow f} N_f + \alpha I(t)$$

or by setting

$$\sum_f k_{f \leftarrow i} N_i = k_{\text{tot}}$$

$$dN_i / dt = -k_{\text{tot}} N_i + \sum_f k_{i \leftarrow f} N_f + \alpha I(t). \quad \text{Eq. 3.11}$$

To simulate the evolution of the population in the initially prepared level for a system of N interacting levels would require knowing all $N-1$ individual state-to-state rate constants. This is not quite all that is necessary. For a detailed kinetic analysis, the rates which interconnect all the final states must also be considered. This means that $N(N-1)/2$ individual rate constants would be necessary to rigorously model one piece of data. Fortunately, for modeling 3-level total depopulation rates two assumptions can be made which drastically simplify Eq. 3.11. The first is to set the summation over final states term in Eq. 3.3 equal to zero. This is to ignore the population which feeds back into the initial level, N_i , from all other levels, N_f . This simplification can be justified for total depopulation measurements by considering the difference in magnitude of the population in the initial level to all other levels. There is essentially no population in the vibrationally excited state compared to that transferred by the pump laser to the initial level, N_i . All N_f then are small compared to N_i , and the summation over final states term can be legitimately dropped. With this simplification the rate equation for the initial level becomes

$$dN_i / dt = -k_{\text{tot}} N_i + \alpha I(t) \quad \text{Eq. 3.12}$$

The solution to this differential equation is a single, decaying exponential with a time constant k_{tot} convoluted with a pulse shape function, $I(t)$. In principle the CO_2 pulse profile is known and could be accounted for by convolving it with an exponential decay. In practice it is simpler to make a second simplifying assumption that the pulse shape function is sufficiently narrow that it can be treated as a delta function. This assumption is valid at pressures for which the collisional relaxation time is long compared to the CO_2 pulse width.

For ground state recovery measurements, the transients which are recorded are qualitatively very similar to those for total depopulation, however the physical picture is different. In total depopulation measurements in a vibrationally excited state, an initial level with population greater than its Boltzmann equilibrium value relaxes to a set of essentially empty states. For ground state recovery measurements, a decrease in the equilibrium Boltzmann population of the pumped ground state level is restored from the bath. The argument used for neglecting the summation over final states term in total depopulation measurements, namely, that the rotational levels in the excited state other than the one pumped have very little population, is not valid when considering ground state recovery since the other ground state levels certainly are populated. Nevertheless, the GSR transients recorded in these experiments have also been fit to single exponentials. The GSR rates obtained from these fits must then be viewed as a lower limit.

All of the total depopulation and ground state recovery transients were fit as a single decaying exponential using the functional form given in Eq. 3.13.

$$S(t) = p(1)e^{-P(2)t} + p(3) \quad \text{Eq. 3.13}$$

As discussed earlier, for the TD measurements, the population feedback into the initial level from all other accessible levels causes the transient decay to deviate from strictly exponential behavior. As the population in the initial level approaches that of the other levels it is feeding into, ignoring the feedback into the initial level caused by the $\sum_f k_{i \leftarrow f} N_f$ term in Eq. 3.11 is no longer valid, and the exponentially decaying behavior is lost. To account for this behavior, a constant offset was added to the exponential decay in the fitting procedure (parameter $p(3)$ in Eq. 3.13). It is possible to justify this by considering the time scales for different types of energy transfer processes. The largest rates for single step processes are for rotational relaxation in the vibrationally excited state. Other relaxation processes which change the vibrational excitation occur much more slowly. The fastest of these, near resonant $V \rightarrow V$, is an order of magnitude slower than rotational relaxation. A quasi-equilibrium is reached wherein the relative populations of the rotational levels in the vibrationally excited state return to a Boltzmann distribution, but with a greater overall population in the excited state than at room temperature. This excess population is returned to room temperature equilibrium by the much slower vibrational relaxation which is the same irregardless of the rotational level probed. At times long compared to rotational equilibration, but shorter than vibrational relaxation, the transient absorption of a hot-band transition is greater than zero and can be adequately modeled as a baseline offset. In this regard, the total depopulation rate obtained from a fit to Eq. 3.13 may be more adequately described as a rotational equilibration rate.

Eq. 3.5 was fit to the experimental data using the nonlinear fitting routine LEASTSQ provided in the MATLAB Optimization Toolbox. The LEASTSQ routine used the Levenberg-Marquardt algorithm for nonlinear minimization. MATLAB proved to be a very powerful and convenient environment in which to manipulate, analyze, and display the data.

As can be seen in the traces shown in Figs. 3.6 and 3.7, the peak of the transient absorption curve arrives approximately 0.5 μsec after the beginning of the laser pump pulse. This delay was due to the length of the CO_2 laser pulse. The fitting of the transient decay was begun at or after the signal peak. Experience showed that where the fit began somewhat affected the decay rate. Beginning exactly at the peak often led to fits with unacceptably large residuals. Beginning far after the peak always gave a better looking fit, but led to doubts about the accuracy of the rate constant obtained. To be able to fit all data in a consistent manner, a method was devised where the fit to each transient decay curve was begun at three different times after the peak; 100, 200, and 500 nsec. The best fit parameters were taken as the mean of those obtained for each of the three starting points and their standard deviation gave a good semi-quantitative estimate of how good the piece of data was. The point at which the fit is begun becomes increasingly

more important for higher pressure, faster decaying transients. At higher pressures the amount of relaxation which occurs during the laser pulse becomes significant. In effect one is seeing less of the early time behavior where ignoring the feedback into the initial level caused by the $\sum_f k_{i \leftarrow f} N_f$ term in Eq. 3.11 is justifiable. The rate constants for higher pressure data always systematically deviate lower than the value which would be predicted by linear extrapolation from the behavior at lower pressures. The effect already becomes significant at pressures which cause transient decay rates which are a factor of 10 or less slower than the decay of the CO₂ pulse itself. For the experiments described here, this translates into a limit on the fastest decay rates which can be accurately measured of approximately 1.5 μsec^{-1} . The decreased validity of fitting transient decays at high pressure to a single exponential is uncovered by the method of determining and weighting rate constants by systematically adjusting the point at where the fit is begun. Data recorded at higher pressures always have larger error estimates. The obvious solution to the problem of significant relaxation occurring during the laser pulse is to develop a pump laser system which has a much shorter pulse length. Such a system has been developed using a Nd:YAG pumped Raman-shifted Ti:sapphire laser which is described in Chapter 4. For the CO₂ laser experiments described here, careful work in fitting and analyzing the data has also led to well determined TD and GSR rates.

Transient curves were recorded at pressures ranging from 5.0 to 100.0 mtorr for both TD and GSR measurements using the ν_6 RP(9,3) "A", ν_3 QQ(12,7) "E", and ν_3 QQ(12,9) "A" pump transitions. Also, the ν_3 QQ(16,14) "E" transition, which is also pumped by the 10R(34) CO₂ laser transition along with the ν_3 QQ(12,9) "A", was used for GSR measurement. In the standard way, the inverse relaxation times obtained from the fit to Eq. 3.13 were plotted versus pressure. The resulting plot was fit to a straight line to obtain the TD and GSR rates in $\mu\text{sec}^{-1} \text{ torr}^{-1}$. Figs 3.8-3.14 show these plots for self-relaxation using these pump transitions. In cases where more than one TD or GSR measurement was made at the same pressure, weighted averaging was used to combine those measurements.

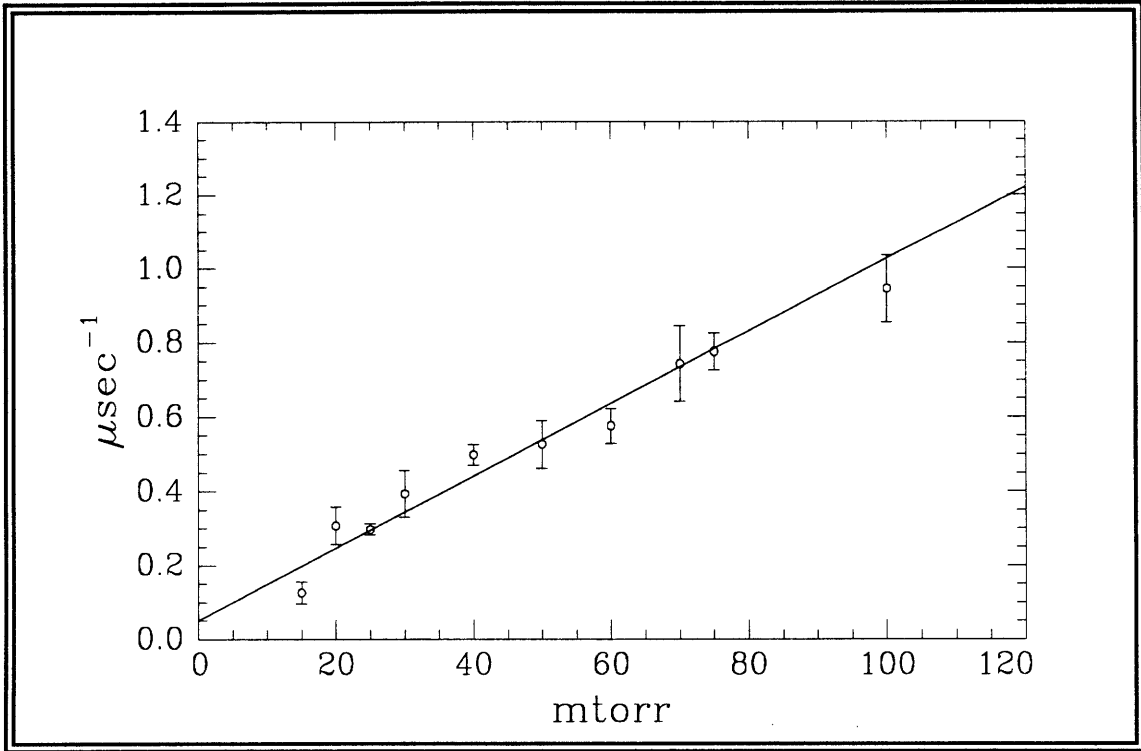


Figure 3.8

pt plot for GSR of $J'' = 9, K'' = 3, "A"$. CO_2 10R(22) pump. GSR rate = $8.4 \pm 1.0 \mu\text{sec}^{-1} \text{ torr}^{-1}$.

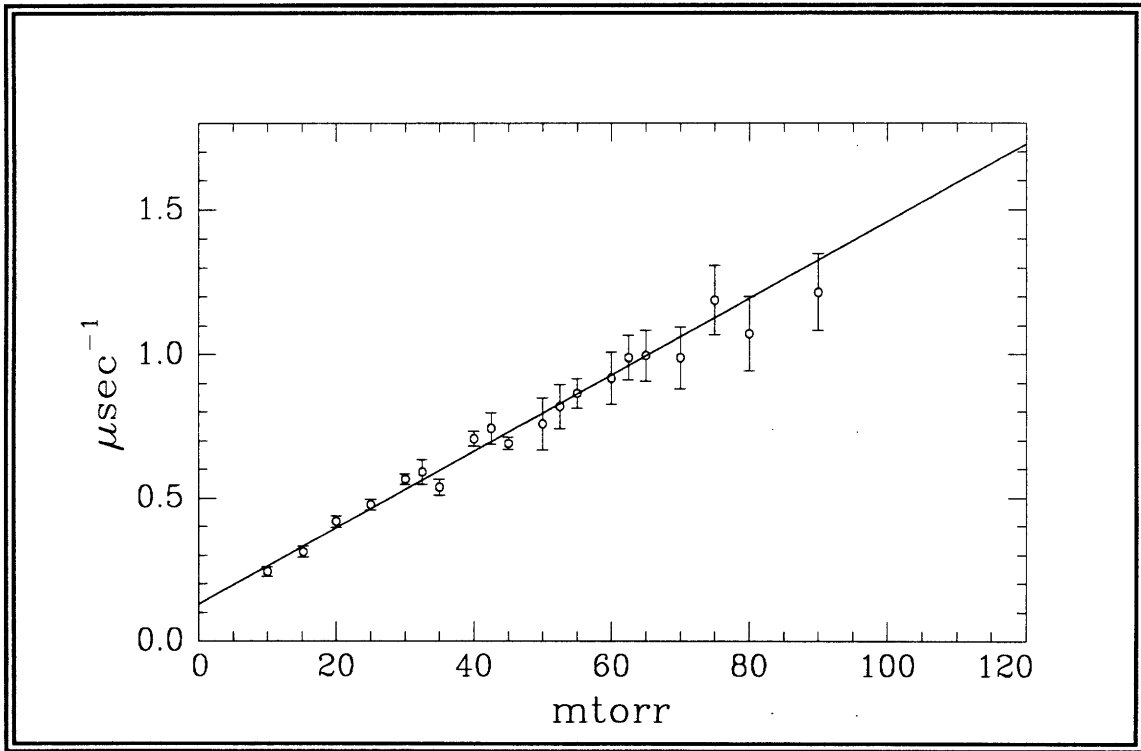


Figure 3.9

pt plot for TD of $v_6 = 1, J' = 8, K' = 4, l = +1, "A"$. CO_2 10R(22) pump. TD rate = $13.3 \pm 0.9 \mu\text{sec}^{-1} \text{ torr}^{-1}$.

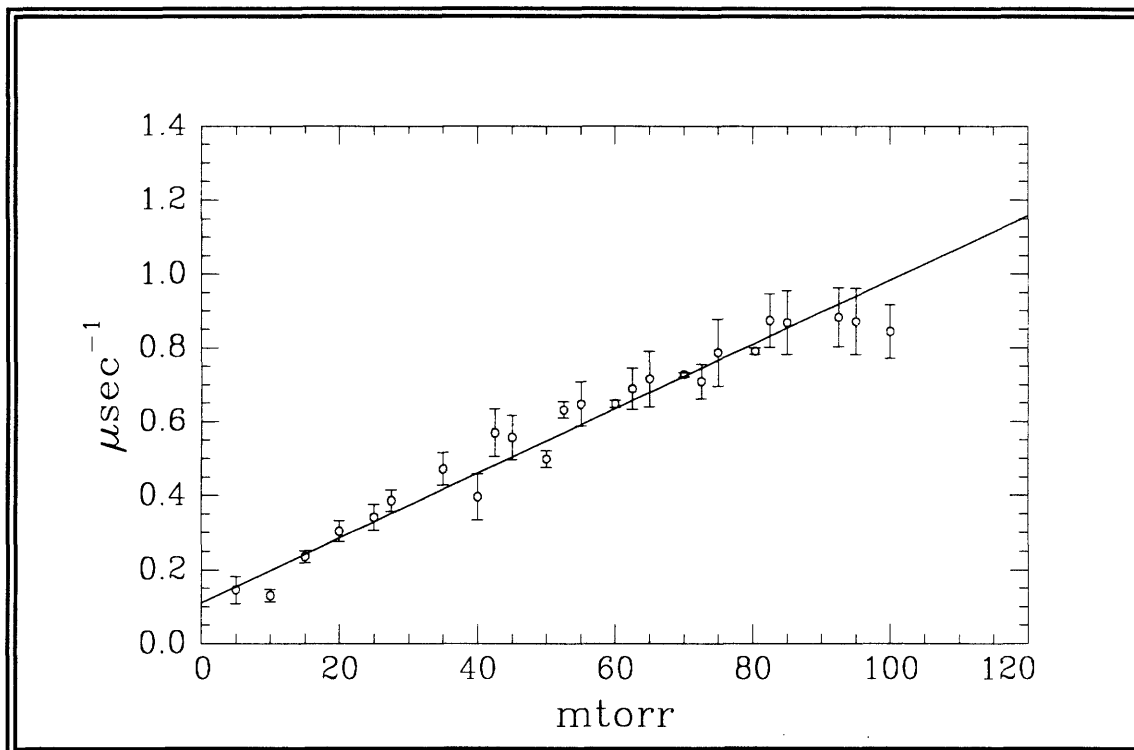


Figure 3.10

pt plot for GSR of $J'' = 12, K'' = 7, "E"$. CO_2 10R(24) pump. GSR rate = $8.7 \pm 0.3 \mu\text{sec}^{-1} \text{ torr}^{-1}$.

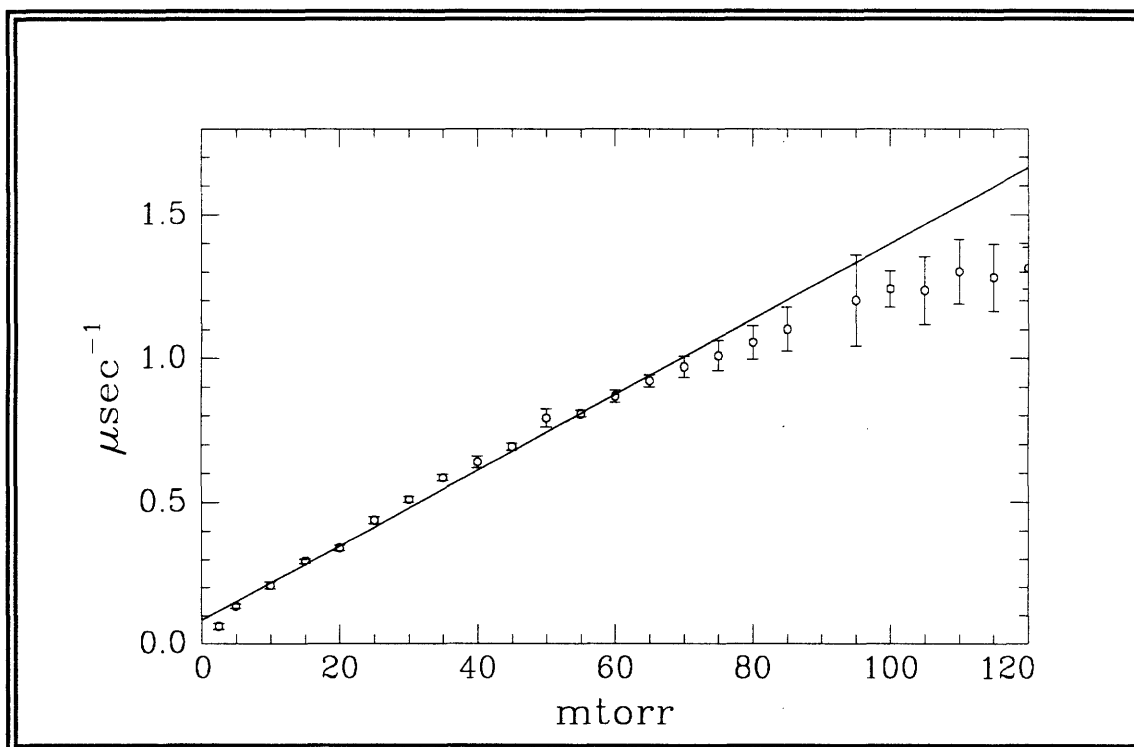


Figure 3.11

pt plot for TD of $\nu_3 = 1, J' = 12, K' = 7, "E"$. CO_2 10R(24) pump. TD rate = $13.6 \pm 0.2 \mu\text{sec}^{-1} \text{ torr}^{-1}$.

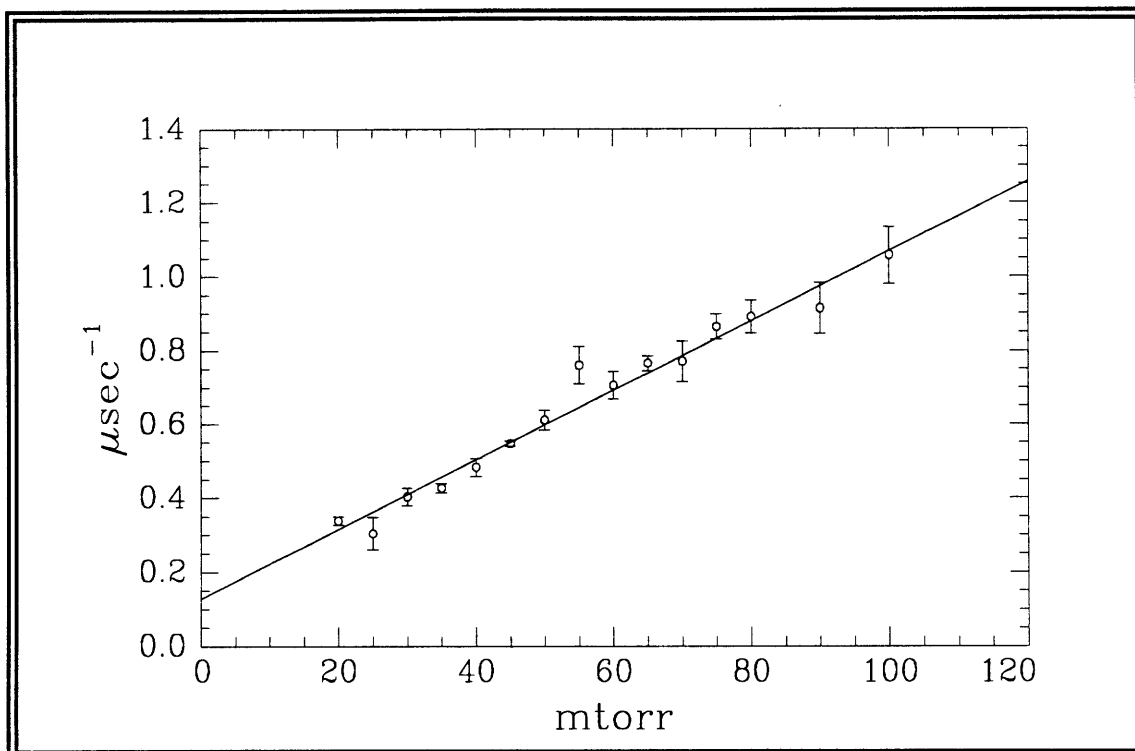


Figure 3.12

pt plot for GSR of $J'' = 12, K'' = 9, "A"$. CO_2 10R(34) pump. GSR rate = $9.4 \pm 0.6 \mu\text{sec}^{-1} \text{ torr}^{-1}$.

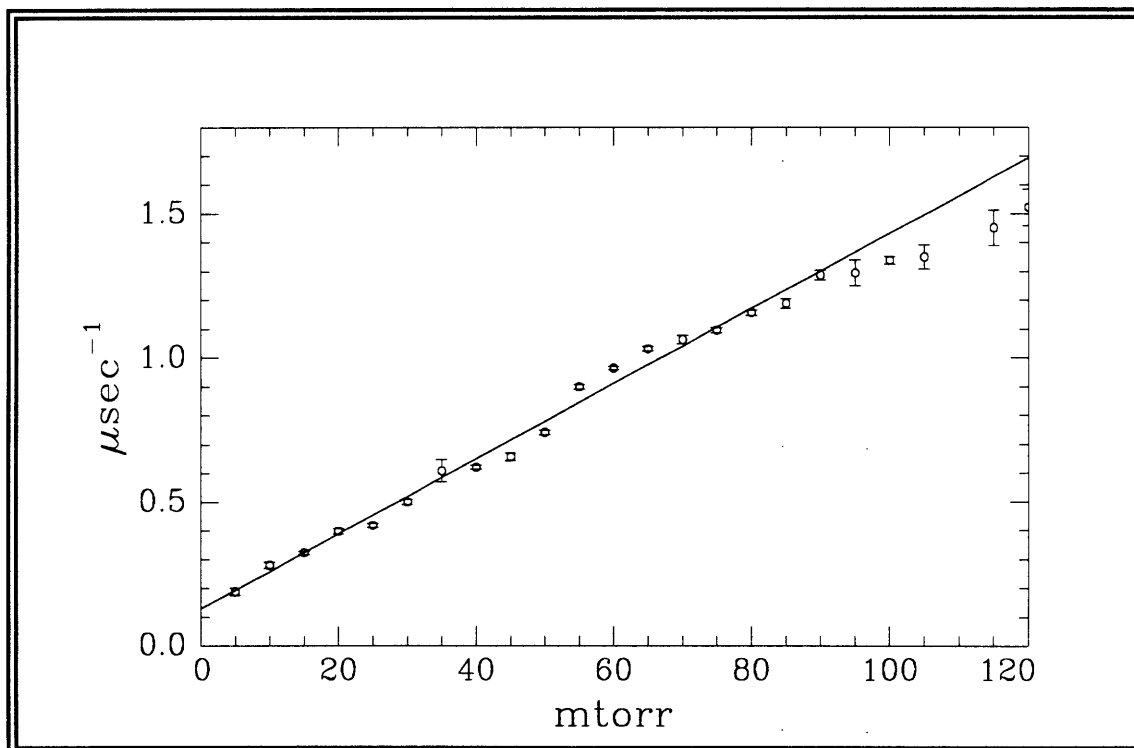


Figure 3.13

pt plot for $\nu_3 = 1: J' = 12, K' = 9, "A"$. CO_2 10R(34) pump. TD rate = $12.73 \pm 0.04 \mu\text{sec}^{-1} \text{ torr}^{-1}$.

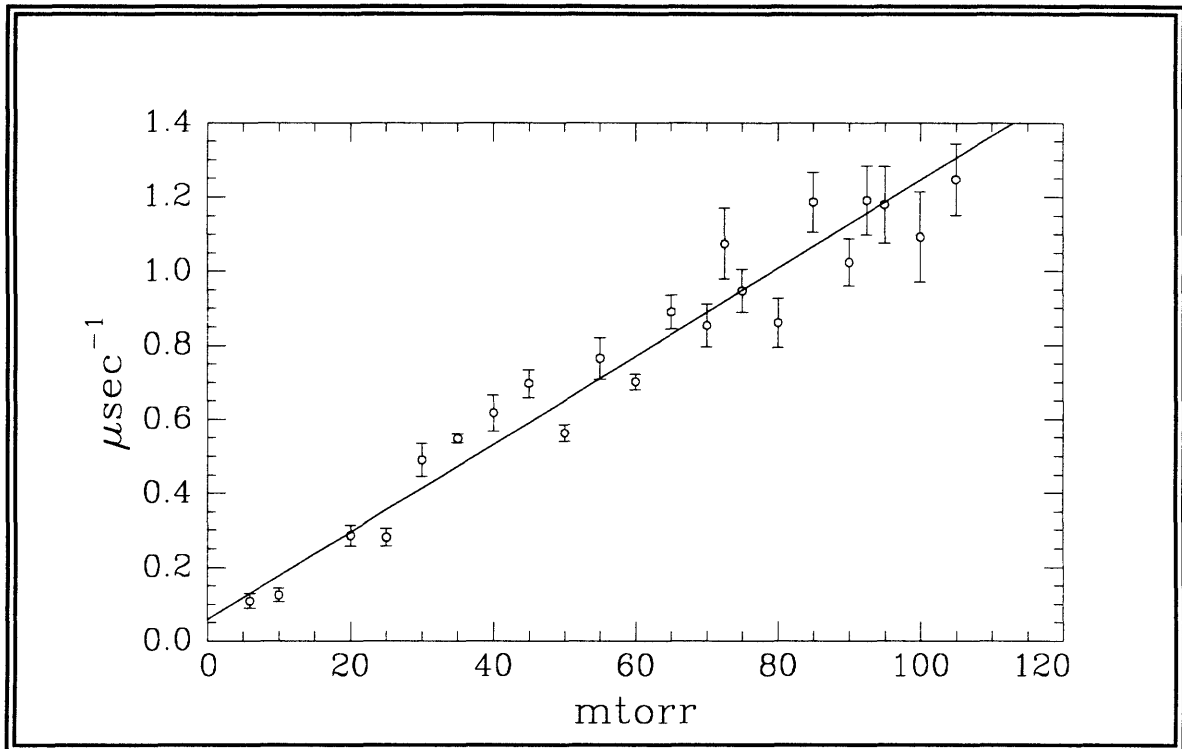


Figure 3.14

$\rho\tau$ plot for $\nu_3 = 1: J' = 16, K' = 14, "E"$. CO₂ 10R(34) pump. TD rate = $11.88 \pm 0.60 \mu\text{sec}^{-1} \text{ torr}^{-1}$.

All of the $\rho\tau$ plots displayed in Figures 3.8-3.14 have small, positive y-intercepts of approximately $0.1 \mu\text{sec}^{-1}$. This implies that in the limit of zero pressure there is still a mechanism for removing molecules from the state which is being probed. Spontaneous emission limits the lifetime of vibrationally excited states, but as was demonstrated in the example given in the previous section, the lifetime of low energy vibrational states is very long, and the corresponding spontaneous emission rates are very small, on the order of $10^{-3} \mu\text{sec}^{-1}$. The process which can account for a significant decay rate in the zero pressure limit is beam flyout, simple ballistic transport out of the probe laser volume. Analytical solutions to the mass transport equation in the ballistic transport limit have been derived in the paper by Bialkowski *et al.* [BIALKOWSKI80]. Their equation for the time evolution of transport out of the probe volume in the low pressure limit for collinear pump and probe beams is

$$S(t) = S_0 \frac{R_{\text{pump}}^2 + R_{\text{probe}}^2}{R_{\text{pump}}^2 + R_{\text{probe}}^2 + c^{*2} t^2} \quad \text{Eq. 3.14.}$$

In this equation S is the probe signal, R_{pump} and R_{probe} are the radii of the pump and probe beams, and c^* is the most probable molecular speed.

The $1/e$ time for Eq. 3.14 can be calculated from the measured cross sections of the pump and probe beams and the molecular velocity of CHD_3 . Using the parameters $R_{\text{pump}} = 0.15$ cm, $R_{\text{probe}} = 0.25$ cm, and $c^* = 5.1 \times 10^4$ cm/s, Eq. 3.14 gives a $1/e$ time of 13 μsec and a corresponding effective decay rate of $0.075 \mu\text{sec}^{-1}$, which is in fair agreement with the experimental zero pressure intercept.

In addition to the TD and GSR measurements for CHD_3 self-collisions, TD rates for the $\nu_3 J' = 12, K' = 9$ "A" and $\nu_6 J' = 8, K' = 4, l = +1$ "A" levels were measured with other collision partners; H_2 , He, Ar, CH_4 , CHF_3 , and NH_3 . These measurements were made by using a constant base pressure of 20.0 or 25.0 mtorr of CHD_3 and systematically increasing the partial pressure of the collision partner. Mixing of the gases was carried out in the double resonance cell. The collision partner was leaked into the cell from a much higher pressure reservoir (~ 10 torr) on the vacuum line. Transient decay curves were obtained and fit to single exponentials in the same way as for self-collisions. The $\rho\tau$ plots for these data are shown in Figures 3.15-3.21. The abscissae of these plots are the total pressure, $\text{CHD}_3 + \text{collision partner}$, of the gases in the double resonance cell.

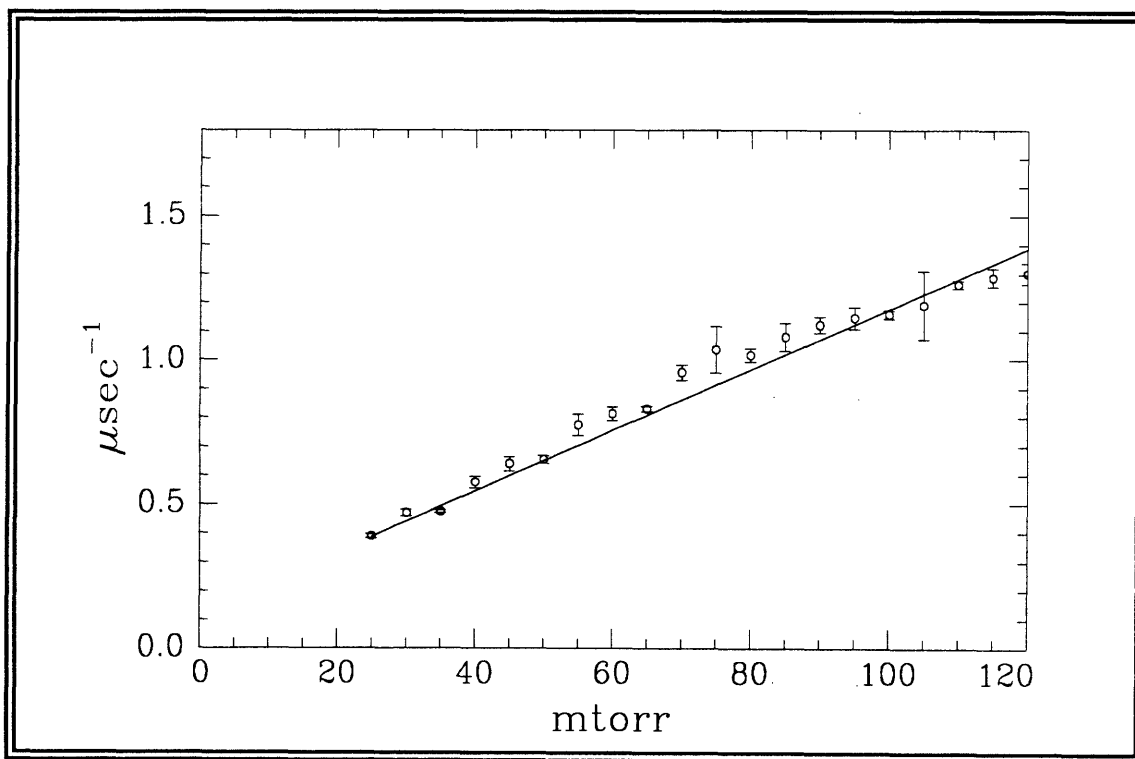


Figure 3.15

$\rho\tau$ plot for $\nu_3 = 1: J' = 12, K' = 9, \text{"A"}$. CO_2 10R(34) pump. Total depopulation rate of 25.0 mtorr CHD_3 with Hydrogen (H_2) as collision partner. TD rate = $10.52 \pm 0.46 \mu\text{sec}^{-1} \text{ torr}^{-1}$.

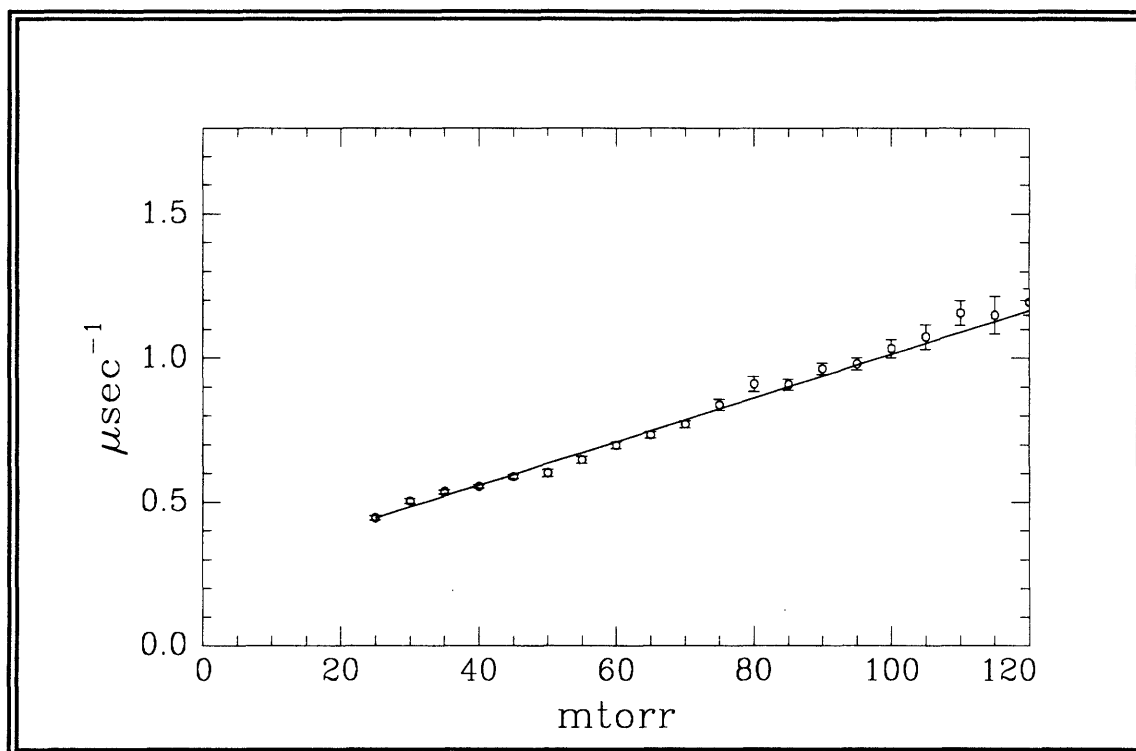


Figure 3.16

$\rho\tau$ plot for $\nu_3 = 1: J' = 12, K' = 9, "A"$. CO_2 10R(34) pump. Total depopulation rate of 25.0 mtorr CHD_3 with Helium as collision partner. TD rate = $7.58 \pm 0.27 \mu\text{sec}^{-1} \text{ torr}^{-1}$.

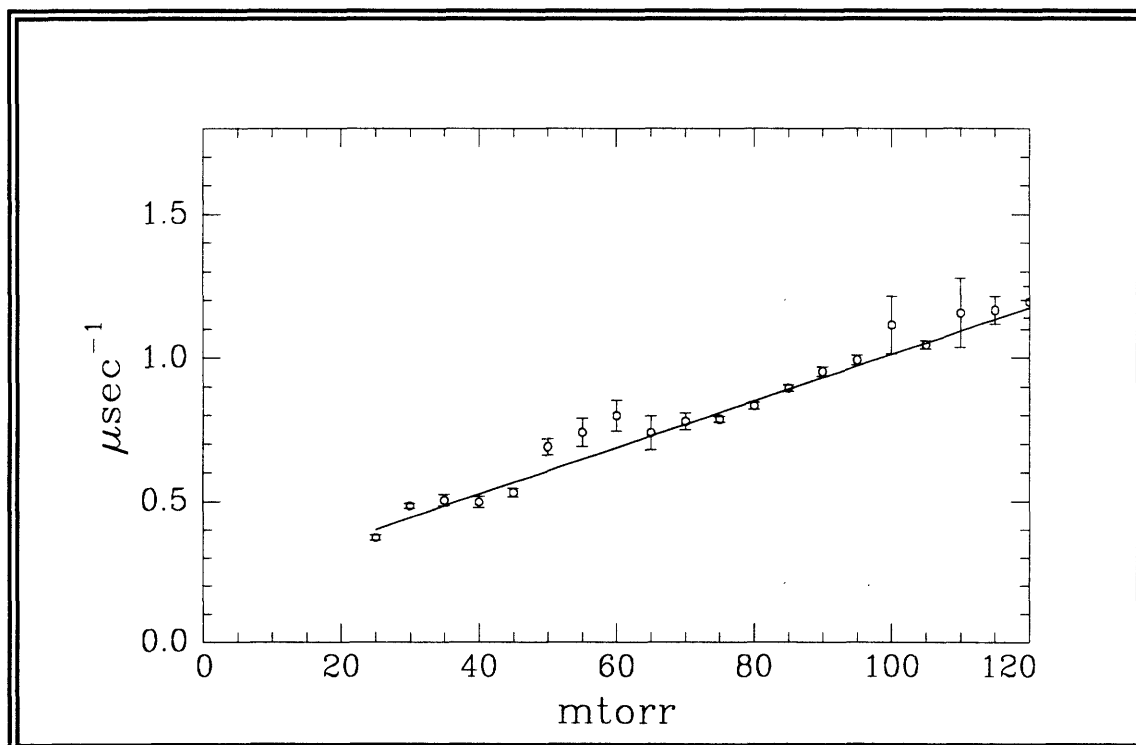


Figure 3.17

$\rho\tau$ plot for $\nu_3 = 1: J' = 12, K' = 9, "A"$. CO_2 10R(34) pump. Total depopulation rate of 25.0 mtorr CHD_3 with Argon as collision partner. TD rate = $8.14 \pm 0.27 \mu\text{sec}^{-1} \text{ torr}^{-1}$.

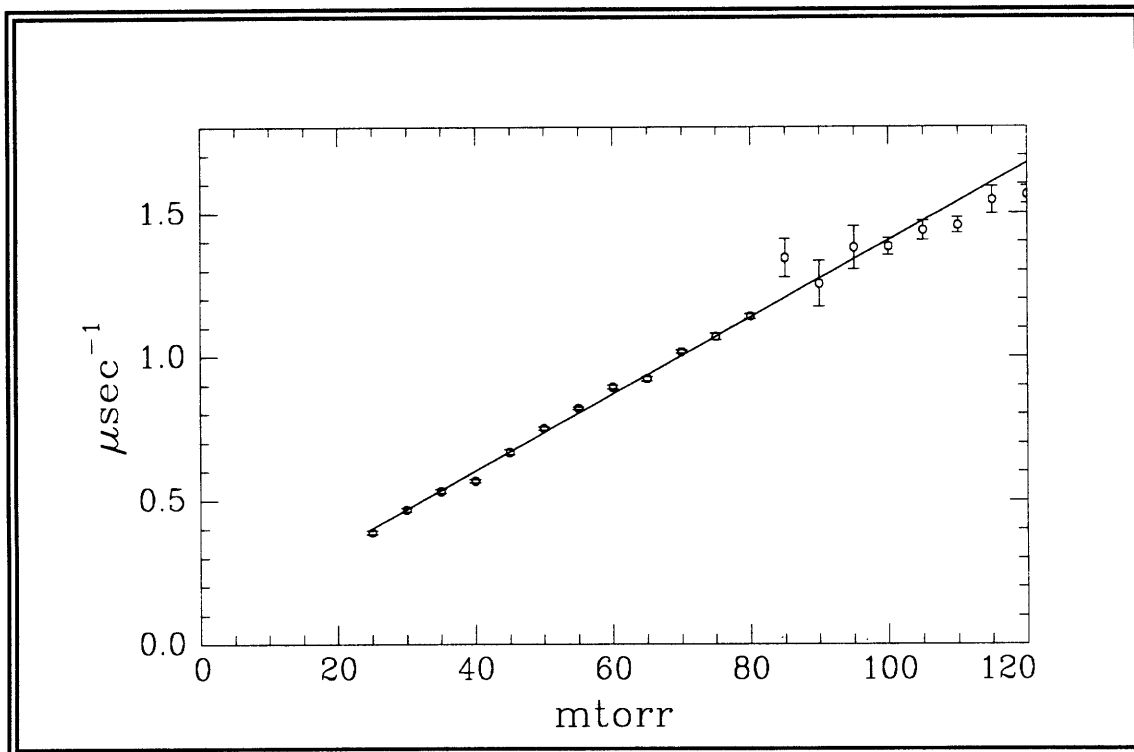


Figure 3.18

pt plot for $\nu_3 = 1: J' = 12, K' = 9, "A"$. CO₂ 10R(34) pump. Total depopulation rate of 25.0 mtorr CHD₃ with Methane (CH₄) as collision partner. TD rate = $13.38 \pm 0.21 \mu\text{sec}^{-1} \text{ torr}^{-1}$.

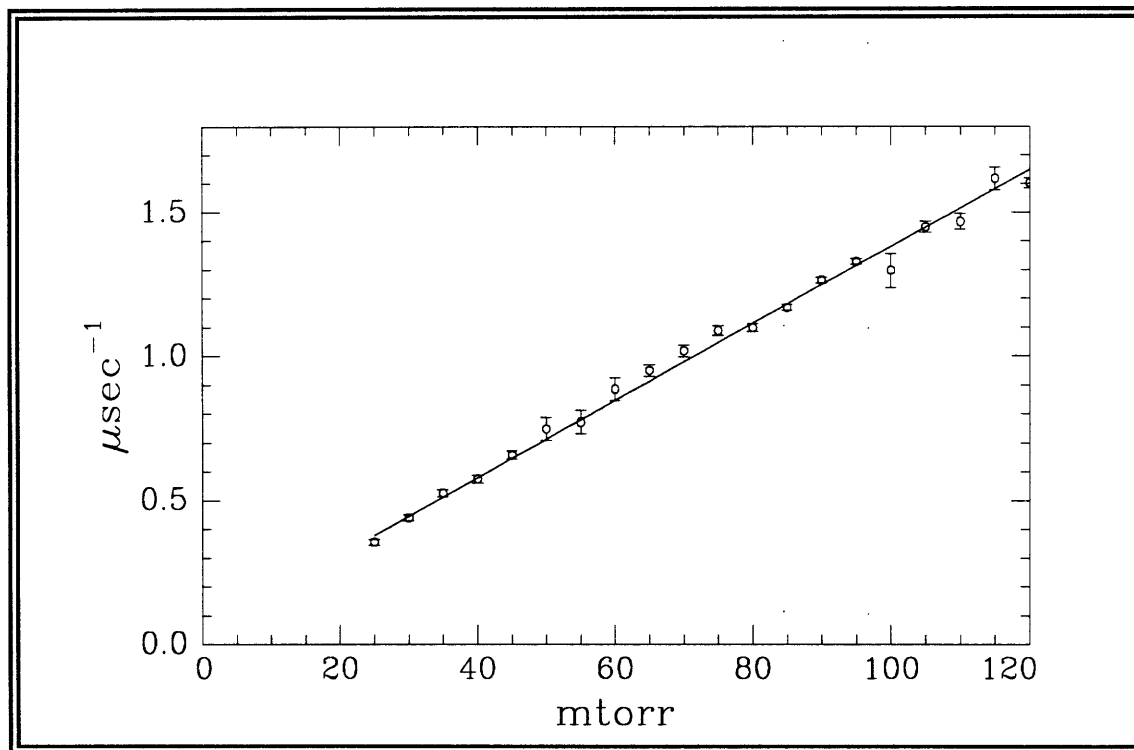


Figure 3.19

pt plot for $\nu_3 = 1: J' = 12, K' = 9, "A"$. CO₂ 10R(34) pump. Total depopulation rate of 25.0 mtorr CHD₃ with Fluoroform (CHF₃) as collision partner. TD rate = $13.38 \pm 0.22 \mu\text{sec}^{-1} \text{ torr}^{-1}$.

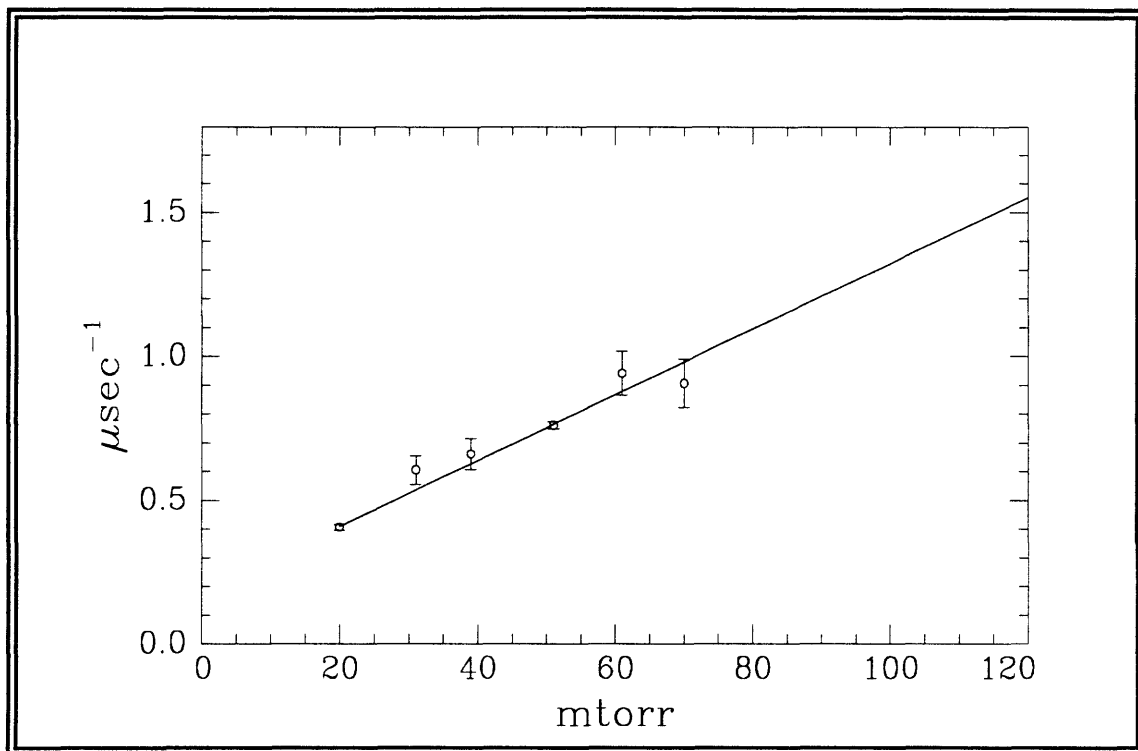


Figure 3.20

$\rho\tau$ plot for $\nu_6 = 1: J' = 8, K' = 4, l = 1$ "A". CO₂ 10R(22) pump. Total depopulation rate of 20.0 mtorr CHD₃ with Hydrogen (H₂) as collision partner. TD rate = $11.43 \pm 0.97 \mu\text{sec}^{-1} \text{ torr}^{-1}$.

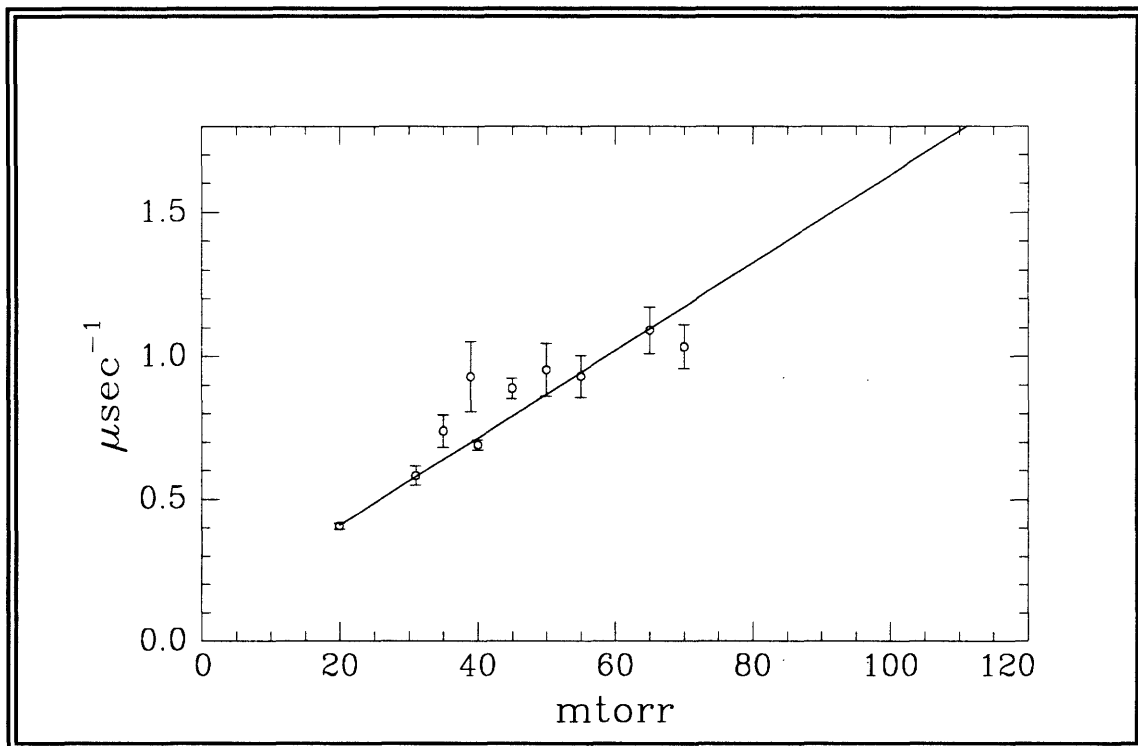


Figure 3.21

$\rho\tau$ plot for $\nu_6 = 1: J' = 8, K' = 4, l = 1$ "A". CO₂ 10R(22) pump. Total depopulation rate of 20.0 mtorr CHD₃ with Ammonia (NH₃) as collision partner. TD rate = $15.3 \pm 1.4 \mu\text{sec}^{-1} \text{ torr}^{-1}$.

TD and GSR rates can provide some important insights into molecular collision dynamics. The sum of individual rates for all processes that take population out of the pumped level must equal the independently determined TD rate. This rate then serves as an important check on the more detailed state-to-state kinetics. The magnitude of the TD rate also provides insight about the types of intermolecular forces which are dominant in the collision dynamics. In this regard, it is insightful to express the TD rate as an effective hard sphere collision cross section [YARD80]. This conversion is accomplished by dividing the TDR, in $\text{cm}^3 \text{ molecule}^{-1} \text{ s}^{-1}$, by the mean relative velocity of the collision partners:

$$\sigma = k(\pi\mu/8kT)^{1/2} \quad \text{Eq. 3.15.}$$

TD and GSR rates when expressed as effective cross section give an easily visualized range to the intermolecular forces. This form is also convenient for comparing the measured rates to those predicted by kinetic theory, such as the collision cross sections derived from Lennard-Jones (L-J) parameters. L-J cross sections are found from the potential parameters using the expression [HIRSCHFELDER54]

$$\sigma_{\text{LJ}} = \frac{1}{4}\pi(\sigma_A + \sigma_B)^2 \Omega^{(2,2)*} \quad \text{Eq. 3.16.}$$

σ_A and σ_B are the L-J diameters for the colliding species. $\Omega^{(2,2)*}$ is the reduced collision integral which provides a correction to the hard sphere collision rate due to attractive intermolecular forces, as expressed by the L-J well depth ϵ , and the temperature of the gas [STEINFELD89]. For binary mixtures, the well depth ϵ_{AB} for the interaction between species A and B is estimated as the square root of the product of the ϵ values for the pure gases.

$$\epsilon_{AB} = \sqrt{\epsilon_A \epsilon_B} \quad \text{Eq. 3.17}$$

Tables of $\Omega^{(2,2)*}$ are given in [HIRSCHFELDER54] as a function of the reduced temperature, T^* .

$$T^* = Tk_B/\epsilon \quad \text{Eq. 3.18}$$

Close similarity between the experimental effective cross section and hard sphere cross sections calculated from theory indicates that short-range forces are more important, as for $^{13}\text{CD}_4$ and SiH_4 , whereas effective cross sections much larger than hard sphere cross sections indicate that long-range forces, e.g. dipole-dipole, are dominant in the collision dynamics. Such is the case for formaldehyde self-collisions [TEMPS88]. Other molecular or atomic collision partners are useful for evaluating the

importance of near resonant V-V energy transfer, rotational quanta exchange, and other types of forces like dipole-induced dipole.

The results for all the TD and GSR measurements for CHD₃ are summarized in Table II of Appendix 3. The measured rates are expressed as thermally averaged cross sections as defined by Eq. 3.15, and for comparison the Lennard-Jones cross sections have also been calculated from potential parameters in [HIRSCHFELDER54] and [NASA61].

GSR rates for self-collisions have been measured for four different ground state levels. These rates are all very similar and are also comparable to the GSR rate measured for the ¹³CD₄ J = 12, F₁¹ of 10.5 μsec⁻¹ torr⁻¹ [FOY85]. The GSR rates for self-collisions are all somewhat lower than the corresponding rates for the vibrationally excited states. As discussed earlier this is most likely due to the greater population feedback occurring in the ground state. The GSR rates must be viewed as a lower limit.

The total depopulation rates for self-collisions measured for the three levels in the ν₃/ν₆ dyad are all the same within experimental error. The CHD₃ TD rate of ~13 μsec⁻¹ torr⁻¹ is also comparable to that for ¹³CD₄ ν₄ = 1, J = 11, F₂⁷ of 16.6 μsec⁻¹ torr⁻¹. The CHD₃ experimental cross section of 50±1 Å² is in good agreement with the L-J cross section of 54 Å². There is no apparent difference in the TD rates for the "A" and "E" symmetry levels, unlike the case for SiH₄ where there was a distinct ordering to total depopulation rates with respect to nuclear spin symmetry [HETZLER89]. Also, there is no significant difference in TD rates based on whether the level belongs to ν₃ or to ν₆.

The cross sections for CHD₃ collisions with other molecular are all of the same order as the L-J cross sections. The largest deviations occur for the monatomic or very light collision partners, He and H₂. This is likely because of the impossibility of intermolecular rotational energy transfer with He and the improbability of such a process with H₂ because of its large rotational spacing. Similar observations have been made for energy transfer of other polyatomic species with H₂ and light noble gases [FOY85], [FROST92]. The cross sections for collisions with other polyatomic molecules are all nearly equal to the L-J cross sections. Of particular note, the highly polar species, NH₃ and CHF₃, are not more effective collision partners than nonpolar species.

The close similarity between the measured thermally averaged cross sections to the L-J cross sections indicates that short range, repulsive forces of the intermolecular potential dominate in energy transfer. These results for TD and GSR measurements indicate that the overall magnitude of energy transfer in CHD₃ is more like the spherical top form of methane, ¹³CD₄, than like other C_{3v} molecules with larger dipole moments, see Table 3.2 for a few examples. This gives part of the answer to the questions initially

raised in this work as to how energy transfer in the symmetric top form of methane compares to spherical methane. With its miniscule dipole moment, long range forces are not significant in CHD₃, so short range interactions dominate in collisional processes. The details of these interactions on R.E.T. must be deduced from the state-to-state measurements, as will be described in sections 3.10 and 3.11.

Molecule	σ_{eff}	σ_{LJ}	$\sigma/\sigma_{\text{LJ}}$	Reference
	\AA^2	\AA^2		
CHD ₃	32-45	54	0.55-0.74	this work
NH ₃	123	58	2.1	[ABEL92]
CH ₃ Cl	590	95	6.2	[PAPE94]
CDF ₃	170	84	2.0	[HARRADINE84]

Table 3.2

Comparison of σ_{eff} with σ_{LJ} for several C_{3v} type molecules.

3.6 Connection Between Inelastic Collisions and Pressure Broadening

Total depopulation rates and ground state recovery rates can be related to the pressure-broadening coefficient of a spectroscopic transition according to the expression [FLANNERY92] [DEPRISTO78]

$$\frac{\gamma}{p} = \frac{1}{2\pi} (k_u + k_l) / 2 \quad \text{Eq. 3.19.}$$

This relation is based on the assumption that the pressure-broadening coefficient is the average of the total *inelastic* collision rates of the upper and lower levels of the spectroscopic transition. For CHD₃ we have measured total depopulation and ground state recovery rates for three pairs of transitions. We have also measured the pressure broadening coefficient for two CHD₃ transitions. These are reported in Appendix 3.

The measured self-broadening coefficients are 30-40% larger than the averaged relaxation rate. This can be understood if we interpret the discrepancy as the contribution of *elastic* collisions to the pressure broadened width. Our time resolved measurements for CHD₃ are sensitive only to population changes, whereas frequency domain measurements are sensitive to both inelastic and elastic collisions. A possible experimental technique to directly study the effect of elastic reorientation on the TD and GSR rates is to measure the polarization dependence of these rates. For CHD₃ we always had the case where the relative polarization of the pump and probe lasers were perpendicular and the pump and probe transitions were

either Q's with R probes or a P with a Q probe. In these cases the m_j distribution created by the pump laser was always similar to that sampled by the probe laser. For the energy transfer experiments in CH_4 presented in Chapter 5 we have explicitly studied the polarization dependence of the TD and GSR rates. We find a very significant polarization dependence, as discussed in section 5.7.

In addition to the self-broadening measurements reported in Appendix 3, we have measured pressure-broadening for CHD_3 ν_3 $Q_Q(J=K)$ transitions with CH_4 as a collision partner. The pressure-broadening coefficients are recorded in Table 3.2. The CHD_3/CH_4 pressure-broadening coefficients are quite consistent with the previously reported values for CHD_3 self-broadening.

CHD ₃ transition	Measured γ/p (MHz/torr)
ν_3 $Q_Q(2,2)$	4.0 (0.9)
ν_3 $Q_Q(4,4)$	2.5 (0.7)
ν_3 $Q_Q(5,5)$	3.8 (1.3)
ν_3 $Q_Q(6,6)$	3.2 (0.4)
ν_3 $Q_Q(7,7)$	3.2 (0.8)
ν_3 $Q_Q(8,8)$	2.1 (0.4)
ν_3 $Q_Q(9,9)$	1.7 (0.5)
ν_3 $Q_Q(10,10)$	2.6 (0.3)
ν_3 $Q_Q(11,11)$	2.2 (0.4)
ν_3 $Q_Q(12,12)$	2.4 (0.3)
ν_3 $Q_Q(14,14)$	2.5 (0.4)

Table 3.3

Pressure-broadening coefficients for CHD_3 with CH_4 as collision partner.

3.7 Vibrational Energy Transfer in the Coriolis-coupled ν_3/ν_6 Dyad

An important relaxation pathway for the CHD_3 dyad is vibrational energy transfer between ν_3 and ν_6 . ν_3 and ν_6 are nearly degenerate ($\Delta E = 31.3 \text{ cm}^{-1}$) and are strongly Coriolis-coupled. V→V energy transfer between Coriolis-coupled vibrational states has been shown to be of importance in other small polyatomics [HAUB87] [DOYENNETTE88]. In their experiments with CHD_3 , Menard-Bourcin and Doyennette [MENARD-BOURCIN88] reported a preliminary rate for vibrational energy transfer between ν_3 and ν_6 of $\sim 10 \mu\text{sec}^{-1} \text{ torr}^{-1}$. This is the same magnitude as total depopulation. An important preliminary step in our measurements of state-resolved rotational energy transfer was to obtain a more accurate value for this rate and to evaluate its rotational state dependence.

We made our measurements of ν_3/ν_6 vibrational energy transfer by pumping the ν_6 $R_P(9,3)$ "A" transition with the CO_2 10R(22) laser line. We probed a range of J and K values of "A" type symmetry in ν_3 using the $2\nu_3-\nu_3$ QR hotband transitions. We observed a signal with an exponential rise and an exponential decay which is consistent with the type of signal that has been observed in other measurements of fast $V \rightarrow V$ energy transfer [FOY88] [HAUB87].

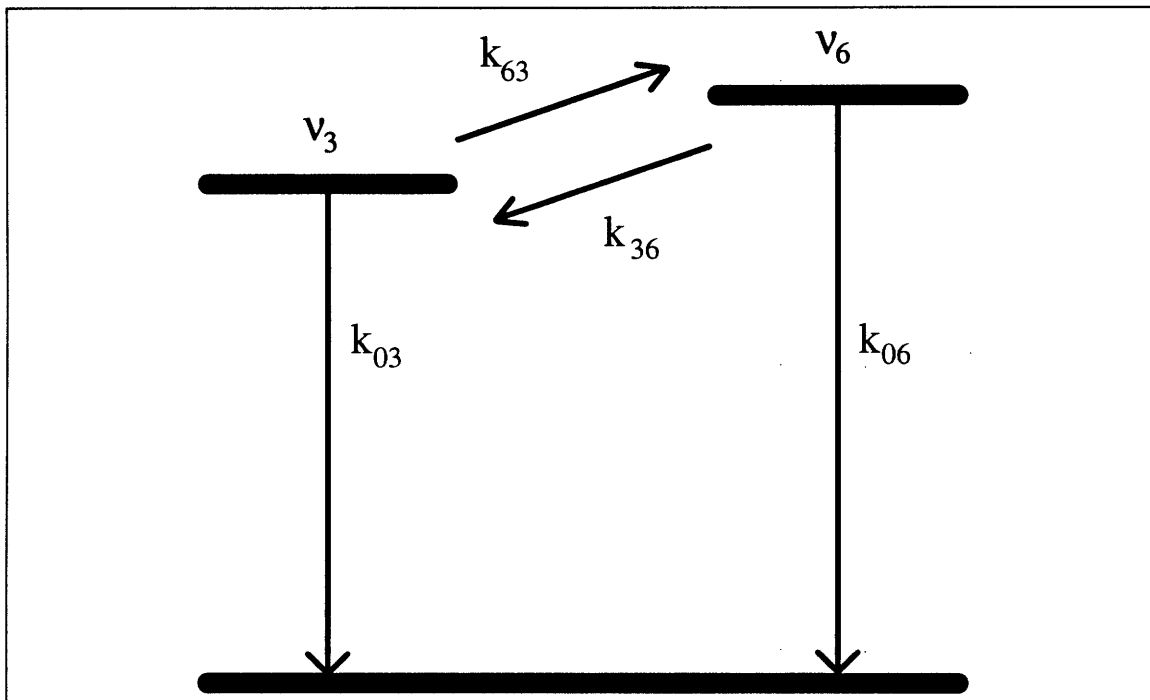


Figure 3.22

Schematic of processes included in the model of ν_3/ν_6 vibrational energy transfer.

The analysis of these signals was accomplished with a simplified model of vibrational energy transfer, see Figure 3.2. This model assumes that the rotational levels are equilibrated on the time scale of vibrational energy transfer [YARDLEY80] [FOY88]. In this approximation the model consists of three levels, ν_3 , ν_6 , and the ground vibrational state and analytic solutions can be found for the time dependence of the populations in ν_3 and ν_6 (see Appendix 3).

From our data, we find a rate constant $k_{\nu_3 \leftarrow \nu_6}$ of $\sim 1 \mu\text{sec}^{-1} \text{ torr}^{-1}$ with no dependence on final J or K. This rate is significantly larger than other vibrational energy transfer rates in CHD_3 which are on the order of $0.1 \mu\text{sec}^{-1} \text{ torr}^{-1}$ [DROZDOSKI78], but is still an order of magnitude less than the total depopulation rate. This is an important point for the analysis of R.E.T. in ν_3 . We expect (and observe) fast rotational energy transfer in ν_3 followed by non-rotational state specific equilibration with ν_6 .

3.8 Symmetry Changing Collisions: A Simple Förster Mechanism

An additional important vibrational energy transfer process was studied. This was the apparent nuclear spin changing, $A \leftrightarrow E$, process which is observed when a vibrationally excited molecule of one symmetry type transfers its vibrational excitation to a ground state molecule of different symmetry, viz.:



We observed this process by pumping the ν_3 $Q_Q(12,7)$ "E" and $Q_Q(11,5)$ "E" transitions with CO_2 laser 10P(24) line and monitoring the increase in absorption of the $2\nu_3-\nu_3$ $Q_R(11,9)$ "A" hotband. A typical signal is shown in Figure 3.23.

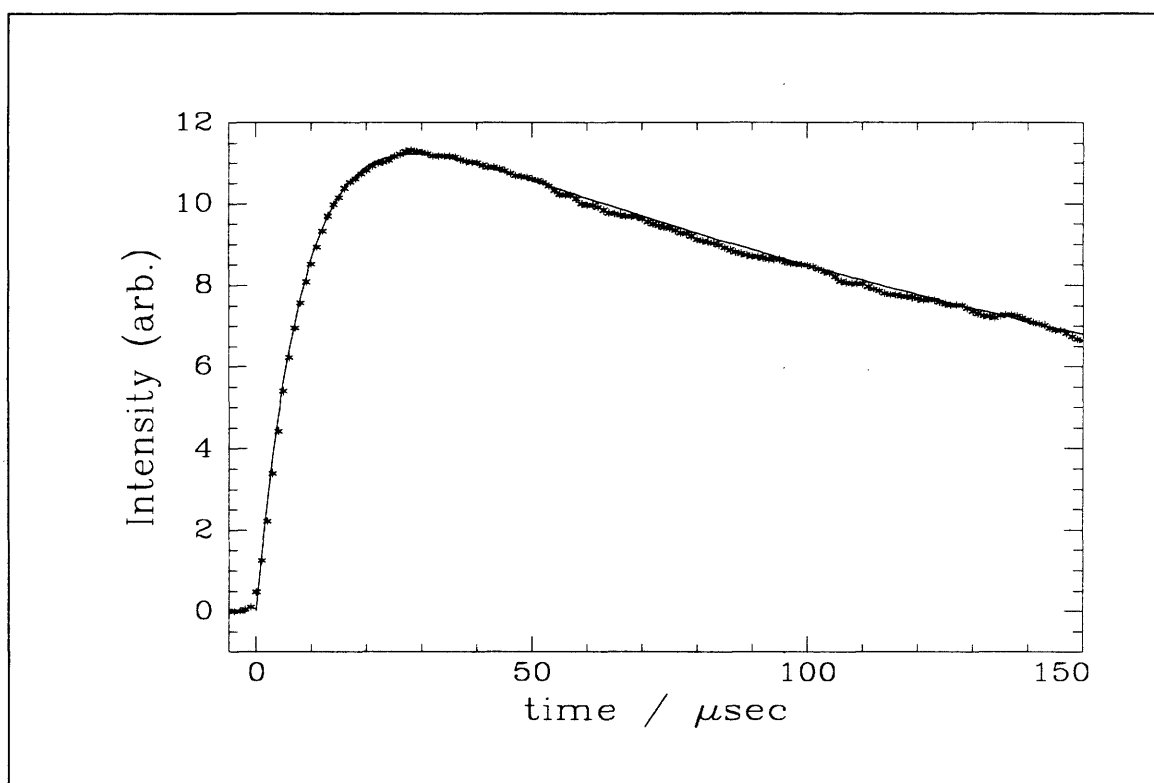


Figure 3.23

Transient signal showing vibrational swap process between "E" and "A" type nuclear spin species. The CO_2 pump laser was tuned to the 10R(24) transition which populates the ν_3 $J' = 12$, $K' = 7$ "E" level. The probe laser was tuned to the $2\nu_3-\nu_3$ $Q_R(11,9)$ "A" transition. The signal shows an initial increase, which indicates an equilibration between the "E" and "A" species, followed by a decay as molecules move out of the probe beam and relax to the ground state. The pressure of CHD_3 was 550 mtorr.

These signals were modeled using the same formalism used for the analysis of ν_3/ν_6 vibrational energy transfer. Signals like that shown in Figure 3.23 were recorded at a series of pressures between 225 and 1000 mtorr. They were fit to biexponential curves, Eq. 4 of Appendix 3, and the pseudo-first-order rates

for the rise of the signals were plotted against pressure, Figure 3.24. The rates show a linear dependence on pressure. The slope of the straight line fit through this plot is the rate constant for the process $A \leftarrow E$, which we find to be $0.17 \pm 0.02 \mu\text{sec}^{-1} \text{ torr}^{-1}$. This is in good agreement with the number reported by Mennard-Bourcin and Doyennette of $0.23 \pm 0.02 \mu\text{sec}^{-1} \text{ torr}^{-1}$ [MENNARD-BOURCIN88].

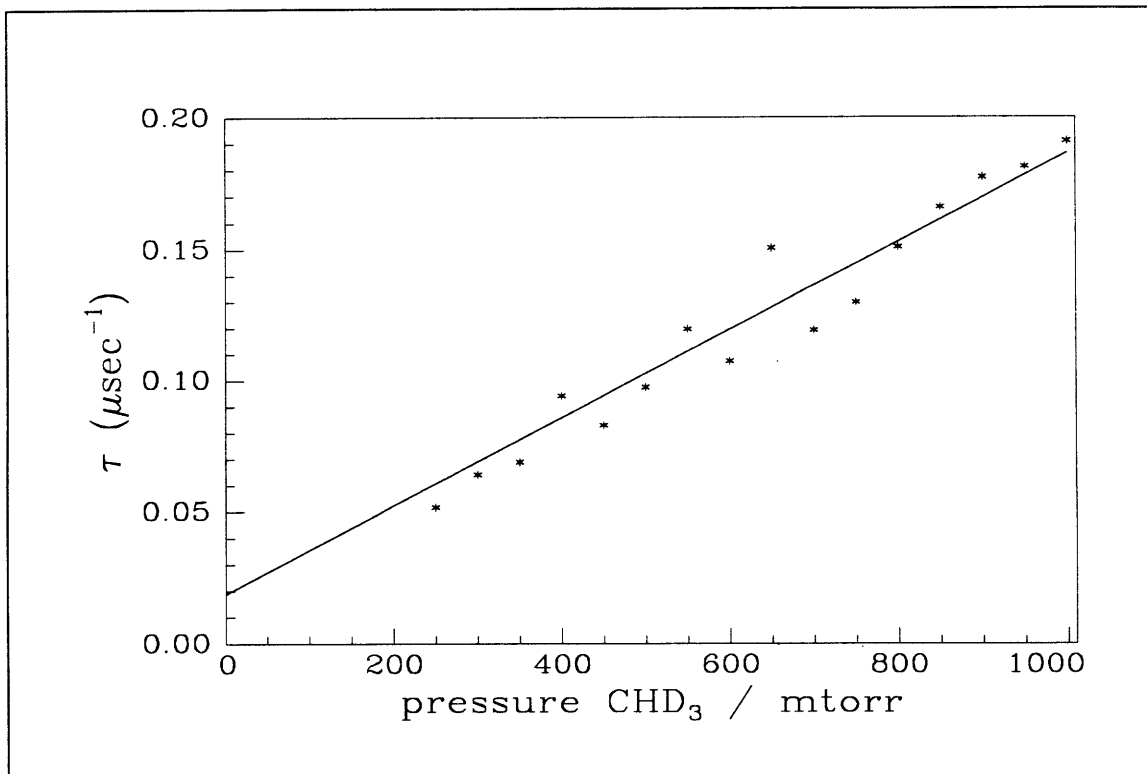


Figure 3.24

$\rho\tau$ plot for vibrational swap in ν_3 . $\text{CHD}_3(\nu_3, E) + \text{CHD}_3(\text{g.s.}, A) \rightarrow \text{CHD}_3(\text{g.s.}, E) + \text{CHD}_3(\nu_3, A)$

An interesting aspect of the vibrational swap process in CHD_3 , and similar symmetry changing processes in other symmetric top molecules [DOYENNETTE88, EVERITT89], is that the rates for these processes are in quantitative agreement with the predictions of a simple model of vibrational exchange [MELTON73, MELTON73, SHARMA69] based on Förster theory of electronic energy transfer in large molecules [FÖRSTER60], as shown in Section V Appendix 3. That this simple theory works so well is even more impressive because it has no adjustable parameters. The vibrational swap rate is determined from the magnitude of the transition dipole moment of the vibration being exchanged.

3.9 Master Equation Kinetics

We turn now to the analysis of 4-level state-to-state rotational energy transfer measurements in the CHD_3 ν_3 vibrational state. These are the most detailed measurements we have made, and they provide the greatest insight into the nature of the dynamics of collisional interactions in CHD_3 . Our overall objective

is to elucidate the propensity rules for rotational energy transfer. We will do this by extracting from our measurements a set of state-to-state rates. Here is the difficulty in the analysis of the data. Our experiment allows us to selectively overpopulate a single rotational level in the ν_3 vibrational state and to monitor the time evolution of the populations of other rotational levels in ν_3 as the excess population is distributed among the ν_3 rotational levels. What we cannot tell from our experiment is what pathway population follows in going from the initially populated level to the level being monitored. Ours is a bulb experiment where the effects of multiple collisions are significant. A single step process with a low probability may have a similar effect as a multi-step process with high probability for each step. For a satisfactory treatment of the data we must use kinetic master equation analysis [STEINFELD89, Appendix 1, Appendix 3].

In kinetic master equation analysis, a set of coupled first order differential equations is written for the time evolution of the population in each level in the system. In principle, each state $|i\rangle$ can be connected to any other state $|j\rangle$ with a rate constant k_{ji} . For the time evolution of the population in each state $|i\rangle$ there is a differential equation

$$\frac{dN_i}{dt} = \sum_j k_{ij} N_j \quad \text{Eq. 3.21.}$$

Conservation of population requires that the sum of all rates from other states into $|i\rangle$ must equal the sum of rates from $|i\rangle$ to all other levels, i.e.

$$k_{ii} = - \sum_{j \neq i} k_{ij} \quad \text{Eq. 3.22.}$$

If \mathbf{N} is a vector of level populations, and \mathbf{K} is a matrix of rates connecting these levels, i.e. the matrix element K_{ij} is the rate k_{ij} , then the set of coupled first order differential equations may be succinctly written as

$$\dot{\mathbf{N}} = \mathbf{K}\mathbf{N} \quad \text{Eq. 3.23.}$$

An additional requirement on the rate matrix \mathbf{K} is that when the elements of the elements of the population vector \mathbf{N} are proportional to the Boltzmann distribution, all elements of $\dot{\mathbf{N}}$ are zero. This is the requirement of detailed balance. The ratio of rates between states $|i\rangle$ and $|j\rangle$ must equal the ratio of their Boltzmann factors.

$$\frac{k_{ij}}{k_{ji}} = \frac{(2J_i + 1) e^{-E_i/kT}}{(2J_j + 1) e^{-E_j/kT}} \quad \text{Eq. 3.24}$$

For modeling energy transfer, the differential equation for the state directly populated must be modified to account for the time dependence of the pump laser, viz.:

$$\frac{dN_p}{dt} = \sum_j k_{pj} N_j - \alpha I(t) \quad \text{Eq. 3.25}$$

$I(t)$ is the temporal intensity profile of the pump pulse, and α is a scaling parameter.

There are two possible approaches to solving the master equation, numerical integration and eigenvalue decomposition [STEINFELD89]. Numerical integration was used for all the analyses presented here. The numerical integration routine in the MATLAB, ODE45, which utilizes automatic step size Runge-Kutta-Fehlberg integration, was used in all cases. Numerical integration simplifies the inclusion of the pump pulse profile, and the automatic step-size integration routine is quite efficient. However, in cases where the pump pulse can be treated as a delta function, the eigenvalue approach to solving the master equation may be more efficient. The master equation written in its matrix form, Eq. 3.?, has the formal solution

$$N(t) = \exp[Kt] \cdot N(0) \quad \text{Eq. 3.26.}$$

$N(0)$ is the initial population vector, and $N(t)$ is the population vector at time t . The matrix exponential, $\exp[Kt]$, is handled very efficiently in MATLAB™. The population vector $N(t)$ can be found immediately for any time using the eigenvalue technique unlike numerical integration where one must always begin integration from time zero.

Regardless of how the mechanics of solving the master equation is handled, the real difficulty in using master equation analysis to model state-to-state rotational energy transfer is in finding the rate matrix. The rate matrix contains all the state-to-state rates we wish to extract from the data. Given a rate matrix we can compute simulated transient signals and compare these with the experimental data. The difficulty is in going from the experimental data back to the rate matrix. For a system of N levels there are $N(N-1)/2$ independent state-to-state rates in the rate matrix. Even for very modest systems this can be a formidable number of independent parameters. For example, for CHD_3 we have used the CO_2 10R(24) pump to populate the v_3 $J' = 12, K' = 7$ "E" rovibrational level. Including only energetically accessible levels in v_3 of the same nuclear spin symmetry there are still a total of 96 levels that must be included in the rate matrix. This means that there are 4,560 independent state-to-state rates in the matrix. In comparison we have only 30 pieces of data. The situation is not completely hopeless although it is far from ideal. The details of the master equation modeling for CHD_3 have been published in the paper reproduced as Appendix 3 of this thesis and the reader should refer to it for more discussion. The point we wish to emphasize here is that for CHD_3 we are limited to pumping only transitions which are coincident with CO_2 laser lines. In an ideal world we would have both tunable pump and tunable probe lasers for our double resonance experiments. This limitation was the motivation for the Raman-shifted

Ti:sapphire I.R. source described in Chapter 4 and resulted in the CH₄ energy transfer experiments presented in Chapter 5.

3.10 State-to-state R.E.T. in ν_3 "A" and "E" Rotational Levels

The state-to-state rotational energy transfer measurements in the CHD₃ ν_3 vibrational level using the CO₂ 10R(34) and 10R(24) laser lines to pump respectively the CHD₃ ν_3 Q_Q(12,9) "A" and ν_3 Q_Q(12,7) "E" transitions have been described in detail in the paper reproduced as Appendix 3. The reader should refer to this Appendix for the thorough discussion of this material. Here, we summarize the principal conclusions.

The state-to-state R.E.T. measurements in CHD₃ were modeled using master equation analysis. The results of this analysis show that the individual rates span a broad distribution in both energy and angular momentum. Non-zero rates are found for changes in ΔE as large as 400 cm⁻¹ and for ΔJ and ΔK by as much as nine units. The falloff of the rates with ΔE or angular momentum is reasonably well fit with exponential energy-gap or angular momentum power gap laws. However, superimposed on the broad distribution of state-to-state rates are a few rates which are distinctly faster. These correspond to dipolar processes $\Delta J = \pm 1$, $\Delta K = 0$. The broad distribution of rates in ΔE and angular momentum is consistent with previous work on collisions between nonpolar, spherical tops ¹³CD₄ [FOY88] and SiH₄ [HETZLER89]. The dipole-like processes observed in CHD₃ are more surprising. The CHD₃ dipole moment of 0.006 D gives an interaction energy in self-collisions of only 0.02 cm⁻¹, which is far less than the CHD₃ rotational spacing. The propensity for dipole-like collisional transitions even though the interaction potential does not possess a leading dipole-dipole term, suggests that the symmetric-top level structure of the molecule plays a dominant role in determining inelastic collision propensity rules.

Chapter 4. Raman-shifted Ti:sapphire I.R. Source

4.1 Incentive for Broadly Tunable I.R. Laser Source

In studying molecular energy transfer, the systems that are investigated depend as much on the availability of suitable laser sources for double resonance as on the intrinsic interest in the molecule itself. For a molecule like CH₄, for which there is much interest in studying energy transfer both from the theoretical viewpoint because of its small size and high symmetry and practically because of its importance as a constituent of Earth's and other planetary atmospheres, it has been impossible to make detailed measurements of state-to-state energy transfer simply because to date suitable laser sources have not been available in the regions where this molecule has its vibrational transitions. It has been possible to study energy transfer in *methane* by using rare isotopes that happen to have coincidences with CO₂ laser lines, an example of "tuning the molecule to the laser." While CO₂ lasers have proven excellent pump lasers for energy transfer measurements of those molecules that have coincidence with a laser transition, they are extremely limited in which molecules are amenable to study and the choice (or no choice) of which ro-vibrational state is populated. It is the experimentalist desire to have a laser source of such versatility that the important features of the molecular system itself dictate what the appropriate experimental measurements should be and to not be limited by the deficiencies of the experimental setup. We present in this chapter a Raman-shifted Ti:sapphire I.R. source which can provide high pulse energy, narrow bandwidth radiation completely tunable over the mid and near I.R. This source is ideally suited for double resonance experiments with many molecular systems which have previously been inaccessible.

4.2 Basic Principles of Stimulated Raman Scattering

Stimulated Raman scattering (SRS) has been widely used as a means of extending the tunability of dye lasers into the near infrared [BIERRY77, FREY77, GRASIUK78, DEMARTINO80]. With the increased commercial availability of high power, tunable paramagnetic-ion solid-state lasers, in particular, Titanium doped sapphire (Ti:sapphire), already operating in the near infrared, SRS becomes a very powerful, general technique for efficiently and easily generating tunable infrared radiation to wavelengths as long as 3.7 μm .

The physics of stimulated Raman scattering has been discussed in many sources [MAIER76, SHEN84, STEINFELD85, WHITE87]. The basic principles of SRS are quite straightforward, although the details can become quite complex. What we present here is not a treatise on SRS, but rather the application of SRS as a tool for spectroscopic and energy transfer studies. The schematic diagram in Figure 4.1 illustrates the most common process involved in SRS, Stokes scattering. Photons of the fundamental laser frequency $\tilde{\nu}_f$ are converted to photons of frequency $\tilde{\nu}_s$ by inelastic scattering off molecules initially in

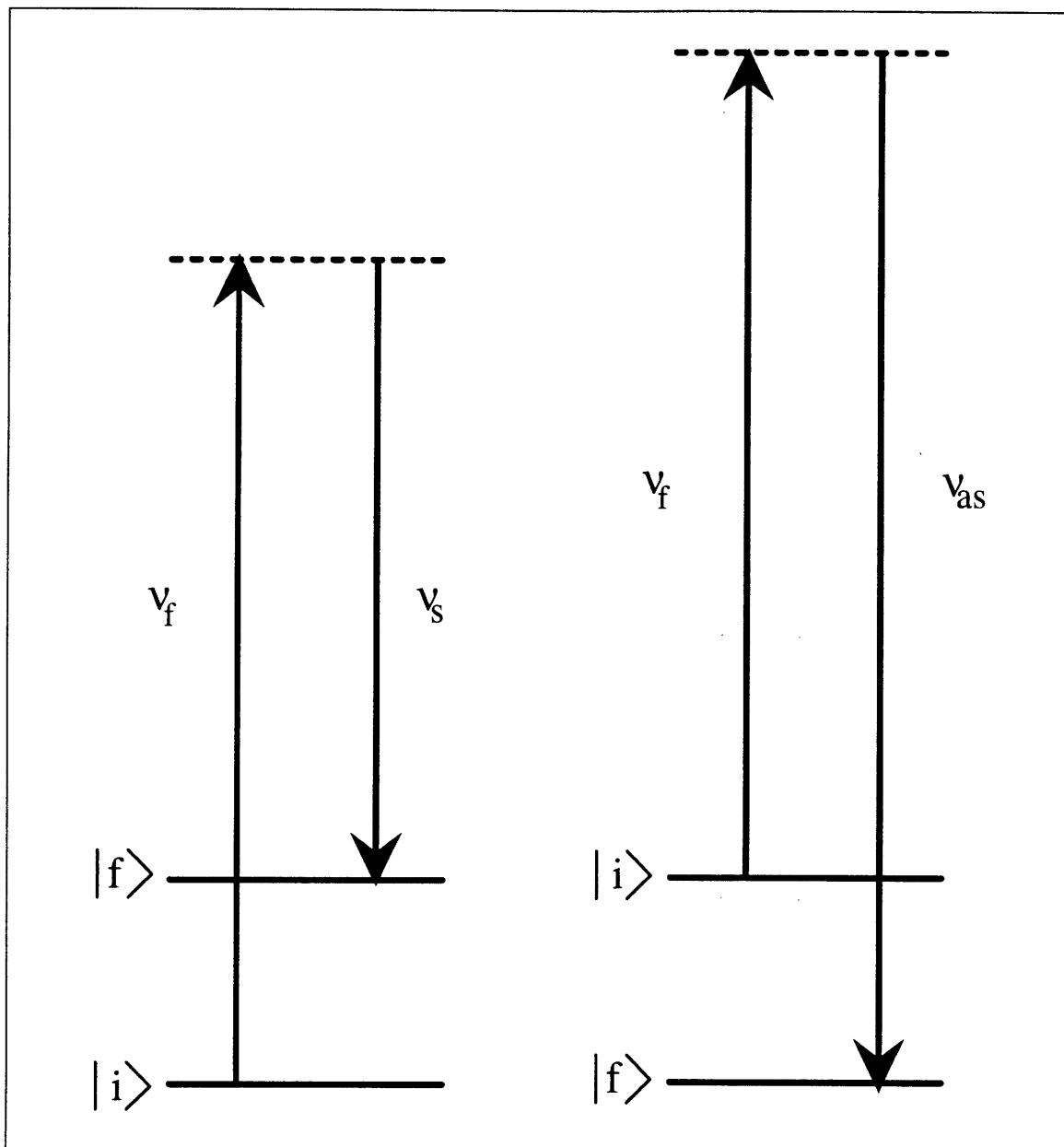


Figure 4.1

Energy level diagram for stimulated Raman scattering

state $|i\rangle$. The molecules which undergo a scattering event are promoted from state $|i\rangle$ to state $|f\rangle$, and the frequency of the scattered light, $\tilde{\nu}_s$, is shifted down in frequency by an amount corresponding to the energy spacing between levels $|i\rangle$ and $|f\rangle$,

$$\tilde{\nu}_s = \tilde{\nu}_f - \tilde{\nu}_v \quad \text{Eq. 4.1.}$$

$\tilde{\nu}_v$ is the Raman transition frequency between states $|i\rangle$ and $|f\rangle$. When the final state of the Raman transition is higher in energy than the initial state, $\tilde{\nu}_s$ is red-shifted from $\tilde{\nu}_f$ and is called the 1st Stokes component of $\tilde{\nu}_f$. Under our experimental conditions the photon number in the 1st Stokes can become very large, exceeding that in the depleted fundamental. The 1st Stokes photons can undergo a second scattering event which results in the production of photons shifted in frequency from the fundamental by twice the Raman transition. This is called the 2nd Stokes. It is also possible to scatter off molecules in an initially excited state with a Raman transition to a final state lower in energy. In this case the photons generated are called the 1st anti-Stokes of $\tilde{\nu}_f$. The frequency of the 1st anti-Stokes, $\tilde{\nu}_{as}$, is blue-shifted from $\tilde{\nu}_f$,

$$\tilde{\nu}_{as} = \tilde{\nu}_f + \tilde{\nu}_v \quad \text{Eq. 4.2.}$$

The intensity of the 1st anti-Stokes is always much less than the 1st Stokes since there are essentially no molecules in the excited state. However, 1st and 2nd Stokes production involves promotion to the excited state. The number of molecules moved to the excited state can become significant (although we are always two to three orders of magnitude away from depleting the sample) and we do observe measureable power in the 1st anti-Stokes, see Figure 4.6.

The Stokes and anti-Stokes production described above arises from the amplification of spontaneous Raman scattering by the intense laser fundamental. The spontaneous Raman photons scattered along the laser fundamental wavevector are the most strongly amplified. Almost all of the power in the 1st and 2nd Stokes and in the 1st anti-Stokes comes out collinear with the fundamental laser beam. It is important to note, however, that the Raman medium itself oscillates coherently [SHEN84, STEINFELD85, WHITE87] and that photons can scatter off these oscillations in a parametric type of process. The Stokes and anti-Stokes beams produced by this parametric process must obey a phase-matching requirement. The spontaneously scattered Raman photons which obey this phase-matching requirement are the most strongly amplified by this process. The Stokes and anti-Stokes beams produced by this parametric process are not collinear with fundamental beam, instead they propagate on a cone centered on it (see [STEINFELD85, p. 434] for more detail.) The central feature in the photograph shown in Figure 4.2 is the 1st anti-Stokes of the Ti:sapphire laser in H₂. The bright spot in the center of the ring is the 1st anti-Stokes produced by scattering off vibrationally excited H₂. The ring itself is the 1st anti-Stokes produced by the parametric process. While for the purpose of our experiments the production of anti-Stokes lines is an unimportant secondary process, it is hard to dismiss the aesthetic appeal of the rainbow of colors that can be produced from an invisible infrared laser beam.

This page was intentionally left blank.

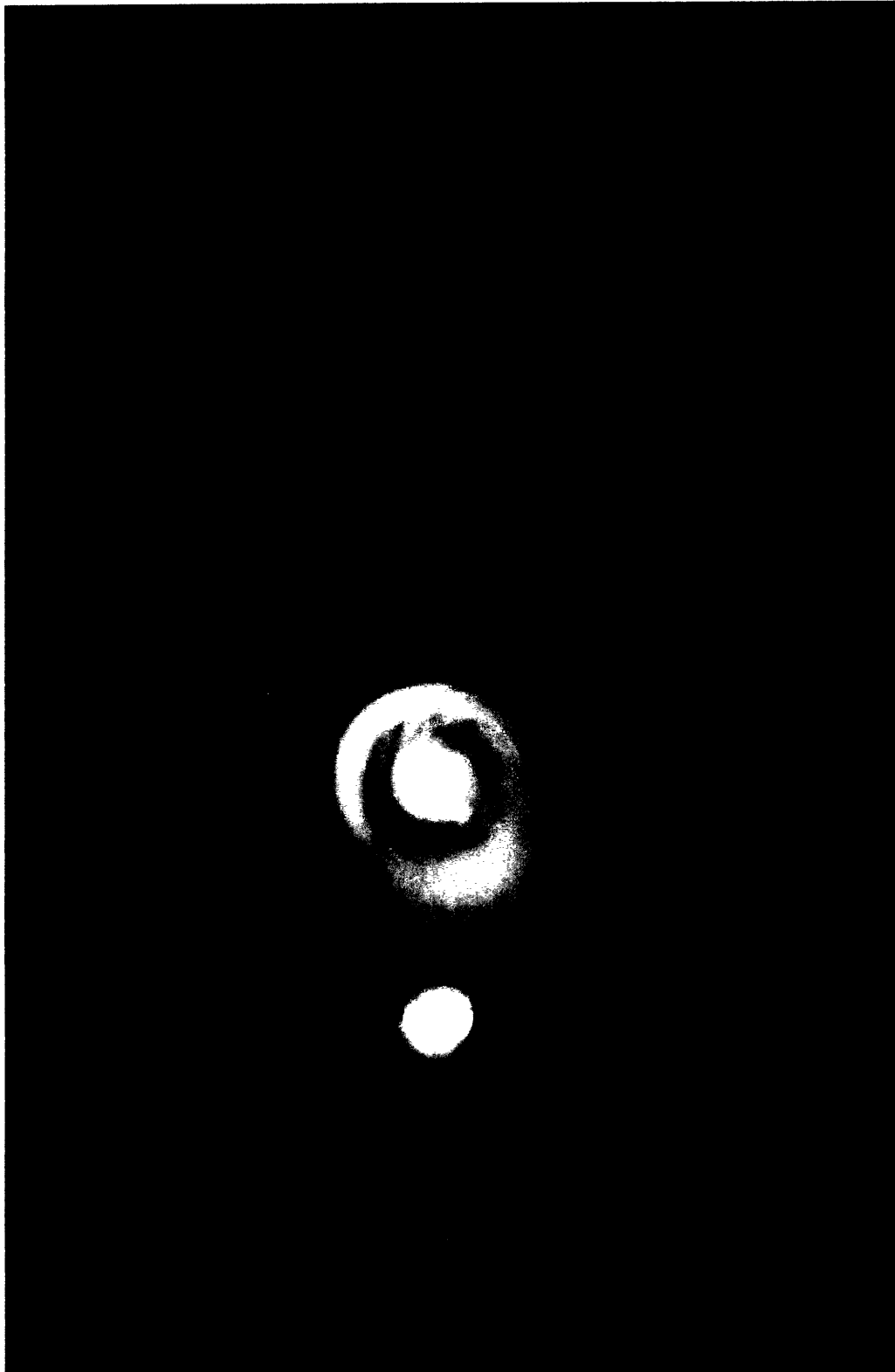


Figure 4.2

Figure 4.2 is a photograph of the 1st anti-Stokes in H_2 of the Ti:sapphire laser, which is operating at 794 nm. The central feature is the Q(1) line. The other spots are rotational Raman transitions.

The power gain of the 1st Stokes component [MAIER76, HANNA86] under the approximation of a plane wave pump source is

$$\text{gain} = \exp(\gamma_R I_p l) \quad \text{Eq. 4.3.}$$

In this equation γ_R (cm/MW) is the Raman gain coefficient, I_p (MW/cm²) is the laser irradiance and l (cm) is the interaction length. The Raman gain coefficient is derived from molecular parameters according to [HANNA86]

$$\gamma_R = \frac{16\pi c^2 \Delta N}{n_s^2 \hbar \omega_s^3 \Delta \omega_R} \left(\frac{d\sigma}{d\Omega} \right) \quad \text{Eq. 4.4.}$$

ΔN is the population difference between states $|i\rangle$ and $|f\rangle$, n_s is the refractive index of the Raman medium at the Stokes frequency ω_s , $\Delta \omega_R$ is the Raman linewidth (FWHM), and $(d\sigma/d\Omega)$ is the Raman scattering cross section in intensity units. Equation 4.3 is too simple to adequately describe the processes occurring for our experimental arrangement. A more detailed model which accounts for the coupling between the fundamental, 1st and 2nd Stokes such as that described by von der Linde et. al. [VONDERLINDE69] would be necessary. Our purpose here is only to present the main points which are of concern for efficient Raman-shifting.

Eq. 4.3 shows that Stokes production is favored by long interaction lengths, high laser irradiance, and a Raman medium with a large gain coefficient. In our experimental arrangement, we use a 2 m Raman cell to make the interaction length as long as possible while still keeping it to reasonable dimensions. We use a very small diameter (~2mm) laser beam to maximize the irradiance over the entire length of the Raman cell, and we focus this beam to increase the irradiance even more when it is necessary to maximize the 2nd Stokes. For the Raman gain medium we have used H₂ and D₂ gas. H₂ is perhaps the best Raman-shifting medium. It has a large Raman shift of 4155.10 cm⁻¹ [STOICHEFF57, HUBER79] on the ν_1 Q(1) vibrational Raman transition and a large Raman scattering cross section [SCHRÖTTER79]. It has no significant absorption in the infrared [FINK65], and it is cheap and rugged (one can hardly do laser damage to H₂ gas).

There are two points worth noting in the equation for Raman gain, Eq. 4.4. The first is that the gain is inversely proportional to the generated Stokes frequency cubed. This means that generating radiation far into the infrared becomes exceedingly difficult as the Raman gain at these low frequencies is very small. The other point is that the Raman gain is directly proportional to the number of molecules in the lower level of the Raman transition and inversely proportional to the Raman linewidth. The Raman gain will

increase with increasing pressure as the number density increases until pressure broadening begins to increase the Raman linewidth. Dicke narrowing [DICKE53] in both H₂ [MURRAY72] and D₂ [MURRAY72, VOLKOV88] causes linewidth to reach its minimum value at a maximum number density. Increasing the pressure beyond this point does not increase the Raman gain, nor does it diminish the Raman gain since both the number density and the line width are increasing linearly and their effects cancel one another. For H₂, the pressure at which the Q(1) linewidth is at a minimum is between 10 and 20 atmospheres. For the D₂ Q(2) transition, the linewidth is at a minimum at ~1 atmosphere. Some of the important parameters of H₂ and D₂ related to the use of these gases as Raman-shifting media are listed in Table 4.1.

Raman medium	Raman Transition	%pop. in $ i\rangle$	$d\sigma/d\Omega$ @ 800nm m ² /sr	γ/p Mhz/atm.
H ₂	Q(1) 4155.10 cm ⁻¹ (a)	66 %	9.1 x 10 ⁻³⁶ (b,c)	51 (c)
D ₂	Q(2) 2987.33 cm ⁻¹ (a)	39 %	9.8 x 10 ⁻³⁶ (b,c)	138 (d)

Table 4.1

SRS parameters for H₂ and D₂. (a) [STOICHEFF57, HUBER79], (b) [SCHRÖTTER79], (c) [HANNA86], (d) [VOLKOV88].

4.3 Experimental Arrangement

The Ti:sapphire laser used in the work presented here was an HRL-100 (Spectra Technology, Inc). It consists of a single-logitudinal-mode (SLM) oscillator in a Littman type cavity and three amplifier stages. The oscillator and amplifiers are pumped with the doubled output of a Nd:YAG laser (Continuum NY61-20). The tuning range of the Ti:sapphire laser is between 730 and 940 nm.

As was mentioned in the previous section, the generation of Stokes radiation becomes increasingly more difficult farther into the infrared due to the falloff of the Raman gain with decreasing Stokes frequency. Efficient production of 1st Stokes at wavelengths as long as 1.4 mm can be easily achieved, but in order to generate significant pulse energies in the 2nd Stokes at wavelengths as long as 3.3 μm, it is necessary to maximize the conditions which enhance Stokes production, namely high pulse energies, tight laser beams and long interaction lengths. We experimented with many different configurations of the Raman shifter, some of which used consecutive focussing of the Ti:sapphire beam and the generated Stokes beams two or three times, and in other cases total Raman-shifter lengths up to three meters long were tried. The best configuration for the generation of 2nd Stokes of all those tried was found to be a 2 m long cell divided into two sections, Fig 4.2. A well collimated, small diameter (~2 mm) Ti:sapphire beam was sent through the first meter of the cell. Enclosed within the center of the cell, in a mount which allowed gas to pass through it, was a 50 cm f.l. BaF₂ lens. This lens focussed the Ti:sapphire

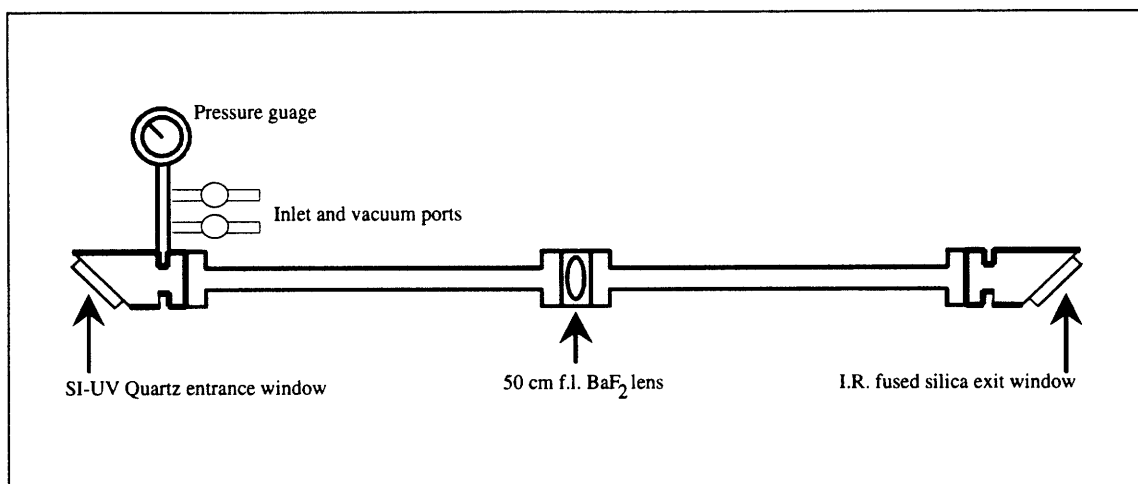


Figure 4.3

Schematic of the 2 m internal lens Raman-shifter

fundamental and the 1st Stokes generated in the first half of the cell to a gentle focus in the second half of the cell. Focussing the Ti:sapphire beam after significant 1st Stokes had been generated seemed to be key to the efficient production of 2nd Stokes. Focussing the Ti:sapphire beam in the first half of the cell was detrimental to the 2nd Stokes. The problem with this was that significant amounts of power were lost to rotational Raman.

In rotational Raman in H₂, the Raman transitions are the S(1) and O(3) rotational transitions in the ground vibrational state. These pure rotational transitions have an important effect on the efficiency of the Raman conversion process because rotational Raman robs power from the vibrational Raman process. The rotational Raman is very evident in the anti-Stokes lines. The additional spots to either side of the 1st vibrational anti-Stokes in Figure 3.2 are rotational Raman. The most significant power loss to rotational Raman comes from the fundamental and 1st Stokes. Figures 4.4 shows the spectra of the output of the Raman-shifted Ti:sapphire laser in the wavelength region near the Ti:sapphire fundamental dispersed through a monochromator. Two consecutive rotational Raman transitions are seen on either side of the fundamental. The spacing between these lines is 10 times the rotational constant for H₂. Figure 4.5 shows a similar spectrum recorded near the 1st anti-Stokes lines.

4.4 Characterization of the Raman-shifted Ti:sapphire I.R. Source

In this section we present some measurements which characterize the Raman-shifted Ti:sapphire I.R. source.

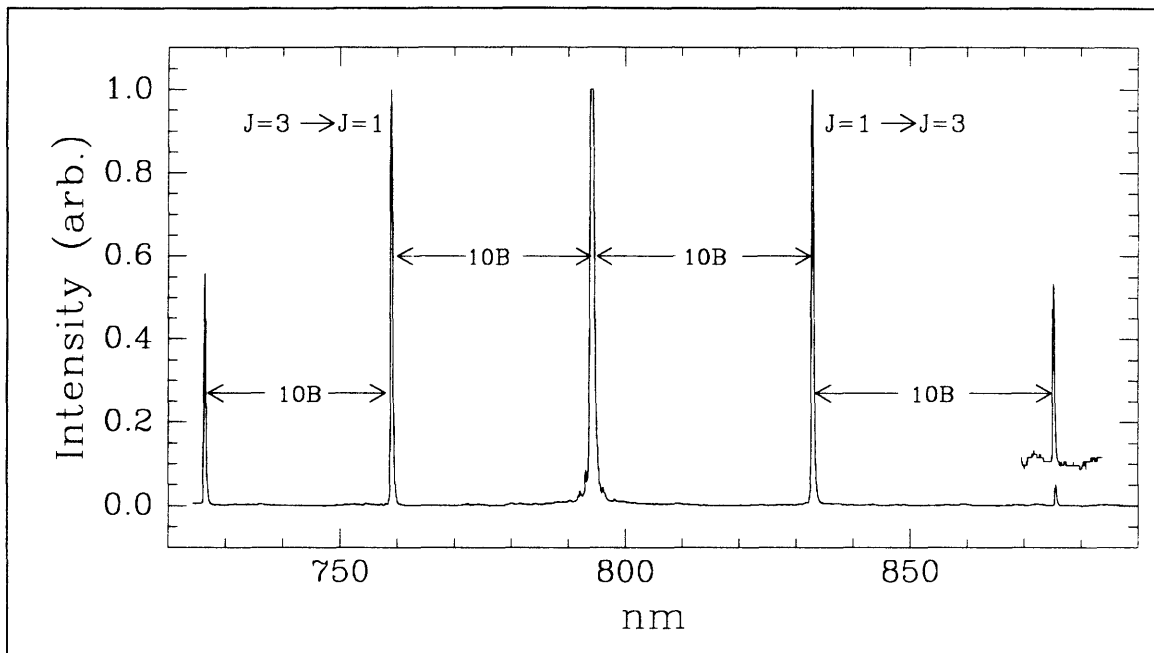


Figure 4.4

The figure shows the dispersed output of the Raman-shifted Ti:sapphire laser in the wavelength region near the fundamental at 794 nm, which is offscale. The additional lines are successive rotational Raman shifts of the Ti:sapphire fundamental. They are all separated by $10B$. B is the rotational constant of the ground vibrational state of H_2 , 59.30 cm^{-1} .

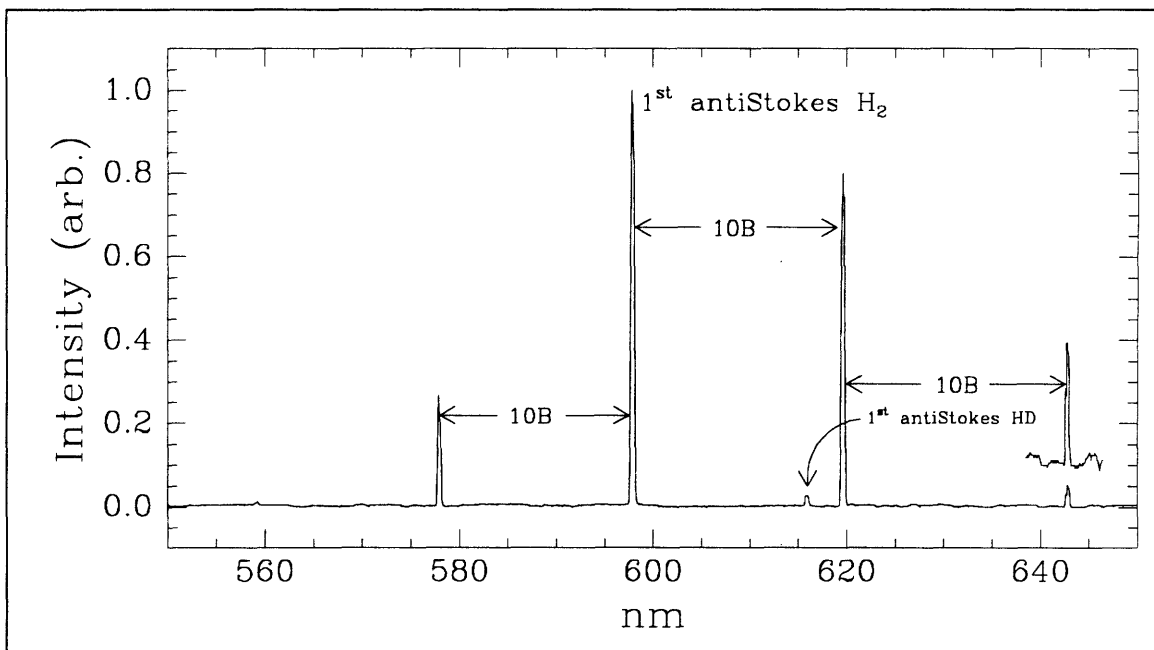


Figure 4.5

The figure shows the dispersed output of the Raman-shifted Ti:sapphire laser (794 nm) in the wavelength region near the 1st anti-Stokes in H_2 . The additional strong lines are rotational Raman. The small line at 617 nm corresponds to the 1st anti-Stokes of HD.

Figure 4.6 shows the pulse energies of the Stokes components and the depleted fundamental as a function of the Ti:sapphire input energy. At low pulse energies the only output is the Ti:sapphire fundamental. There is approximately 25% loss of the fundamental passing through the Raman-shifter. This is consistent with the total reflection losses for all the optical elements in the beam path. The threshold for Stokes production is ~ 2 mJ. The 1st Stokes grows rapidly and exceeds the depleted Ti:sapphire fundamental at an input pulse energy of 7 mJ. The 1st Stokes reaches a plateau between 10 and 15 mJ input while the energy in the 2nd Stokes rapidly increases. At the highest input energy measured, both the 1st and 2nd Stokes pulse energies exceed the depleted fundamental. 2.8 mJ of 2nd Stokes is obtained with an input energy of 23.5 mJ. This is an impressive 12% energy conversion efficiency and a 35% photon

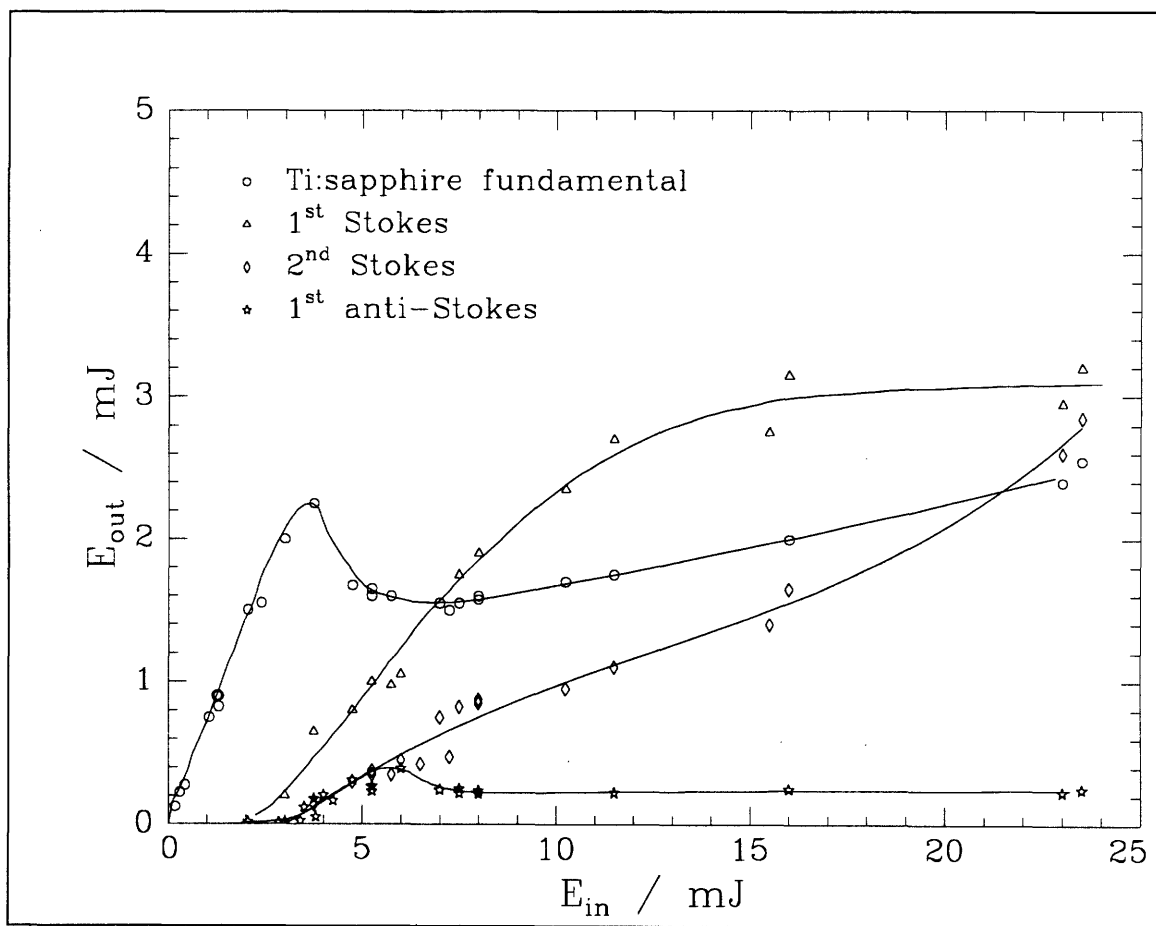


Figure 4.6

Output power of the main Raman lines in H_2 as a function of input power. The Ti:sapphire fundamental was at 794 nm.

conversion efficiency. From the slope of the 2nd Stokes curve at the highest input energy measured it appears that the 2nd Stokes will increase even more at higher input energies, becoming the dominant output at high Ti:sapphire input energies: compare with the similar measurements in [HARTIG79] and

the analysis presented in [VONDERLINDE69]. Somewhat higher energies, ~40 mJ, are possible with this laser in its current configuration with careful attention to the alignment, but significantly higher energies can only be achieved by having more energy in the 532 nm pump laser.

Figure 4.7 shows the the temporal profiles for a single pulse of the doubled Nd:YAG pump laser and Ti:sapphire laser recorded simultaneously on a fast photodiode. There is ~30 nsec of delay between the 532 nm pump and the generation of the Ti:sapphire pulse. The FWHM of the 532 nm pulse is ~9.5 nsec while the Ti:sapphire pulse is ~4 nsec FWHM. A shot-to-shot jitter of ~2-4 nsec was observed between the 532 nm pump pulse and the Ti:sapphire pulse. The Ti:sapphire laser was operating at 835 nm.

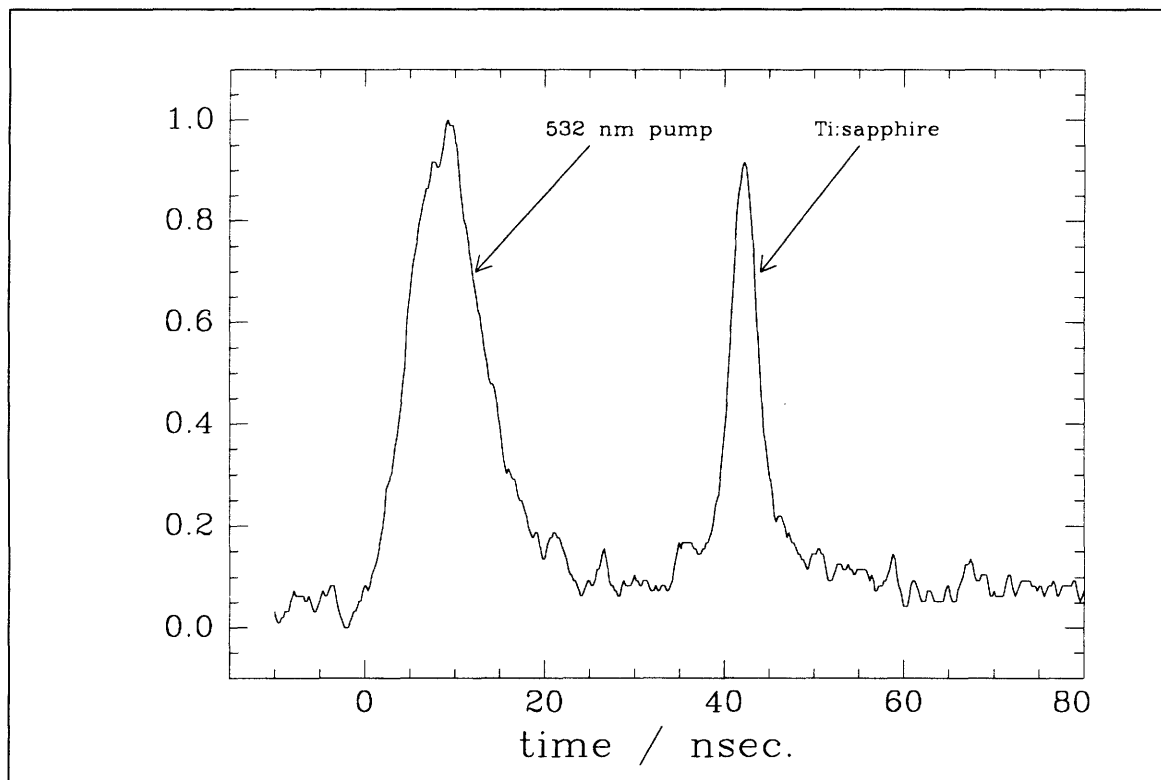


Figure 4.7

Temporal profile of the 532 nm Nd:YAG laser and the Ti:sapphire laser at 835 nm

Figure 4.8 shows the temporal profiles of the depleted fundamental and the main Raman lines in D_2 at the output of the Raman shifter. The Ti:sapphire laser was operating at 835 nm. All of the peak heights have been scaled to 1.0 for convenience of comparison, they do not represent pulse energies. The duration of the fundamental is shortened due to energy flow into the 1st and 2nd Stokes. It is interesting to note that the 1st Stokes continues after the fundamental is depleted.

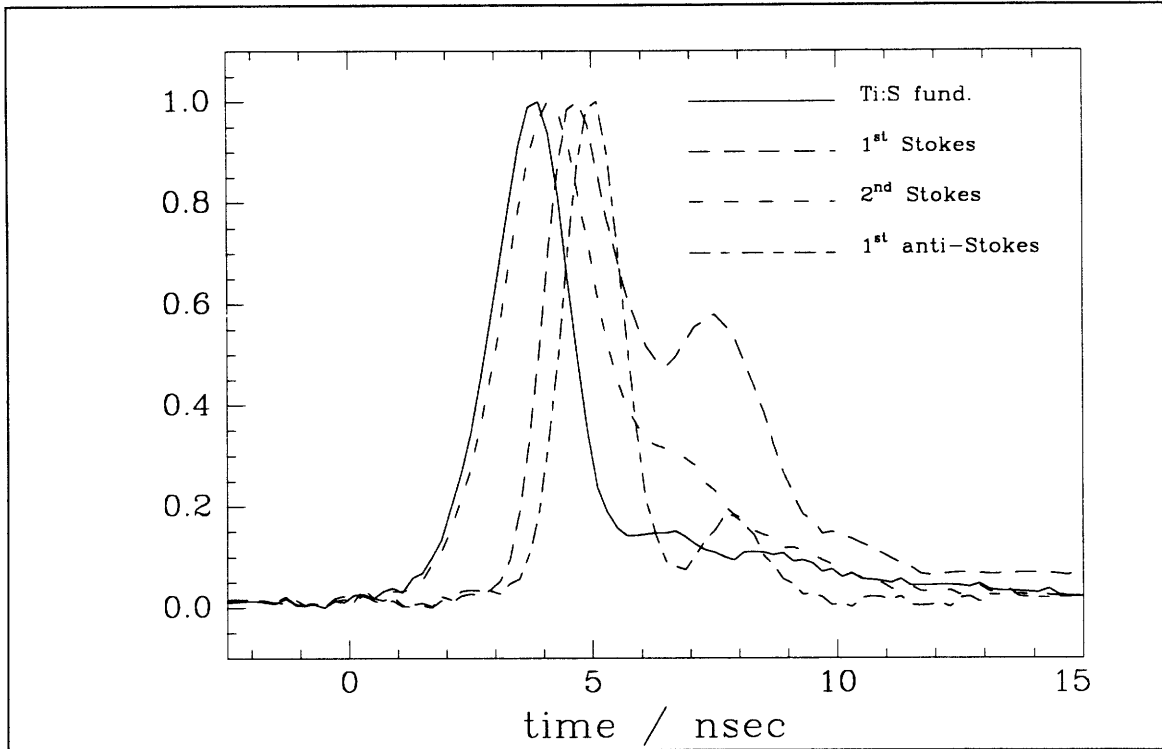


Figure 4.8
Pulse widths and delays of the Raman shifted Ti:sapphire

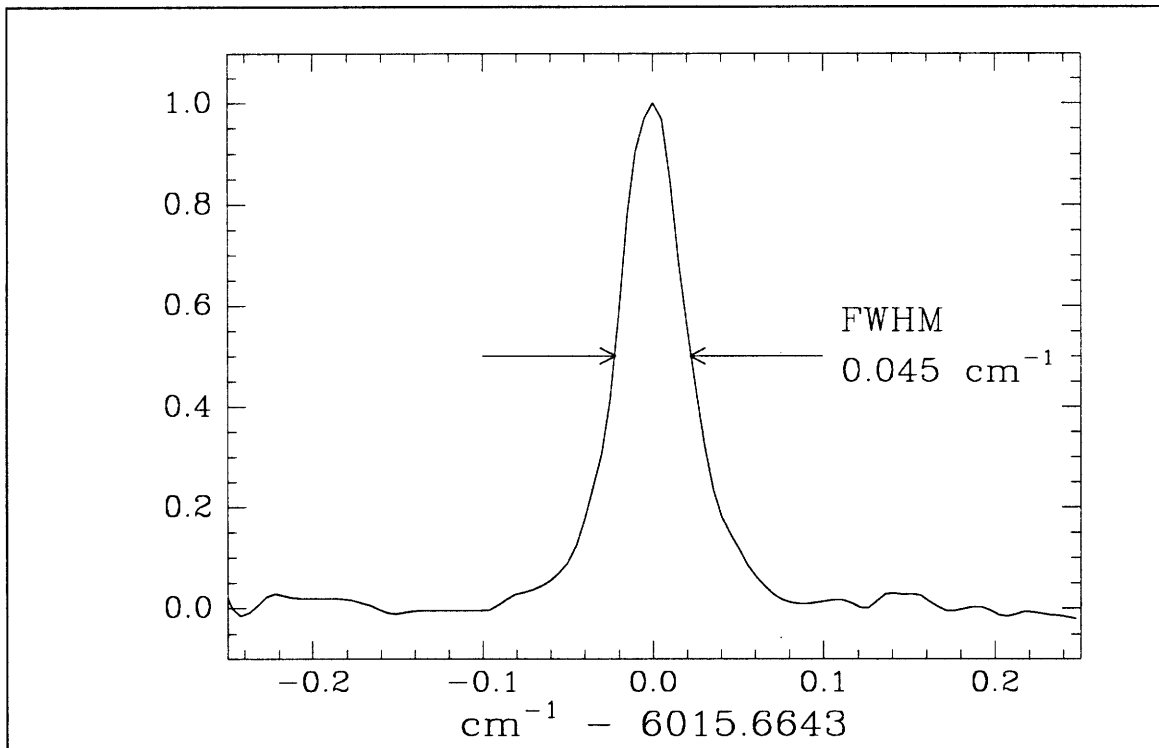


Figure 4.9
2nd Stokes bandwidth measured at the CH_4 $2\nu_3$ R(0) transition

The FWHM bandwidth of the 2nd Stokes of the Ti:sapphire laser in D₂ was measured by recording the photoacoustic spectrum of the CH₄ 2ν₃ R(0) transition at 6015.6643 cm⁻¹. The pressure of methane in the photoacoustic cell was 1 torr to reduce pressure broadening effects. The doppler width for CH₄ at this frequency is 0.018 cm⁻¹. The observed width of the transition is primarily the 2nd Stokes bandwidth.

4.5 Fluorescence-detected double resonance in HCCH

As an initial test of the applicability of our tunable I.R. pump source, we* performed some I.R./U.V. double resonance experiments in acetylene. The 2nd Stokes of the Raman-shifted Ti:sapphire at 3.3 μm was used to pump individual rotational transitions in the ν₃ fundamental of acetylene. The frequency doubled output of an excimer pumped dye laser (Lambda Physik LPX 200 and FL2002 EC) was used to probe ν₃ hotbands to the ungerade vibrational levels of the \tilde{A} state [UTZ93, TOBIASON93]. Acetylene was a good candidate for the initial tests of the efficiency of the Raman-shifted Ti:sapphire as a pump source in a double resonance scheme for two reasons. First, the transition dipole moment for the ν₃ fundamental of acetylene at 3300 cm⁻¹ is very large. Individual line strengths are on the order of 1x10⁻¹⁹ cm molecule⁻¹ [HITRAN92]. Since we were not sure how much population could be moved with the 2nd Stokes pump, strong I.R. transitions were likely to give the best chance for success. The second reason that acetylene was a good choice for the initial experiments is that the means of detection of double resonance was U.V. fluorescence from the \tilde{A} state. This is a very sensitive technique which would assure the greatest chance for success.

Our concerns about the efficacy of the experimental setup turned out to be for naught. We observed very large double resonance signals. An initial search for the ν₅ B_u fundamental [TOBIASON93] in the \tilde{A} state revealed two previously unrecorded bands, the Coriolis-coupled 2ν₃+ν₆ and 2ν₃+ν₄. These were much stronger in double resonance than the ν₅ fundamental. In Figure 4.10 we show an example of the double resonance spectrum recorded with the 2nd Stokes pump fixed to the ν₃ R(2) transition while the doubled dye laser was scanned through the \tilde{A} state bands. The marked transitions are from 3-level double resonance. The unmarked features are 4-level double resonance due to collisional energy transfer in ν₃. The intensity of the ν₅ Q(3) line is more than an order of magnitude less the Q(3) line for 2ν₃+ν₆. From this initial work we have obtained spectroscopic terms for the 2ν₃+ν₆/2ν₃+ν₄/ν₅ bands.

Having had great success in observing I.R./U.V. double resonance in acetylene, we undertook a series of state-to-state energy transfer measurements in the HCCH ν₃ fundamental using this technique. The results of this work will be presented elsewhere, but here we list some of the total depopulation rates which were measured in Table 4.2. These rates are in good agreement with other total depopulation

* Stephani Solina and Jon O'brien are gratefully acknowledged for their considerable assistance with these experiments.

measurements in HCCH [DOPHEIDE94, FROST93, TOBIASON92, UTZ91, CARRASQUILLO88, CHADWICK93].

ν_3 rotational level	$\rho\tau / \mu\text{sec}^{-1} \text{ torr}^{-1}$
J = 6	26 (3)
J = 8	26 (4)
J = 10	30 (6)

Table 4.2

Total depopulation rates in the acetylene ν_3 vibrational level.

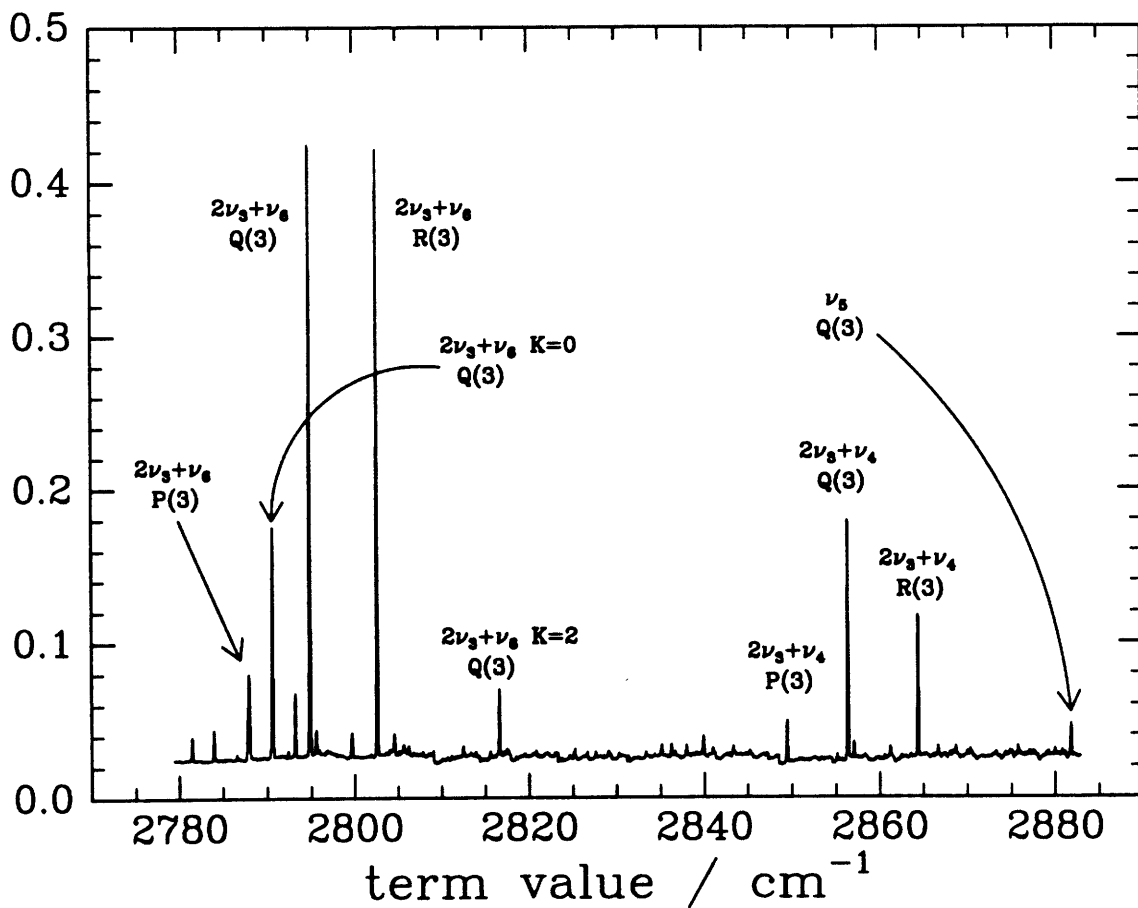


Figure 4.10

The figure shows an example of I.R./U.V. double resonance in acetylene. The I.R. pump was fixed to the ν_3 R(2) transition and the U.V. probe was scanned through the $2\nu_3+\nu_6/2\nu_3+\nu_4/\nu_5$ \tilde{A} state vibrational bands.

Chapter 5. CH₄ Energy Transfer

5.1 Introduction

The Raman-shifted Ti:sapphire laser system described in Chapter 4 is an excellent solution to the difficulty of studying energy transfer in CH₄. The 2nd Stokes shift of the Ti:sapphire in H₂ and D₂ falls favorably across several of the low overtone bands and the infrared active ν_3 fundamental. In the experiments described here, this tunable laser source has been used to directly pump specific rotational levels in the overtone and combination bands $\nu_3+\nu_4$ and $2\nu_3$. These bands are sufficiently strong to allow a significant amount of population to be moved to the excited state with the 2-5 mJ available in the 2nd Stokes. An experimental arrangement analogous to that described for the CO₂/diode laser double resonance experiments with CHD₃ has been used for the study of energy transfer in CH₄. The principal differences were that the CO₂ laser has been replaced by the Raman-shifted Ti:sapphire laser and an ultrastable liquid nitrogen cooled 3.3 μm c.w. infrared diode laser was used instead of the noisier diode lasers cooled by closed-cycle helium refrigeration units.

Several preliminary investigations of energy transfer processes in CH₄ are presented in this chapter. GSR rates have been measured for self-collisions for several transitions. Similar measurements have been made of TD rates in the $\nu_3+\nu_4$ combination band. These experiments are the first direct, time-resolved measurements of rotational relaxation in CH₄. The total rates allow us to make a comparison with the extensive work that exists about pressure broadening in CH₄. We have also studied the polarization dependence of the GSR and TD rates, since this dependence is indicative of the importance of reorientation collisions, which are often neglected in pressure broadening theory. A very significant difference (~35%) was observed for the GSR rates measured with perpendicular or parallel relative polarization of the pump and probe lasers. Vibrational energy transfer among the methane overtone levels has been measured and is compared here to a simplified model of $V\leftarrow V$. We also present a detailed analysis of state-to-state rotational energy transfer at low J in the $\nu_3+\nu_4$ vibrationally excited state and in the ground state. These data have been analyzed using kinetic master equation analysis. We find strong propensity rules for parity and vibrational angular momentum conserving collisions in $\nu_3+\nu_4$. The parity conservation propensity rule is also evident in the ground vibrational state. For the ground state, we have determined the state-to-state R.E.T. rates connecting the three lowest J states of A symmetry.

5.2 Overview of CH₄ Spectroscopy

Before discussing the energy transfer studies in CH₄ we briefly outline some of the important aspects of its rovibrational structure and spectroscopy. More detail can be found in the books by Herzberg and Papoušek and Aliev [HERZBERG45, PAPOUSEK82]. Bobin and Moret-Bailly have recently written an

historical review of the important theoretical and experimental work on the spectroscopy of T_d molecules with an emphasis on CH_4 [BOBIN94].

CH_4 is a spherical top molecule belonging to the point group T_d . There are four normal modes for tetrahedral XY_4 molecules [HERZBERG45]. For CH_4 they are: ν_1 (A_1), the symmetric CH stretch; ν_2 (E), the doubly degenerate deformation; ν_3 (F_2), the triply degenerate asymmetric CH stretch; and ν_4 (F_2), the triply degenerate deformation.

The ν_3 and ν_4 F_2 states have a vibrational angular momentum $l_v = 1$. The three-fold degeneracy of F_2 states, however, is removed by Coriolis interaction. Coriolis interaction between J and l in the rotating molecule causes a splitting of the F_2 states into three Coriolis components. A pure rotational quantum number R is defined as $R = J - l$ [HECHT60]. R can have the values $J, J \pm 1$. The three Coriolis components are designated as F^+ , F^0 , or F^- according to the value of $(R - J) = +1, 0$, or -1 . The energies of the Coriolis components are

$$\begin{aligned} F^+(J) &= BJ(J + 1) + 2B\zeta J \\ F^0(J) &= BJ(J + 1) - 2B\zeta J \\ F^-(J) &= BJ(J + 1) + 2B\zeta(J + 1). \end{aligned} \quad \text{Eqs. 5.1}$$

B is the rotational constant and ζ is the Coriolis constant. Both ν_3 and ν_4 are split by this Coriolis interaction, but the splitting for ν_4 is much larger than for ν_3 as expressed by the larger value of the ζ_4 constant. The vibrational degeneracy of the other degenerate CH_4 fundamental, the ν_2 (E), can not be removed by Coriolis interactions, because by Jahn's rule [JAHN39], the E X E product does not contain F_1 , the species of the rotation.

The vibrational spacing of CH_4 is such that the fundamentals and overtones are clustered in groups of closely spaced levels, as is illustrated in the vibrational energy level diagram shown in Figure 5.1. A common and convenient terminology is to refer to the sets of closely spaced vibrational levels as polyads. The lowest energy set of levels is the Coriolis-coupled ν_4 and ν_2 pair. These are referred to as the dyad. The next higher set is the group of five levels formed from the three binary combinations of the dyad levels and the ν_1 and ν_3 fundamentals. These form the pentad. In a similar fashion, the binary combination of the dyad with the pentad results in a set of eight levels which are known as the octad. The vibrational levels within a polyad interact strongly with each other but are more or less isolated from other polyads. Because of the strong interaction between the vibrational levels in a polyad, the standard spectroscopic analysis of CH_4 is to simultaneously analyze all vibrational levels within a polyad [CHAMPION92].

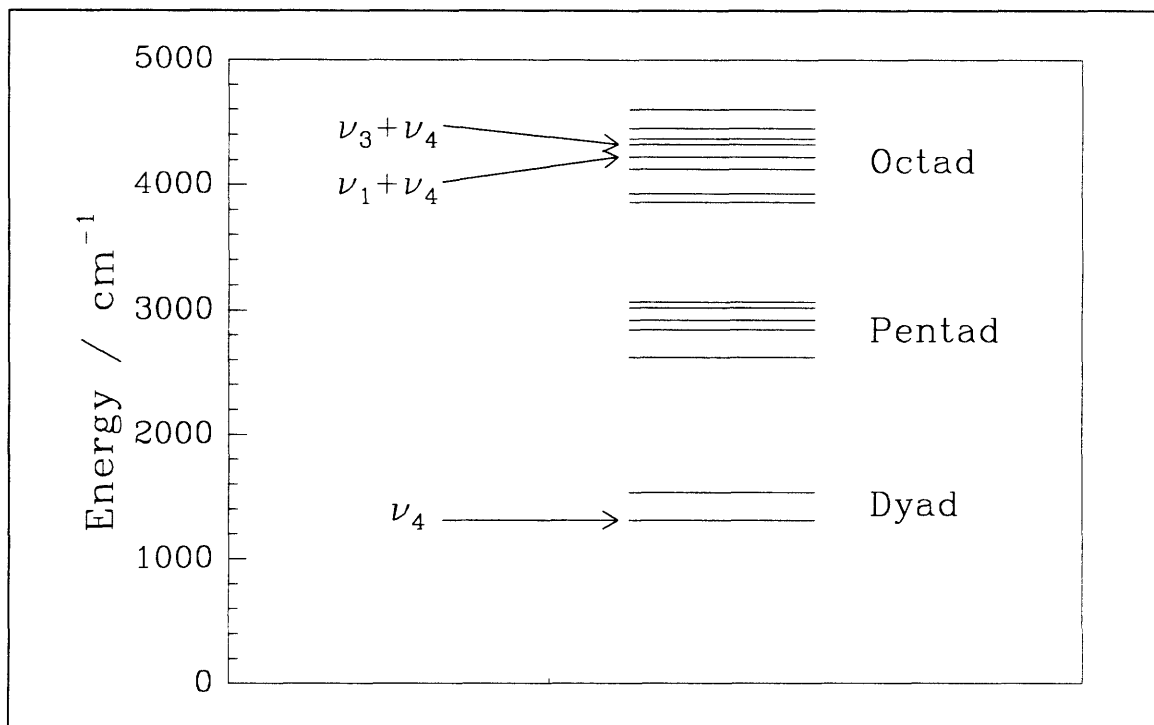


Figure 5.1

Vibrational energy level diagram for CH₄.

A spherical top molecule would have a very simple rotational structure if the effects of centrifugal distortion and Coriolis interaction could be neglected. If this were the case, the rotational energy levels would be given by $E_J = B_J J(J+1)$. Each E_J would have a $2J+1$ degeneracy in addition to the m_J degeneracy. For the ground state of CH₄ [CHAMPION89] this degeneracy is removed by centrifugal distortion and in vibrationally excited states by both centrifugal distortion and Coriolis interaction [BUNKER79, p.300]. With these interactions, the molecule fixed $2J+1$ rotational degeneracy is split into tetrahedral fine structure components which are classified by the irreducible representations of T_d , A_1 , A_2 , E , F_1 , F_2 . The variation of the number and type of fine structure components for each J can be calculated from group theory [WILSON35, BUNKER79], but in general is quite complicated. In the ground state the splitting between the different tetrahedral fine structure components for low J is only a few mK. For the low J levels, not all symmetry species are present for each J . Some rotational levels are very isolated from others of the same symmetry. This has a significant effect on rotational energy transfer in the ground state, since only the same species can interconvert through collisions.

The transition dipole moment of CH₄ is of species F_2 , thus dipole transitions are only allowed between vibrational states whose cross product contains F_2 [HERZBERG45, p.252]. Only vibrational states of species F_2 can be observed for transitions from the ground state. The rotational selection rules are $\Delta J = 0, \pm 1$ (except $J = 0 \leftrightarrow J = 0$ is forbidden) and $A_1 \leftrightarrow A_2$, $E \leftrightarrow E$, and $F_1 \leftrightarrow F_2$. For triply degenerate

vibrations there is an additional approximate selection rule, $\Delta R = 0$. In the ground state $R = J$, so this selection rule means that P transitions access the F^+ Coriolis component, Q transitions, the F^0 , and R transitions, the F^- . This prevents using combination differences for help in assigning spectra, which only adds to the complexity of methane spectroscopy.

In the energy transfer experiments presented here we utilized five different vibrational bands for pump and probe transitions. The overtone and combination bands $2\nu_3$ [RANK60, BOBIN72, FOX80], $\nu_3+\nu_4$ [HUNT81A], and $\nu_1+\nu_4$ [BROWN82] were used for pump transitions and the ν_3 [PINE75] fundamental and $\nu_3+\nu_4-\nu_4$ [HUNT81B] hotband were used for probe transitions. The HITRAN spectroscopic data base [HITRAN92] was a very reliable and convenient source for transition frequencies and intensities. Spectra simulated from the listings in the data base were valuable in identifying the correct pump and probe transitions.

The most extensive use was made of the $\nu_3+\nu_4$ vibrational level for pump transitions. Because rotational energy transfer was also studied in this level, some additional comment is necessary to describe the structure of this band and to establish the spectroscopic notation. The $\nu_3+\nu_4$ combination has three vibrational components, A_1 , E, and F_2 . In our work we are only involved with the infrared active component, F_2 . Both l_3 and l_4 contribute to the vibrational angular momentum of $\nu_3+\nu_4$. Because ζ_4 is approximately an order of magnitude larger than ζ_3 , the most significant Coriolis splitting is determined by l_4 . In each of the Coriolis components determined by the value of l_4 , there is an additional, smaller splitting due to the ν_3 Coriolis interaction. This results in the $\nu_3+\nu_4$ vibrational level being split into nine different Coriolis components. An intermediate quantum number, S, is introduced for the major Coriolis splitting, where $S = J - l_4$ and $S = J, J \pm 1$ [BOBIN78]. The pure rotational quantum number R is defined by $R = S - l_3$. R can have values of S, $S \pm 1$. Confusion can arise here because the R quantum number defined for the $\nu_3+\nu_4$ vibrational level is not the same as R in ν_4 . It is the S quantum number in $\nu_3+\nu_4$ which is the same as R in ν_4 .

For the full designation of a rotational level in $\nu_3+\nu_4$ it is necessary to specify J, S, R, and C^n . J, S, and R are as described above. C is the overall symmetry species of the state and n is a running index of states of the same symmetry species with the same J. We use the level notation convention used by Hunt et. al. [HUNT81A] where J will be followed by a +, 0, or - and another +, 0, or - depending on the value of S with respect to J and the value of R with respect to S. For example, The designation 2-- A_1 corresponds to the $J = 2, S = 1, R = 0, A_1$ level. Also, if there is only one state of a particular symmetry species with a JSR designation, the running index, n, is dropped.

5.3 Experimental Arrangement for Time-resolved Raman-shifted Ti:sapphire-Infrared Diode Laser Double Resonance

The double resonance experiments in CH₄ were made using the Raman-shifted Ti:sapphire laser system described in Chapter 4 to pump the 2ν₃ and ν₃+ν₄ overtone transitions. A 3.3 μm diode laser was used to probe the ν₃ fundamental for the ground state experiments and ν₃+ν₄-ν₄ hotband transitions for excited state. The diode laser (Laser Photonics, Analytics Division L5621) used in these experiments is of a fairly new variety that can operate at temperatures >77 K. Because these lasers are cooled with liquid nitrogen, they do not suffer from the instability due to mechanical vibrations which has always plagued diode lasers cooled by closed cycle helium compressors. This particular diode laser also had the unique property of running on a single mode. This is not a normal feature of diode lasers, although it was immensely convenient. Single mode operation eliminated the need for a monochromator to separate the modes and greatly simplified the setup of the experiment.

The experimental arrangement for the double resonance measurements is shown in Fig. 5.2. The pump beam was generated as the 2nd sequential Stokes shift of the Ti:sapphire laser. Hydrogen ($\Delta \tilde{\nu}_{\text{Raman}} = 4155 \text{ cm}^{-1}$) was used as the Raman medium for reaching the ν₃+ν₄ combination band at 2.3 μm and deuterium ($\Delta \tilde{\nu}_{\text{Raman}} = 2987 \text{ cm}^{-1}$) was used for the 2ν₃ overtone at 1.7 μm. The Ti:sapphire laser and internal lens Raman shifter has been described in Chapter 4. The 2nd Stokes pump beam was collimated with a 50 cm BaF₂ lens after generation in the Raman shifter to a beam diameter of ~2-3 mm. A small percentage of the 2nd Stokes was separated with a MgF₂ flat and directed to a photoacoustic cell containing ~1 torr of methane. The photoacoustic spectrum of the 2ν₃ and ν₃+ν₄ bands was used to identify the overtone pump transitions and also to fix and monitor the pump transition resonance for the time resolved experiments. The diode laser probe beam was collimated with an off-axis paraboloidal mirror to a diameter slightly greater than 1 cm. To achieve a better match to the pump beam, a 1 m BaF₂ lens was used to reduce the probe beam to 5-10 mm through the cell. The 2nd Stokes pump and diode laser probe beams were counterpropagated through the double resonance cell. Both lasers were linearly polarized. In the usual configuration the relative polarizations were chosen to be perpendicular. With perpendicular polarization, a MgF₂ Rochon polarizer placed in front of the diode laser detector was used to help prevent scattered pump radiation from falling onto the detector and interfering with the double resonance signal. For reorientation studies, when it was necessary to have the relative polarizations parallel, a Fresnel rhomb prism placed in the 2nd Stokes beam was used to rotate its polarization. Alternatively, when the 2nd Stokes was so far in the infrared as to not pass with little loss through the Fresnel rhomb, a waveplate in the Ti:sapphire fundamental was used to rotate its polarization before entering the Raman shifter. The pump and probe beams were crossed at a small angle at the pump entrance to the double resonance cell. For the experiments utilizing the ν₃+ν₄ pump transitions at 2.3 μm, a dichroic mirror which was transmissive for the 2.3 μm pump and reflective for the 3.3 μm probe

was advantageously used here to obtain closer overlap between the beams. At the probe end of the cell the beams were spatially separated. When pumping with 1.7 μm radiation, a small pick-off mirror was used at this end of the cell to direct the pump beam back on itself for a second pass through the double resonance cell. With the 2.3 μm pump this was not possible because the scattered pump radiation reaching the diode laser detector was not adequately blocked with the infrared filters. For this pump wavelength the beam was directed to a beam dump. The diode laser probe was detected by a photovoltaic InSb detector (EG&G Judson, J10D) which has a rise time of 100 nsec. Both the InSb detector and the diode laser were extremely sensitive to scattered pump radiation. Several longpass infrared filters were used to reduce the scattered pump light into these devices.

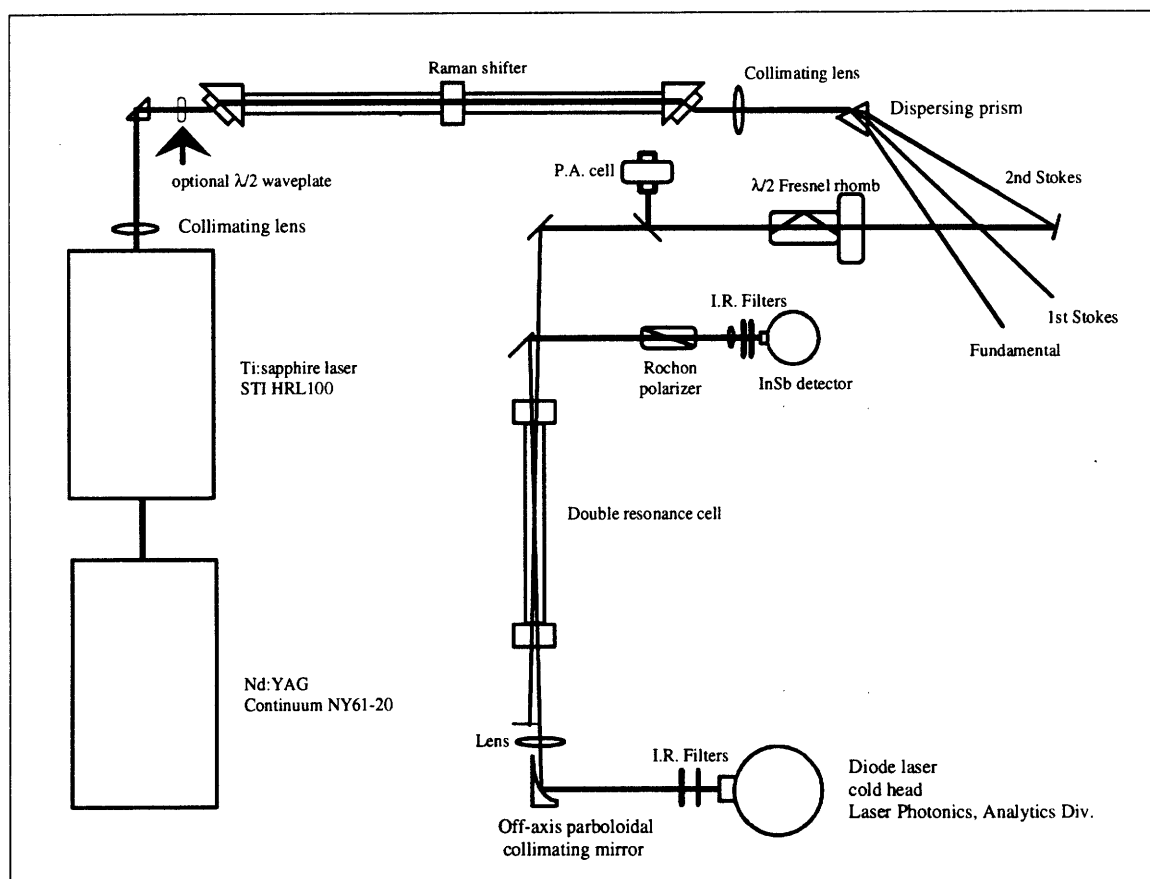


Figure 5.2

Raman-shifted Ti:sapphire/diode laser double resonance experimental arrangement used for CH_4 energy transfer experiments.

The double resonance cell was made of sections of stainless steel tubing fitted with 3.5" Conflat flanges. The length of the cell was varied to best suit the measurements being made. For transient gain measurements using the $\nu_3+\nu_4-\nu_4$ hotbands as the probe transitions, a long path length was preferable, so

a 1 m cell was used. For ground state recovery measurements using the ν_3 fundamental for the probe transitions a long pathlength was not desirable since these transitions would be completely absorbing even at very low pressures. For these measurements the cell length was reduced to 50 cm. The cell windows were of CaF_2 .

The methane gas used in the experiments was from Matheson, U.H.P. grade. It was used directly from the cylinder. The cell was refilled with each new measurement. Pressures were measured with a 1.0 torr capacitance baratron (MKS).

The time-resolved transient gain and ground state recovery signals were made by averaging 1000 to 20,000 shots on a digital oscilloscope (LeCroy 9400A). The number of shots averaged depended on the type of measurement being made. For the transient gain measurements in $\nu_3+\nu_4$, the signals were reasonably large and averaging 1000 shots produced an acceptable signal-to-noise ratio. For the state-to-state measurements in the ground state, the signals were exceedingly small and long averaging times were needed for each measurement. A baseline was recorded for each measurement by detuning the Raman shifted Ti:sapphire laser from resonance. By subtracting the baseline from the signal, small scattered light peaks and electrical pickup were removed from the signal.

A lockin circuit was constructed to keep the diode laser exactly on resonance when the Ti:sapphire laser was fired. For measuring energy transfer in the ground state the process being monitored was the decrease in absorption of a fundamental transition due to the removal of population in the ground state by the pump laser. The difficulty in making these measurements was that the probe transitions were narrow lines which have substantial absorption of the diode laser power. If during the course of the measurement the diode laser were to drift even slightly off resonance, there was a much larger change in the diode laser power on the detector than the signal itself. To make good measurements with long averaging times the diode laser must be exactly on resonance when the pump laser is fired. This is accomplished by using an external trigger circuit both to create a lock modulation frequency for the diode laser and to control the firing of the YAG laser to occur only when the diode laser is exactly on resonance.

The circuitry described in Appendix 5 and utilized for the fluorescence detected HCCH double resonance experiments mentioned in Section 4.5 was utilized here as part of the electronics used to actively lock the diode laser to a probe transition and to control the flashlamp and Q-switch firing of the YAG laser. To lock the diode laser to an absorption feature it was necessary to use a lockin amplifier (PAR 122) and to modulate the diode laser frequency with a small amplitude sine wave. The small amplitude sine wave was applied as the reference signal to a lockin amplifier and the output of the diode laser detector was applied as the signal. The output of the lockin amplifier when the modulated diode laser scanned through a transition was the 1st derivative of the absorption which crossed zero when the diode laser was centered

on the transition. This first derivative output of the lockin amplifier was used to provide a correction signal to keep the diode laser on the center of the line.

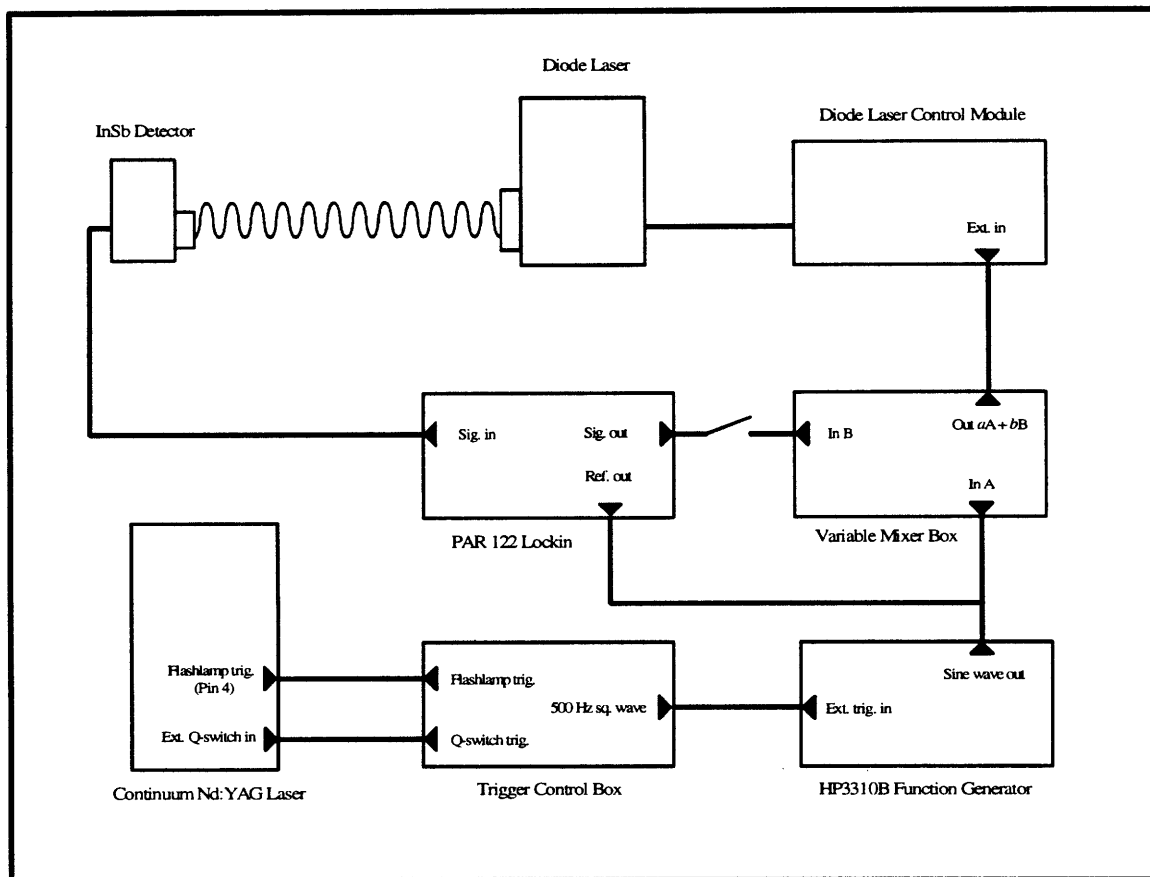


Figure 5.3

Schematic of the circuitry used to lock the diode laser to the center of an absorption peak and to control the phase of the lock modulation to be in sync with the Ti:sapphire pump laser.

A schematic of the lock circuit is shown in Fig. 5.3. In addition to locking the diode laser to an absorption, it is important to synchronize the diode laser modulation frequency and the repetition rate of the pump laser. This done by taking a 500 Hz square wave from the same clock which generates the 20 Hz YAG trigger. The 500 Hz square wave is taken to the External Trigger of an HP 3310B function generator. The HP 3310B creates a synchronous 500 Hz sine wave with phase adjustable by a front panel control. This signal is fed to the Reference input of the PAR 122 lockin amplifier and to one half of a variable mixer box. From the mixer box it goes to the External In input of the diode laser control module (LCM). The output of the InSb detector is buffered through a Keithley 105 Pulse Amplifier (x10) and is provided as the Signal input to the PAR 122 lockin. When the diode laser is on resonance, a connection is made between the Output of the PAR 122 lockin and the second half of the variable mixer box closing the lock loop and locking the diode to the probe line. An important feature of this arrangement is that the

diode laser modulation is synchronous with the firing of the YAG laser. The phase control provided by the HP 3310B function generator allows the modulation to be adjusted so that the laser will fire exactly when the diode laser is centered on the absorption. The sweep modulation amplitude is very small, approximately one tenth the absorption linewidth, and the sweep period is one thousand times longer than the time duration for energy transfer, so the change in frequency during the measurement is insignificant.

5.4 Vibrational Energy Transfer from the Octad*

A number of studies of V←V and V←T processes in methane have been reported. Perrin and coworkers [JOLICARD83, PERRIN84, PERRIN86] used a modulated I.R. beam/photoacoustic experimental technique to study the relaxation of the dyad levels of CH₄ over a broad range of temperatures and with several collision partners. This work demonstrated that the vibrational deactivation of the dyad in pure methane mixtures occurs on a very slow time scale; the rate constant for the deactivation is $0.86 \times 10^{-3} \mu\text{sec}^{-1} \text{ torr}^{-1}$ at 300 °K. In a series of early I.R. laser excitation experiments (modulated I.R. HeNe, HCl chemical laser, and LiNbO₃ OPO), Moore and coworkers [YARDLEY68, YARDLEY70, ZITTEL73, HESS76] also studied V←V and V←T processes in methane. Using laser excitation of the ν_3 fundamental in the pentad and detecting I.R. fluorescence from both ν_3 and ν_4 , they were able to measure the total vibrational deactivation rate of ν_3 and the rate of vibrational energy transfer from the pentad to the dyad. They reported a total deactivation rate constant for ν_3 of $0.26 \mu\text{sec}^{-1} \text{ torr}^{-1}$ in pure methane and a surprising result of a somewhat faster rate constant of $0.36 \mu\text{sec}^{-1} \text{ torr}^{-1}$ for the rise of the ν_4 fluorescence. They draw the conclusions from their kinetic analysis that the ν_3 population flows through other pentad levels, such as $2\nu_4$ and $\nu_2+\nu_4$, to ν_4 where it becomes trapped until the much slower V←T processes relax ν_4 .

In this work we have studied vibrational energy transfer processes out of the CH₄ octad vibrational levels. This work provided new information about vibrational relaxation processes in polyatomic molecules with multiple quanta of excitation and was also a necessary preliminary step in our studies of rotational relaxation in $\nu_3+\nu_4$ and in the methane ground vibrational state. Vibrational energy transfer in CH₄ was studied by directly pumping overtone transitions in the octad and observing the change in absorption of an octad←dyad hotband transition. A schematic diagram of the pump and probe scheme is shown in Figure 5.4. Pump transitions for two different vibrational levels in the octad were used. $\nu_3+\nu_4$ was pumped using the P(3) A₂ transition at $4272.8266 \text{ cm}^{-1}$. The upper state of this transition is the $\nu_3+\nu_4$ 2⁻ A₁. $\nu_1+\nu_4$ was pumped at the R(6) A₁ transition at $4253.5180 \text{ cm}^{-1}$. The $\nu_1+\nu_4$ vibrational band has F₂ symmetry and has rovibrational structure analogous to the ν_4 fundamental. The $\nu_1+\nu_4$ level populated was the J' = 7 A₂ of the F⁻ Coriolis component. For both cases, the probe transition was the

* Dr. Stephen L. Coy is gratefully acknowledged for his considerable work on this analysis.

$\nu_3+\nu_4-\nu_4$ R(1) A_2 hotband transition at 3024.2728 cm^{-1} . The lower level of this probe transition was the ν_4 $J'' = 1$ A_2 of the F^- Coriolis component. The upper level of the probe was the same as that of the $\nu_3+\nu_4$ pump, the $\nu_3+\nu_4$ 2^- A_1 . Only CH_4 self relaxation was studied. Signals were recorded at pressures were between 200 and 1200 mtorr.

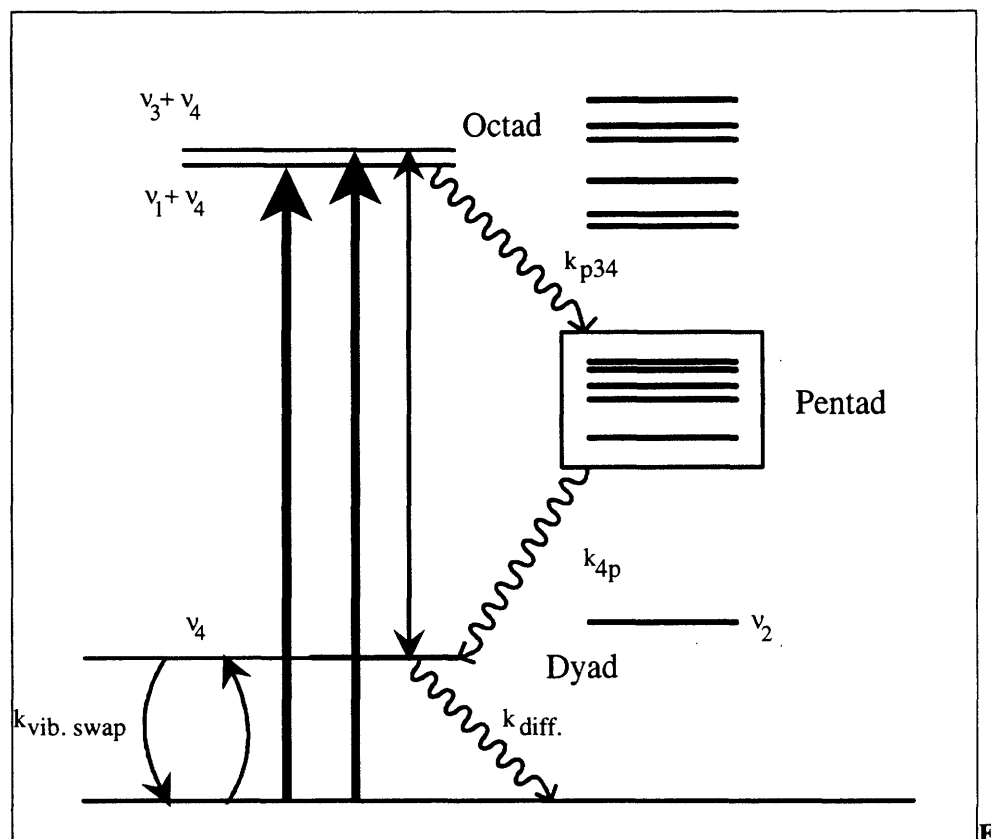


Figure 5.4

Schematic diagram of pump and probe transitions and vibrational energy transfer processes

This $\nu_3+\nu_4-\nu_4$ hotband probe transition produces a signal which contains a great deal of information about energy transfer in CH_4 , however, the features of this signal need some explanation. A typical signal, recorded with 800 mtorr CH_4 , is shown in Figure 5.5. The pump transition used in this case was the $\nu_3+\nu_4$ P(3) A_2 . In Figure 5.5 the diode laser signal at negative time is the equilibrium absorption of the $\nu_3+\nu_4-\nu_4$ hotband transition and is proportional to the equilibrium population in the ν_4 $J = 1$ A_2 rotational level. The signal has been scaled so that the equilibrium absorption value is zero. Since the pump transition directly populates the upper level of the probe transition, immediately after the pump, which occurs at $t = 0$, there is more population in the upper level of the hotband probe transition than in the lower level. This population inversion results in a gain signal which is shown as negative absorption. We observed real gain, not just a reduction in absorption. The gain signal quickly disappears as rotational energy transfer redistributes the population which was initially all in the upper level of the probe

transition to all other rotational levels of A symmetry in $\nu_3 + \nu_4$. The diode laser absorption signal passes through zero and then begins to increase as vibrational energy transfer causes population to cascade down into ν_4 . After passing through a maximum the absorption of the diode laser at the $\nu_3 + \nu_4 - \nu_4$ hotband transition slowly begins to decrease as slower processes remove population excited state population from the probe beam.

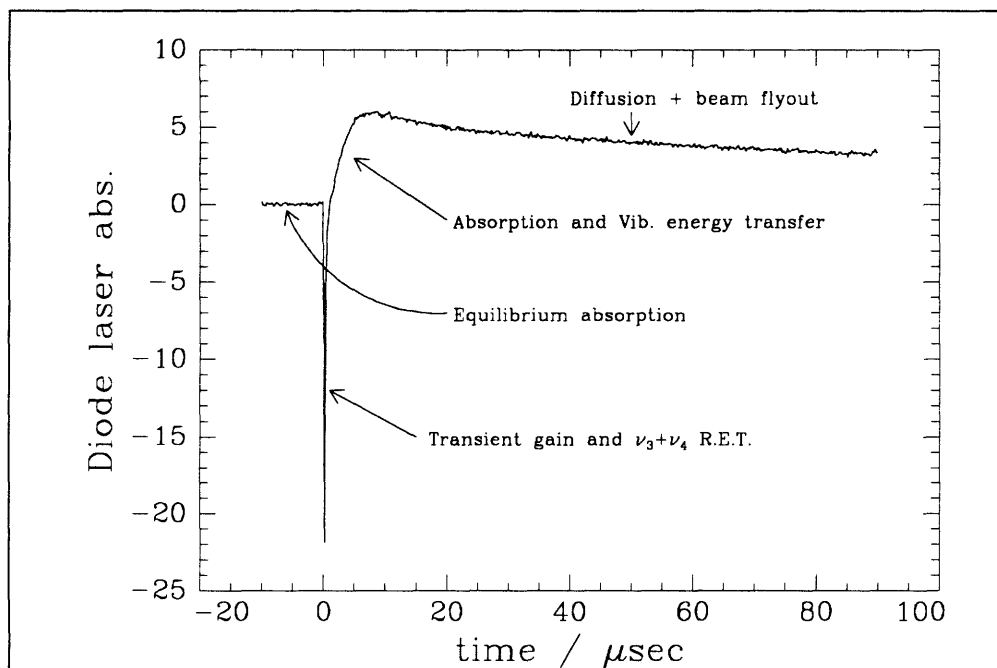
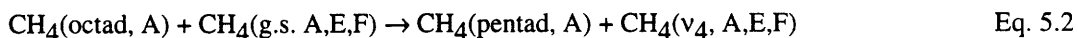


Figure 5.5

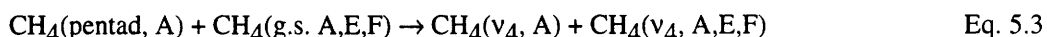
Example of transient gain and absorption on CH_4 $\nu_3 + \nu_4 - \nu_4$ hotband transition

There are many $V \rightarrow V$ processes which are involved in the relaxation of $\nu_3 + \nu_4$ and $\nu_1 + \nu_4$. A complete kinetic analysis would have to include distinct state-to-state rates between every vibrational level in the octad, pentad, and dyad. Our experiments are not sensitive to all of these individual rates. Our signals are only proportional to the population difference between $\nu_3 + \nu_4$ and ν_4 . In order to model our data, we have developed a simplified model of vibrational energy transfer in CH_4 which accurately reproduces our experimental results and also provides insight into the important vibrational relaxation mechanisms. In this model it is assumed that the population initially delivered to a single rotational level rapidly equilibrates with the other rotational levels in the same vibrational state. Rotational equilibration is maintained during subsequent vibrational energy transfer. We assume that the primary deactivation process from the octad in pure methane is a vibrational exchange mechanism which minimizes the amount of energy going into translation. In collisions with a ground state (g.s.) CH_4 molecule, an excited state molecule in $\nu_3 + \nu_4$ or $\nu_1 + \nu_4$ transfers a quantum of ν_4 vibrational excitation to the g.s. molecule

and is reduced in energy to a pentad level, Eq. 5.2. The symmetry species of both the octad molecule and the g.s. molecule are preserved in the collision.

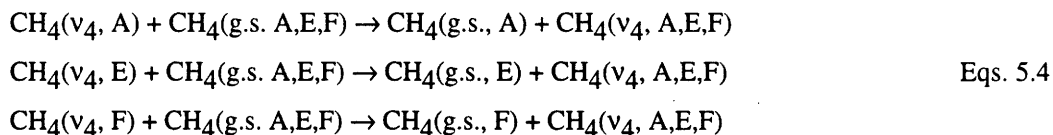


In a similar fashion, an excited state molecule in the pentad is deactivated to ν_4 in a collision with a g.s. molecule, also promoting it to ν_4 .



After reaching the ν_4 vibrational level, population becomes trapped there as $V \rightarrow T$ processes are very slow [PERRIN86, YARDLEY70]. Under our experimental conditions these slow processes are a combination of diffusion, ballistic transport, and $V \rightarrow T$.

A very important fact that arises from this model of vibrational deactivation of octad and pentad states accompanied by vibrational excitation ν_4 is that the states of A symmetry in ν_4 are overpopulated in comparison with the E and F states. This is because the initially excited molecules are of A symmetry and they remain in A symmetry as their quanta of vibrational excitation are reduced to ν_4 . After the collisional deactivation of the octad and pentad, the proportion of population in ν_4 A symmetry levels is greater than that of the ground state. A mechanism which can equilibrate the excess vibrationally excited ν_4 population in A symmetry states with the E and F states is the Förster-type vibrational swap mechanism [Appendix 3, Section V]. In this process a ν_4 molecule of one symmetry type exchanges its vibrational excitation with a g.s. molecule of any symmetry type. The result is an apparent nuclear spin changing process.



This equilibration between symmetry species is an important part of the model. In all of our signals, we observe a decrease in the ν_4 population after reaching its maximum which is far too rapid to be accounted for by $V \rightarrow T$, diffusion, beam flyout or even equilibration of ν_4 with ν_2 . This effect can only be adequately modeled by allowing an equilibration between the different symmetry species by the vibrational swap mechanism.

An important vibrational relaxation process to which we are not completely sensitive is the vibrational equilibration among the levels in the octad. In the process of modeling the data with for which the initial level was the $\nu_1+\nu_4$ vibrational mode, we discovered that it was necessary to include a direct rate to $\nu_3+\nu_4$. Our probe laser is sensitive to this process since the upper level of the probe is in $\nu_3+\nu_4$. We do

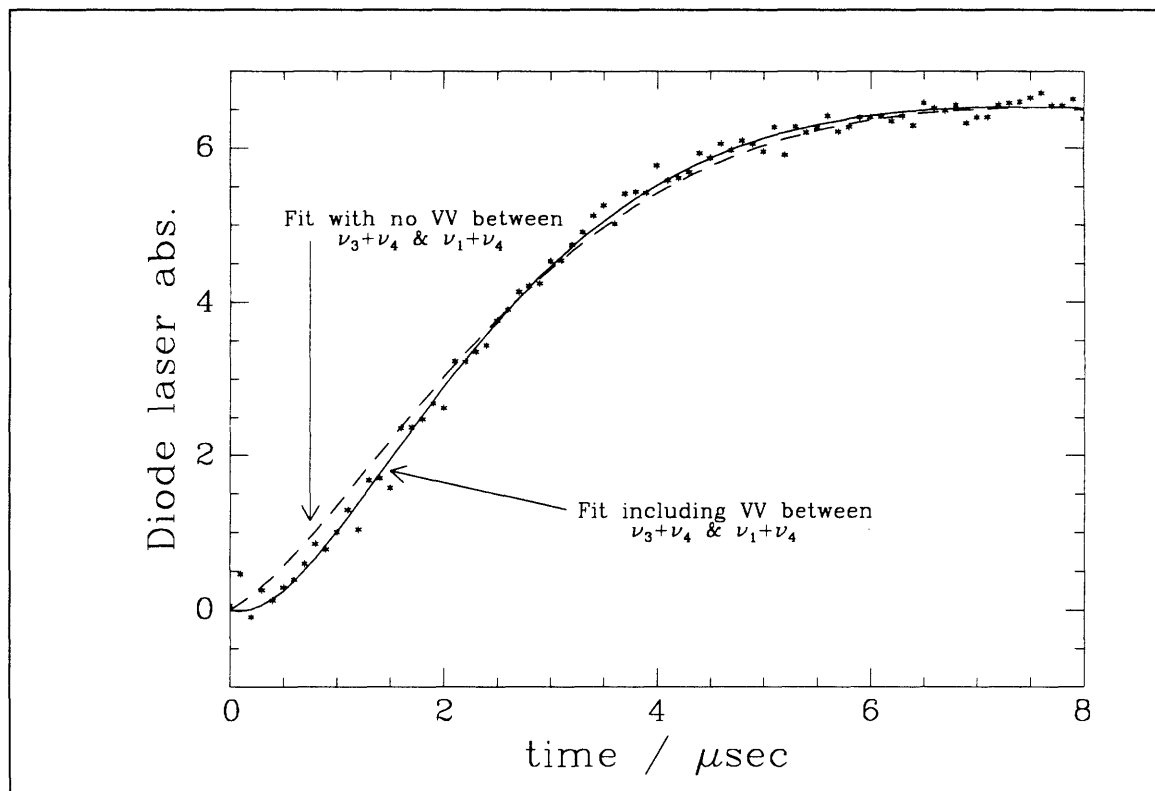


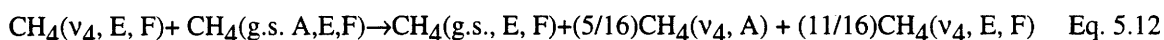
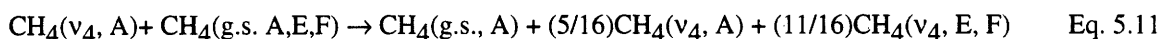
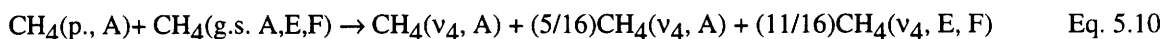
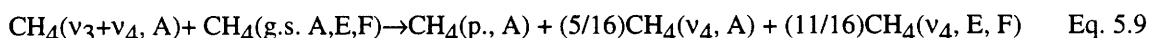
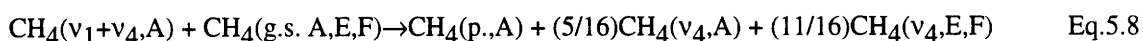
Figure 5.6

Vibrational relaxation transient for $\nu_1+\nu_4$ pump at 800 mtorr CH_4 monitored at the $\nu_3+\nu_4-\nu_4$ hotband transition. The dashed line shows the best fit to the curve for a model which does not include a vibrational relaxation pathway connecting $\nu_1+\nu_4$ with $\nu_3+\nu_4$. The solid curve is the best fit for a model which does include this pathway.

not observe any gain on the $\nu_3+\nu_4-\nu_4$ hotband probe when we pump into $\nu_1+\nu_4$, but in order to model the data we must assume some reduction in absorption due to population flow into $\nu_3+\nu_4$. In Figure 5.6 we show an example of an experimental transient for the $\nu_1+\nu_4$ pump at a pressure of 800 mtorr CH_4 and two fits, one for no energy transfer to $\nu_3+\nu_4$ and one with this process allowed. Including a kinetic process between $\nu_1+\nu_4$ and $\nu_3+\nu_4$ clearly improves the fit of the model simulation to the data. It is possible that facile $V \rightarrow V$ also occurs between $\nu_1+\nu_4$ and other vibrational states of the octad such as $2\nu_4+\nu_2$ and $3\nu_4$, but our data do not give information about these processes. For the purpose of interpreting the data currently in hand, we do not include $V \rightarrow V$ processes among any vibrational states in the octad other than between $\nu_1+\nu_4$ and $\nu_3+\nu_4$.

There are several other processes about which our experiments do not contain information. We do not know which pentad levels are populated by the vibrational deactivation of the octad levels. In our model we simply treat the pentad as a single state. We do not know how much population is transferred to the ν_2 vibrational level. We have left it out since previous experiments of relaxation from the pentad [HESS76] indicate that transfer is primarily to ν_4 . We also do not have direct evidence that a Förster-type mechanism for vibrational exchange is not occurring with the ν_3 vibrational state. This may be an important process, but we have not included it because we have no direct evidence to support it.

With this interpretation of the vibrational relaxation processes from the octad, we have created a kinetic model with five states, $\nu_1+\nu_4$, $\nu_3+\nu_4$, the pentad, ν_4 A symmetry levels, and ν_4 E and F symmetry levels. The kinetic equations for vibrational energy transfer between these levels are given below.



From the analysis of our data using this model we have determined rates for V→V exchange between $\nu_3+\nu_4$ and $\nu_1+\nu_4$ (k_{1434}), for vibrational deactivation from the octad to the pentad (k_{pO}), for vibrational deactivation from the pentad to ν_4 (k_{4p}), and the vibrational swap rate for ν_4 (k_{ν_4}). The rate constants for these processes are listed in Table 5.1.

Vibrational process	Rate / $\mu\text{sec}^{-1} \text{ torr}^{-1}$
$\nu_1+\nu_4 \leftarrow \nu_3+\nu_4, k_{1434}$	0.4
pentad \leftarrow octad, k_{pO}	0.5
$\nu_4 \leftarrow$ pentad, k_{4p}	0.6
ν_4 vib. swap, k_{ν_4}	0.35

Table 5.1

Rate constants for the vibrational energy transfer processes among the CH_4 octad, pentad, and dyad levels

These are the first measurements of vibrational energy transfer from methane octad levels, so there are no other studies with which to compare. Hess and Moore [HESS76] reported a rate constant of $0.25 \mu\text{sec}^{-1} \text{ torr}^{-1}$ for the total depopulation out of ν_3 . This process is comparable to our measurement of the $\nu_4 \leftarrow$ pentad relaxation. Their number is considerably less than the rate constant we find. A possible explanation for this is that the Hess and Moore number was for population initially in ν_3 . We do not know which states in the pentad are populated in our experiments. It is possible that ν_3 is not greatly populated, and that our number is more strongly dominated by energy transfer from other vibrations in the pentad such as $2\nu_4$ and $\nu_2+\nu_4$.

Finally, we can compare the ν_4 vibrational swap rate calculated from the model to that predicted by the Förster mechanism described in Appendix 3, Section V. Using the ν_4 transition dipole moment of 0.0605 D [FOX76] we calculate a ν_4 vibrational swap cross section of 1.7 \AA^2 which corresponds to a rate constant of $0.47 \mu\text{sec}^{-1} \text{ torr}^{-1}$. This is remarkably good agreement with the experiment and provides another piece of evidence for the validity of the Förster mechanism.

5.5 Rotational Energy Transfer in $\nu_3+\nu_4$

We have studied rotational energy transfer in the $\nu_3+\nu_4$ combination band by the technique of transient gain double resonance spectroscopy. The double resonance scheme was similar to that described for the vibrational energy transfer study. The 2nd Stokes of the Raman-shifted Ti:sapphire laser was used to directly pump overtone transitions in $\nu_3+\nu_4$. The $3.3 \mu\text{m}$ diode laser was tuned to $\nu_3+\nu_4-\nu_4$ hotband transitions in order to monitor the time dependence of the transient gain signal. We observed both 3-level and 4-level double resonance. The 3-level signals were recorded at pressures between 5 and 250 mtorr. Using the same techniques described in Section 3.5 the 3-level signals were fit to single exponentials, the rates plotted against pressure, and the resulting $p\tau$ curves fit to straight lines to find the pressure independent rate coefficients. A difference between this work and that described in Chapter 3 is that in the present case, the pulse length was very short. There was no significant relaxation during the pulse, even at the highest pressures, and the fits could be successfully begun at the very peak of the signal. Only a single fit beginning at the peak of the signal was used to obtain the decay rate. Error estimates for each point, necessary to obtain an estimate of the error of the $(p\tau)^{-1}$ coefficients, were the standard deviation of the residuals for the straight line fit to the data. The results for the total depopulation rates in $\nu_3+\nu_4$ are listed in Table 5.2.

$\nu_3+\nu_4$ level J S R C ⁿ	Pump trans. $\nu_3+\nu_4$	Pump freq. cm ⁻¹ (a)	Probe transition $\nu_3+\nu_4-\nu_4$	Probe freq. cm ⁻¹ (a)	Rel. pol.	(μsec^{-1} torr) ⁻¹	k /10 ⁻¹⁰ cm ³ molec ⁻¹ s ⁻¹	σ_{eff} Å ²
2 1 0 A ₁	P(3) A ₂	4272.8262	R(1) A ₂	3024.2728	⊥	21.2 (1.4)	6.54	73.6
3 3 4 A ₁	Q(3) A ₂	4315.6847	Q(3) A ₂	2990.3310	⊥	19.0 (1.6)	5.88	66.2
4 3 3 A ₂	Q(4) A ₁	4294.5707	Q(4) A ₁	3009.3934	⊥	16.2 (0.8)	5.00	56.3
4 3 3 A ₂	Q(4) A ₁	4294.5707	Q(4) A ₁	3009.3934	∥	18.0 (1.0)	5.55	62.5
0 1 2 F ₂	P(1) F ₁	4308.7285	P(1) F ₁	2993.3880	⊥	17.7 (2.3)	5.47	61.6
2 3 3 F ₁	Q(2) F ₂	4330.1089	Q(2) F ₂	3009.7304	⊥	17.2 (0.9)	5.31	59.8
2 3 3 F ₁	Q(2) F ₂	4330.1089	Q(2) F ₂	3009.7304	∥	18.0 (0.9)	5.55	62.5

Table 5.2

Total depopulation rates for the CH₄ $\nu_3+\nu_4$ combination band. (a) Frequencies were taken from the HITRAN database.

For the study of state-to-state rotational energy transfer in $\nu_3+\nu_4$, we also recorded 4-level double resonance signals. For these measurements our probe transition was always the $\nu_3+\nu_4-\nu_4$ R(1) hotband transition at 3024.2728 cm^{-1} , the upper level of which is the $\nu_3+\nu_4$ 2-- A_1 . Using this one probe transition we were able to study rotational energy transfer by pumping different transitions in the $\nu_3+\nu_4$ combination band with the 2nd Stokes of the Raman-shifted Ti:sapphire laser. We limited our study to low J states, $J \leq 5$, of A symmetry since these would have the most significant rates to the $J = 2-- A_1$ level. An energy level diagram for the $\nu_3+\nu_4$ rotational levels is shown in Figure 5.7. The rotational levels that were pumped in these experiments are indicated. The rotational levels have been grouped according to the value of l_4+l_3 , more for convenience in display than for any physically significant reason.

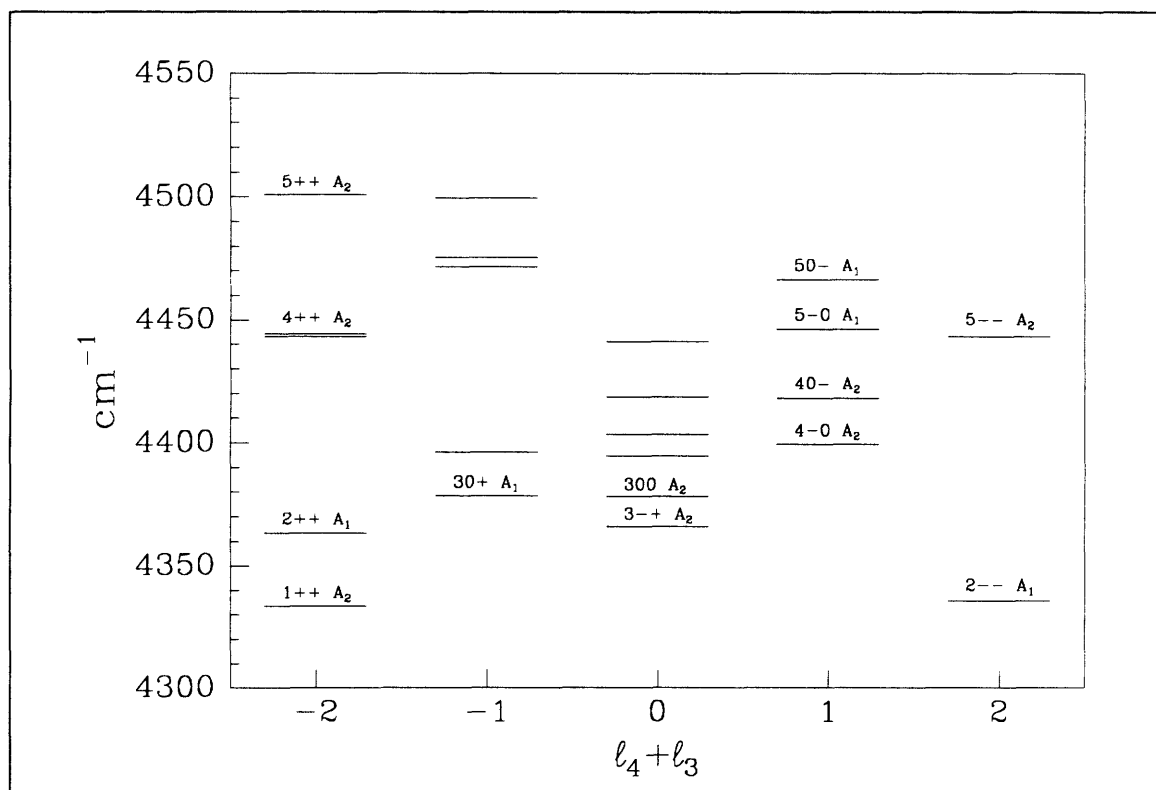


Figure 5.7

Rotational energy level diagram for $\nu_3+\nu_4$. The probed level was always the 2-- A_1 . The levels that were pumped are indicated by their quantum labels above the corresponding level.

The signals we observed in the state-to-state R.E.T. measurements were the diode laser transient gain/absorption on the $\nu_3+\nu_4-\nu_4$ R(1) hotband transition. The signals were initially gain as population from the pumped level was transferred into the 2-- A_1 probe level. The signals went over to absorption as vibrational energy transfer brought population down into the ν_4 vibrational level. The vibrational energy

transfer model described in the previous section was an essential first step to analyzing these $\nu_3+\nu_4$ rotational energy transfer data, since the long time behavior of the signals was entirely vibrational energy transfer.

We have used the fact that the long time behavior of the 4-level signals is entirely due to vibrational energy transfer to assist in scaling their amplitude. At 400 mtorr, rotational equilibration is completed in $\sim 2 \mu\text{sec}$. For times longer than this, all the signals look very much the same. They all show the same increase in absorption as population flows down into the ν_4 vibrational level. At the longest time recorded, $9 \mu\text{sec}$, the percentage of initial population that has reached ν_4 is the same regardless of the initial rotational level populated in $\nu_3+\nu_4$. Since the probe was always the $\nu_3+\nu_4-\nu_4$ R(1) hotband transition, the $9 \mu\text{sec}$ absorption value should be the same for all 4-level signals if the same amount of population was initially pumped into $\nu_3+\nu_4$. All 4-level signals were scaled so that the average absorption value between 8.75 and $9 \mu\text{sec}$ was 1.0. Figure 5.8 shows all the 4-level signals that were measured in $\nu_3+\nu_4$ along with the transients calculated from the model.

The model for vibrational energy transfer included five states; $\nu_1+\nu_4$, $\nu_3+\nu_4$, the pentad, ν_4 A symmetry levels, and ν_4 E and F symmetry levels. For the analysis of rotational energy transfer in $\nu_3+\nu_4$, we used the same model including all these states, but with the $\nu_3+\nu_4$ vibrational state expanded into all the rotational levels of A symmetry for $J \leq 10$. All of these individual rotational states couple to the pentad and $\nu_1+\nu_4$ with the same rate as would $\nu_3+\nu_4$ in the vibrational model. $\nu_1+\nu_4$ coupled to each of these rotational states by rates proportional to their Boltzmann factors and scaled so that the sum was equal to the k_{3414} rate. At times long compared to rotational equilibration, this model is the same as the vibrational model used earlier.

What we wish to determine from the model of rotational energy transfer in $\nu_3+\nu_4$ are the state-to-state rates connecting these levels. To do this we must couple a master equation analysis for the $\nu_3+\nu_4$ rotational levels to the vibrational energy transfer model already developed. The basic description of the master equation was presented in Section 3.9 and in Appendix 3, section IV.D. The same type of formalism used for the analysis of rotational energy transfer in the ν_3 vibrational level of CHD_3 was applied here. All 4-level double resonance signals were simulated by setting up and solving the rate matrix equation, Eq. 3.23.

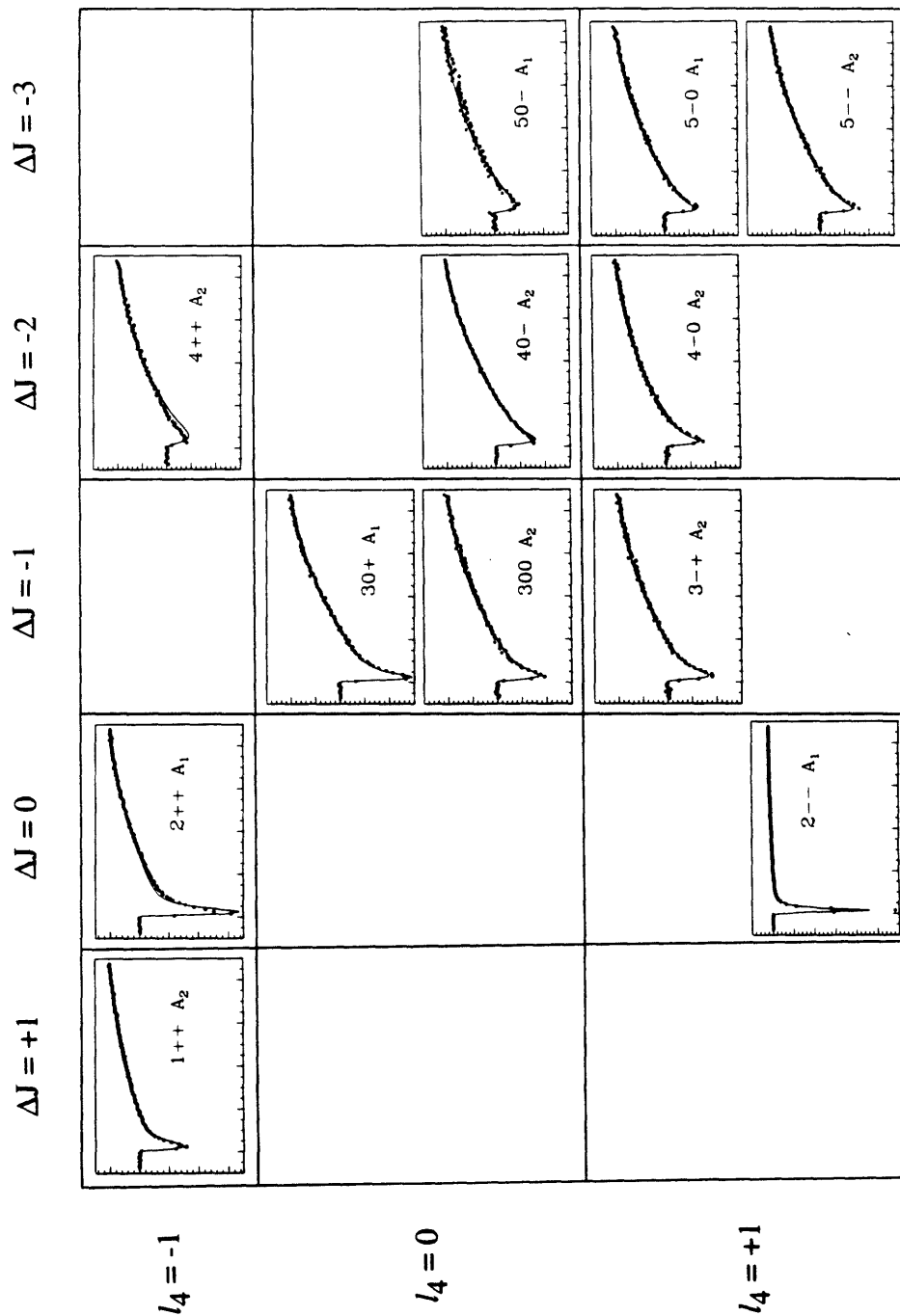


Figure 5.8
 Experimental R.E.T. transient gain/absorption signals and model simulations for CH_4 v_3+v_4 A symmetry levels at 400 mtorr CH_4 . The time scale for all transients is -1 to 9 μsec . The amplitude scale is -30 to 5 arb. units for the 3-level 2-- transient. For the 1++ and 2++ it is -3.5 to 1.5. For all others it is -1.5 to 1.5.

A very simple approximation was used for initially setting up the rate matrix for the state-to-state rates in $\nu_3+\nu_4$. Only processes which changed J by 0, 1, 2, or 3 were allowed. All exothermic processes with the same ΔJ were assigned the same rate. The reverse endothermic rates were calculated from detailed balance, Eq. 3.24. These rates were adjusted using the criteria that 1) they should decrease monotonically with ΔJ , 2) they should be in good agreement with the total depopulation rates found from the 3-level double resonance experiments, and 3) they should cause reasonable agreement between the simulated and experimental transients on visual inspection. The set of rates given in Table 5.3 satisfied these requirements.

ΔJ	$k / \mu\text{sec}^{-1} \text{ torr}^{-1}$
0	3.125
1	0.9375
2	0.625
3	0.500

Table 5.3
Initial estimates for rotational energy transfer rates in $\nu_3+\nu_4$

Using this simple approximation gives qualitatively good agreement between the simulated and experimental transients, but more quantitative values for the state-to-state rates are desirable. We obtain these in a manner similar to that described in Appendix 3, section IV.D for the R.E.T. measurements in the ν_3 fundamental of CHD_3 . The most important rate in the rate matrix for a particular 4-level signal is that which directly connects the pumped and probed levels. If the rest of the rate matrix is approximately correct, adjusting this direct rate to give the best possible fit to the experimental data is a reasonable means of obtaining the direct state-to-state rate between the pumped and probed levels. We applied this technique to the data shown in Figure 5.9. For each 4-level signal we allowed the rate constant in Table 5.3 which directly connected the pump and probe levels to be an adjustable parameter in a least squares minimization. All other rates constants were held to the values in Table 5.3. We also allowed the rate constant for the vibrational deactivation rate from the octad to the pentad, k_{po} , to float in the least squares minimization. This rate constant did not vary significantly from the value found in the vibrational energy transfer measurements. Fixing it did not effect the value determined for the direct state-to-state rate. Allowing it to float improved the quality of the fits. The best fit, direct state-to-state rates determined from the least squares minimization are listed in Table 5.4.

$\nu_3+\nu_4$ Level Pumped	ΔJ	Direct rate to 2-- A_1 level / $\mu\text{sec}^{-1} \text{ torr}^{-1}$
1++ A_2	+1	1.1
2++ A_1	0	3.1
30+ A_1	-1	1.6
300 A_2	-1	0.76
3-+ A_2	-1	0.78
4++ A_2	-2	~0
40- A_2	-2	0.60
4-0 A_2	-2	0.80
50- A_1	-3	0.66
5-0 A_1	-3	0.90
5-- A_2	-3	0.66

Table 5.4

Best fit, direct state-to-state rates between pumped level and 2-- A_1 probed level in $\nu_3+\nu_4$

Two observations about the propensity rules for rotational energy transfer in $\nu_3+\nu_4$ can be made from the state-to-state rates. There is a strong propensity for parity preserving collisions, and there is a propensity for maintaining the (S-J) quantum number in collisions. Oka has shown that the A_1 levels of CH_4 are of - parity and the A_2 levels are of + parity [OKA73B], i.e. A symmetry levels with the same subscript have the same parity. The probed level was of A_1 symmetry. The pumped levels with the fastest rates, the 2++ A_1 and 30+ A_1 , also have the same parity. This propensity rule is clearly evident in the $\Delta J = -1$ rates. The 30+ A_1 and 30- A_2 levels are nearly degenerate and are both have the same (S-J), yet the rate for the parity preserving collision, A_1 to A_1 , is more than twice that of the parity changing process. The (S-J) conservation rule can be clearly seen among the ΔJ of -2 rates. The rate for the 4-0 A_2 level is significant and larger than that for the 40- A_2 level, and the rate for the 4++ A_2 pump is ~0. The transient for the 4++ A_2 pump can be adequately modeled without a direct rate to the 2-- A_1 at all, multiple collisions account for the observed transient gain. For $\Delta J = -3$ transitions both propensity rules become obvious. There are two levels which have the same (S-J) as the probed level, the 5-0 A_1 and the 5-- A_2 . The faster of these is again the parity conserving, A_1 to A_1 process. Also worth note are the rates from the 40- A_2 and the 50- A_1 , both of which have the same (S-J). Although the 40- A_2 is closer to the 2-- A_1 probe level in both ΔE and ΔJ , the rate for the parity conserving A_1 to A_1 process to the 50- A_1 is greater.

5.6 Energy Transfer in the CH₄ Ground State

Rotational energy transfer in the CH₄ ground vibrational state was measured by the double resonance technique using the scheme shown in Figure 5.9. For these experiments the 2nd Stokes of the Raman-shifted Ti:sapphire laser was used to pump transitions from the ground state to either the 2ν₃ overtone at 1.7 μm or the ν₃+ν₄ combination band at 2.3 μm. The 3.3 μm diode laser was used to probe transitions from the ground state to ν₃. The observed signal was the decrease in absorption of the diode laser absorption at these fundamental transitions due to population being moved out of the ground state by the 2nd Stokes pump. We were able to measure both 3-level double resonance (pump and probe transitions having the same lower level) and 4-level double resonance (pump and probe transitions have different lower levels; the observed signal is due to rotational relaxation.) The significance of the latter measurements should be emphasized. That 4-level signals could be observed at all is testimony to the efficacy of the experimental setup. Such 4-level double resonance was not observable with the CO₂/diode laser double resonance technique used for the CHD₃ experiments of Chapter 3. (I tried and was unsuccessful.) This is primarily due to the improved performance of liquid nitrogen cooled diode lasers over their mechanically cooled counterparts. It should also be noted that the ability to measure state-to-state rotational energy transfer in the ground vibrational state with completely tunable pump and probe lasers opens the possibility of obtaining inelastic state-to-state cross sections in a bulb experiment which complement and even surpass that attainable in molecular beam experiments [BUCK85A, BUCK85B, BROUGHTON85, NESBITT93].

The 2ν₃ and ν₃+ν₄ bands both provided useful pump transitions. There were advantages and disadvantages for both. The fine structure components of the ν₃+ν₄ band are well resolved whereas for the 2ν₃ band the lines of a particular transition (P, Q, or R) which differ only in the Cⁿ designation are overlapping. The ν₃+ν₄ band is also somewhat stronger than 2ν₃. However, 2ν₃ is significantly more "blue" than ν₃+ν₄ and slightly higher pulse energies (~25%) with better pulse-to-pulse stability were obtainable with the 2nd Stokes at 1.7 μm. (Raman gain increases with frequency.) Also the I.R. filters used to prevent scattered pump radiation from hitting the InSb detector and the diode laser were more effective at blocking 1.7 μm than 2.3 μm. It was possible to reflect the 1.7 μm pump radiation back on itself for a second pass through the cell without increasing the observed scattered light on the InSb detector. This was not possible with the 2.3 μm pump.

Using pump transitions in either band, a significant amount of population could be moved out of the ground state. To investigate the efficiency of our overtone pumping technique, we measured the change in the ground state population of the J" = 6 A₂ state using the 2nd Stokes of the Raman-shifted Ti:sapphire laser to pump the 2ν₃ R(6) A₂ transition at 6076.9540 cm⁻¹. The effect measured was the change in the absorption of the diode laser power at the center of ν₃ Q(6) A₂ fundamental at 2998.9940

cm^{-1} . With 50 mtorr of CH_4 in a 50 cm cell the transmission at the peak center for this transition was 0.35. Immediately following the pump laser pulse the diode laser transmission increased to 0.37. This 2% change in transmission corresponds to a 5% change in the population of the ground state $6 A_2$ level, i.e. $n_2/n_1 = A_2/A_1 = \ln(T_2/T_1)$.

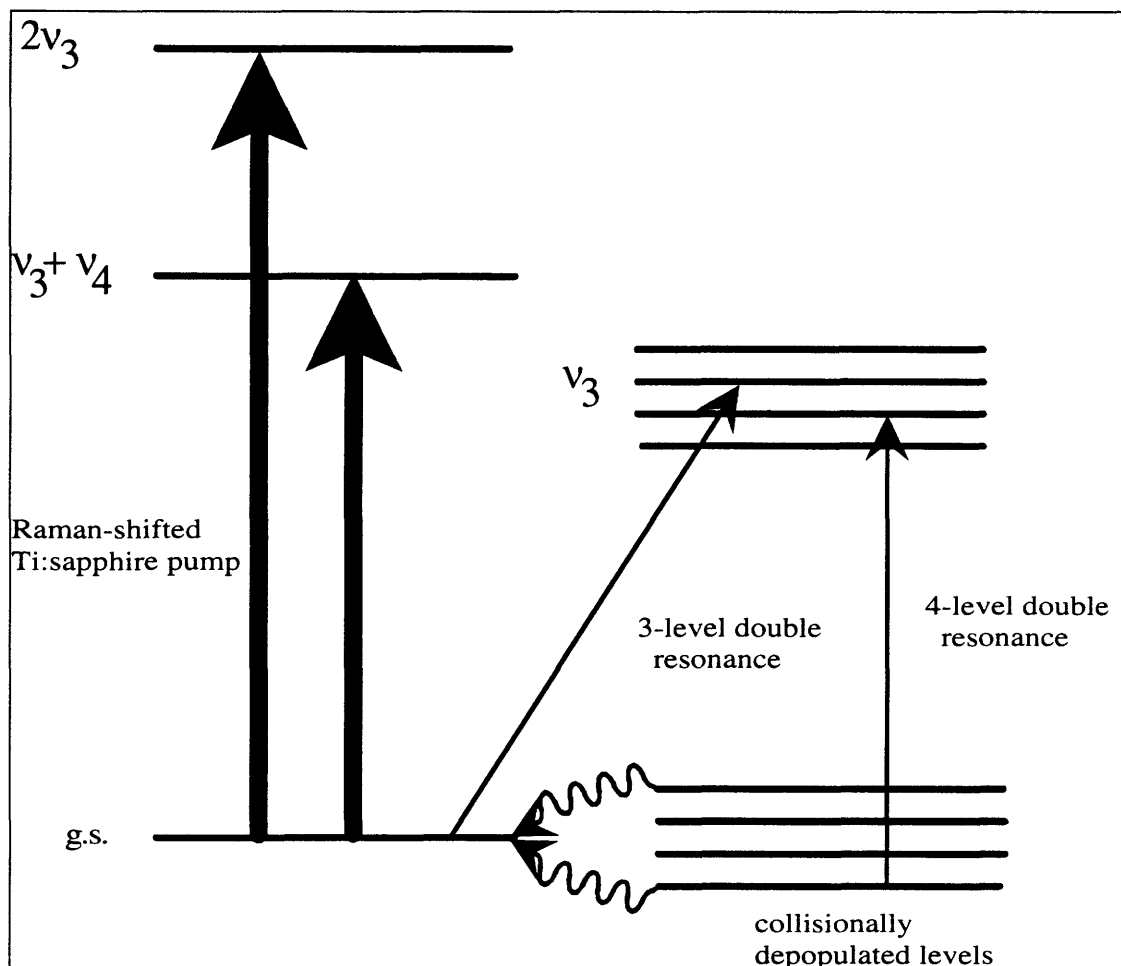


Figure 5.9

Pump-probe scheme used for CH_4 ground state energy transfer.

The measured amount of population moved by the pump laser can be compared to that calculated with the equations given in Chapter 3, Eq. 3.2-3.9. The relevant parameters for the pump laser are the pulse energy, $E_{\text{pulse}} = 5 \text{ mJ}$, pulse duration, $\Delta t_{\text{pulse}} = 2.5 \text{ nsec}$, bandwidth, $\Delta \tilde{\nu}_{\text{pulse}} = 0.045 \text{ cm}^{-1}$, and the beam cross sectional area, $\phi = 0.0314 \text{ cm}^2$ ($d = 2\text{mm}$). The line strength for the $2v_3$ R(6) A_2 transition [HITRAN92] is $1.209 \times 10^{-21} \text{ cm molecule}^{-1}$. Being an R transition, the degeneracy of the upper state differs from that of the lower state due to the $2J + 1$ factor, $g_2 = 15$ and $g_1 = 13$. Using these parameters to calculate Einstein B coefficients, Eq. 3.8, and the corresponding rate constants for induced absorption and stimulated emission, Eq. 3.7, the calculated percentage of population moved is 2.6%. This is fair

agreement with the experimental value considering the approximations in the calculation and the uncertainties of the pulse laser parameters.

This calculation allows us to make an estimate of the line strength of the weakest transition that can be detected with this experimental technique. A factor of ~ 100 in S/N is possible with reasonable, though not excessive, averaging. We then estimate that the weakest transitions detectable with the current experimental setup would be those having line strengths on the order of 10^{-23} cm molecule⁻¹. While the work presented here has concentrated on using bands for which the spectroscopy is well known in order to study energy transfer in methane, the possibility also exists for using this double resonance technique to assign transitions in overtone and combination bands which are not well understood.

For the study of energy transfer in the ground state it did not matter which vibrational band was used for pumping population out of the ground state, since the vibrationally excited population does not return to the ground state on the timescale (~ 15 μ sec) of the measurements. Vibrationally excited molecules become trapped primarily in the ν_4 vibrational state. However, from our study of vibrational energy transfer from the octad we showed that the vibrational deactivation occurs primarily by a vibrational exchange mechanism. This mechanism does have an effect on the ground state population. As overtone population moved by the 2nd Stokes pump cascades back down, vibrational exchange actually causes more population to be removed from the ground state. We took this effect into account in the same manner as was done for the R.E.T. measurements in $\nu_3+\nu_4$. The vibrational energy transfer model was incorporated with the model of R.E.T. in the ground state. We found that the vibrational exchange mechanism did have a measureable effect on our ground state R.E.T. signals, but this effect was only evident in the long time behavior of the signals, not in the state-to-state rates. The vibrational exchange part of the model only effected the beam flyout loss parameters.

Of more concern in these experiments is the interference that may be caused by the population moved by the pump laser to $2\nu_3$ and $\nu_3+\nu_4$ cascading down to the upper level of the ν_3 probe transitions. Increased population in ν_3 causes the same type of signal as decreased population in the ground state, a decrease in absorption. With our experimental setup it is impossible to distinguish which of process causes the observed effect, but the latter, population cascade into ν_3 from the overtone and combination bands, may be justifiably ignored for several reasons. The population moved to a specific rotational level in $2\nu_3$ or $\nu_3+\nu_4$ is spread out by rotational relaxation to all other rotational states of the same nuclear spin symmetry in that vibrational state. It is further spread out by vibrational relaxation to the other vibrational states. The net effect is that the increase of population of any ν_3 rotational level is significantly less than the change in the ground state population. Also the rate for vibrational relaxation is more than an order of magnitude smaller than for rotational relaxation. On the basis of these arguments for neglecting the effect

of excited state population on the double resonance signals and the consistency of this interpretation with the observed signals, we treat our data as measurements of rotational energy transfer in the ground vibrational state.

Using this interpretation of the data as measurement of rotational energy transfer in the ground state, it is important to carefully recognize the physical processes being measured. In the more common case of double resonance measurements of rotational relaxation in a vibrationally excited state, the pump laser delivers population to a specific excited state rotational level which is in great excess of its Boltzmann equilibrium value. The excess population then rotationally relaxes to a set of levels which have insignificant populations compared to that of the pumped level. In contrast, these ground state energy transfer measurements were done in a room temperature cell where the rotational levels have significant Boltzmann populations. The pump laser only creates a small decrease in the population of one of these levels. Immediately after the pump laser removes a fraction of the population of the pumped level, it is no longer in Boltzmann equilibrium with the other ground state levels. Collisional energy transfer acts to restore equilibrium, but now to a smaller total population. In both 3- and 4-level double resonance, the signal which is observed is the time evolution of the probed level as the population distribution of the rotational states returns to Boltzmann equilibrium. For 3-level double resonance, the signal is well approximated as an exponential decay. The decay rate found from fitting 3-level signals to single exponentials is a lower bound to the total rate of population flowing into that level.

We measured 3-level double resonance for several levels in the ground state at pressures between 5 and 100 mtorr. The resulting rate coefficients for ground state recovery (GSR) are compiled in Table 5.5 along with the pump and probe transitions and the relative polarization of the lasers. It is important to note that the GSR rates obtained in this manner are not exactly the same as the sum of all rates from the pumped/probed level. This is because population in the depleted 3-level level is feeding back into the levels which are refilling it. The kinetics of rotational energy transfer is complex, particularly in the present case of ground state rotational energy transfer where all levels have significant Boltzmann populations. To correctly model 3-level double resonance and to interpret 4-level signals, it is necessary to use master equation analysis.

What we wish to extract from our experiments are the individual state-to-state rates, k_{ij} . For a system of N levels there are $N(N-1)/2$ independent rates. As the number of levels in the system increases, the number of independent rates becomes extremely large. The advantage with the current experimental arrangement is that the complete tunability of the pump laser allows us to obtain enough data to determine some state-to-state rates directly. In the work described here, we have concentrated on low J'' levels of A-type symmetry. The level structure of the A symmetry fine structure components at low J'' in

	Pump transition	Pump freq. cm ⁻¹ a	Probe transition	Probe freq. cm ⁻¹ a	Relative pol.	(pt) ⁻¹ μsec ⁻¹ torr ⁻¹	k / 10 ⁻¹⁰ cm ³ molec ⁻¹ s ⁻¹	σ _{eff} Å ²
0 A ₁	v ₃ +v ₄ R(0) A ₁	4333.6694	v ₃ R(0) A ₁	3028.7522	⊥	18.6 (1.1)	5.75	64.7
3 A ₂	v ₃ +v ₄ P(3) A ₂	4272.8262	v ₃ Q(3) A ₂	3018.5288	⊥	b		
	v ₃ +v ₄ Q(3) A ₂	4315.6846	v ₃ Q(3) A ₂	3018.5288	⊥	9.3 (2.2) b	2.88	32.4
4 A ₁	2v ₃ R(4) A ₁	6057.0861	v ₃ Q(4) A ₁	3017.7112	⊥	14.2 (0.9)	4.39	49.4
6 A ₂	2v ₃ R(6) A ₂	6076.9540	v ₃ Q(6) A ₂	3016.5656	⊥	16.3 (0.9)	5.02	56.5
6 A ₁	2v ₃ R(6) A ₁	6077.0636	v ₃ Q(6) A ₁	3017.4669	⊥	23.5 (0.6)	7.25	81.6
7 A ₂	2v ₃ R(7) A ₂	6086.7454	v ₃ Q(7) A ₂	3016.4982	⊥	19.2 (1.3)	5.94	66.9
2 E	2v ₃ R(2) E	6036.6536	v ₃ P(2) E	2999.0603	⊥	12.6 (0.5)	3.87	43.6
2 E	2v ₃ Q(2) E	6004.6527	v ₃ P(2) E	2999.0603	⊥	11.2 (3.5)	3.44	38.7
2 E	2v ₃ Q(2) E	6004.6527	v ₃ P(2) E	2999.0603		6.7 (0.8)	2.06	23.2
6 E	2v ₃ Q(6) E	6002.5969	v ₃ Q(6) E	3016.4580	⊥	10.7 (1.5)	3.29	37.0
6 E	2v ₃ Q(6) E	6002.5969	v ₃ Q(6) E	3016.4580		16.7 (1.8)	5.17	58.2
1 F ₁	2v ₃ R(2) F ₂	6036.6584	v ₃ P(2) F ₂	2998.9940	⊥	17.8 (2.9)	5.48	61.7
2 F ₂	v ₃ +v ₄ R(1) F ₁	4348.9380	v ₃ P(1) F ₁	3009.0113	⊥	13.7 (2.4)	4.24	47.7

Table 5.5 Ground State Recovery Rates for CH₄(a) Frequencies were taken from the HITRAN database.(b) Ground state recovery data for the v₃+v₄ P(3) and v₃+v₄ Q(3) pumps were pooled.

The ground state is very sparse, see Fig 5.10. There is only one component each for $J'' = 0, 3,$ and 4 . There are no A levels for $J'' = 1, 2,$ or 5 . For J'' of 6 and greater there always exists at least one level of A symmetry, but the total number of A levels for $J'' \leq 10$ is only 11. This sparsity in the level structure for the A symmetry components at low J'' coupled with the fact that the different nuclear spin species do not interconvert on the time scale of our experiments, greatly reduces the size of the rate matrix. Due to the missing levels of A symmetry for $J'' = 1, 2,$ and 5 , the $J'' = 0, 3,$ and 4 levels are fairly isolated. The only levels within kT of $J'' = 0$ are $J'' = 3$ and 4 . There are only three state-to-state rates connecting $J'' = 0, 3,$ and 4 . For this very limited, but important, set of levels the state-to-state rates have been determined directly from a least squares analysis of the double resonance data.

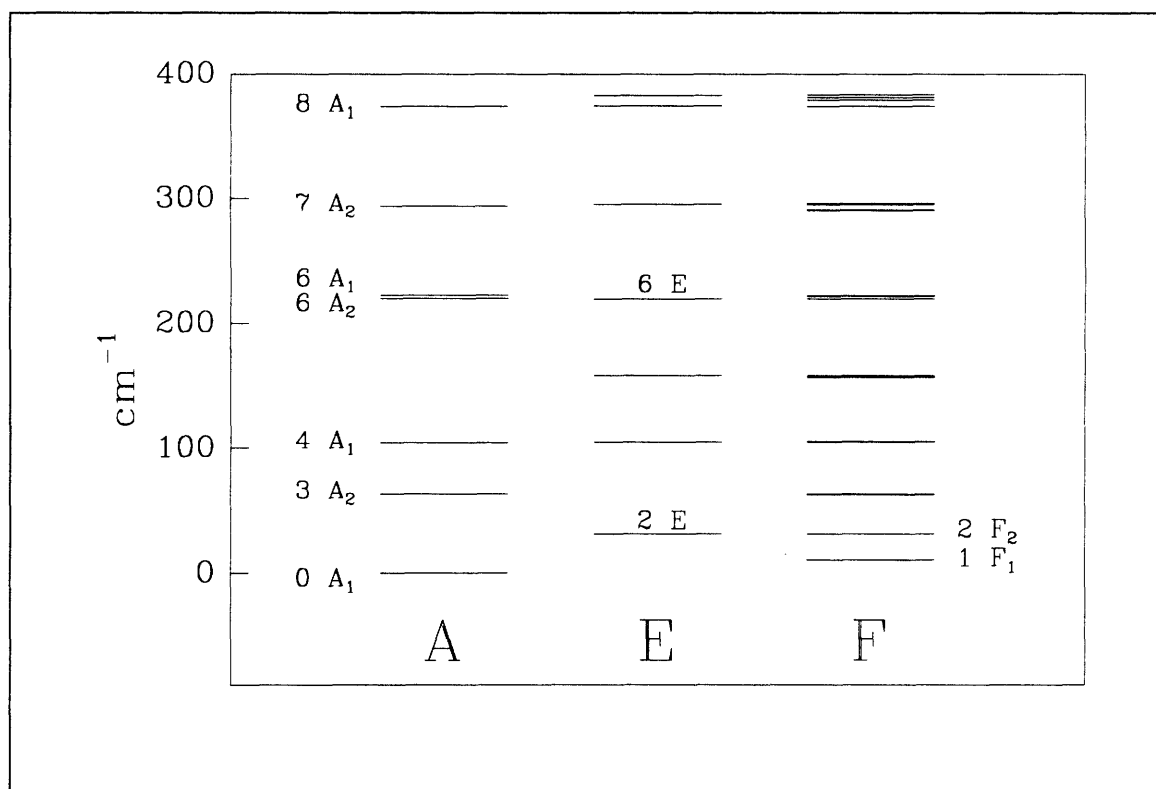


Figure 5.10

Ground state energy level diagram for CH_4 . The rotational levels are grouped according to symmetry species. The tetrahedral fine structure splitting has been magnified 100X.

The pump and probe transitions used for measuring state-to-state energy transfer are listed in Table 5.6. In all cases we have taken care that the pump and probe transitions sample similar distributions of m_j levels. By this we take note that a linearly polarized pump laser creates an anisotropic disturbance in the m_j distribution. A linearly polarized probe laser will either sample a distribution of m_j 's like or unlike that effected by the pump laser depending on the type of pump and probe transitions, (P, Q, or R), and the relative polarization of the lasers. Taking care in this regard is particularly important in light of the

depolarization measurements presented in Section 5.7. For all the cases presented here with one exception, the pump transitions were either R's or P's, the probe transitions Q's, and the relative polarization was perpendicular. These are all cases where the m_j distribution created by the pump laser is similar to that sampled by probe laser. The exception is for the total repopulation measurement of $J'' = 0$ A_1 for which the probe transition was the ν_3 R(0), but in this case it does not matter since $J = 0$ has only $m_j = 0$; the distribution is the same regardless of the pump and probe transitions and the relative polarizations.

Pump transition	Probe transition	Relative polarization
$\nu_3+\nu_4$ R(0) A_1 4333.6695 cm^{-1}	ν_3 R(0) A_1 3028.7522 cm^{-1}	\perp (irrelevant)
	ν_3 Q(3) A_2 3018.5288 cm^{-1}	\perp
	ν_3 Q(4) A_1 3017.7112 cm^{-1}	\perp
$\nu_3+\nu_4$ P(3) A_2 4272.8262 cm^{-1}	ν_3 Q(3) A_2 3018.5288 cm^{-1}	\perp
$\nu_3+\nu_4$ Q(3) A_2 4315.6846 cm^{-1}	ν_3 Q(4) A_1 3017.7112 cm^{-1}	\parallel
$2\nu_3$ R(4) A_1 6057.0861 cm^{-1}	ν_3 Q(4) A_1 3017.7112 cm^{-1}	\perp
$2\nu_3$ R(6) A_2 6076.9540 cm^{-1}	ν_3 Q(6) A_2 3016.5656 cm^{-1}	\perp
	ν_3 Q(4) A_1 3017.7112 cm^{-1}	\perp
$2\nu_3$ R(6) A_1 6077.0636 cm^{-1}	ν_3 Q(6) A_1 3017.4669 cm^{-1}	\perp
	ν_3 Q(4) A_1 3017.7112 cm^{-1}	\perp

Table 5.6

Pump and probe transitions and relative polarizations used for the ground state rotational energy transfer experiments.

It is not possible to model the $J'' = 0, 3,$ and 4 A levels as a completely isolated system. While energetic constraints may justify limiting $J'' = 0$ to interaction with only $J'' = 3$ and 4 , both $J'' = 3$ and 4 interact with higher J'' . These higher J'' in turn interact with even higher J'' and so on in an inverted pyramid sort of way. An adequate model must be truncated at sufficiently high J'' so that the omission of higher J'' 's does not effect the dynamics occurring at low J'' . We have truncated our model at $J'' = 10$, which is more than adequate in the present case, since we are primarily interested in the $J'' = 0, 3,$ and 4 levels.

For $J'' \leq 10$, there are 11 levels of A_1 or A_2 type symmetry. Only these levels were included in the model. The initial population of each level, N_j , was proportional to its Boltzmann factor,

$$N_j(0) \propto (2J + 1) e^{-E_j/kT} \quad \text{Eq. 5.13}$$

with the proportionality determined by normalizing the sum of populations of all the levels included in the model to one.

Initially, the rate matrix was set up according to a set of rates for upward going transitions, i.e. endothermic, according to the change in J'' . Downward going rates were found from detailed balance. The initial set of rates used is given in Table 5.7. It must be emphasized that these rates were *not* determined from a fit to the data. They represent reasonable estimates of the state-to-state rates and were based largely on reproducing total repopulation rates as determined from the GSR measurements. Also valuable in estimating this initial set of rates was a measurement of the $\Delta J = 1$ process going from $J'' = 7 A_2$ to $J'' = 6 A_2$ which was not included in the final fit. The $\Delta J = 3$ rate was set largely by the need to include a term between $J'' = 3$ and $J'' = 6$ to account for the observed time behavior of the signals involving the $J'' = 3 A_2$ pump. The goal here was to have a reasonable representation of the rates which connect levels not directly measured in the experiments.

ΔJ	$k(J_j; J_f) / \mu\text{sec}^{-1} \text{ torr}^{-1}$
0	4.00
1	3.50
2	2.25
3	1.51

Table 5.7

State-to-state rates connecting levels not directly measured in the ground state energy transfer experiments.

The set of rates we wish to determine from our experimental data are the five state-to-state rates $J_{0 A_1} \rightarrow J_{3 A_2}$, $J_{0 A_1} \rightarrow J_{4 A_2}$, $J_{3 A_2} \rightarrow J_{4 A_1}$, $J_{4 A_1} \rightarrow J_{6 A_2}$, and $J_{4 A_1} \rightarrow J_{6 A_1}$. The rates for these processes are treated as independent parameters in our model. They are determined from a least squares fit to the experimental data.

An additional feature necessary to model the experimental transients is to account for the long time (post-rotational equilibration) behavior of the experimental transients. The pretrigger feature of the digital oscilloscope used for recording the energy transfer signals allows us to measure the detector output immediately before the pump laser pulse. This establishes an accurate zero level for each signal. The long time behavior of the signals shows an overall decay back to this zero level. Longtime decay is primarily due to ballistic transport of the pumped molecules and their collision partners out of the probe beam. In the model, this ballistic transport out of the probe beam volume is simulated using the equation for beam flyout given in Chapter 3, Eq. 3.14, i.e.

$$S(t) = S_0 \frac{R_{\text{pump}}^2 + R_{\text{probe}}^2}{R_{\text{pump}}^2 + R_{\text{probe}}^2 + c^{*2} t^2} \quad \text{Eq. 5.14.}$$

S_0 and the sum of the squares of the pump and probe beam radii was allowed to be additional adjustable parameters in the model. The value for the sum of the squares of the pump and probe beam radii accounted for the long time decay of the transients, and S_0 was an overall scaling factor. The time dependences of the level populations, $N_j(t)$, calculated from integrating the set of 1st order differential rate equations, Eq. 3.21, were multiplied by the $S(t)$ of Eq. 5.2 to obtain the curve which could be directly compared with the experimental signals. The most probable speed, c^* , for CH_4 is $0.056 \text{ cm } \mu\text{sec}^{-1}$.

It is also necessary in modeling the data to account for the finite duration of the laser pulse and the response time of the diode laser detector. The pump pulse duration is only $\sim 4 \text{ nsec}$. This is essentially a delta function on the time scale of our measurements. However, the InSb detector has a finite rise time of $\sim 100 \text{ nsec}$. The pulse duration and response function of the detector are modeled by including an additional time-dependent loss term in the rate equation for the pumped level.

$$\frac{dN_{\text{pump}}}{dt} = \sum_j k_{ij} N_j - \alpha I(t) \quad \text{Eq. 5.15}$$

$I(t)$ was well approximated as a gaussian with a FWHM of 30 nsec centered at $t = 100 \text{ nsec}$. α was constrained to 1 since it is an overall scaling factor just like S_0 in Eq. 5.14.

The magnitudes of the experimental data needed to all be on the same intensity scale. They were scaled according to two rules. The peaks of the 3-level signals were all scaled to the same value which is equivalent to imposing the condition that the amount of population moved out of the ground state is the same irregardless of the pump transition. The "tails" of the 4-level signals (i.e. their mean value at $15 \mu\text{sec}$) were scaled to the corresponding values calculated in the model. The assumption here was that the rotational distribution will reach a quasi- Boltzmann equilibrium among the levels of the same nuclear spin species long before vibrational relaxation returns the excited state population back to the ground state. This is a good assumption, and it has been used many times in past experiments of modeling rotational energy transfer in vibrationally excited states [FOY88, HETZLER89].

Using the model described here, the numerical integration and least squares fitting were carried out in the MATLAB software package. The best fit state-to-state rates among the lowest levels of A symmetry in CH₄, $J_{0 A_1} \rightarrow J_{3 A_2}$, $J_{0 A_1} \rightarrow J_{4 A_2}$, $J_{3 A_2} \rightarrow J_{4 A_1}$, $J_{4 A_1} \rightarrow J_{6 A_2}$, and $J_{4 A_1} \rightarrow J_{6 A_1}$, are given in Table 5.8. The errorbars on each rate were determined in the standard way from the square root of the inverse diagonal elements of the Hessian matrix.

	$k(J_i, J_f) / \mu\text{sec}^{-1} \text{ torr}^{-1}$	$k / 10^{-10} \text{ cm}^3 \text{ molec}^{-1} \text{ s}^{-1}$	$\sigma / \text{\AA}^2$
$0 A_1 \rightarrow 3 A_2$	8.8 (1.1)	2.72	30.6
$0 A_1 \rightarrow 4 A_1$	13.0 (1.4)	4.01	45.2
$3 A_2 \rightarrow 4 A_1$	6.4 (0.8)	1.98	22.3
$4 A_1 \rightarrow 6 A_2$	4.5 (1.1)	1.39	15.7
$4 A_1 \rightarrow 6 A_1$	3.4 (1.2)	1.05	11.8

Table 5.8
State-to-state rates for CH₄ g.s. "A" symmetry levels

The experimental data recorded at a pressure of 50 mtorr CH₄ are overlaid with the best fit simulations from the model and are displayed in Fig 5.11. The data are laid out in the form of the rate matrix. All elements in a row have the same pump; all elements in a column have the same probe. The diagonal elements are the 3-level signals, and the off-diagonal elements are the 4-level signals. The diagonal elements are on the same scale, as are the off-diagonal elements. The difference is that the scale for the diagonal elements is a factor of three greater than that for the off-diagonal elements. Several calculated curves are shown for which there were no experimental data for comparison. These transients would depend primarily on the rates already measured. Measurement of these additional signals would help in improving the accuracy of the rate constants.

The propensity rule for parity conserving collisions is evident in these data. The rate for the parity conserving $0 A_1 \rightarrow 4 A_1$ process is more than 30% larger than the $0 A_1 \rightarrow 3 A_2$ process even though it is farther away in both ΔE and ΔJ . For the $4 A_1 \rightarrow 6 A_2$ and $4 A_1 \rightarrow 6 A_1$ processes this propensity rule seems to be reversed, although these rates could be the same within errorbar of the measurement.

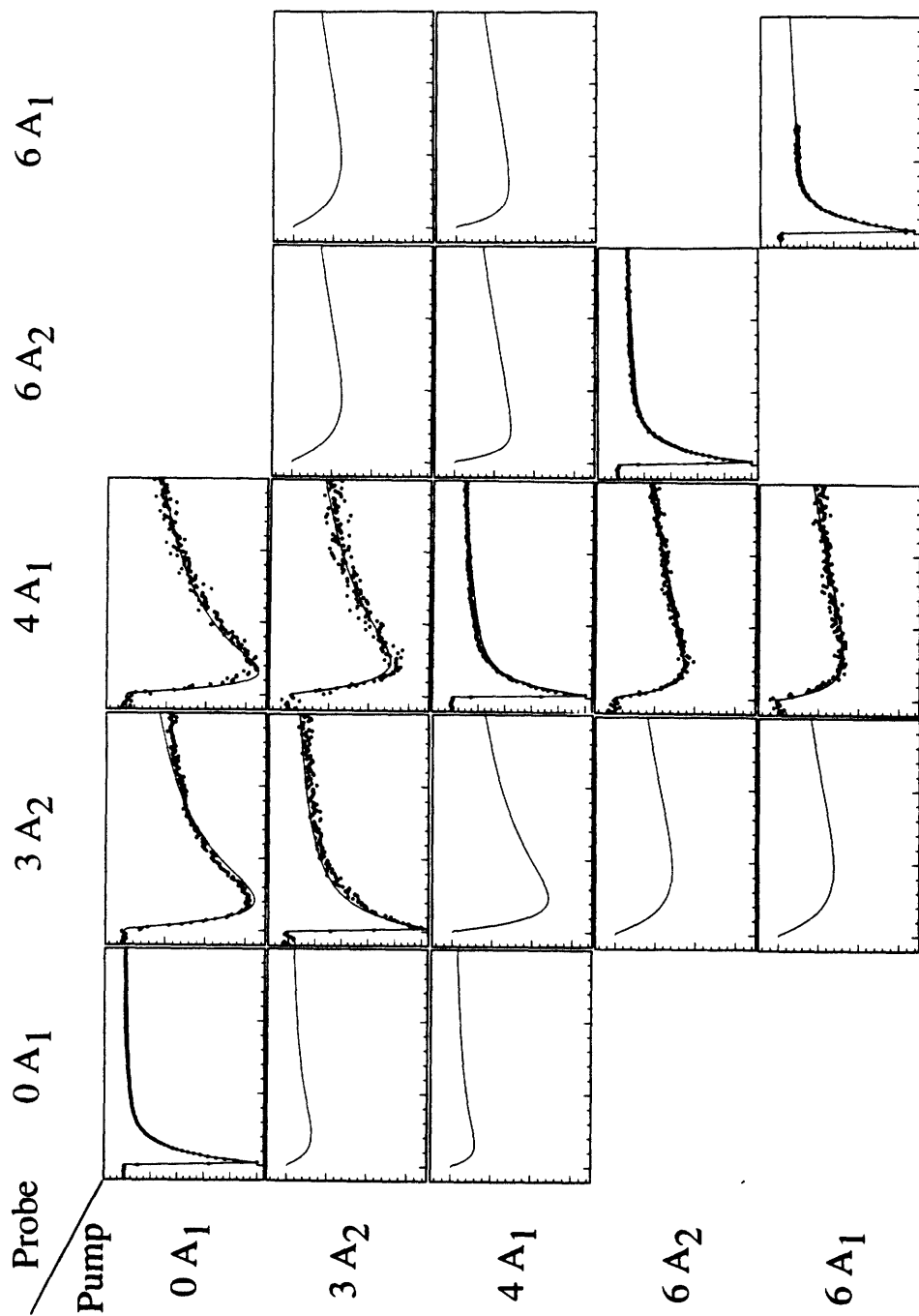


Figure 5.11
 Experimental R.E.T. signals and model simulations for CH₄ ground state A symmetry levels.

5.7 Reorientation Measurements

To examine the significance of molecular reorientation in energy transfer processes, the polarization dependence of the total depopulation and ground state recovery rates were measured for several transitions. In the ground state, the $J'' = 2 E$ and $J'' = 6 E$ levels were studied and in the $\nu_3 + \nu_4$ vibrational state, the $J' = 2 A$ and $J' = 4 A$ levels. The ground state E levels show very large differences (~35%) in the GSR rates for the cases where the relative polarization of the pump and probe beams was parallel or perpendicular. The differences for the $\nu_3 + \nu_4$ A levels are smaller (~5-10 %), but still significant.

As an example of the results of these experiments we will consider the case for the $J'' = 2 E$ ground state level. The measurements of this level were done by pumping a Q transition ($2\nu_3$ Q(2) E, $6004.6527 \text{ cm}^{-1}$) and probing a P transition (ν_3 P(2) E, $2999.0603 \text{ cm}^{-1}$) with the relative polarization of the two lasers either parallel or perpendicular. The polarized pump laser removes population from the ground state $J'' = 2 E$ level and creates a distribution of m_J levels having less than the equilibrium Boltzmann population. The distribution of m_J levels is found in the standard way from the 3-j coefficients [TINKHAM64, p124; SATCHLER71, p.36]. For the Q(2) pump transition the relative m_J distribution is found from evaluating Eq. 5.16.

$$m_J \propto \begin{pmatrix} 2 & 1 & 2 \\ -m' & 0 & m \end{pmatrix}^2 \quad \text{Eq. 5.16}$$

The evaluation of this equation shows that the deviation in the equilibrium population of the m_J levels is proportional to m^2 , as is shown in Figure 5.12.

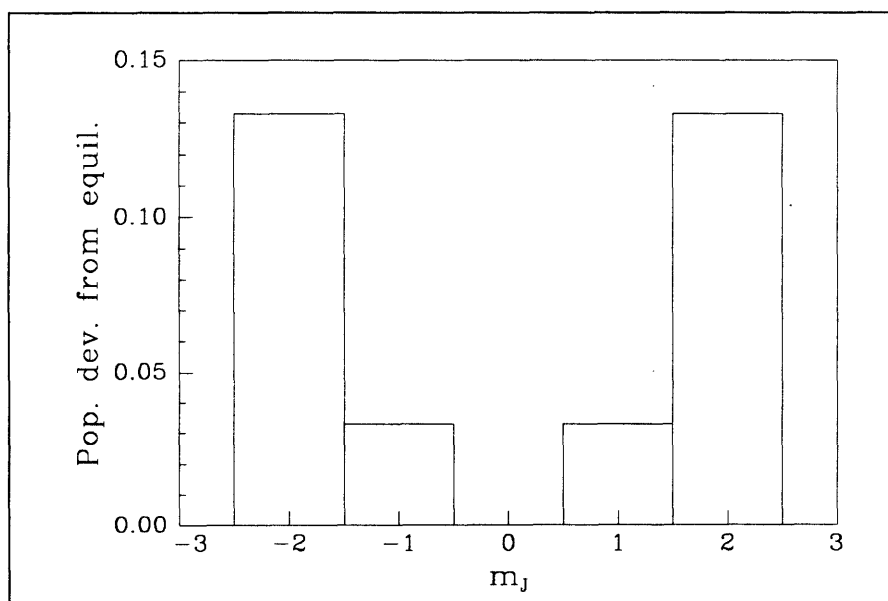


Figure 5.12

Relative population deviations in the $J'' = 2 E$ level caused by the $2\nu_3$ Q(2) E pump.

The distribution of m_J 's created by the Q(2) pump is sampled differently by the P(2) probe dependent on whether the relative polarizations of the lasers are parallel or perpendicular. The polarization of the pump laser defines the space-fixed axis. The absorption of the probe laser depends on the population in each m_J level times a weighting factor. For the case where the probe laser polarization is parallel to the pump, the relative weights by which the $J'' = 2$ m_J levels are sampled is given by Eq. 5.17.

$$w_{J=2}^{\parallel} \propto \begin{pmatrix} 1 & 1 & 2 \\ -m' & 0 & m \end{pmatrix}^2 \quad \text{Eq. 5.17}$$

The selection rule on Δm for parallel polarization is $\Delta m = 0$. This is illustrated in Figure 5.13. There are no transitions allowed for the $m_J = \pm 2$ levels with parallel polarization. The relative weights by which the $m = 0, \pm 1$ levels are sampled is indicated by the thickness of the transition arrows.

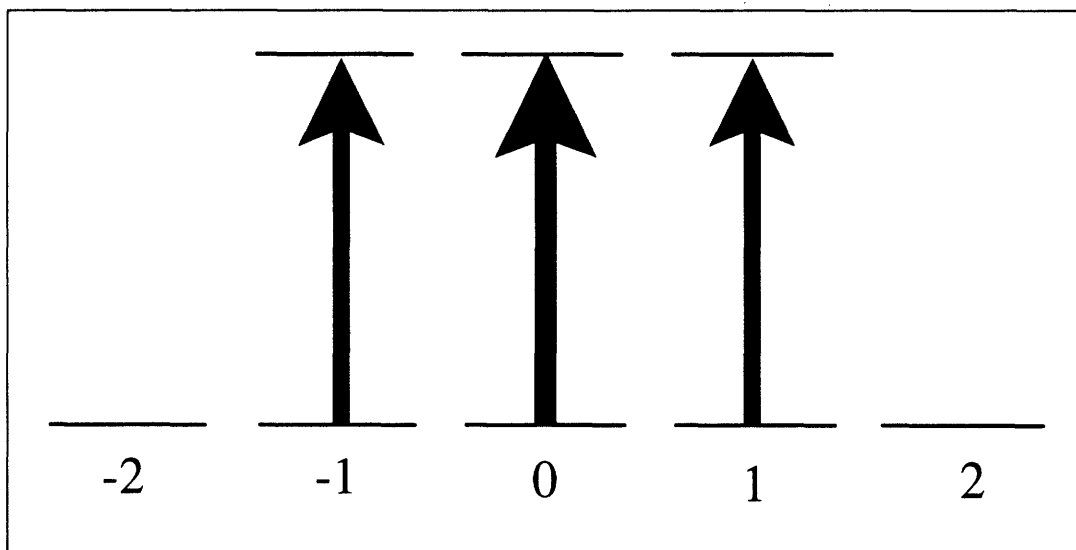


Figure 5.13

Allowed transitions between the m_J levels for the P(2) probe transition for parallel polarization of the pump and probe lasers.

For perpendicular polarization of the pump and probe lasers, the weights by which the $J'' = 2$ m_J levels are sampled is given by Eq. 5.18.

$$w_{m_J=2}^{\perp} \propto \frac{1}{2} \begin{pmatrix} 1 & 1 & 2 \\ -m' & -1 & m \end{pmatrix}^2 + \frac{1}{2} \begin{pmatrix} 1 & 1 & 2 \\ -m' & +1 & m \end{pmatrix}^2 \quad \text{Eq. 5.18}$$

Here the selection rule on Δm is $\Delta m = \pm 1$. The relative weights by which the $m = 0, \pm 1, \pm 2$ levels are sampled is indicated by the thickness of the transition arrows. In Figure 5.14, we show the transition diagram between the m_J levels for P(2) probe. This figure is analogous to the one shown in Figure 5.13 for the case of parallel polarization.

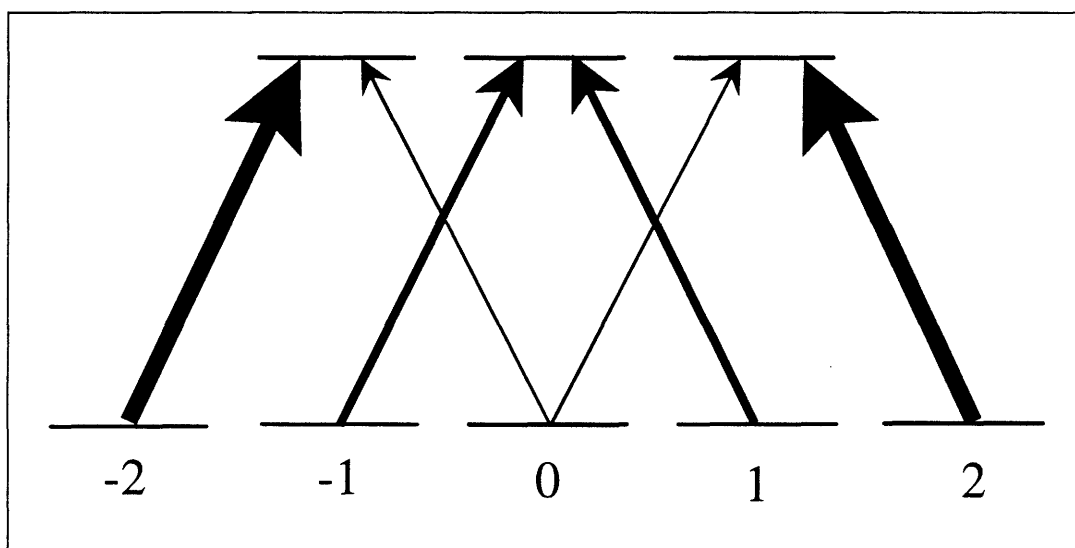


Figure 5.14

Allowed transitions between the m_J levels for the P(2) probe transition for perpendicular polarization of the pump and probe lasers. The width of the transition arrows indicates the relative weight with which that transition contributes to the total.

We can see from Figures 5.12 that the population of the m_J levels most strongly disturbed by the pump laser are the $m = \pm 2$. The population of the $m = \pm 1$ levels is disturbed a factor of four less, and the population of the $m = 0$ level is not affected at all. For the case of perpendicular polarization these m_J levels in $J'' = 2$ that have their populations most strongly disturbed by the pump laser are also those that weight most heavily in the absorption of the probe laser. From Figure 5.12 we see that the opposite is true for the case of parallel polarization. The levels most strongly disturbed by the pump laser ($m = \pm 2$) are not sampled at all by the probe.

The relative distribution of m_J population disturbances created by a polarized laser and the relative weights by which this disturbance is sampled by a polarized probe laser affects both the intensity of the double resonance signal and its time evolution. Chevalier and DeMartino [CHEVALIER87] have given simple analytical expressions for the intensity ratio of the double resonance signal for parallel and perpendicular polarizations. They also tabulate these ratios for all possible pump and probe combinations

for $J \leq 4$. For the example we are considering here, a Q(2) pump and a P(2) probe, the ratio of the double resonance intensity for perpendicular to parallel polarization is 4.5.

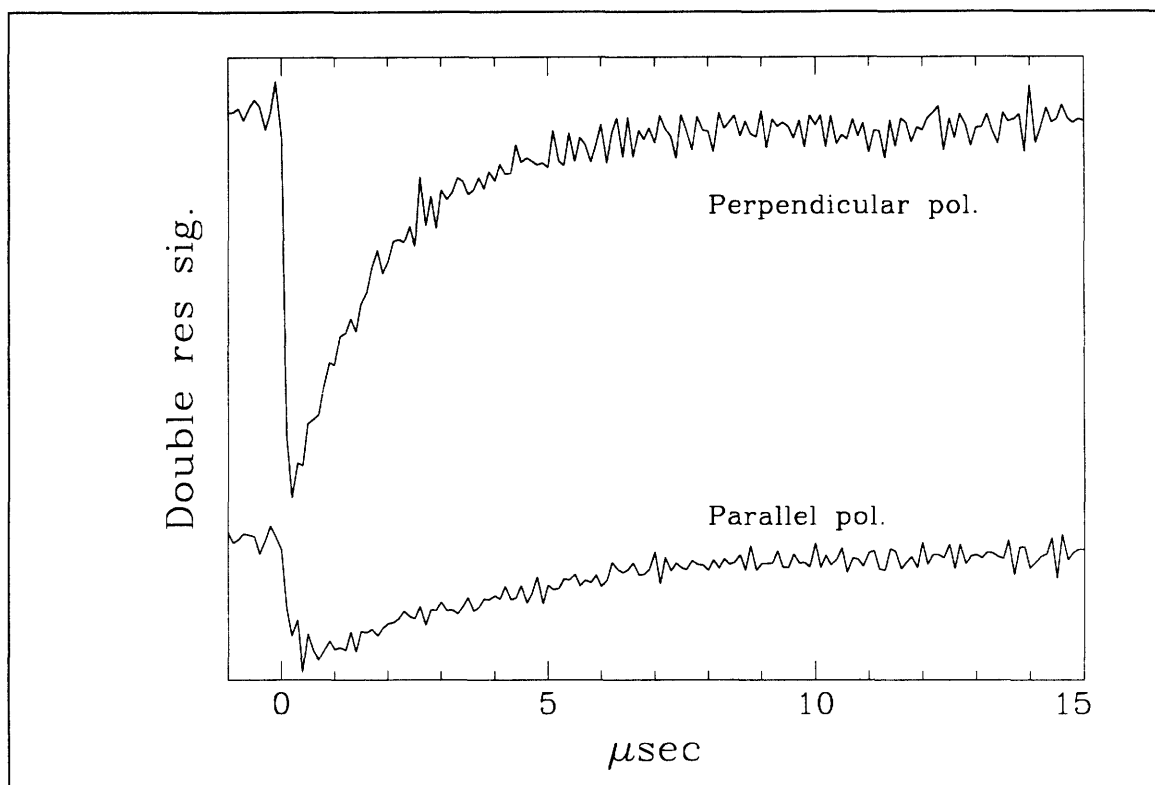


Figure 5.15

Time-resolved double resonance signals for the $2\nu_3$ Q(2) E pump and the ν_3 P(2) E probe with parallel and perpendicular polarization of the pump and probe lasers.

In Figure 5.15 we show the double resonance signals obtained for the parallel and perpendicular polarizations. The signals were recorded sequentially and no adjustments were made to the experimental apparatus other than rotating the polarization of the pump laser. The intensity of the double resonance signal for the parallel case is approximately the expected factor of 4.5 smaller than that for the perpendicular case. It is also clear that the decay rate for the parallel polarization signal is much slower than the perpendicular. From single exponential fits to these decays, the parallel case is found to be 35% slower than the perpendicular. The actual rates obtained from $\ln I$ plots are tabulated in Table 5.5.

This large difference in decay rates indicates the importance of elastic reorientation collisions. The total rate for population from all m_j levels within the same J must be the same in a bulb experiment. For the perpendicular polarization case any collision event, either inelastic or elastic, takes population out of the levels being probed. The much smaller rate for the parallel polarization case results from population in

the m_J levels not probed flowing into and repopulating these levels. The observed time dependent signal for the parallel case is actually more like 4-level double resonance.

To see this effect more fully, we show in Figure 5.16 the parallel polarization signal multiplied by 4.5 to put it on the same intensity scale as the perpendicular signal. On this adjusted scale, the amplitude of the parallel signal actually increases with respect to the perpendicular as elastic reorientation transfers population to the low m_J levels. The difference between the two signals roughly illustrates the pure reorientation signal. We cannot extract a precise value for the pure reorientation rate since there are multiple collision processes contributing to these signals. A complete analysis of the state-to-state rotational energy transfer such as that done for formaldehyde by Coy *et. al.* [COY92] would be necessary for quantitative rates. However, from these preliminary experiments we can draw the important qualitative conclusion that elastic reorientation is significant in CH_4 .

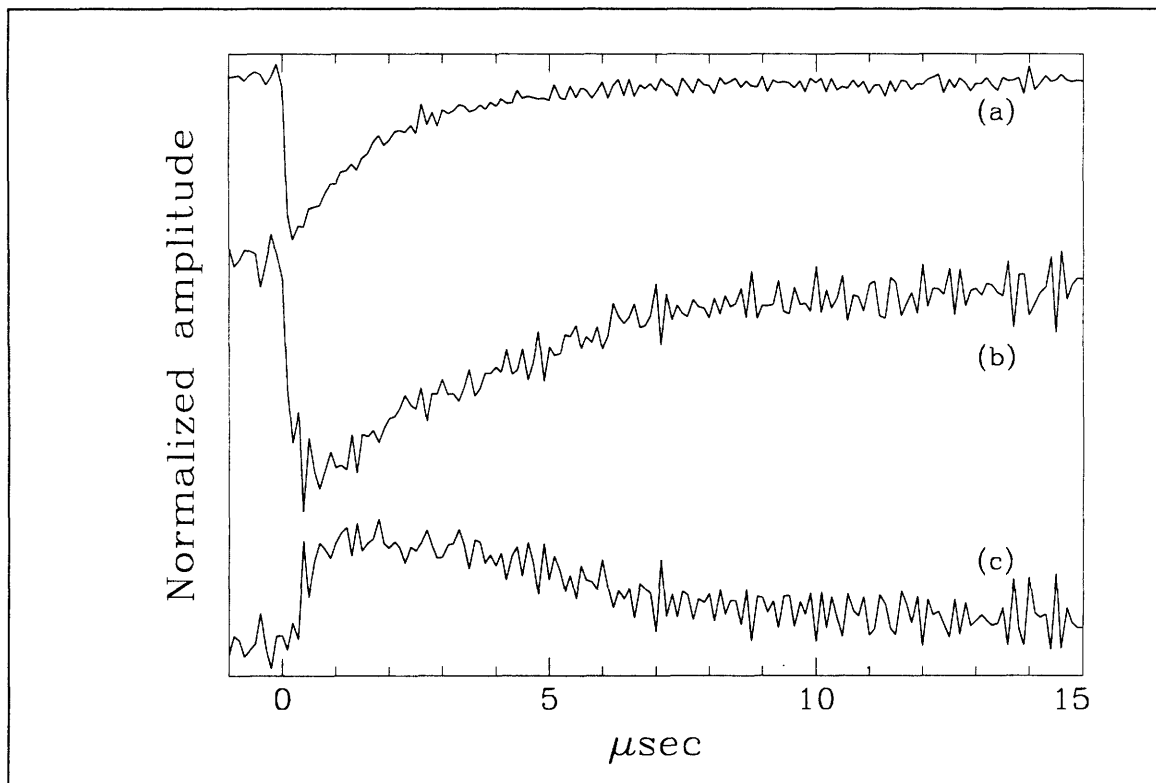


Figure 5.16

Time-resolved double resonance signals for the $2\nu_3$ Q(2) E pump and the ν_3 P(2) E probe. (a) perpendicular polarization double resonance signal, (b) parallel polarization double resonance signal multiplied by 4.5 so that it is on the same intensity scale as (a), (c) difference between perpendicular and scaled parallel signals which is roughly the pure reorientation rate.

Chapter 6. Conclusions and Future Work

The CHD₃ energy transfer studies reported in Chapter 3 and in Appendix 2 were done to explore how a symmetric top molecule with essentially no dipole moment behaves in the collision process. We can compare the results of our CHD₃ experiments with two other quite different molecular systems, ¹³CD₄ and NH₃, which nonetheless both have characteristics in common with CHD₃. CHD₃ and ¹³CD₄ are isotopomers. They have similar intermolecular interactions. Both experience strong collisions. CHD₃ and NH₃ both belong to the same symmetry class. They share common features in their energy level structure.

One of the most notable features of the R.E.T. pathways in CHD₃ is the strong adherence to the symmetric top propensity rule $\Delta k = 3n$, which holds even for the case when $\Delta k \neq 3n$ transitions are not excluded by nuclear spin statistics. This propensity is clearly demonstrated by the TRIRDR signals shown in Fig. 2 of Appendix 2. The pump transition in this case was the ν_3 Q_{Q(12,7)} "E". Consider the $J = 11$ row of this figure. The fastest rates among the different K-stacks are definitely for those processes which change K by an integer multiple of three. This propensity rule is very indicative of a symmetric top, and it illustrates the similarity in energy transfer pathways between CHD₃ and NH₃.

While the Δk selection rule is indicative of symmetric-top behavior, the distribution of rates is more like that of ¹³CD₄. The CHD₃ rotational relaxation processes show considerable rates to a wide distribution of final states. The dipole-like processes $\Delta J = 0, \pm 1$, $\Delta k = 0$ are the dominant rates but there are also significant contributions from higher ΔJ and ΔK terms. While this broad distribution of rates to final rotational states is reminiscent of what was observed for ¹³CD₄, there are no unique pathways discerned for CHD₃. The distribution of rates is very uniform.

From these observations we are led to the conclusion that CHD₃, in its rotational relaxation pathways is much more like a symmetric-top molecule such as NH₃, than like a spherical top such as ¹³CD₄. These results for CHD₃ reemphasize that spherical top molecules have very unique rotational energy transfer pathways and that the uniqueness of these pathways arises from the energy level structure of spherical tops. Clearly there is a need for more experimental data on these molecules. The preliminary experiments on CH₄ reported here are a good starting point.

From these preliminary experiments we have observed that the strongest propensity rule for rotational energy transfer at low J is a conservation of parity. From the experiments in the $\nu_3 + \nu_4$ vibrational state

we observed a propensity to stay within the same ν_4 Coriolis manifold. This is the same as the $(R-J) = 0$ propensity rule that was observed in the $^{13}\text{CD}_4$ experiments.

For the ground rotational state we have been able to obtain quantitative measurements of the important state-to-state R.E.T. rates at very low J . These rates indicate that there is a "lumpiness" to the state-to-state rates at low J which is due to the sparsity of levels. This observation is in qualitative agreement with the scattering calculations presented by Nesbitt *et. al.* [NESBITT94] for Ar- CH_4 scattering.

In the CHD_3 experiments described here, we changed the symmetry of the methane molecule by making a substitution of the hydrogen isotope. Another potentially interesting way of examining the effect of a change in symmetry from T_d to C_{3v} would be to study rotational energy transfer in a spherical top molecule in a local mode state which has C_{3v} symmetry. Zhu and coworkers [ZHU90A, ZHU90B] have analyzed the local mode (3000), (4000), and (5000) Si-H stretching overtones of silane. Their spectra show that the rotational structure for these local mode vibrational states in a spherical top molecule is exactly analogous to that of a parallel band in a symmetric top, including the expected stronger transitions for $K = 3n$ features. For the CHD_3 experiments we had the case of a symmetric top molecule with similarities to a spherical top. For these local mode states of SiH_4 , we have a spherical top molecule which is behaving like a symmetric top. It would be an interesting and insightful experiment to study rotational energy transfer in these local mode states.

REFERENCES

- [ABEL92] B. Abel, S.L. Coy, J.J. Klaassen, and J.I. Steinfeld, *J. Chem. Phys.* **96**, 8236 (1992).
- [ATREYA89] S.K. Atreya, J. Bergstralh, J.J. Caldwell, K. Fox, J.F. Kasting, J.G. Luhmann, J. Lunine, D.J. McCleese, J. Rahe, and R.E. Young, Planetary Atmospheres Management Operations Working Group, subgroup on Strategies for Planetary Atmospheres Exploration, Laboratory Research for Planetary Atmospheres: An initiative (1989).
- [BIALKOWSKI80] S.E. Bialkowski, D.S. King, and J.C. Stephenson, *J. Chem. Phys.* **72**, 1156 (1980).
- [BIERRY77] M. Bierry, R. Frey, and Pradere, *Rev. Sci. Instrum.* **48**, 733 (1977).
- [BOBIN72] B. Bobin, *J. De Phys.* **33**, 345 (1972).
- [BOBIN78] B. Bobin and G. Guelachvili, *J. Phys.* **39**, 33 (1978).
- [BOBIN94] B. Bobbin and J. Moret-Bailly, *Spect. Acta*, in press.
- [BROUGHTON85] C.V. Broughton, R.E. Miller, and R.O. Watts, *Mol. Phys.* **56**, 363 (1985).
- [BROWN82] L. R. Brown, *J. Mol. Spec.* **96**, 94 (1982).
- [BUCK85A] U. Buck, A. Kohlhase, D. Secrest, T. Phillips, G. Scoles, and F. Grein, *Mol. Phys.* **55**, 1233 (1985).
- [BUCK85B] U. Buck, K.H. Kohl, A. Kohlhase, M. Faubel, and V. Staemmler, *Mol. Phys.* **55**, 1255 (1985).
- [BUNKER79] P.R. Bunker, *Molecular Symmetry and Spectroscopy* (Academic Press, New York, 1979).
- [CARRASQUILLO88] E. Carrasquillo, A.L. Utz, and F.F. Crim, *J. Chem. Phys.* **88**, 5976 (1988).
- [CHADWICK93] B.J. Chadwick, A.P. Milce, and B.J. Orr, *Chem. Phys.* **175**, 113 (1993).
- [CHAMPION89] J. P. Champion, J. C. Hilico, L. R. Brown, *J. Mol. Spec.* **133**, 244 (1989).
- [CHAMPION92] J.-P. Champion, M. Loete, and G. Pierre, in *Spectroscopy of the Earth's Atmosphere and Interstellar Molecules*, edited by K.N. Rao and A. Weber (Academic, New York, 1992).
- [CHEVALIER87] M. Chevalier and A. De Martino, *Chem. Phys. Lett.* **135**, 446 (1987).
- [COY92] S.L. Coy, S.D. Halle, J.L. Kinsey, and R.W. Field, *J. Mol. Spec.* **153**, 340 (1992).
- [CRC93] *CRC Handbook of Chemistry and Physics*, edited by David R. Lide, Ph.D. (CRC Press, Boca Raton, 1993) p. 6-96.
- [DEMARTINO80] A. De Martino, R. Frey, and F. Pradere, *IEEE J. Quant. Elec.* **QE-16**, 1184 (1980).
- [DEPRISTO79] A.E. DePristo and H. Rabitz, *J. Quantum Spectrosc. Rad. Transfer* **22**, 65 (1979).
- [DOPHEIDE94] R. Dopheide, W. Conrath, and H. Zacharias, submitted to *J. Chem. Phys.*
- [DOYENNETTE88] L. Doyennette and F. Mennard-Bourcin, *J. Chem. Phys.* **89**, 5578 (1988).
- [DROZDOSKI77] W. S. Drozdowski, A. Fakhr, and R. D. Bates, Jr., *Chem. Phys. Lett.* **47**, 309 (1977).
- [DROZDOSKI78] W. S. Drozdowski, R. D. Bates, Jr., D. R. Siebert, *J. Chem. Phys.* **69**, (1978).
- [DÜBAL89] H.-R. Dübal, T.-K. Ha, M. Lewerenz, and M. Quack, *J. Chem. Phys.* **91**, 6698 (1989).
- [DUPRE-MAQUAIRE82] J. Dupre-Maquaire and G. Tarrago, *J. Mol. Spec.* **96**, 156 ((1982).
- [EVERITT89] H.O. Everitt and F.C. Delucia, *J. Chem. Phys.* **90**, 3520 (1989).
- [FINK65] U. Fink, T. A. Wiggins, and D. H. Rank, *J. Mol. Spec.* **18**, 384 (1965).
- [FLANNERY92] C.C. Flannery and J.I. Steinfeld, *J. Chem. Phys.* **96**, 8157 (1992).

- [FLANNERY93] C.C. Flannery, Ph.D. Thesis, Massachusetts Institute of Technology (1993).
- [FÖRSTER60] T. Förster, "Excitation Transfer" in *Comparative Effects of Radiation*, edited by M. Burton, J. Kirby-Smith, J. Magee (Wiley, New York, 1960) p. 300.
- [FOX76] K. Fox and W.B. Person, *J. Chem. Phys.* **64**, 5218 (1976).
- [FOX80] K. Fox, G. W. Halsey, and D. E. Jennings, *J. Mol. Spec.* **83**, 213 (1980).
- [FOY85] B. Foy, L. Laux, S. Kable, and J.I. Steinfeld, *Chem. Phys. Lett.* **118**, 464 (1985).
- [FOY88] B. R. Foy, Ph.D. Thesis, Massachusetts Institute of Technology (1988).
- [FREY77] R. Frey, F. Pradere, J. Lukasik, and J. Ducuing, *Opt. Comm.* **22**, 355 (1977).
- [FROST92] M.J. Frost and I.W.M. Smith, *Chem. Phys. Lett.* **191**, 574 (1992).
- [FROST93] M. J. Frost, private communication.
- [GRASIUK78] A. Z. Grasiuk and I. G. Zubarev, *Appl. Phys.* **17**, 211 (1978).
- [GRAY79] D. L. Gray and A. G. Robiette, *Mol. Phys.* **37**, 1901 (1979).
- [GUELACHVILI86] G. Guevalachvili and K.N. Rao, *Handbook of Infrared Standards* (Academic Press, Orlando, 1986).
- [HANNA86] D.C. Hanna, D.J. Pointer, and D.J. Pratt, *IEEE J. Quantum Electron.* **QE-22**, 322 (1986).
- [VONDERLINDE69] D. von der Linde, M. Maier, and W. Kaiser, *Phys. Rev.* **178**, 11 (1969).
- [HARRADINE84] D. Harradine, Ph.D. Thesis, Massachusetts Institute of Technology (1984).
- [HARTER78] W.G. Harter, C.P. Patterson, and F. J. de Paixao, *Rev. Mod. Phys.* **50**, 37 (1978).
- [HARTIG79] W. Hartig and W. Schmidt, *Appl. Phys.* **18**, 235 (1979).
- [HAUB87] J.G. Haub and B.J. Orr, *J. Chem. Phys.* **86**, 3380 (1987).
- [HERZBERG45] G. Herzberg, *Molecular Spectra and Molecular Structure II. Infrared and Raman Spectra of Polyatomic Molecules* (Van Nostrand, New York, 1945).
- [HESS76] P. Hess and C.B. Moore, *J. Chem. Phys.* **65**, 2339 (1976).
- [HETZLER89] J. R. Hetzler, Ph.D. Thesis, Massachusetts Institute of Technology (1989).
- [HILBORN82] R.C. Hilborn, *Am. J. Phys.* **50**, 982 (1982).
- [HIRSCHFELDER54] J.O. Hirschfelder, C.F. Curtiss, and R.B. Bird, *Molecular Theory of Gases and Liquids* (Wiley, New York, 1954).
- [HITRAN92] The "HITRAN" data base is described by L.S. Rothman, R.R. Gamache, R.H. Tipping, C.P. Rinsland, M.A.H. Smith, D.C. Benner, V.M. Devi, J.-M. Flaud, C. Camy-Peyret, A. Perrin, A. Goldman, S.T. Massie, L.R. Brown, and R.A. Toth, *J. Quant. Spectrosc. Rad. Transfer* **48**, 469 (1992). We have used the "HITRAN PC" version available from USF Research Foundation, Tampa, FL 33620 to retrieve the spectroscopic information utilized in our analysis.
- [HUBER79] K.P. Huber and G. Herzberg, *Molecular Spectra and Molecular Structure IV. Constants of Diatomic Molecules* (Van Nostrand Reinhold, New York, 1979).
- [HUNT81A] R. H. Hunt, L. R. Brown, R. A. Toth, and J. W. Brault, *J. Mol. Spec.* **86**, 159 (1981).
- [HUNT86B] R. H. Hunt, L. R. Brown, R. A. Toth, and J. W. Brault, *J. Mol. Spec.* **86**, 170 (1981).
- [JAHN39] H.A. Jahn, *Proc. Roy. Soc. London* **56**, 680 (1939).
- [JOLICARD83] G. Jolicard and M.-Y. Perrin, *Chem. Phys.* **91**, 341 (1984).
- [LEWERENZ88] M. Lewerenz and M. Quack, *J. Chem Phys.* **88**, 5408 (1988).
- [MAIER76] M. Maier, *Appl. Phys.* **11**, 209 (1976).

- [MEERTS81] W.L. Meerts and I. Ozier, *J. Chem. Phys.* **75**, 596 (1981).
- [MELTON73] L.A. Melton and W. Klemperer, *J. Chem. Phys.* **55**, 1468 (1971); **59**, 1099 (1973).
- [MENNARD-BOURCIN88] F. Menard-Bourcin and L. Doyennette, *J. Chem. Phys.* **88**, 5506 (1988).
- [MURRAY72] J. R. Murray and J. Javan, *J. Mol. Spec.* **42**, 1 (1972).
- [NASA61] R.A. Svehla, NASA Technical Report TR R-132 (1961).
- [NESBITT93] D.J. Nesbitt, J.W. Nibler, A. Schiffman, W. Chapman, and J.M. Hutson, *J. Chem. Phys.* **48**, 503 (1973).
- [OKA73A] T. Oka, *Adv. At. Mol. Phys.* **9**, 127 (1973).
- [OKA73B] T. Oka, *J. Mol. Spec.* **48**, 503 (1973).
- [PAPE94] T.W. Pape, F.C. DeLucia, and D.D. Skatrud, submitted *J. Chem. Phys.*
- [PAPOUSEK82] D. Papousek and M.R. Aliev, *Molecular Vibrational-Rotational Spectra* (Elsevier, Amsterdam, 1982).
- [PARSON90] R. Parson, *J. Chem. Phys.* **93**, 8731 (1990).
- [PARSON91] R. Parson, *J. Chem. Phys.* **95**, 8941 (1991).
- [PERRIN84] M.-Y. Perrin and G. Jolicard, *Chem. Phys.* **91**, 341 (1984).
- [PERRIN86] M.-Y. Perrin and G. Jolicard, *Chem. Phys. Lett.* **127**, 118 (1986).
- [PINE75] A. S. Pine, *J. Mol. Spec.* **54**, 132 (1975).
- [PUGH76] L.A. Pugh, K.N. Rao, *Molecular Spectroscopy: Modern Research, Vol. II*, edited by K. Rao (Academic Press, New York, 1976) p. 165.
- [RANK60] D. H. Rank, D. P. Eastman, G. Skorinko, and T. A. Wiggins, *J. Mol. Spec.* **1**, 78 (1960).
- [ROCHE92] C. Roche, Thèse Doctorat de l'Université de Bourgogne, Dijon, 1992.
- [ROCHE93] C. Roche, J.-P. Champion, and A. Valentin, *J. Mol. Spec.* **160**, 517 (1993).
- [SCHRÖTTER79] H.W. Schrötter and H. W. Klockner, *Raman Spectroscopy of Gases and Liquids. Topics in Current Physics Vol. II*. (Springer-Verlag, New York, 1979).
- [SHARMA63] R.D. Sharma and C.A. Brau, *J. Chem. Phys.* **50**, 924 (1969).
- [SHEN84] Y.R. Shen, *Principles of Nonlinear Optics* (Wiley, New York, 1984).
- [SIEGMAN86] A.E. Siegman, *Lasers* (University Science Books, Mill Valley, CA, 1986).
- [SLANINA94] J. Slanina, P. Warneck, N.M. Bazhin, H. Akimoto, and W.M. Kieskamp, *Pure & Appl. Chem.* **66**, 137 (1994).
- [SMITH88] M.A.H. Smith, C.P. Rinsland, B. Fridovich, and K. Rao, *Molecular Spectroscopy: Modern Research, Vol III*, edited by K. Rao (Academic Press, New York, 1988) p.111.
- [STEINFELD74] J.I. Steinfeld, *Molecules and Radiation* (Harper and Row, New York, 1974).
- [STEINFELD85] J.I. Steinfeld, *Molecules and Radiation 2nd Ed.* (MIT Press, Cambridge, MA, 1985).
- [STEINFELD89] J.I. Steinfeld, J.S. Francisco, and W.L. Hase, *Chemical Kinetics and Dynamics* (Prentice-Hall, Englewood Cliffs, NJ, 1989).
- [STOICHEFF57] B. P. Stoicheff, *Can. J. Phys.* **35**, 730 (1957).
- [STRONG93] K. Strong, F.W. Taylor, S.B. Calcutt, J.J. Remidios, and J. Ballard, *J. Quant. Spectrosc. Radiat. Transfer* **50**, 363 (1993).
- [TEMPS88] F. Temps, S. Halle, P.H. Vaccaro, R.W. Field, and J.L. Kinsey, *J. Chem. Soc. Faraday Trans. 2*, **84**, 1457 (1988).
- [TINKHAM64] M. Tinkham, *Group Theory and Quantum Mechanics* (McGraw-Hill, New York, 1964).

- [TOBIASON92] J.D. Tobiason, A.L. Utz, and F.F. Crim, *J. Chem. Phys.* **97**, 7437 (1992).
- [TOBIASON93] J.D. Tobiason, A.L. Utz, and F.F. Crim, *J. Chem. Phys.* **99**, 928 (1993).
- [UTZ91] A.L. Utz, Ph.D. Thesis, University of Wisconsin-Madison, 1991.
- [UTZ93] A.L. Utz, J.D. Tobiason, E. Carrasquillo, L.J. Sanders, and F.F. Crim, *J. Chem. Phys.* **98**, 2742 (1993).
- [VOLKOV88] S. Yu. Volkov, D. N. Kozlov, A. M. Prokhorov, V. V. Smirnov, and V. I. Fabelinskiy, *Laser-Induced Raman Spectroscopy*, edited by P. P. Pashinin (Nova Science Publishers, Commack, 1988).
- [WHITE87] J. C. White, "Stimulated Raman Scattering" in *Tunable Lasers*, edited by L.F. Mollenauer and J.C. White (Springer-Verlag, Berlin, 1987).
- [WILSON35] E.B. Wilson, *J. Chem. Phys.* **3**, 276 (1935).
- [YARDLEY68] J.T. Yardley and C.B. Moore, *J. Chem. Phys.* **48**, 1111 (1968).
- [YARDLEY70] J.T. Yardley, M.N. Fertig, and C.B. Moore, *J. Chem. Phys.* **52**, 1450 (1970).
- [YARDLEY80] J.T. Yardley, *Introduction to Molecular Energy Transfer* (Academic Press, New York, 1980).
- [ZHU90A] Q. Zhu, B. Zhang, Y. Ma, and H. Qian, *Spectrochimica Acta*, **46A**, 1217 (1990).
- [ZHU90B] Q. Zhu, H. Ma, B. Zhang, Y. Ma, and H. Qian, *Spectrochimica Acta*, **46A**, 1323 (1990).
- [ZITTEL73] P.F. Zittel and C.B. Moore, *J. Chem. Phys.* **58**, 2004 (1973).

Appendix One

"State-to-state rotational energy-transfer measurements in the $\nu_2 = 1$ state of ammonia by infrared-infrared double resonance"

J. Chem. Phys. **96**, 8236 (1992).

State-to-state rotational energy-transfer measurements in the $v_2 = 1$ state of ammonia by infrared-infrared double resonance

Bernd Abel,^{a)} Stephen L. Coy, Jody J. Klaassen, and Jeffrey I. Steinfeld
Department of Chemistry and G. R. Harrison Spectroscopy Laboratory, Massachusetts Institute of Technology, Cambridge, Massachusetts 02139

(Received 5 February 1992; accepted 28 February 1992)

An infrared double-resonance laser spectroscopic technique is used to study state-resolved rotational ($R-R$, $R-T$) energy transfer in ammonia ($^{14}\text{NH}_3$) (self-collisions and between ammonia and foreign gases). NH_3 molecules are prepared in selected rovibrational states of the $v_2 = 1$ level using coincidences between CO_2 -laser lines and v_2 fundamental transitions. Measurements of both the total rate of depopulation by collisions, and the rates of transfer into specific final rovibrational states (v, J, K) have been carried out using time-resolved tunable diode laser absorption spectroscopy. For NH_3 - NH_3 collisions, measurements of total depopulation rates of selected JK states in $v_2 = 1$ and ground-state recovery rates are found to be three and eight times larger, respectively, than the Lennard-Jones collision rate, in accord with theoretical expectations for polar molecules. A kinetic master-equation analysis of time-resolved level populations yields state-to-state rate constants and propensity rules for NH_3 - NH_3 and NH_3 -Ar collisions. Individual rotational energy-transfer rates in $v_2 = 1$ are slower than in the vibrational ground state, but still comparable to the Lennard-Jones collision frequency. Our experiments show that rotational energy transfer in $v_2 = 1$ is not governed by simple "dipolelike" selection rules. They show fast rotational energy transfer, which can be related to long-range interaction potentials, but at the same time considerable amounts of $\Delta J = 2$ and 3 , $\Delta K = 0$, and $\Delta J = 1-4$, $\Delta K = 3$, transitions, which may be attributed to higher-order terms in the multipole expansion of the intermolecular potential. No pronounced symmetry-state correlation and no preferred pathways were found except the preference for relaxation within a K stack and the expected separate relaxation of different nuclear-spin species, which can be labeled by their K -quantum number. Rates of collision-induced symmetry change ($a \leftrightarrow s$) in $v_2 = 1$ are on the order of $k_{as} = 4 \mu\text{s}^{-1} \text{ torr}^{-1}$, smaller than k_{aa} in the ground state, but over an order of magnitude larger than that recently reported in the literature. Depopulation rates for other collision partners (Ar, H_2 , N_2 , and He) can be understood in terms of the intermolecular potentials. Comparisons are made between the relaxation rates measured in this work and infrared pressure-broadening coefficients reported in the literature.

I. INTRODUCTION

The ammonia molecule has been the subject of numerous investigations utilizing time-resolved spectroscopy to elucidate energy-transfer and relaxation processes occurring among the rotational and vibrational energy levels of this molecule.¹ In the vibrational ground state of ammonia, each rotational state is split by inversion doubling into a pair of levels of opposite (a and s) parity, between which dipole-allowed transitions occur in the 15–40 GHz region. This is a convenient region for microwave spectroscopy, which has been extensively utilized to study rotational relaxation in the vibrational ground state of ammonia by microwave double-resonance techniques.² As the ammonia molecule is excited in its v_2 out-of-plane mode, the inversion splitting progressively increases. The vibrational fundamental $v_2 = 0$ coincides with several CO_2 and N_2O laser lines, affording a convenient excitation method for transient nutation³ and time-resolved infrared-microwave double-resonance⁴⁻⁷ ex-

periments on ammonia. The vibrational and rotational spectra of ammonia are also of interest for remote-sensing measurements, e.g., in terrestrial combustion systems⁸ and the atmospheres of the outer planets.⁹

In addition to the microwave double-resonance experiments noted above,²⁻⁷ a number of molecular-beam scattering measurements have been carried out on state-to-state rotational energy-transfer processes in the vibrational ground state of ammonia. Klaassen *et al.*¹⁰ investigated rotational- and symmetry-state-changing collisions in a molecular-beam maser. Meyer, Buck, and co-workers¹¹ studied rotationally inelastic scattering with H_2 and He as collision partners, but these experiments were carried out at relatively high collision energies (0.075–0.01 eV, corresponding to 600–800 cm^{-1} or an effective temperature of 800–1200 K). Recently, Schliepen and ter Meulen¹² prepared the 0_0^+ state of ortho- NH_3 with a quadrupole field selector in a molecular beam. They used resonantly enhanced multiphoton ionization to obtain rotational excitation cross sections for collisions with He and H_2 .

In contrast to the vibrational ground state, data on the

^{a)} Present address: Institut für physikalische Chemie, Tammannstrasse 6, Göttingen, Germany.

details of rotational energy transfer in the vibrational excited states of ammonia are much less extensive. The time-resolved infrared double-resonance (TRIRD) technique, using a pulsed CO₂ laser to pump rovibrational transitions and a tunable infrared diode laser as a probe, has been employed in our laboratory¹³⁻¹⁵ and elsewhere to obtain highly detailed descriptions of state-to-state energy transfer among rotational levels in excited vibrational states of small polyatomic molecules. Such experiments have not been carried out on ammonia. Reid and co-workers^{16,17} used this technique to measure vibrational relaxation in the $v_2 = 1$ and 2 levels of ammonia, but at high gas pressures at which rotational relaxation was essentially complete on the time scale of the measurements. Schwendeman and co-workers^{18(a)} carried out infrared double-resonance experiments on ammonia using a sideband-modulated CO₂ laser as a probe, which did not have the tuning range necessary to probe a large number of rotational levels. Their earlier microwave measurements evaluated T_2/T_1 in the ground state for a large number of levels.^{18(b)-18(d)} Veeken, Dam, and Reuss¹⁹ carried out infrared double-resonance experiments (using a color-center laser as a probe) on expansion-cooled ammonia, obtaining overall population relaxation times and symmetry-changing collision rates in the ground and excited vibrational levels.

Resonantly enhanced multiphoton ionization (REMPI) spectroscopy has also been used^{20,21} to follow relaxation in vibrationally excited levels of ammonia following infrared pumping. Using this technique, Shultz and Wei²⁰ reported a rate coefficient for collision-induced transfer between a and s levels in the vibrationally excited state, $k_{as}(v_2 = 1) = 0.21 \times 10^6 \text{ s}^{-1} \text{ torr}^{-1}$, about 50 times slower than the "hard-sphere" collision rate. This is a quite unexpected result, since symmetry-changing collisions should be a strongly dipole-allowed process, and indeed in the vibrational ground state, $k_{as}(v_2 = 0)$ has been found to contribute on the order of 50% to the line-broadening rates for low J levels^{1-5,18(b)-(d),19} where the line-broadening rates range between 110 and 160 $\mu\text{s}^{-1} \text{ torr}^{-1}$. Furthermore, in recent "triple-resonance" experiments on the $v_2 = 2$ level of ammonia,²² we found a lower limit for $k_{as}(v_2 = 2)$ of 2 $\mu\text{s}^{-1} \text{ torr}^{-1}$, and it is expected that k_{as} would be smaller in $v_2 = 2$ than in $v_2 = 1$, because of the larger inversion splitting in $v_2 = 2$.

On the basis of the first Born approximation in scattering theory, rotational energy transfer in ammonia might be expected to follow dipolelike propensity rules, i.e., $\Delta J = 0, \pm 1$ and $\Delta K = 0$, with change in parity. While this is a useful approximation for ammonia colliding with polar molecules, deviations from this behavior have been well documented in the earlier microwave double resonance work.^{2,7,12,23}

Since no systematic study of rotationally inelastic processes in the vibrationally excited state of ammonia is available, and in order to resolve some of the discrepancies noted above, we undertook a series of time-resolved infrared double-resonance experiments on ammonia, in which we determined state-to-state rotational energy-transfer thermal rate coefficients and propensity rules in the excited $v_2 = 1$ state, including the symmetry-changing ($a \leftrightarrow s$) process. These re-

sults are presented here, along with comparisons of our results with other work reported in the literature. In particular, the measured inelastic collision rates are compared with self- and hydrogen-pressure-broadening coefficients for the ammonia $v_2 = 0$ band,²⁴⁻²⁷ which are of particular importance to remote-sensing measurements of the outer planets,⁹ and with theoretical models.

II. EXPERIMENT

The IR-IR double-resonance setup has already been described in recent publications.^{13,14,22} Only those modifications which have been made in the present experiment will be described here. Briefly, a pulsed line tunable CO₂ laser is used as the pump source, in conjunction with a tunable diode laser probe. The pump laser is a grating tuned TE CO₂ laser (Laser Science, Inc. PRF-150S) with a typical pulse energy of 50 mJ/pulse and a pulsewidth of 80-100 ns [full width at half maximum (FWHM)]. The estimated bandwidth is about 4 GHz. In order to avoid complications from long afterpulses the laser was operated at low N₂ partial pressure. Unless otherwise noted the CO₂ laser is set to the 10P(32) (932.960 cm⁻¹) or the 9R(30) (1084.635 cm⁻¹) line, which are coincident with the fundamental $aQ(5,3)$ and $sR(5,0-3)$ transitions in ammonia. The mismatches between the two laser lines and the $v_2 = 0$ transitions are 0.95 and 0.2 GHz, respectively, ensuring efficient near-resonant pumping. For the transient absorption measurements of population prepared in $v_2 = 1$, we used a 10 μm PbSeTe diode laser (Laser Photonics Analytics Division) operated at 35-50 K at a current of 200-700 mA. The multimode output of the 10 μm diode was collimated with a 2 in. focal length lens ($f/1$) and passed through a polarizer oriented with its axis approximately orthogonal to the polarization axis of the pump beam in order to prevent scattered pump light perturbations to the diode. The pump-and-probe beam polarizations were thus approximately perpendicular throughout the double-resonance volume. The bandwidth of the diode had previously been determined to be approximately 0.0004 cm⁻¹ by least-squares fitting of self-broadened infrared absorption lines of ozone.²⁸

The approximately collinear (within 1°-2°) counterpropagating cw diode laser beam and the CO₂ laser pulse were overlapped in a static stainless-steel cell. The two beams were separated behind the cell using a grating. After the separation the diode laser beam passed through a 0.5 m monochromator (Bausch & Lomb) which isolated the mode of interest in the wavelength region between 950 and 1080 cm⁻¹. The diode laser beam was then focused onto a HgCdTe detector [Santa Barbara Research (SBR), ≈ 50 ns rise time]. A confocal Fabry-Pérot étalon (Tec-Optics, FSR: 0.010 05 cm⁻¹) was inserted into the beam path behind the monochromator to provide a frequency reference, calibrated against standard lines taken from Ref. 29. The detector output was amplified with a SBR amplifier, monitored, and averaged on a digital averaging oscilloscope (Le Croy 9400A). Typically 500-1000 traces were averaged for an acceptable signal-to-noise ratio. The data were transferred to a microcomputer for further processing.

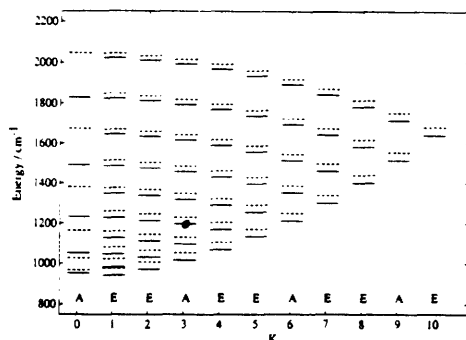


FIG. 1. Rotational level structure of ammonia in the $v_2 = 1$ level; a and s inversion levels are marked by dashed and solid lines, respectively.

The sample cell is a stainless-steel tube 2 m in length, with an inside diameter of 3.5 cm, equipped with antireflection coated ZnSe windows. NH_3 (Matheson) pressures in the cell between 3 and 50 mtorr were measured with a capacitance manometer (MKS Baratron, model 227A, 0–1 torr range). Gases used in the energy-transfer measurements were research-grade materials obtained from Matheson or Air Products.

III. SPECTROSCOPIC CONSIDERATIONS

In order to obtain a detailed picture of rotational energy transfer ($R-R$, $R-T$) in $v_2 = 1$, it is necessary to prepare and probe as many rovibrational levels as possible (see Fig. 1).

Using a line tunable CO_2 laser we are limited in the number of levels that can be prepared. This limitation can partially be overcome by using ammonia coincidences with other gas laser transitions, e.g., N_2O (Refs. 3–7) or isotopic CO_2 ,³⁰ Stark-tuning the ammonia transitions into resonance,³¹ or using isotopically substituted ammonia (e.g., $^{15}\text{NH}_3$).³² Nevertheless, using just the well-known coincidences between the $9R(30)$ and $10P(32)$ lines of the $^{12}\text{CO}_2$ laser and the $aQ(5,3)$ and $sR(5,0-3)$ $v_2 = 0$ transitions in $^{14}\text{NH}_3$, we have been able to prepare JK states having (a) different nuclear-spin species, (b) different parity (a,s) states, and (c) different rotational (J,K) states in $v_2 = 1$. These transitions also play an important role in infrared multiple-photon excitation of ammonia^{22,33–36} and in the optically pumped ammonia laser.^{37–40}

Fortunately, the spectroscopy of the symmetric bend vibration of NH_3 has been extensively studied in the past. Rovibrational assignments and frequencies for $v_2 = 1$, 2, and 3 are available from studies of Urban *et al.*^{41–43} The transition frequencies of the $v_2 = 0$ and $2v_2 - v_2$ bands have been calculated using their assignments and assuming selection rules for parallel band transitions.

The $10\text{ }\mu\text{m}$ diode used in this work has a frequency range between 940 and 1088 cm^{-1} , which enabled us to probe the $s(J,0)$ and $s(J,3)$ rovibrational states shown in Fig. 1 up to $J = 7$. A summary of all pumped and probed levels, transitions, and frequencies is given in Table I.

IV. RESULTS

The $10P(32)$ line of the CO_2 laser at 932.960 cm^{-1} is coincident with the $v_2 = 0$ $aQ(5,3)$ transition in ammonia.

TABLE I. Pump and probe transitions in NH_3 , $v_2 = 0$ band. For pump transitions, the offsets from line center are also given.

CO_2 pump	Frequency (cm^{-1})	NH_3 transitions	$\delta\nu$ (cm^{-1})
10P(32)	932.960	$s(5,3) - a(5,3)$ [$aQ(5,3)$]	0.032
9R(30)	1084.635	$a(6,0) - s(5,0)$ [$sR(5,0)$]	0.007
		$a(6,1) - s(5,1)$ [$sR(5,1)$]	0.010
		$a(6,2) - s(5,2)$ [$sR(5,2)$]	0.025
Probed levels	Probe transitions	ν (cm^{-1})	
Ground state			
$(v_2 = 0$ transitions)			
$a(5,3)$	$s(6,3) - a(5,3)$ [$aR(5,3)$]	1053.1304	
$s(5,1)$	$a(5,1) - s(5,1)$ [$sQ(5,1)$]	966.5324	
$v_2 = 1$			
$(2v_2 - v_2$ transitions)			
$s(5,3)$	$2a(6,3) - s(5,3)$ [$2sR(5,3)$]	1058.8584	
$s(6,1)$	$2a(7,1) - s(6,1)$ [$2sR(6,1)$]	1070.9098	
$s(7,3)$	$2a(8,3) - s(7,3)$ [$2sR(7,3)$]	1088.7434	
$s(6,3)$	$2a(7,3) - s(6,3)$ [$2sR(6,3)$]	1074.0258	
$s(4,3)$	$2a(5,3) - s(4,3)$ [$2sR(4,3)$]	1043.1512	
$s(3,3)$	$2a(4,3) - s(3,3)$ [$2sR(3,3)$]	1026.8147	
$s(5,0)$	$2a(6,0) - s(5,0)$ [$2sR(5,0)$]	1055.0956	
$s(3,0)$	$2a(4,0) - s(3,0)$ [$2sR(3,0)$]	1022.7527	
$s(1,0)$	$2a(2,0) - s(1,0)$ [$2sR(1,0)$]	987.7378	

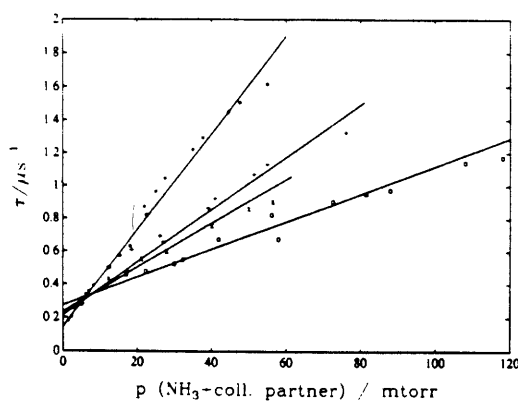


FIG. 2. Plot of $v_2 = 1$ $s(5,3)$ depopulation rates vs pressure for ammonia self- and foreign-gas relaxation. Points are denoted as follows: \bullet , $\text{NH}_3\text{-NH}_3$; $+$, $\text{NH}_3\text{-N}_2$; \times , $\text{NH}_3\text{-H}_2$; \circ , $\text{NH}_3\text{-Ar}$.

Using this excitation wavelength only the $s(5,3)$ level in $v_2 = 1$ is populated (see Table I); this pump frequency has been used for most of the experiments described here. The $9R(30)$ line at 1084.635 cm^{-1} is coincident with the $sR(J = 5; K = 0, 1, 2, \text{ and } 3)$ transitions in ammonia resulting in a much less selective population of $v_2 = 1$. Nevertheless, the $9R(30)$ line enabled us to carry out a direct measurement of the transition rate between a and s levels of $J = 6$ and $K = 1$ in $v_2 = 1$.

With use of the $10P(32)$ pump transition, the prepared s levels could be probed directly with the diode laser. In addition to these three-level double-resonance (DR) signals, we observed a large number of four-level DR signals, which are also listed in Table I. Measured inverse relaxation times k_T ($\mu\text{s}^{-1}\text{ torr}^{-1}$) were converted to rate coefficients k_r ($\text{cm}^3\text{ s}^{-1}$) and effective cross sections using the ideal-gas law and the standard relationship

$$\sigma_{\text{rot}} = k_r / (8kT/\pi\mu)^{1/2}, \quad (1)$$

where μ is the collision reduced mass. Numerically, k_T ($\mu\text{s}^{-1}\text{ torr}^{-1}$) is equal to 0.282σ (\AA^2) for $\text{NH}_3\text{-NH}_3$ at 293 K.

A. Total depopulation and ground-state recovery rates

Rates for removal of population from the $s(5,3)$ level in $v_2 = 1$, summed over all final states, after CO_2 laser excitation were determined by monitoring the absorption on the $2sR(5,3)$ ($2v_2 - v_2$) transition for a series of pressures. A plot of the signal relaxation time τ vs p gave a total depopulation rate for the $s(5,3)$ level of $34 \pm 4\ \mu\text{s}^{-1}\text{ torr}^{-1}$. A ground-state recovery rate of $80 \pm 25\ \mu\text{s}^{-1}\text{ torr}^{-1}$ for the $a(5,3)$ level was determined by the same procedure, monitoring the $aR(5,3)$ transition of $v_2 = 0$. Total depopulation and ground-state recovery rates for both the upper and lower states of the fundamental transition $aQ(5,3)$ in ammonia were determined. They enable us to compare the average relaxation rates of the upper and lower levels with pressure-broadening coefficients of this transition, as will be done in the discussion. With use of the different collision partners, depopulation rates of the $s(5,3)$ in $v_2 = 1$ were determined by a fit of a sum of two exponentials to the data. Although the contribution of feedback from adjacent levels makes this result somewhat ambiguous, the longer time constant includes diffusion and free-flight losses of the excited molecules, while the shorter time constant more closely approximates the phenomenological depopulation rate which we wish to extract from the data. A more detailed discussion of this point occurs below. The depopulation results are shown in Fig. 2. Table II gives a summary of measured ground-state recovery and total $v_2 = 1$ depopulation rates for $\text{NH}_3\text{-NH}_3$ collisions, and total $v_2 = 1$ depopulation rates in the presence of foreign gas collision partners. These depopulation measurements, like all the transients measured in this study, were performed with pump-and-probe polarizations perpendicular.

B. Symmetry changing collisions

For direct measurements of a - s transfer the $[v_2 = 1, a(6,1)]$ state has been excited and probed via the $sR(6,1)$ $2v_2 - v_2$ transition. Figure 3 shows a transient absorption signal measured for the $s(6,1)$ level, along with the prediction for the time variation of the population in this level from the kinetic model described in the following section. Although this measurement is not free from interferences of other levels due to the population of the levels $a(6,0)$,

TABLE II. Total depopulation rates for $s(5,3)$, $v_2 = 1$ and ground-state recovery rates for $a(5,3)$.

	k_T ($\mu\text{s}^{-1}\text{ torr}^{-1}$)	k_r ($\text{cm}^3\text{ s}^{-1}$)	σ (\AA^2)	
Ground-state recovery [$a(5,3)$]				
$\text{NH}_3\text{-NH}_3$	80 (20)	$25 (6) \times 10^{-10}$	291 (75)	
Total depopulation [$v_2 = 1, s(5,3)$]				
$\text{NH}_3\text{-NH}_3$	34 (4)	$10.7 (1.3) \times 10^{-10}$	123 (14)	57.8
$\text{NH}_3\text{-N}_2$	16 (2)	5.0 (0.6)	65 (8)	
$\text{NH}_3\text{-H}_2$	13.4 (2)	4.2 (0.6)	22 (3)	
$\text{NH}_3\text{-Ar}$	8.5 (2)	2.7 (0.6)	36 (8)	
$\text{NH}_3\text{-He}$	6 (3)	1.9 (0.9)	13.5 (7)	

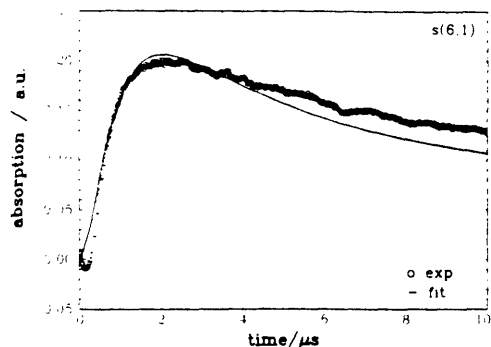


FIG. 3. Four-level DR signal showing rapid $a \rightarrow s$ parity-changing collisions in ammonia (15.2 mtorr). The $9R(30)$ CO_2 laser line pumps the $a(6,1)$ level in $v_2 = 1$, and the probed transition is $sR(6,1)$, $2v_2 - v_2$. The solid curve is the prediction of the kinetic model described in the text. This should be compared with Fig. 8 of Ref. 20.

$a(6,1)$, and $a(6,2)$, it provides a direct measurement of the $a \rightarrow s$ transfer rate, which is estimated from the model to be $4 \mu\text{s}^{-1} \text{ torr}^{-1}$.

C. State-to-state rotational energy transfer

In this section we examine rotational (R - R , R - T) energy transfer in $v_2 = 1$. In this region V - V and V - T , R energy transfer is slow and can be neglected.¹⁶ The initially excited levels are $v_2 = 1$, $s(5,3)$ and $a(6,0)$. Measurements were made at NH_3 pressures between 5 and 50 mtorr. A complete list of observed transitions has been given in Table I.

1. Nuclear-spin restrictions on collisional energy transfer

Each rotational level in $^{14}\text{NH}_3$ is associated with a characteristic nuclear-spin wave function. The different nuclear-spin species are labeled as A and E for the ortho and para species and can be distinguished by their K quantum number (K is an integer multiple of 3 for the A species, the other K values are of E symmetry). Since the nuclear spins are not effectively relaxed by collisions, the symmetry species cannot interconvert under our experimental conditions except via exchange collisions. The rigorous collision propensity rule $A \leftrightarrow A$ and $E \leftrightarrow E$, all others forbidden, was checked by preparing the $s(5,3)$ and probing the $s(5,2)$ level of NH_3 . From the small amplitude of the observed signal, we estimated an upper bound of $k(A \leftrightarrow E) < 0.5 \mu\text{s}^{-1} \text{ torr}^{-1}$ for collisional transfer between these levels with different nuclear-spin wave functions. Resonant exchange between A and E species has been reported for other systems,^{44,45} and resonant vibrational exchange transferring excitation between NH_3 spin species has been measured by Danagher and Reid¹⁶ to be $0.69 \mu\text{s}^{-1} \text{ torr}^{-1}$. Their result is a total rate obtained without rotational resolution, so our state-to-state rate is, as expected, somewhat lower, and is sufficiently low to neglect in the model.

2. Simple kinetic model for absorption time profiles using a master-equation approach

In order to obtain quantitative estimates of the state-to-state energy-transfer rates, we used a master-equation approach⁴⁶⁻⁴⁸ which enables us to model population transfer among a specified set of levels. If \mathbf{N} is the array of level populations and \mathbf{K} is the matrix of rates connecting these levels, the time evolution of \mathbf{N} is given by

$$\dot{\mathbf{N}} = \mathbf{K}\mathbf{N}. \quad (2)$$

Although the initial and final states are completely resolved in our experiments, the complete state-to-state rate matrix \mathbf{K} can be obtained only by modeling the population changes in the detected levels. This is an inherent problem of this type of experiment, in which one is always summing over a number of possible pathways connecting the initial and final states.^{13,14,49} The array of time-varying populations $\mathbf{N}(t)$ in Eq. (2) can be obtained either by calculating the eigenvalues of \mathbf{K} or by integrating the set of coupled differential equations. In the latter case, the set of equations (2) which has to be integrated can be written as

$$dN_i/dt = \sum_{j \neq i} k_{ji}N_j + k_{ii}N_i = \sum_j k_{ij}N_j, \quad (3)$$

where k_{ij} is the rate of transfer of population from level j to level i , and the depopulation rate of level i , k_{ii} , is related to the rates of transfer of population into the level by the conservation criterion:

$$k_{ii} = - \sum_{j \neq i} k_{ij}. \quad (4)$$

Total depopulation rates of the directly pumped level (see Sec. IV A) are in this sense eigenvalues of the rate matrix \mathbf{K} .^{46,47} In the equation for the directly pumped level, a term has been added to account for the time-dependent population of this level by the CO_2 laser:

$$dN_p/dt = \sum_{all j} k_{pj}N_j + \alpha I(t), \quad (5)$$

where $I(t)$ is the experimental pulse profile and α is a phenomenological proportionality coefficient.

In order to reduce the number of energy levels and differential equations which need to be considered, we used a simplified model for rotational energy transfer in $v_2 = 1$ of NH_3 . First, we expect the interconversion of nuclear-spin species to be slow on the time scale of our experiments. Indeed, Oka² argues that the transition between *ortho* and *para* species of ammonia should be strictly forbidden. Since we have verified this experimentally (see the preceding section), we assumed that the interconversion propensity rule holds strictly, and included in the model only states of the same nuclear-spin species as the initially pumped level. States with $J > 8$ ($K = 0, 3$, and 6), and all states with $K = 9$, were grouped together into four baths of states which were not allowed to feed back into the system of levels in the numerical model. These simplifications and assumptions resulted in a condensed system with 30 equations in which every pair of J, K states with $J < 9$ and $K < J$ could be explicitly taken into account. Eight of the s levels in the case of $aQ(5,3)$ excitation, three s levels in the case of $sR(5,0)$ exci-

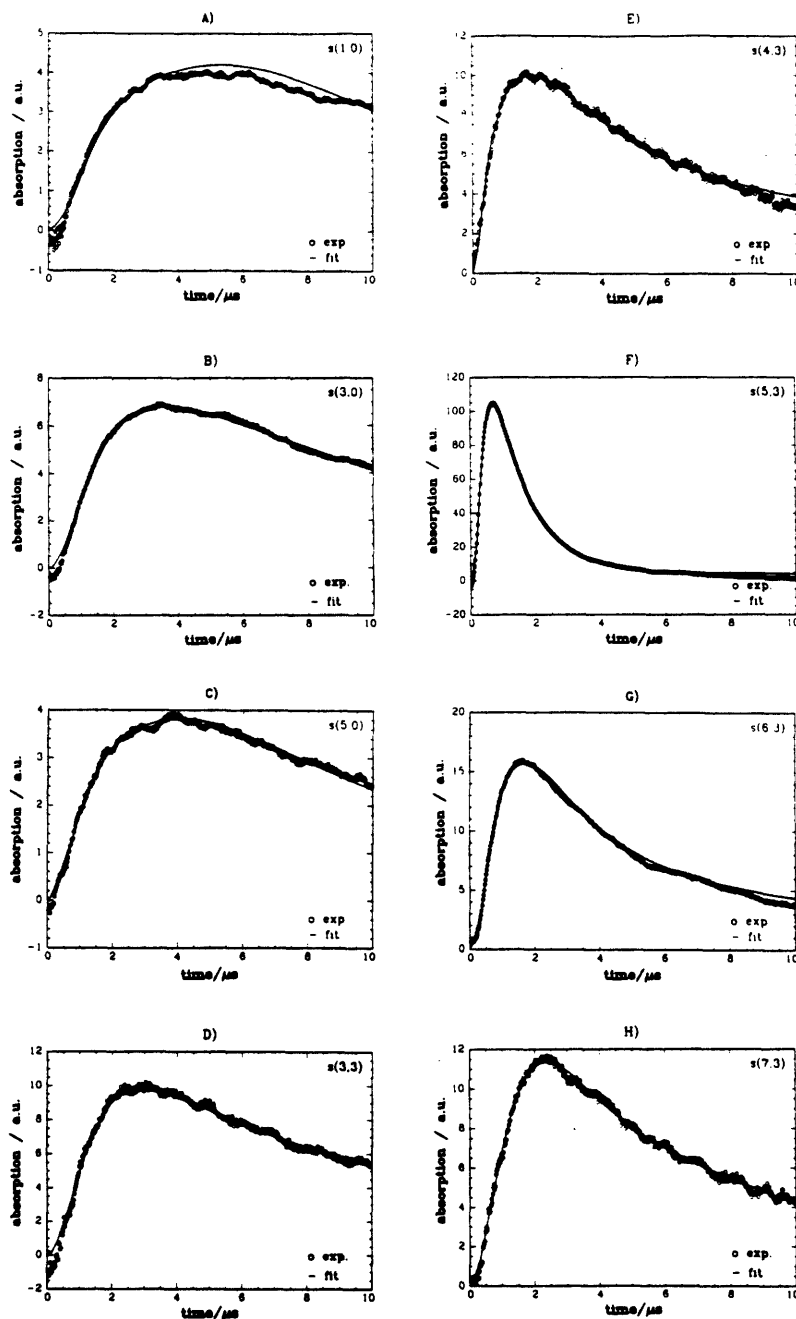


FIG. 4. Three- and four-level DR signals in ammonia (25 mtorr). The $10R(32)$ CO_2 laser line pumps the $s(5,3)$ level in $v_2 = 1$. The levels probed are (a) $s(1,0)$, (b) $s(3,0)$, (c) $s(5,0)$, (d) $s(3,3)$, (e) $s(4,3)$, (f) $s(5,3)$ (showing total relaxation out of pumped level), (g) $s(6,3)$, and (h) $s(7,3)$. The symbols (\circ) are experimental points; the solid curve is the fit to the master-equation model described in the text. Note in panel (f) the slow decrease in absorbance (population) at long times ($> 7 \mu\text{s}$), due to the loss of vibrationally excited molecules resulting from transport out of the beam and $V-T$ relaxation which is not explicitly included in the kinetic model.

tation, and one a - s transition ($J = 6$, $K = 3$) could be probed directly, resulting in a large number of observables compared to the parameters to be determined.

Using this model, we determined rate coefficients $k(a \leftrightarrow s)$, $k(\Delta J, \Delta K = 0)$ and $k(\Delta J, \Delta K = -3)$ for NH_3 - NH_3 and NH_3 -Ar collisions. Even though levels resulting from $\Delta K = +3$ changes were not directly monitored, parameter values could be estimated for these channels in the context of the global model; they make a small but non-negligible contribution to the total relaxation process. The downward rates for the ($\Delta J, \Delta K = 0$) processes were represented by a simple exponential-gap scaling law, but those for ($\Delta J, \Delta K = 3$) processes could not be satisfactorily scaled using either an exponential-gap or power-gap law,⁵⁰⁻⁵² and were therefore fitted individually. The average rate coefficient for the $a \leftrightarrow s$ symmetry changing process was fitted independently. Upward rate coefficients were calculated by detailed balancing. The cutoff for ΔJ in our model was $|\Delta J_{\text{max}}| = 4$, and that for ΔK was $|\Delta K| = 3$; these seemed to be reasonable choices for a polar molecule which might be supposed to follow "dipolelike" propensity rules. We first tried to incorporate the $a \leftrightarrow s$ propensity rule into the model, but we were unable to reproduce the data satisfactorily under this constraint. Ultimately, we allowed both symmetry-changing and symmetry-preserving collisions to take place, with a variable ratio $\beta = k(a \leftrightarrow a)/k(a \leftrightarrow s) = k(s \leftrightarrow s)/k(a \leftrightarrow s)$.

The master equation was integrated numerically with a FORTRAN program using a standard Runge-Kutta algorithm with adaptive step size.⁵³ The system response was

taken into account by convoluting the calculated signal with an experimentally determined response function. Minor losses due to vibrational relaxation and transport out of the detection region have not been included in the model; their effect may be noted in Fig. 4(f).

The parameter values which gave the best overall correspondence with the measured curves for NH_3 - NH_3 collisions, as shown in Figs. 4(a)-(h), are given in Table III, and those for NH_3 -Ar collisions [Figs. 5(a)-(c)], are given in Table IV. In Tables III and IV we also show the sums of the inelastic rate coefficients for two values of the ratio β defined above, viz., $\beta = 1.0$ (symmetry-changing and symmetry-preserving collisions equally likely) and $\beta = 0.7$. While it was not possible to determine a precise value for β , it is nevertheless clear from the fits that a substantial fraction of the rotationally inelastic collisions in $v_2 = 1$ must preserve the (a, s) symmetry, in contradiction to a simple dipole-propensity model. The sums may be compared with the total relaxation rates reported in Table II, $34 \pm 4 \mu\text{s}^{-1} \text{ torr}^{-1}$ for NH_3 - NH_3 collisions, and $8.5 \pm 2 \mu\text{s}^{-1} \text{ torr}^{-1}$ for NH_3 -Ar. Since these relaxation rates, which are eigenvalues of the rate coefficient matrix \mathbf{K} , are always expected to be slightly smaller than the sum Σk_{ij} [Eq. (4)], as a result of "feedback" from populated nearby levels, they furnish a definite, albeit not very precise, lower bound on β of about 0.7 for NH_3 - NH_3 and about 0.6 for NH_3 -Ar.

Once a suitable set of energy-transfer parameters for the $aQ(5,3)$ excitation had been determined, the set of rate coefficients was used to model the experimental traces for $sR(5,0)$ excitation. The calculated curves match the experi-

TABLE III. Energy-transfer parameters for NH_3 - NH_3 rotational energy transfer within $v_2 = 1$ with the initial level: $v_2 = 1, s(5,3)$, at 298 K. The rates given are those for parity-changing collisions (change of inversion level). The parity-conserving transitions are related by the parameter β , which gives the ratio of parity-conserving to parity-changing transitions, and is estimated to be between 0.7 and 1.0.

$\Delta J, \Delta K$	$k_r (\mu\text{s}^{-1} \text{ torr}^{-1})$	$k_p (\text{cm}^3 \text{ s}^{-1})$
Directly observed, rates for parity-changing transitions		
+ 3, 0	0.25	0.08×10^{-10}
+ 2, 0	0.67	0.21
+ 1, 0	3.87	1.22
0, 0	4	1.26
- 1, 0	5.71	1.79
- 2, 0	2.21	0.69
+ 3, - 3	0.12	0.038×10^{-10}
+ 2, - 3	0.29	0.09
+ 1, - 3	0.69	0.22
0, - 3	1.5	0.47
- 1, - 3	1.1	0.35
- 2, - 3	0.90	0.28
- 3, - 3	0.78	0.24
- 4, - 3	0.70	0.22
Predicted by model, rates for parity-changing transitions		
+ 1, + 3	0.80	0.26×10^{-10}
+ 2, + 3	0.35	0.11
+ 3, + 3	0.15	0.05
$\Sigma k_{ij} = 38.1 \mu\text{s}^{-1} \text{ torr}^{-1}$ ($\beta = 1$)		12.2×10^{-10}
$33.9 \mu\text{s}^{-1} \text{ torr}^{-1}$ ($\beta = 0.7$)		

mental traces reasonably well without further adjustment [Figs. 6(a)–(c)], thus providing additional validation of the results obtained from the modeling.

From systematic variation of the rate coefficients, we

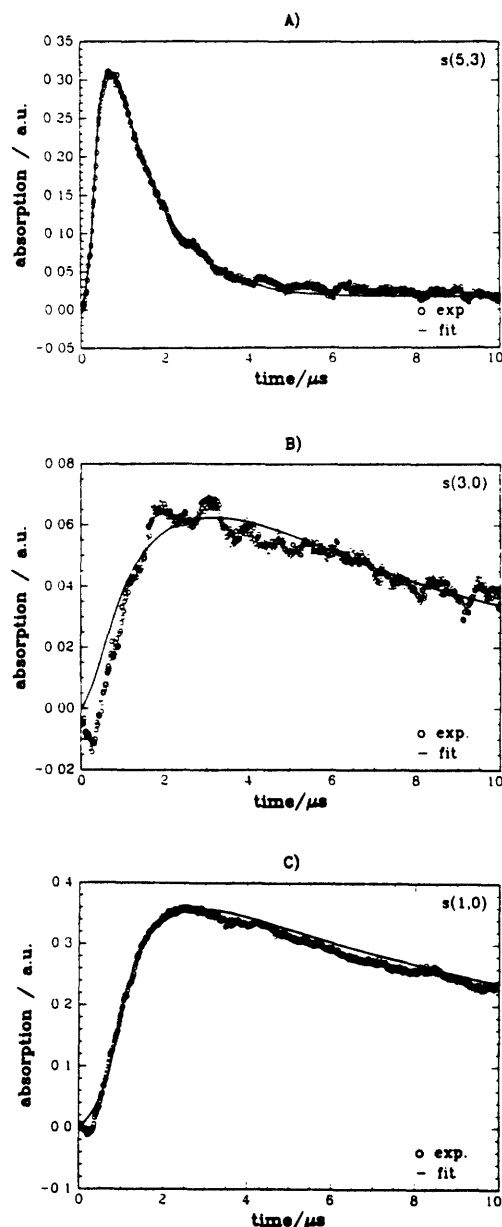


FIG. 5. Three- and four-level DR signals in ammonia-argon mixtures. The 10R(32) CO₂ laser line pumps the $s(5,3)$ level in $v_2 = 1$. The levels probed are (a) $s(5,3)$, 5 mtorr NH₃ + 56 mtorr Ar, showing total relaxation out of pumped level; (b) $s(3,0)$, 25 mtorr NH₃ + 100 mtorr Ar; (c) $s(1,0)$, 16 mtorr NH₃ + 307 mtorr Ar. The symbols (O) are experimental points; the solid curve is the fit to the master-equation model described in the text.

TABLE IV. Energy-transfer parameters for NH₃-Ar rotational energy transfer within $v_2 = 1$ with the initial level: $v_2 = 1, s(5,3)$, at 298 K. The rates given are those for parity-changing collisions (change of inversion level). The parity-conserving transitions are related by the parameter β , which gives the ratio of parity-conserving to parity-changing transitions, and is estimated to be between 0.7 and 1.0.

$\Delta J, \Delta K$	k_r ($\mu\text{s}^{-1} \text{ torr}^{-1}$)	k_o ($\text{cm}^3 \text{ s}^{-1}$)
directly observed, rates for parity-changing transitions		
+ 3, 0	0.15	0.47×10^{-11}
+ 2, 0	0.29	0.91
+ 1, 0	1.07	3.37
0, 0	1.18	3.72
- 1, 0	1.5	4.73
- 2, 0	0.75	2.36
predicted by model, rates for parity-changing transitions		
+ 3, - 3	0.04	0.13×10^{-11}
+ 2, - 3	0.08	0.24
+ 1, - 3	0.18	0.57
0, - 3	0.37	1.16
- 1, - 3	0.29	0.91
- 2, - 3	0.24	0.75
- 3, - 3	0.21	0.65
- 4, - 3	0.19	0.59
predicted by model, rates for parity-conserving transitions		
+ 1, + 3	0.25	0.79
+ 2, + 3	0.12	0.38
+ 3, + 3	0.06	0.18
$\Sigma k_y = 11.1 \mu\text{s}^{-1} \text{ torr}^{-1}$ ($\beta = 1.0$)		35.1×10^{-11}
$9.8 \mu\text{s}^{-1} \text{ torr}^{-1}$ ($\beta = 0.7$)		

have estimated an overall error limit of $\pm 20\%$ for the resulting coefficients, which includes uncertainties due to the simplified model, the cutoff for ΔJ and ΔK , and losses due to vibrational energy transfer and diffusion. The key finding is that in order to reproduce the experimental data, nondipolar energy-transfer processes must be included in the model.

V. DISCUSSION AND CONCLUSIONS

In this work, time-resolved infrared double resonance has been used to obtain a large set of state-to-state rate coefficients for rotational energy transfer in excited NH₃ vibrational states. The state-resolved collisional relaxation of ammonia rotational states in $v_2 = 1$ presents some interesting features, several of which will be considered in this section. The connection of "propensity rules" for J, K, M , and parity-changing collisions with the corresponding intermolecular interaction potentials, and with collision broadening of the $v_2 = 1-0$ infrared transitions, will also be discussed.

A. Total depopulation rates and ground-state recovery rates

The total rotational relaxation and the ground-state recovery rates in NH₃ self-collisions are on the order of three to eight times the corresponding Lennard-Jones collision rates. This is comparable with results for CDF₃,²⁴ another symmetric-top molecule, but much more efficient than rotational relaxation in nonpolar molecules such as CHD₃ (Ref. 55) or spherical tops such as SF₆ (Ref. 56) and ¹³CD₄ (Ref. 13). The mechanism of the interaction between an ammonia

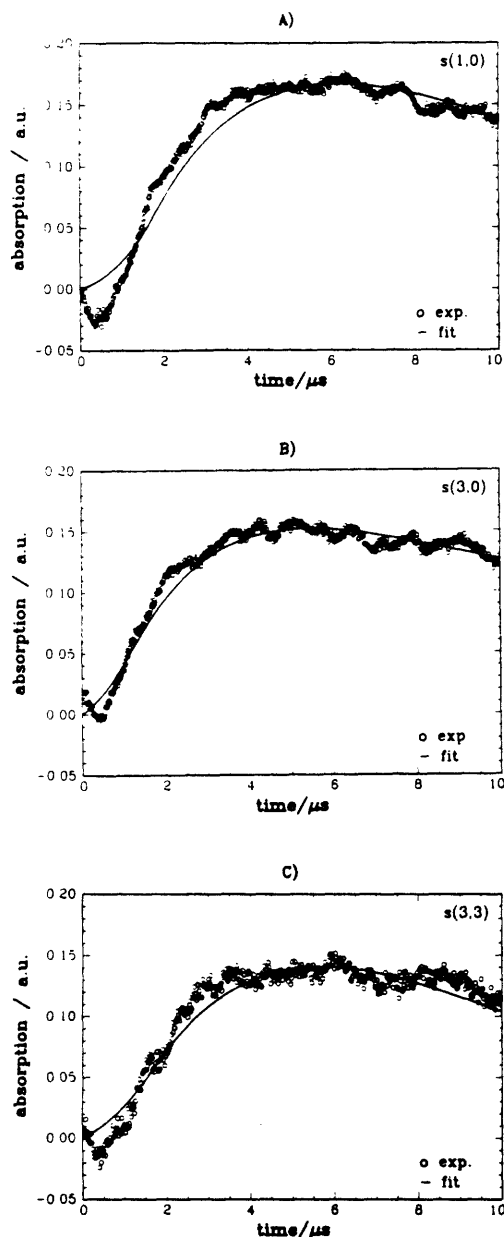


FIG. 6. Four-level DR signals in ammonia. The $9R(30)$ CO_2 laser line pumps (mostly) the $a(6,0)$ level in $v_2 = 1$. The levels probed are (a) $s(1,0)$, 23 mTorr; (b) $s(3,0)$, 33.6 mTorr; and (c) $s(3,3)$, 23 mTorr. The symbols (\circ) are experimental points; the solid curve is the fit to the master-equation model described in the text using the kinetic parameters derived from fitting the $s(5,3)$ data.

molecule and a rare-gas atom is expected to be quite different from that between two polar NH_3 molecules. First, in the NH_3 -rare-gas collisions, the intermolecular interaction is caused by an induced moment or a fluctuation moment

(which leads to a dispersion force) in a rare-gas atom while in the NH_3 - NH_3 collision the main intermolecular interaction is caused by the long-range dipole-dipole force. Second is the effect of rotational resonances between incoming and outgoing channels in collision processes. Although rotational resonances are reduced in $v_2 = 1$ NH_3 colliding with ground-state NH_3 from the pervasive inversion-doublet resonance in ground-state-ground-state collisions, ΔJ resonances, and rotational inelasticity in the perturber are still available to absorb energy, while in the NH_3 -rare-gas case the energy defect must be supplied or dissipated by the translational motion of the rare-gas atom. The cross sections (averaged over thermal velocity distribution) for total depopulation in NH_3 -Ar and NH_3 -He collisions reflect this behavior. However, as will be discussed below, the state-to-state propensity rules differ from those which would be predicted by a simple first-order dipolar interaction.

B. Choice of rotational energy transfer model and rate-constant scaling

When using a kinetic model to determine rate coefficient parameters in a highly coupled system, it is especially important to consider the possible model dependence of the results.^{49,57} The initial picture of rotational energy transfer in NH_3 was a very simple one. In addition to the rigorous propensity rules based on spin statistics, which allow the *ortho* ($K = 3n$) and *para* ($K \neq 3n$) levels to be treated separately, inelastic processes in NH_3 were expected to follow dipolelike behavior, viz., $\Delta J = 0, 1$ and $\Delta K = 0$ with $a \leftrightarrow s$ being the only allowed channels.

Although these "dipolelike" propensity rules for collision-induced transitions are by no means as rigorous as optical selection rules, we expected to be able to model the experimental rotational energy-transfer data with a combination of fast $\Delta J = 0$ and 1, very slow $\Delta K = 3$, and very fast $a \leftrightarrow s$ transitions. However, we could not describe the rotational energy transfer in NH_3 with this model at all. A drastic relaxation of the constraints on the propensity rules resulted in a model which included $a \leftrightarrow a$ and $s \leftrightarrow s$, $\Delta K > 1$, and $\Delta J > 1$ transitions, with probabilities comparable to those of the "dipolelike" transitions. In principle, any level could be accessed by any other level within the nuclear-spin constraint.

An examination of the details of some of the kinetic fits will illustrate the validation of the model described above. If we look at the signal for $s(1,0)$ [Fig. 4(a)], we see an immediate increase in population after the CO_2 laser pulse; after 2 μs , the population of the $s(1,0)$ state has already reached half of its maximum value. If we do not assume ridiculously large cross sections for direct transitions from $s(5,3)$ to $s(1,0)$ (many times larger than the Lennard-Jones cross section), we have to allow for a considerable amount of $\Delta K = 3n$, $\Delta K, \Delta J$ transitions and perhaps $s \leftrightarrow s$ and $a \leftrightarrow a$ transitions. The $s \leftrightarrow s$ and $a \leftrightarrow a$ transitions are even more evident from the $s(4,3)$ and the $s(3,3)$ levels [Figs. 4(d) and 4(e)]. The rapid population of these levels cannot be explained by sequential $a \leftrightarrow s$ and $\Delta J = 1$ transitions. If we allow explicitly for $a \leftrightarrow a$ and $s \leftrightarrow s$ transitions the rate for the $s(5,3) \rightarrow s(4,3)$ or $s(6,3)$ and for $s(5,3) \rightarrow s(5,0)$ are the $\Delta J = 1$ and the

$\Delta K = 3$ transitions, respectively, in a first approximation. The measurement for $a(6,1) \rightarrow s(6,1)$ has been taken as a direct measure for the $a \leftrightarrow s$ transfer.

If we compare the traces for the population of the $s(5,3)$ and $s(4,3)$ or $s(6,3)$ levels, we can see the relative difference in the rates for $\Delta J = 1$ and $\Delta K = 3$ processes. The differences in the features of the population of $s(6,1)$ and the $a(6,1)$ ($a \rightarrow s$ transfer) are small. This means that the rate for $a \rightarrow s$ transfer is of the same order of magnitude than that for $\Delta J = 1$ transfer.

A further verification of the model is obtained by using the unadjusted parameters obtained from simulating the $aQ(5,3)$ excitation to predict the results of $aR(5,0)$ excitation. As Fig. 6 shows, quite satisfactory agreement is obtained.

A fundamental problem in rotational energy-transfer studies on polyatomic molecules is that the number N of levels, and especially the number $N(N-1)/2$ of collisional rates that connect these levels, can be large. Not only would it be difficult to measure all of these rates, it is especially unrealistic to vary every constant individually in simulating these systems. A more practical approach is to calculate the whole rate coefficient matrix by an angular-momentum-based scaling law with a set of basis rate constants. These can be obtained from coupled states, infinite-order sudden, or energy-corrected sudden approximation.⁵⁸ However, to date, the intermolecular potential for the NH_3 system has not been characterized well enough to be able to implement such an approach. Therefore it would be difficult to obtain *ab initio* basis rate constants for this system.

Scaling laws can therefore seldom be used to fit data for polyatomic molecules because there are so many basis rate constants that the number of free parameters in the fit becomes too large. Fitting laws represent the rate constants by simple functions which have a small number of adjustable parameters. For scaling the J -changing rate coefficients in our model, we used a simple and widely used exponential-gap law⁵⁰⁻⁵² (EGL) for downward transitions,

$$k_{l,-j_f} = (2j_f + 1)k_0 \exp[-C(E_i - E_j)/k_B T]. \quad (6)$$

The EGL has been given theoretical respectability by surprisal theory⁵⁹ and quantum-mechanical considerations, although this of course does not constitute a proof of the law. The EGL was found to work reasonably well for scaling the J -changing rates in $\text{NH}_3\text{-NH}_3$ and $\text{NH}_3\text{-Ar}$ collisions.

C. Changes of J , $\Delta K=0$, in $\text{NH}_3\text{-NH}_3$ and $\text{NH}_3\text{-Ar}$ collisions

$\text{NH}_3\text{-NH}_3$. The detailed kinetic analysis provided rate constants and cross sections for J -changing collisions in which $\Delta K = 0$. Surprisingly, there are no simple dipolelike propensity rules. Although the largest cross sections were found for $\Delta J = 1$ transitions, there are also considerable amounts of $\Delta J = 2$ and 3 transitions. The rates for these processes could be scaled well by an EGL with $C = 1.8$ [Fig. 7(a)]. As expected, this is higher than for nonpolar molecules such as methane¹³ ($C = 0.8$) or silane⁶⁰ ($C = 0.05\text{--}0.08$), but it is sufficiently low that "higher-order" transitions with $\Delta J = 2, 3, \dots$ play a non-negligible role in the rota-

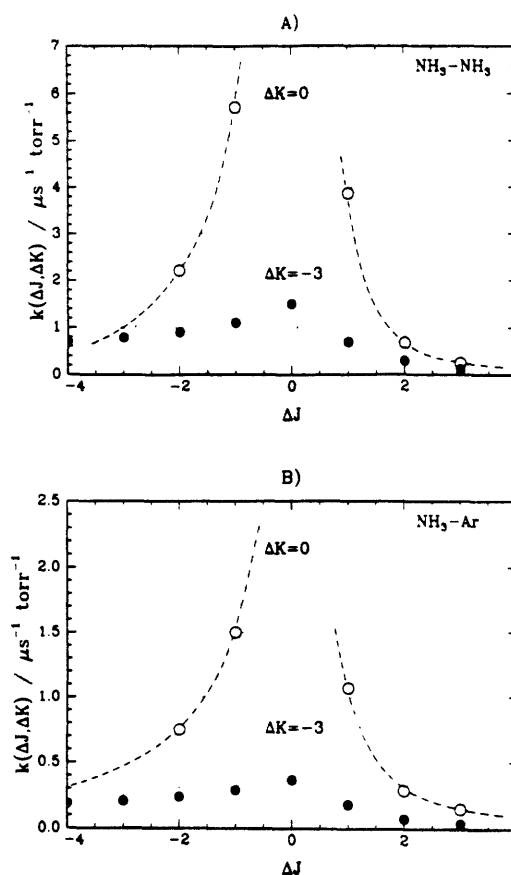


FIG. 7. Rate coefficients for J -changing collisions in (a) $\text{NH}_3\text{-NH}_3$ collisions and (b) $\text{NH}_3\text{-Ar}$ collisions, as a function of ΔJ , with $\Delta K = 0$ (open circles) and 3 (solid circles). The dashed curve shows the EGL fit to the $\Delta K = 0$ rates, with (a) $C = 1.8$ and (b) $C = 1.1$; the dotted curve shows the ECS fit to the $\Delta K = -3$ rates, as described in the text. Note that the estimated error on each rate parameter from the fit of the kinetic equation is approximately $\pm 20\%$.

tional relaxation in the different K stacks. We want to point out that the kinetic analysis unambiguously proves that these transitions are not equivalent to sequential dipolelike transitions with $\Delta J = 1$.

The first state-to-state collision data in the ground state of NH_3 were obtained by Oka *et al.*,² who performed microwave-microwave (MWMWDR) and IR-microwave double-resonance experiments yielding information on collision-induced transitions between two specific J_K inversion doublets. They found that the rotational relaxation of NH_3 in the ground state is governed by dipolelike propensity rules. Any "higher-order" transitions were found to be at least an order of magnitude slower than $\Delta J = 0$ or 1 transitions. In the $v_2 = 1$ state, however, nondipolar transitions make a significant contribution to the relaxation process.

$\text{NH}_3\text{-Ar}$. In the case of $\text{NH}_3\text{-Ar}$ collisions, the propen-

sity rules are expected to be more complicated than in the $\text{NH}_3\text{-NH}_3$ case. Higher-order transitions with $\Delta J > 1$ are expected. The absolute rate constants for $\Delta J = 1$ transitions are considerably reduced compared to the self-relaxation in NH_3 , and the individual rates follow the trend of the total depopulation rates [see Fig. 7(b)]. An EGL parameter $C = 1.1$, deduced from the kinetic model, shows that $\Delta J > 1$ transitions are relatively more probable than in the $\text{NH}_3\text{-NH}_3$ case. The qualitative picture here is in good agreement with the propensity rules derived by Oka from his microwave double-resonance studies.² In the recent experiments of Schliepen and ter Meulen,¹² they find large cross sections for $\Delta J > 1$ transitions (up to $\Delta J = 6$) in the ground state for $\text{NH}_3\text{-He}$ at a collision energy of 54 meV. It is therefore quite reasonable that these transitions occur in the excited states of NH_3 in collisions with argon as well.

D. Changes of J , $\Delta K = 3$, in $\text{NH}_3\text{-NH}_3$ and $\text{NH}_3\text{-Ar}$ collisions

$\text{NH}_3\text{-NH}_3$. From our kinetic model calculations we derived rate constants and cross sections for $\Delta J = 0, 1, \dots, 4$ with $\Delta K = 3$ transitions for $\text{NH}_3\text{-NH}_3$ and $\text{NH}_3\text{-Ar}$ collisions. The results are given in Table IV and Fig. 7(b). Direct evidence for the presence of these transitions is the early population of the $s(5,0)$ and especially the $s(1,0)$ states of NH_3 . The rates for $\Delta J\text{-}\Delta K$ transitions decrease with increasing ΔJ (or energy gap) but not as fast as the pure J -changing collision rates with $\Delta K = 0$. They are always smaller than the corresponding pure J -changing rates. The results indicate that in a J -changing collision with a large J change it becomes more and more probable that K changes as well. These results do not agree with previous results of ground-state MWMWDR experiments in $\text{NH}_3\text{-NH}_3$, in which $\Delta K = 3$ transitions are at least 1 order of magnitude slower than $\Delta J = 0$ and 1. It is not entirely clear why this should be different in $v_2 = 1$. However, Kuze *et al.*²³ found in steady-state IR-IR double-resonance experiments a ratio of 2.5 between the rate for $\Delta J = 1$ and $\Delta K = 3$ transitions. This result agrees well with our observations. A possible explanation for the discrepancy of these experiments and Oka's might be that the effective rate for $\Delta K = 3$ transitions is nearly the same for the upper and the lower levels (whose population difference is monitored in MWMWDR) of an inversion doublet in the ground vibrational state if the $a \leftrightarrow s$ propensity rule does not hold for this process. The probability of $\Delta K = 3$ transitions seems to be larger at low temperatures. Surprisingly, Veeken, Dam, and Reuss¹⁹ found that the $\Delta J = 1$, $\Delta K = 0$ ($J, K = 4, 3 \rightarrow 3, 3$) relaxation in the *ortho* species is not faster than the $\Delta K = 3$ transition ($J, K = 0, 0 \rightarrow 3, 3$) at low jet temperatures.

$\text{NH}_3\text{-Ar}$. Contrary to the self-relaxation results, $\Delta K = 3$ transitions have been expected and are observed for $\text{NH}_3\text{-Ar}$ (rare-gas) collisions. In our case we derived rate constants and cross sections for $\Delta J = 0, 1, \dots, 4$ transitions with $\Delta K = 3$ for $\text{NH}_3\text{-Ar}$ collisions. As with $\text{NH}_3\text{-NH}_3$ collisions, the rates for $\Delta J\text{-}\Delta K$ transitions decrease with increasing ΔJ but not as much as the pure J -changing collision rates with $\Delta K = 0$.

The $\Delta K = 3$ collisional energy transfer that we have ob-

served occurs with rates on the order of $1 \mu\text{s}^{-1} \text{ Torr}^{-1}$, corresponding to very small inelastic cross sections, on the order of 3.5 \AA^2 . The energy-corrected sudden (ECS) approximation^{52,61,62} is applicable to systems in which the ratio of the collision duration to the rotational dephasing time is on the order of 1. For $\text{NH}_3\text{-NH}_3$ transitions between the 5,3 and 4,0 levels, this ratio is about 1, with the collision duration calculated as described in Ref. 61.

Since the collisional parameters for $\Delta K = 3$ are in an appropriate range, the ECS approximation should be applicable to these highly inelastic collisions. In this calculation, for such short-range collisions, we assume a high-order interaction with the potential having a high- n , r^{-n} dependence, and with the amplitudes spread over a wide range of tensor basis rate ranks, L , with little variation as a function of L . We estimated the collision duration from the observed cross sections for the 5,3 to 4,0 levels, giving $\tau_c \sim 0.1$ ps, and scaled the maximum of each curve to the $\Delta J = 0$ rate. As shown for $\text{NH}_3\text{-NH}_3$ in Fig. 7(a), and for $\text{NH}_3\text{-Ar}$ in Fig. 7(b), the ECS approximation correctly predicts the scaling relationship between all of our observed $5,3$ to $J,0$ rates. The slow falloff with J of the rates to $J < 5$ is qualitatively predicted by the ECS scaling law. For the transitions to $J > 5$, the ECS behavior is dominated by the detailed balance correction, and again qualitatively agrees with our experimental data. All of our observed $\Delta K = 3$ rates had been adjusted independently in the fit (Sec. IV C 2), without reference to the expected ECS behavior, so this result provides an unbiased verification of its predictions.⁵²

E. Changes of parity in collisions

The effective rate of $a \leftrightarrow s$ transfer has been measured directly for the transition $s(6,1) \rightarrow a(6,1)$ after population of $a(6,1)$ with the 9R(30) line of the CO_2 laser. The kinetic model, with an average value of $k_{as} = 4 \mu\text{s}^{-1} \text{ torr}^{-1}$, fits the direct measurement very well, as can be seen from Fig. 3. Small variations of symmetry changing rates as a function of J and K have been neglected in the model.

Our value for k_{as} of about $4 \mu\text{s}^{-1} \text{ torr}^{-1}$ is lower than in the vibrational ground state [$50\text{--}80 \mu\text{s}^{-1} \text{ torr}^{-1}$ (Refs. 18(b)–18(d), and 19)], but is more than an order of magnitude higher than that recently reported by Shultz and Wei.²⁰ It is also higher than the $a \leftrightarrow s$ transfer in $v_2 = 2$ (approximately $2 \mu\text{s}^{-1} \text{ torr}^{-1}$),²² although, in that case, the $a \leftrightarrow s$ transfer is probably a sequence of $a \leftrightarrow s$ and $\Delta J = 1$ transitions because the separations between the a and s levels is higher than the J, K spacing. Looking at the trend of this process in the v_2 progression, it is unlikely that the previously reported²⁰ value of $0.2 \mu\text{s}^{-1} \text{ torr}^{-1}$ can be correct.

Most striking, and against all dipolelike behavior, is the fact that we did not find a propensity rule for $a \leftrightarrow s$ processes in rotationally inelastic collisions. We could model the rotational energy transfer only if we relaxed this propensity rule. From our kinetic model we derived a ratio $\beta = k(a \leftrightarrow a) / k(a \leftrightarrow s) = k(s \leftrightarrow s) / k(a \leftrightarrow s) > 0.7$ for both self- and argon collisions. This means that there is no specific (a, s) correlation between states of opposite parity. In the case of ammonia self-relaxation, this is in sharp contrast to the results

inferred from the microwave double-resonance experiments.²

F. Collision rate and pressure-broadening coefficient

The total depopulation rates of the $s(5,3)$ level in $v_2 = 1$ and the ground-state recovery rate in $a(5,3)$ can be related to measurements of the pressure-broadening coefficients γ/p in the ammonia v_2 infrared band²⁴⁻²⁷ using the generally accepted relation^{63,64}

$$\gamma/p(\text{MHz/torr}) = (1/2\pi)(k_u + k_l)/2;$$

that is, the broadening rate is the average of the inelastic collision rates k_u and k_l , expressed in $\mu\text{s}^{-1} \text{ torr}^{-1}$, in the upper and lower levels of the spectroscopic transition. This relation assumes no contribution from inelastic dephasing or other non-state-changing processes.

For ammonia self-broadening, measurements²⁴⁻²⁷ on rotational levels in the v_2 fundamental comparable to those studied in this work yield values of 13.4 [for the $aR(0,0)$ line²⁷] to 22 MHz/Torr, and 8–10 MHz/torr for the $2v_2-v_2$ hot-band lines. Use of our measured values for ground-state recovery and excited-state depopulation (Table II) in the preceding relation would predict broadening coefficients of about 9 MHz/torr, around 40% smaller than the experimental values. We believe that the explanation of this difference most consistent with existing data is a significant elastic contribution in the $v_2 = 1$ and $v_2 = 2$ levels to the linewidths, but not in the ground state. Our observed ground-state depopulation rate of $80 \mu\text{s}^{-1} \text{ torr}^{-1}$ is in close agreement with the microwave T_2/T_1 measurements of Schwendeman *et al.*^{18(b)-18(d)} if a zero contribution from adiabatic processes is assumed, and our phenomenological rate is assumed to correspond to the rate of population transfer out of the combined inversion doublet pair. Schwendeman's measurements also indicate that, for high J levels, the sum of adiabatic processes and processes leaving the inversion doublet levels is less than 5% of the linewidth. Since the adiabatic contribution should depend only weakly on J , we infer a small contribution to low J levels from adiabatic collisions. Furthermore, a zero or very small adiabatic contribution in the ground state is in accord with Schwendeman's Anderson theory and sudden approximation calculations.^{18(b)} Supporting Schwendeman's high J measurements, the line-mixing measurements of Henck and Lehmann⁶⁵ indicate that a large fraction of the linewidth for both $J = 4$ and $J = 8$ is due to the sum of elastic and inversion-doublet transitions. Even if k_l in the linewidth expression is set to the microwave value of 18.4 MHz/Torr (which would include any adiabatic contribution), the resulting values for γ are lower than the observed linewidths. This indicates that elastic processes make a significant contribution to relaxation in $v_2 = 1$ even though that contribution is negligible in $v_2 = 0$. A similar situation occurs in the $2v_2-v_2$ hot band, indicating adiabatic contributions in both $2v_2$ and v_2 . The triple-resonance measurements²² yielded only a lower bound on the $v_2 = 2$ relaxation rate, $> 3 \mu\text{s}^{-1} \text{ torr}^{-1}$; if we assume that the relaxation rate in $v_2 = 2$ is the same as that in $v_2 = 1$, $34 \mu\text{s}^{-1} \text{ torr}^{-1}$, we can estimate an upper bound for the inelastic contribution to the $2v_2-v_2$ broadening rate of 5.4 MHz/torr.

For hydrogen-,²⁵ nitrogen-,²⁴ and argon-broadening,²⁴ the coefficients are ~ 3 , 2.9–4.3, and 1.3–1.9 MHz/torr, respectively, for transitions between levels with J and K similar to those studied in this work. While we were able to obtain excited-state depopulation rates (see Table II), we did not obtain precise ground-state recovery rates for these gases as collision partners. Ground-state recovery rates about twice as large as the excited-state depopulation rates, as in ammonia self-collisions, would allow the foreign-gas line-broadening rates to be accounted for by the average of the inelastic collision rates in the upper and lower spectroscopic levels, in accordance with the standard model.^{63,64}

A similar situation obtains for ozone, which has also been studied in our laboratory.⁶⁶ For that system, the self-broadening coefficient is about 20% larger than that which would be determined from upper- and lower-level relaxation rates measured by TRIRDR spectroscopy, while foreign-gas (nitrogen, oxygen) broadening can be accounted for in terms of these rates. In the case of d_4 -methane, in which the inelastic collision rates are smaller than for polar species such as ozone or ammonia, the measured⁶⁷ self- and argon-Raman broadening coefficients are 30%–60% larger than the averaged relaxation rate.

These results can be understood if we interpret the discrepancies as contributions of elastic collision processes to the pressure-broadening coefficient. Since the time-resolved measurements probe the population difference of states, and thus the inelastic part of the collision process, while measurements in the frequency domain reflect the sum of all elastic and inelastic processes, it may be expected that the pressure-broadening coefficient will be greater than the corresponding inelastic collision rate whenever elastic processes are non-negligible. Recognition of this point may influence future theoretical calculations of pressure-broadening coefficients, which often neglect the elastic, or nonstate-changing, processes.⁶⁸ Analysis of the temperature dependence of the linewidths and relaxation rates would also be of interest, particularly in connection with remote sensing of the atmospheres of the outer planets.⁹

G. State-to-state rate constants and the intermolecular interaction potential

The rotational energy transfer of ammonia in self-collisions and collisions with rare-gas atoms, N_2 and H_2 , has been the subject of many experimental and theoretical investigations in the past. One principal goal of these studies is the determination of the intermolecular potential of the collision partners.^{11,69,70} It is obvious that this can only be done by the measurement of state-to-state rate constants and cross sections. Knowing the state-to-state inelastic cross sections or rate constants from experiment, it should be possible to construct the intermolecular potential by fitting the calculated cross sections to the experimental values. This "potential modeling" based on theoretical calculations will provide insight into the dynamics of the intermolecular collision process.

A detailed evaluation of the potential-energy surface parameters of the two collision partners (NH_3 , Ar) is, in principle, possible¹¹ although not trivial for polyatomic collision

partners. Even without a detailed treatment it is possible to get a qualitative picture about the nature of the intermolecular forces by a careful examination of the cross sections for different processes and propensities obtained. In the following we try to explain the observed cross sections for ΔJ and ΔK and parity-changing collisions in terms of contributions of the different terms of the multipole expansion of the interaction potential.

One method for the description for the potential surface is the Hartree-Fock dispersion model (HFD).^{11,69,70} In this model the interaction energy is partitioned into a Hartree-Fock energy contribution, obtained from accurate self-consistent-field calculations and a correlation energy contribution, which is in turn approximated by a damped multipolar dispersion expansion.^{11,69,70} In the following section we want to discuss briefly which information can be obtained from state-resolved bulk experiments that can serve as first input data for the calculations mentioned above.

In our present investigations we extracted effective state-to-state rotational energy-transfer (RET) rates which can be converted into velocity-averaged cross sections (averaged over the thermal relative-velocity distribution). While the total depopulation cross sections are most sensitive to the total range of interaction (isotropic part of the interaction potential), the single state-to-state rates are sensitive to the anisotropic part of the potential as well. Different $\Delta J, \Delta K$ processes of NH_3 in collisions with NH_3 or Ar are correlated with different interaction forces and different "characters" of the collision process. The character of the collision process is sometimes expanded in an S matrix or tensor opacity decomposition which indicates the multipole nature of the collision-induced transitions, as is done in recent work on H_2CO .⁷¹ The multiplicity of pathways in NH_3 , $v_2 = 1$ relaxation makes it impossible to apply that method quantitatively.

In the following we want to examine the different cross sections obtained in the experiments and to correlate the cross sections and the multipole nature of the interaction potential. Since dipole, quadrupole, octopole, or higher-order multipole interactions have different ranges, and different induced transitions in the first Born approximation, the measurements of the different processes through observing different levels in $v_2 = 1$, probe different parts of the interaction potential.

Oka^{2(f)} pointed out that, for a dipolar absorber, collision-induced transitions following $+\leftrightarrow-$ and $\Delta J = 0, 1$ ($\Delta K = 0$) are expected in first order. The "selection rules" $\Delta J = 0, 1, 2$ and $s(a) \leftrightarrow s(a)$ and $\Delta J = 0, 1, 2, 3$, $s \leftrightarrow a$, $\Delta K = 0, 3$ hold for quadrupole and octopole transitions, respectively. Expected propensities for a second-order dipole transition would be $\Delta J = 0, 1, 2$ and $s(a) \leftrightarrow s(a)$, $\Delta K = 0$. Generally, for an n -order process the "selection rule" would be $a(s) \leftrightarrow a(s)$ if n is even and $a \leftrightarrow s$ if n is odd and $\Delta J = 1, 2, \dots, n$, $\Delta K = 0$. Furthermore, according to Oka,^{2(e)} a $(2^n\text{-pole})_1 - (2^m\text{-pole})_2$ interaction gives $a(s) \leftrightarrow a(s)$ transitions for even n and $s \leftrightarrow a$ transitions for odd n in molecule 1. A $(2^n\text{-pole})_1 - (2^m\text{-pole induced dipole})_2$ interaction causes $a(s) \leftrightarrow a(s)$ for even $n + m$ and $s \leftrightarrow a$ transitions for odd $m + n$.

We believe that the rather unsystematic parity selection rule in $\text{NH}_3 - \text{NH}_3$ and $\text{NH}_3 - \text{Ar}$ collisions obtained in our experiments cannot be explained by any single interaction mentioned above. In the case of $\text{NH}_3 - \text{NH}_3$ collisions the leading term in the multipole expansion is certainly the dipole term. The cross sections obtained for $s \leftrightarrow a$ and $\Delta J = 0, 1$ are the largest. This was verified by a direct measurement of the $s(6, 1)$ and $s(5, 1)$ levels for $a(6, 1)$ excitation (9R 30). On the other hand, we derive from direct measurements of the $s(4, 3)$ and $s(6, 3)$ with $s(5, 3)$ excitation (10P 32) that $s \leftrightarrow s$ transitions in the case of $\Delta J = 1$ are fast as well. Without a fast tunneling process during the collision duration,¹² these transitions can be regarded as quadrupolar transitions with probabilities, according to the cross sections we obtained, on the same order as the dipolar transitions. Similarly, for $\Delta J = 2$, $\Delta K = 0$, transitions, the probability for $s(a) \leftrightarrow s(a)$ and $s \leftrightarrow a$ transitions are almost the same. The $s(a) \leftrightarrow s(a)$ transitions correspond most closely to a high-order dipole or a quadrupole transition (or the dispersion interaction of r^{-6}) and the $s \leftrightarrow a$ to an octopolar transition. In case of $\Delta J = 3$, $\Delta K = 0$, the different $a(s) \leftrightarrow a(s)$ and $s \leftrightarrow a$ transitions can be regarded as higher-order dipole, or octopole or higher multipole interactions. These multipolar arguments apply only to transitions in the same "K stack." For $\Delta J, \Delta K$ transitions, octopolar interactions, a vibrational-mixing-induced dipole⁷²⁻⁷⁴ ($\Delta J = 0, 1$ only), or the dispersion interaction of r^{-7} , are necessary to account for a change of K by 3 and simultaneous change in J . In the case of $\text{NH}_3 - \text{Ar}$ collisions, similar arguments are possible in terms of $(2^n\text{-pole})_1 - (2^m\text{-pole induced dipole})_2$ interactions.

In summary, we want to point out that by probing different states in the $K = 0$ ($\Delta K = -3$) and $K = 3$ ($\Delta K = 0$) "stacks" in $v_2 = 1$ we are able to probe the short-range and long-range parts of the interaction potential. We are of course aware of the problems of converting the data obtained into potential surface parameters, but it seems to be clear that higher terms in the multipole expansion play a considerable role in the RET behavior of NH_3 in collisions with other molecules. Therefore one has to consider carefully where to truncate the expansion terms in the interaction potential expression in a calculation of NH_3 RET cross sections.

Our conclusion is that the rotational relaxation of NH_3 by NH_3 and by Ar have significant contributions from "hard" collisions. During a collision the molecules approach sufficiently close that the interaction is strong enough to cause the nondipolar transitions that we unambiguously observed. In these collisions, information about the initial state (J, K parity) is almost completely lost.

This behavior in $v_2 = 1$ is in contrast to the collision behavior in the vibrational ground state where dipolar $a \leftrightarrow s$ and $\Delta J = 1$ transitions dominate rotational energy transfer. In this case the collisions are "soft" collisions. Parity-changing [$s(a) \leftrightarrow a(s)$] transitions can be induced by the smallest long-range perturbation due to the small energy gap of the inversion doublets.

The information about the real "nature" of the collision process between NH_3 and NH_3 (Ar) in $v_2 = 1$ can at this point only be qualitative; however, our results show that the interactions in both $\text{NH}_3 - \text{NH}_3$ and $\text{NH}_3 - \text{Ar}$ collisions are

not due to one single multipole or multipole-(induced multipole) interaction and that rotational energy transfer is not governed by simple dipolar "selection rules." The obtained cross sections are, in any case, a critical test and a benchmark for any quantum-dynamical calculation.

ACKNOWLEDGMENTS

This work was supported by NASA Office of Space Science and Applications Upper Atmosphere Research Program Grant No. NAGW-1667 and Planetary Atmospheres Program Grant No. NAGW-2387, and by NSF Grant No. CHE89-14953 to the G. R. Harrison Spectroscopy Laboratory. B. A. has been supported by a fellowship from the Deutsche Forschungsgemeinschaft. S.L.C. has been supported by the Donors to Petroleum Research Fund, administered by the American Chemical Society. We thank Dr. G. Millot and M. G. Fanjoux of the Laboratoire de Spectrométrie Moleculaire, Université de Bourgogne, Dijon, France, for carrying out a fit of the exponential-gap scaling law similar to that shown in Fig. 5, and for cordial discussions. We dedicate this paper to Professor Takeshi Oka on the occasion of his 60th birthday and thank him for insightful comments on the paper.

- ¹ For reviews of early work on this system, see J. I. Steinfeld and P. L. Houston, in *Laser and Coherence Spectroscopy*, edited by J. I. Steinfeld (Plenum, New York, 1978), pp. 1-123; T. G. Schmalz and W. H. Flygare, *ibid.*, pp. 125-196.
- ² (a) T. Oka, *J. Chem. Phys.* **45**, 754 (1966); (b) **47**, 13, 4852 (1967); (c) **48**, 4919 (1968); (d) **49**, 3135 (1968); (e) P. W. Daly and T. Oka, *ibid.*, **53**, 3272 (1970); (f) T. Oka, *Adv. At. Mol. Phys.* **9**, 12, (1973); (g) A. R. Fabris and T. Oka, *J. Chem. Phys.* **56**, 3168 (1972); (h) T. Oka, in *Interstellar Molecules*, edited by B. H. Andrews (IAU, 1980), p. 221; (i) A. R. Fabris and T. Oka, *J. Chem. Phys.* **78**, 3462 (1983).
- ³ (a) J. M. Levy, J. H.-S. Wang, S. G. Kukolich, and J. I. Steinfeld, *Phys. Rev. Lett.* **29**, 395 (1972); (b) J. H.-S. Wang, J. M. Levy, S. G. Kukolich, and J. I. Steinfeld, *Chem. Phys.* **1**, 141 (1972); (c) G. M. Dobbs, R. H. Micheels, J. I. Steinfeld, J. H.-S. Wang, and J. M. Levy, *J. Chem. Phys.* **63**, 1904 (1975).
- ⁴ (a) T. Shimizu and T. Oka, *J. Chem. Phys.* **53**, 2536 (1970); (b) T. Shimizu and T. Oka, *Phys. Rev. A*, **2**, 1177 (1970).
- ⁵ J. M. Levy, J. H.-S. Wang, S. G. Kukolich, and J. I. Steinfeld, *Chem. Phys. Lett.* **21**, 598 (1973).
- ⁶ A. Das and C. H. Townes, *J. Chem. Phys.* **85**, 179 (1986).
- ⁷ S. Kano, T. Amano, and T. Shimizu, *Chem. Phys. Lett.* **25**, 119 (1974).
- ⁸ J. A. Silver, D. S. Bomse, and A. C. Stanton, *Appl. Opt.* **30**, 1505 (1991).
- ⁹ Proceedings of the Conference on Laboratory Research for Planetary Atmospheres, Bowie, Maryland, 1989, edited by T. R. Spilker and V. R. Eshleman (unpublished); P. Varanasi, *J. Quantum Spectrosc. Radiat. Transfer* **39**, 13 (1988).
- ¹⁰ D. B. M. Klaassen, J. M. H. Reijnders, J. J. ter Meulen, and A. Dymanus, *J. Chem. Phys.* **76**, 3019 (1982); D. B. M. Klaassen, J. J. ter Meulen, and A. Dymanus, *ibid.*, **77**, 4972 (1982); **78**, 767 (1983).
- ¹¹ G. Ebel, R. Krohne, H. Meyer, U. Buck, R. Schinke, T. Seeleman, P. Andresen, J. Schliepen, J. J. ter Meulen, and G. H. F. Dierksen, *J. Chem. Phys.* **93**, 6419 (1990); H. Meyer, U. Buck, R. Schinke, and G. H. F. Dierksen, *ibid.*, **84**, 4976 (1986).
- ¹² J. Schliepen and J. J. ter Meulen (unpublished).
- ¹³ B. Foy, J. Hetzler, G. Millot, and J. I. Steinfeld, *J. Chem. Phys.* **88**, 6838 (1988).
- ¹⁴ J. R. Hetzler and J. I. Steinfeld, *J. Chem. Phys.* **92**, 7135 (1990).
- ¹⁵ C. Flannery, Y. Mizugai, J. I. Steinfeld, and M. N. Spencer, *J. Chem. Phys.* **92**, 5164 (1990).
- ¹⁶ D. J. Danagher and J. Reid, *J. Chem. Phys.* **86**, 5449 (1987).
- ¹⁷ P. Dube and J. Reid, *J. Chem. Phys.* **90**, 2892 (1989).
- ¹⁸ (a) Y. Matsuo, S. K. Lee, and R. H. Schwendeman, *J. Chem. Phys.* **91**, 3948 (1989); (b) K. L. Peterson and R. H. Schwendeman, *ibid.* **75**, 5662 (1981); (c) T. Amano, T. Amano, and R. H. Schwendeman, *ibid.* **73**, 1238 (1980); (d) T. Amano and R. H. Schwendeman, *ibid.* **65**, 5133 (1976).
- ¹⁹ K. Veeken, N. Dam, and J. Reuss, *Chem. Phys.* **100**, 171 (1985).
- ²⁰ M. J. Shultz and J. Wei, *J. Chem. Phys.* **92**, 5951 (1990).
- ²¹ T. Seelemann, P. Andresen, and E. W. Rothe, *Chem. Phys. Lett.* **146**, 82 (1988).
- ²² B. Abel, J. J. Klaassen, S. L. Coy, and J. I. Steinfeld, *Spectrochim. Acta* **47A**, 973 (1991).
- ²³ H. Kuze, H. Jones, M. Tsukakoshi, A. Minoh, and M. Takami, *J. Chem. Phys.* **80**, 4222 (1984).
- ²⁴ D. H. Beckwith, D. J. Danagher, and J. Reid, *J. Mol. Spectrosc.* **121**, 209 (1987).
- ²⁵ J. S. Margolis and S. Sarangi, *J. Quantum Spectrosc. Radiat. Transfer* **16**, 405 (1976).
- ²⁶ (a) G. Baldacchini, S. Marchetti, V. Montelatici, G. Buffa, and O. Tarrini, *J. Chem. Phys.* **76**, 5271 (1982); (b) G. Baldacchini, A. Bizzarri, L. Nencini, G. Buffa, and O. Tarrini, *J. Quantum Spectrosc. Radiat. Transfer* **42**, 423 (1989).
- ²⁷ T. Shimizu, F. O. Shimizu, R. Turner, and T. Oka, *J. Chem. Phys.* **55**, 2822 (1971).
- ²⁸ C. Flannery, J. J. Klaassen, M. Gojer, J. I. Steinfeld, M. Spencer, and C. Chackerian, Jr., *J. Quantum Spectrosc. Radiat. Transfer* **46**, 73 (1991).
- ²⁹ G. Guelachvili and K. N. Rao, *Handbook of Infrared Standards* (Academic, New York, 1986).
- ³⁰ H. Jones, *Appl. Phys.* **15**, 261 (1978).
- ³¹ M. Fourier and M. Redon, *Appl. Phys. Lett.* **21**, 463 (1972); M. Redon, H. Gurel, and M. Fourrier, *Chem. Phys. Lett.* **30**, 99 (1975).
- ³² S. M. Freund and T. Oka, *Appl. Phys. Lett.* **21**, 60 (1972).
- ³³ R. V. Ambartzumyan, V. S. Letokhov, G. N. Makarov, and A. A. Puzetkii, *JETP Lett.* **15**, 501 (1972); **17**, 63 (1973).
- ³⁴ Ph. Avouris, M. M. T. Loy, and I. Y. Chan, *Chem. Phys. Lett.* **63**, 624 (1979).
- ³⁵ J. D. Campbell, G. Hancock, J. B. Halpern, and K. H. Weige, *Chem. Phys. Lett.* **44**, 404 (1976).
- ³⁶ Yu. A. Kuritsyn, G. N. Makarov, V. R. Mironenko, and I. Pak, *Opt. Spektrosk. (USSR)* **69**, 543 (1990).
- ³⁷ J. Eggleston, J. Dallarossa, W. K. Bischel, J. Bokor, and C. K. Rhodes, *J. Appl. Phys.* **50**, 3867 (1979).
- ³⁸ H. D. Morrison, J. Reid, and B. K. Garside, *Appl. Phys. Lett.* **45**, 321 (1984).
- ³⁹ A. N. Bobrovskii, A. A. Vedenov, A. V. Kozhevnikov, and D. N. Soblenko, *JETP Lett.* **29**, 536 (1979).
- ⁴⁰ P. Pinson, A. Delage, G. Girard, and M. Michon, *J. Appl. Phys.* **52**, 2634 (1981).
- ⁴¹ S. Urban, D. Papousek, J. Kauppinen, K. Yamada, and G. Winnewisser, *J. Mol. Spectrosc.* **101**, 1 (1983).
- ⁴² S. Urban, R. D'Cunha, K. N. Rao, and D. Papousek, *Can. J. Phys.* **62**, 1775 (1984).
- ⁴³ S. Urban, V. Spirko, D. Papousek, R. S. McDowell, N. G. Nereson, S. P. Belov, L. I. Gershstein, A. V. Maslovskij, A. F. Krupnov, J. Curtis, and K. N. Rao, *J. Mol. Spectrosc.* **79**, 455 (1980).
- ⁴⁴ H. O. Everett and F. C. De Lucia, *J. Chem. Phys.* **92**, 6480 (1990).
- ⁴⁵ F. Menard-Bourcin and L. Doyennette, *J. Chem. Phys.* **88**, 5506 (1988).
- ⁴⁶ I. Oppenheim, K. E. Shuler, and G. H. Weiss, *Adv. Mol. Relaxation Processes* **1**, 13 (1967-68).
- ⁴⁷ I. Oppenheim, K. E. Shuler, and G. H. Weiss, *Stochastic Processes in Physical Chemistry: The Master Equation* (MIT, Cambridge, MA, 1977).
- ⁴⁸ J. I. Steinfeld, J. S. Francisco, and W. L. Hase, *Chemical Kinetics and Dynamics* (Prentice-Hall, Englewood Cliffs, NJ, 1989), pp. 474-488.
- ⁴⁹ B. J. Orr, *Int. Rev. Phys. Chem.* **9**, 67 (1990).
- ⁵⁰ T. Brunner and D. Pritchard, *Adv. Chem. Phys.* **50**, 589 (1982).
- ⁵¹ A. J. McCaffery, M. J. Proctor, and B. J. Whitaker, *Annu. Rev. Phys. Chem.* **37**, 223 (1986).
- ⁵² J. I. Steinfeld, P. Ruttenberg, G. Millot, G. Fanjoux, and B. Lavorel, *J. Phys. Chem.* **95**, 9638 (1991).
- ⁵³ W. H. Press, B. P. Flannery, S. A. Teukolsky, and W. T. Vetterling, *Numerical Recipes (FORTRAN)* (Cambridge University, Cambridge, 1985).
- ⁵⁴ D. Harradine, B. Foy, L. Laux, M. Duba, and J. I. Steinfeld, *J. Chem. Phys.* **81**, 4267 (1984).
- ⁵⁵ J. J. Klaassen and B. Abel (unpublished).
- ⁵⁶ C. C. Jensen, T. G. Anderson, C. Reiser, and J. I. Steinfeld, *J. Chem.*

- Phys. 71, 3648 (1979); M. Dubs, D. Harradine, E. Schweitzer, and J. I. Steinfeld, *ibid.* 77, 4267 (1984).
- ⁵⁷ F. Temps, S. Halle, P. H. Vaccaro, R. W. Field, and J. L. Kinsey, *J. Chem. Soc. Faraday Trans. 2* 84, 1457 (1988).
- ⁵⁸ *Atom-Molecule Collision Theory: A Guide for the Experimentalist*, edited by R. B. Bernstein (Plenum, New York, 1979), pp. 259-375.
- ⁵⁹ I. Procaccia and R. D. Levine, *J. Chem. Phys.* 63, 4261 (1975); M. Rubinson and J. I. Steinfeld, *Chem. Phys.* 4, 167 (1975).
- ⁶⁰ J. R. Hetzler and J. I. Steinfeld, *J. Chem. Phys.* 92, 7135 (1990).
- ⁶¹ A. E. DePristo, A. D. Augustin, R. Ramaswamy, and H. Rabitz, *J. Chem. Phys.* 74, 5037 (1981).
- ⁶² T. A. Brunner, N. Smith, A. W. Karp, and D. E. Pritchard, *J. Chem. Phys.* 74, 3324 (1981).
- ⁶³ A. E. DePristo and H. Rabitz, *J. Chem. Phys.* 69, 902 (1978).
- ⁶⁴ A. E. DePristo and H. Rabitz, *J. Quantum Spectrosc. Radiat. Transfer* 22, 65 (1979).
- ⁶⁵ S. Henck and K. K. Lehmann, *Chem. Phys. Lett.* 144, 281 (1988).
- ⁶⁶ C. C. Flannery and J. I. Steinfeld, *J. Chem. Phys.* (in press).
- ⁶⁷ G. Millot, B. Lavorel, and J. I. Steinfeld, *J. Quantum Spectrosc. Radiat. Transfer* (in press).
- ⁶⁸ A. Levy, N. Lacombe, and C. Chackerian, Jr., in *Spectroscopy of the Earth's Atmosphere and Interstellar Molecules*, edited by K. N. Rao and A. Weber (Academic, New York, in press), and references therein.
- ⁶⁹ C. Douketis, J. M. Hutson, B. J. Orr, and G. Scoles, *Mol. Phys.* 52, 763 (1984).
- ⁷⁰ R. Alrichs, R. Penco, and G. Scoles, *Chem. Phys.* 19, 119 (1979).
- ⁷¹ S. L. Coy, S. Halle, J. L. Kinsey, and R. W. Field, *J. Mol. Spectrosc.* (in press).
- ⁷² T. Oka, F. O. Shimizu, T. Shimizu, and J. K. G. Watson, *Astrophys. J.* 165, L15-19.
- ⁷³ T. Oka, in *Molecular Spectroscopy: Modern Research, Vol. II* (Academic, New York, 1976), p. 229.
- ⁷⁴ D. Laughton, S. M. Freund, and T. Oka, *J. Mol. Spectrosc.* 62, 263 (1976).

Appendix Two

"Overtone and hot-band assignments in the $2\{v_3, v_6\}$ levels of CHD_3 "

J. Chem. Phys. **100**, 5508 (1994).

Overtone and hot-band assignments in the $2\{\nu_3, \nu_6\}$ levels of CHD_3

Ch. Roche^{a)} and J.-P. Champion

Laboratoire de Spectronomie Moléculaire et Instrumentation Laser, Unité Associée au CNRS No 777, Université de Bourgogne, 6 bd Gabriel, 21000 Dijon, France

S. L. Coy, J. J. Klaassen, and J. I. Steinfeld

Department of Chemistry and G. R. Harrison Spectroscopy Laboratory, Massachusetts Institute of Technology, Cambridge, Massachusetts 02139

A. Valentin

Laboratoire de Physique Moléculaire et Applications, Université de Paris, Tour 13, Jussieu, Paris, France

Y. Mizugai

Faculty of Science and Technology, Sophia University, Tokyo, Japan

J. W. C. Johns

Herzberg Institute of Astrophysics, National Research Council of Canada, Ottawa, Ontario K1A 0R6, Canada

(Received October 18 1993; accepted 4 January 1994)

Assignments have been carried out for the $2\nu_3/(\nu_3 + \nu_6)/2\nu_6$ (triad)—ground state overtone bands and the triad— ν_3/ν_6 hot-band system of CHD_3 . A vibrational extrapolation method, using correspondences between a spherical-tensor formalism and the more conventional description of symmetric-rotor spectra, was used to facilitate the assignment and analysis of these bands. The resulting assignments have been confirmed by time-resolved double-resonance measurements.

I. INTRODUCTION

The way that collisions affect the internal levels of atoms and molecules is both of fundamental interest for our understanding of scattering theory and the intermolecular potential,¹ and of considerable importance for numerous applications. The study of such collision processes at the state-to-state level² requires as a prerequisite a detailed spectroscopic analysis of the molecule under study. This is necessary for the precise assignment of pumped and probed vib-rotational levels, and it is also essential for proper interpretation of energy-transfer pathways and propensity rules.

Previous infrared double resonance investigations of energy transfer in the spherical top molecules $^{13}\text{CD}_4$ (Ref. 3) and SiH_4 (Ref. 4) have shown that there is a high degree of selectivity in which rotational states receive population from an initially populated state. A recent theoretical proposal^{5,6} has linked these observations to a collisional energy transfer propensity rule derived from the Harter-Patterson^{7,8} theory of spectral clustering in spherical top molecules. Harter-Patterson theory allows us to assign a cluster quantum number, k_R , for those rotational states associated with deformations of the spherical rotor to a symmetriclike rotor. In this case, the new propensity rule relates k_R to the symmetric top propensity rule, $\Delta K = mn$, which allows collisional transitions in which the angular momentum K changes by an integer multiple (m) of the order of the symmetry axis (n). For rotational states that are not involved in clusters, the propensity rules may be more subtle and have to be investigated.

In order to explore the relationship of molecular symmetry to energy transfer pathways, we have been carrying out time-resolved infrared pump/probe double-resonance experi-

ments on CHD_3 . CHD_3 is an oblate symmetric-top molecule ($A_0 = B_0 = 3.279 \text{ cm}^{-1}$, $C_0 = 2.629 \text{ cm}^{-1}$; $\kappa = +1$)⁹ and its energy level structure is that expected for such a molecule. However, its permanent dipole moment $\mu_0 = 0.006 \text{ D}$,^{10,11} so long-range dipole-dipole intermolecular interactions should not dominate the energy transfer processes, as is the case for many symmetric tops. Rather, short-range interactions, such as those expected for spherical tops, should be of primary importance. CHD_3 should prove an important model system for relating the energy transfer processes observed in spherical tops to those in the more well known symmetric tops.

Infrared double-resonance experiments on CHD_3 have been reported previously by Menard-Bourcin and Doyennette,¹² using a grating-tuned CO_2 laser as the probe. They measured intermode $V-V$ energy transfer, apparently including exchange of excitation between the A and E symmetry species. However, the restriction to a relatively small number of fixed-frequency probe lines in their experiments did not permit energy transfer pathways to be completely mapped out at the rotational state-to-state level. To accomplish this objective, we have carried out measurements on this system using a tunable semiconductor diode probe laser, similar to the experiments reported earlier on methane³ and silane.⁴ The results of these experiments will be reported separately.¹³

In order to interpret these measurements properly, we must possess secure assignments for the excited-state (hot-band) transitions which are probed following pulsed laser excitation. While the spectroscopy of the CHD_3 ground state and fundamental bands is well known,^{9,14-17} that of the overtone region, as well as the hot band system associated with it, is almost completely unknown.

The vibrational level structure of CHD_3 is shown for reference in Fig. 1. The polyad situated at about 2000 cm^{-1}

^{a)}Present address: Department of Chemistry, University of Durham, England, UK.

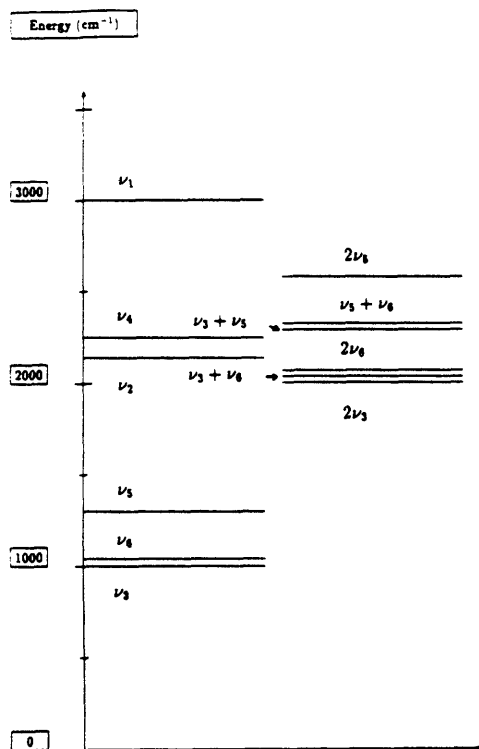


FIG. 1. Lowest vibrational polyads of CHD₃ (adapted from Ref. 23). The symmetry species of the vibrational fundamentals are $a_1(\nu_1, \nu_2, \nu_3)$ or $e(\nu_4, \nu_5, \nu_6)$. Symmetry species of overtone and combination levels follow the usual multiplication properties of the C_{3v} group, as shown in Table I [see also J. Steinfield, *Molecules and Radiation*, 2nd ed., (M.I.T., Cambridge, Mass., 1985), p. 454].

involves a number of vibrational levels including the fundamentals ν_4 and ν_2 , the harmonics $2\nu_3$, $2\nu_5$, and $2\nu_6$, and the combination levels $\nu_3 + \nu_5$, $\nu_3 + \nu_6$, and $\nu_5 + \nu_6$. These interacting levels form an "octad" (or a "nonad," if the ν_1 level is also included) having a vibrational degeneracy $g_v = 18$. It is noteworthy that in searching the possible partner states constituting a polyad, one has to take into consideration not only the clustering of levels, as shown in energy diagrams, but also the order of magnitude of the interaction coupling terms. For instance, in CHD₃, even though the $\nu_1 = 1$ and $\nu_3 = 3$ levels are predicted to lie close together (around 2993 and 3012 cm^{-1} , respectively), the predominant coupling term between these states is a second order purely vibrational operator, the first rovibrational coupling term being of third order. This interaction thus need not *a priori* be introduced explicitly to account for the infrared absorption spectrum in the region considered.

There are relatively few detailed studies in this region. Jennings and Blass¹⁸ determined ground- and excited-state spectroscopic constants from an analysis of the ν_2 band. Katzenberg and Brodersen¹⁹ studied the ν_2 and ν_4 bands using an isolated-band model, but noted the presence of interactions

with the other bands of the nonad. The $2\nu_5(E)$ band has been analyzed by Allen and Plyler,²⁰ but they were able to assign only the $\Delta J = \Delta K$ transitions owing to the weakness of this band. The C-H stretching mode (ν_1) overtones have also been analyzed up to quite high excitation levels,^{11,21,22} but these levels are not involved in the analysis described here.

The standard framework for the analysis of spherical-top rovibrational spectra is the spherical tensor model developed by Moret-Bailly, Champion, and their co-workers.²³ This model has now been extended to lower-symmetry cases, specifically symmetric-top molecules whose equilibrium configuration belongs to the C_{3v} point group.^{24,25} Application of this formalism to a Fourier-transform spectrum of the 1000 cm^{-1} region of CHD₃ recorded by Valentin (described in greater detail below) enabled Roche^{24,25} to reanalyze the ν_3/ν_6 dyad with an agreement (nonweighted standard deviation of observed-calculated wave numbers) of 0.000 21 cm^{-1} . Note that the ν_5 mode was not included in this treatment since, at least for the lower J values, interactions between ν_5 and the ν_3 or ν_6 mode induce only small perturbations. In the present paper, the analysis is extended to the $2\nu_3/(\nu_3 + \nu_6)/2\nu_6$ overtone/combination band system and the "triad-dyad" hot-band system associated with it.

The structure of the rest of the paper is as follows. In the next section, we describe the experimental spectra obtained for CHD₃ in the 1000 and 2000 cm^{-1} regions, which form the basis for the present analysis. Section III outlines the tensorial formalism employed in the analysis of the spectra. In Sec. IV, we report the analysis and assignment of these bands. As mentioned above, the application of these results to analysis of time-resolved infrared double-resonance experiments is reported separately.¹³ Table I of Ref. 13 lists all of the observed double-resonance transitions, which were of considerable importance in verifying the assignments presented here.

II. EXPERIMENTAL SECTION

The experimental data employed in this analysis consist of two sets of Fourier transform infrared (FTIR) spectra recorded under varying conditions.

A. 1000 cm^{-1} absorption region

The spectrum in this region was recorded on the FTIR spectrometer at the Laboratoire de Physique Moléculaire et Applications in Paris. It consists of 2076 lines in the range 886–1350 cm^{-1} at a resolution of 0.003 cm^{-1} . The CHD₃ sample (98.5% d_3), obtained from Merck Sharpe and Dohme of Canada via the Bureau des Isotopes Stables du CEA, was at a pressure of 0.18 Torr at ambient temperature (298 K). The effective path length was 5 m. This spectrum contained both dyad ($\nu_3/\nu_6 \leftarrow$ ground state) and hot-band ($\{2\nu_3/(\nu_3 + \nu_6)/2\nu_6 \text{ triad}\} \leftarrow$ dyad) absorption lines, in addition to $\nu_3 \leftarrow$ ground state and associated hot-band features. The dyad \leftarrow ground state spectra have been separately analyzed;^{24,25} by subtracting the fundamental transitions from the recorded spectrum, as described in Sec. IV B, the hot-band features could be easily distinguished.

B. 2000 cm^{-1} absorption region

We had available four spectra in this region:

(i) A FTIR spectrum recorded on the BOMEM DA 3.002 at the NASA Ames Research Center over the range 1950–2150 cm^{-1} at a resolution of 0.005 cm^{-1} . The CHD_3 sample, obtained from Merck Sharpe and Dohme of Canada and containing 98 atom % D, was at a pressure of 50 Torr in a single-pass 10 cm cell, at ambient temperature (298 K).

(ii) A FTIR spectrum recorded on a BOMEM 8 spectrometer in Professor Y. Hamada's laboratory at the University of the Air (Tokyo, Japan), covering the range 1800–2300 cm^{-1} at a resolution of 0.006 cm^{-1} . The CHD_3 sample, from ICON Ser. Inc., 98 atom % D, was at a pressure of 6 Torr in a multipass cell with an effective path length of 5.6 m, at ambient temperature (298 K).

(iii) Two FTIR spectra taken on the BOMEM spectrometer at NRCC Ottawa, covering the range 1850–2150 cm^{-1} at a resolution of 0.003 cm^{-1} . Frequency calibration was accomplished by measuring the positions of CO lines and comparing with the absolute positions as given in the HITRAN data base.²⁶ The CHD_3 sample was also from Merck Sharpe and Dohme of Canada. The conditions employed were

temperature = 103 K, pressure = 0.332 Torr,
path length = 24 m;

temperature = 264 K, pressure = 0.358 Torr,
path length = 48 m.

Survey spectra at these two temperatures, covering the most highly congested region of the overtone bands, are shown in Fig. 2. These spectra were the principal data base for the analysis described below.

III. THEORETICAL MODEL

We have recently proposed²⁴ a new formulation of the rotation–vibration Hamiltonian adapted to symmetric top molecules. As is the case with the so-called tetrahedral formalism,^{23,27} this treatment makes extensive use of group theory and tensorial algebra. It allows us, first, to construct all operators, whether part of the Hamiltonian, dipole moment, or contact transformation operators, in a systematic

way. This consistency, resulting from the use of group theory, naturally enables us to include all the interaction terms thus permitted. In addition, we can use the power of tensorial algebra (operators and wave functions are expressed as tensors) to calculate the matrix elements of all Hamiltonian or dipolar terms quite generally, by using a unique basic formula expressing the Wigner–Eckart theorem. As we will see in the following discussion, the classification of Hamiltonian terms is based, as far as possible, on the polyad structure of the molecule under study.

A. The vibrational extrapolation

An important aspect of our approach is that a unique set of transformed operators (Hamiltonians and transition moments) is used to describe the transitions between the three polyads (ground state, dyad, and triad). For a given type of operators $\{\nu\}$, the effective Hamiltonians $H_{\{\nu\}}^{(P_1)}, H_{\{\nu\}}^{(P_2)}, H_{\{\nu\}}^{(P_3)} \dots$ (which correspond to the projections of the transformed Hamiltonian $\tilde{H}_{\{\nu\}}$ on the Hilbert spaces spanned by the vibrational functions associated with the sets of interacting bands P_1, P_2, P_3, \dots) involve the same unique set of spectroscopic parameters. The so-called process of vibrational extrapolation^{23,27–29} is essentially based on this property. The terminology used in this discussion is summarized in the Appendix to this paper.

An example of the application of this method is provided in the present study. Most of the “preponderant” Hamiltonian parameters are determined and then fixed to the values previously determined when studying the fundamental bands. The new parameters to be determined are then less numerous and typically less correlated (which is helpful with respect to the numerical process used to retrieve the spectroscopic parameters). This was especially valuable when assigning the $2\nu_6(A_1)$ band of CHD_3 and when checking assignments in $2\nu_3$: the consistency between assignments resulting from ground state combination differences and predictions resulting from the vibrational extrapolation was tested before performing any fit.

B. Prediction of the $2\nu_3(\nu_3 + \nu_6)/2\nu_6$ bands

The transformed Hamiltonian corresponding to this combination triad may be written as follows:

$$\begin{aligned} \tilde{H}_{\{2\nu_3/\nu_3 + \nu_6/2\nu_6\}} = & \sum \tilde{t}_{33,33}^{\Omega(L,K,\gamma)} T_{33,33}^{\Omega(L,K,\gamma)} + \sum \tilde{t}_{66,66}^{\Omega(L,K,\gamma)\gamma_1\gamma_2} T_{66,66}^{\Omega(L,K,\gamma)\gamma_1\gamma_2} + \sum \tilde{t}_{36,36}^{\Omega(L,K,\gamma)} T_{36,36}^{\Omega(L,K,\gamma)} \\ & + \sum \tilde{t}_{33,36}^{\Omega(L,K,\gamma)\gamma_1\gamma_2} T_{33,36}^{\Omega(L,K,\gamma)\gamma_1\gamma_2} + \sum \tilde{t}_{33,66}^{\Omega(L,K,\gamma)\gamma_1\gamma_2} T_{33,66}^{\Omega(L,K,\gamma)\gamma_1\gamma_2}, \end{aligned} \quad (1)$$

where the first three sums involve the same operators as $\tilde{H}_{\{2\nu_3\}}$, $\tilde{H}_{\{2\nu_6\}}$, and $\tilde{H}_{\{\nu_3 + \nu_6\}}$ but with spectroscopic coefficients \tilde{t} associated with a polyad treatment. The other terms refer to interacting terms between the upper states of $2\nu_3$, $2\nu_6$ and $\nu_3 + \nu_6$. In Eq. (1) Ω stands for the degree of the operator with respect to the components of the total angular

momentum J of the molecule; L is the tensorial rank with respect to $SO(3)$. L takes the values $\Omega, \Omega - 2, \dots, 1$ or 0 (depending on the parity of Ω); K is the unsigned value of k , the component of the spherical tensor in the familiar $|J, k\rangle$ basis; and γ and γ_i ($i = 1, 2$) designate the symmetry species in the C_{3v} group.

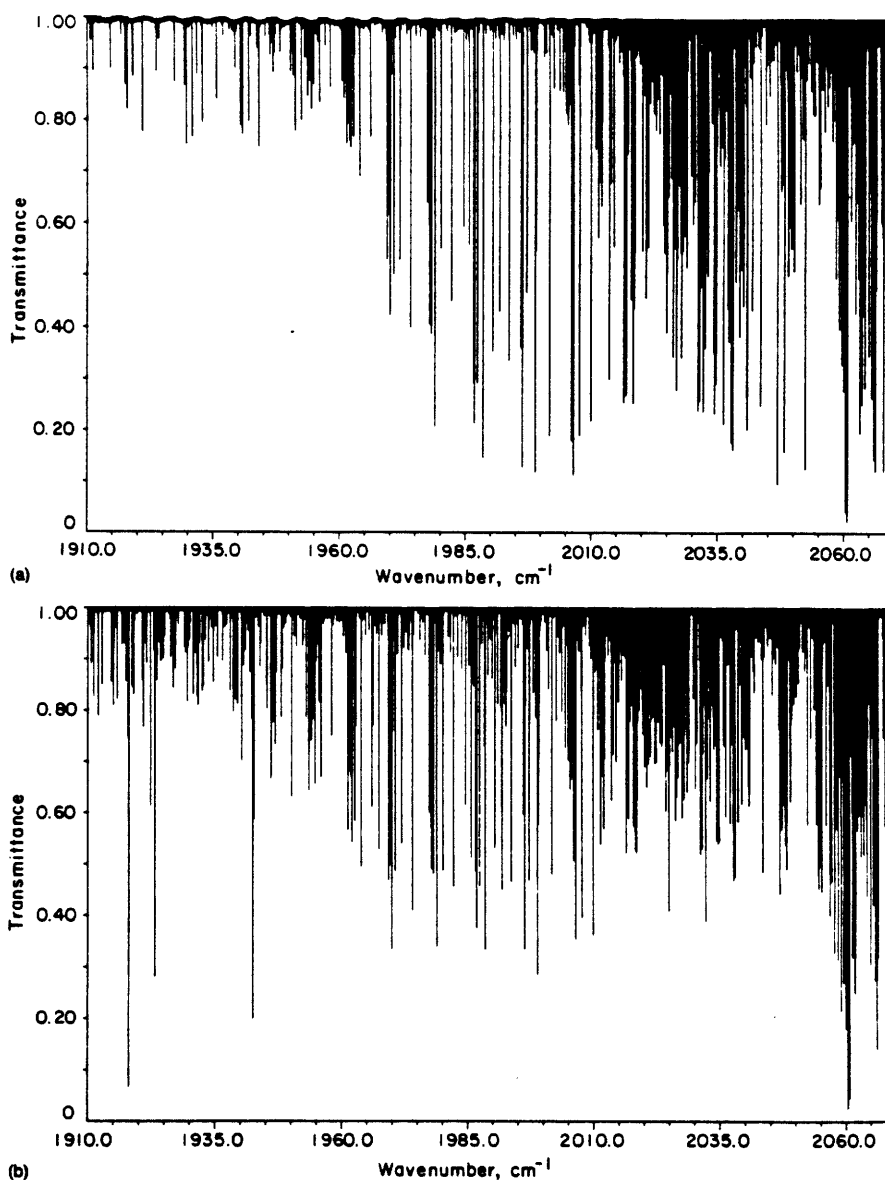


FIG. 2. CHD₃ survey spectra recorded on the BOMEM spectrometer at NRC Ottawa. Top: temperature=103 K, pressure=0.332 Torr, path length=24 m. Bottom: temperature=264 K, pressure=0.358 Torr, path length=48 m.

An effective Hamiltonian associated with the previous expression (1) is written as follows:

$$H^{(\text{Triad})} = H_{(\text{G.S.})}^{(\text{Triad})} + H_{(\nu_3/\nu_6)}^{(\text{Triad})} + H_{(\text{Triad})}^{(\text{Triad})}, \quad (2)$$

where (Triad) stands for the $\{v_3 = 2/(v_3 = v_6 = 1)/v_6 = 2\}$ set of states. The spectroscopic parameters present in the expansions of $H_{(\text{G.S.})}^{(\text{Triad})}$ and $H_{(\nu_3/\nu_6)}^{(\text{Triad})}$ are the same as those we previously determined^{24,25} from the analyses of the ground state and ν_3/ν_6 dyad of CHD₃.

As a first step, we expanded the Hamiltonian concerned with the upper state of the $2\nu_3, (\nu_3 + \nu_6), 2\nu_6$ triad to fourth order (see Table I). Among the lower-degree spectroscopic parameters involved, four are associated with the centers of the $2\nu_3, (\nu_3 + \nu_6), 2\nu_6(A_1 \text{ and } E)$ bands while the other two refer to purely vibrational interaction terms between $2\nu_3$ and $2\nu_6^{(A_1)}$ on the one hand and $\nu_3 + \nu_6$ and $2\nu_6^{(E)}$ on the other hand.

The effective Hamiltonian associated with the triad,

TABLE I. Fourth-order Hamiltonian of the $2\nu_3/\nu_3 + \nu_6/2\nu_6$ triad. This table presents the various rotational and vibrational operators involved in our model. The vibrational operators are defined according to Ref. 23. a and a^+ stand for the elementary annihilation and creation operators, while A and A^+ represent the coupling of a number of a and a^+ operators, respectively. The rotational operators are characterized by a set of superscripts $\Omega(K, L, \gamma)$ where these have the same meaning as in formula (1) of this paper. Vibrational and rotational operators presented in this model are coupled to form the rovibrational operators of the Hamiltonian.

Basic vibrational coupling	Vibrational operators	Associated rotational operators
Ground state		
		$R^{2(0,0,A_1)}, R^{2(2,0,A_1)}, R^{4(0,0,A_1)},$ $R^{4(2,0,A_1)}, R^{4(4,0,A_1)}, R^{4(4,3,A_1)},$ $R^{6(0,0,A_1)}, R^{6(2,0,A_1)}, R^{6(4,0,A_1)},$ $R^{6(4,3,A_1)}, R^{6(6,0,A_1)}, R^{6(6,3,A_1)},$ $R^{8(0,0,A_1)}, R^{8(2,0,A_1)},$ $R^{8(4,0,A_1)}, R^{8(4,3,A_1)}, R^{8(6,0,A_1)},$ $R^{8(6,3,A_1)}, R^{8(8,0,A_1)},$ $R^{8(8,3,A_1)}, R^{8(8,6,A_1)}$
ν_3/ν_6 dyad		
ν_6 band		
$(a_6^+(E) \times a_6^-(E))_{(A_1)}$	$+V_{6,6}^{EE(A_1)}$	$R^{0(0,0,A_1)}, R^{2(0,0,A_1)}, R^{2(2,0,A_1)},$ $R^{4(0,0,A_1)}, R^{4(2,0,A_1)}, R^{4(4,0,A_1)},$ $R^{4(4,3,A_1)}$
$(a_6^+(E) \times a_6^-(E))_{(A_2)}$	$-V_{6,6}^{EE(A_2)}$	$R^{1(1,0,A_2)}, R^{3(1,0,A_2)}, R^{3(3,0,A_2)},$ $R^{3(3,3,A_2)}$
$(a_6^+(E) \times a_6^-(E))_{(E)}$	$+V_{6,6}^{EE(E)}$	$R^{2(2,1,E)}, R^{2(2,2,E)}, R^{4(2,1,E)},$ $R^{4(2,2,E)}, R^{4(4,1,E)}, R^{4(4,2,E)},$ $R^{4(4,4,E)}$
ν_3 Band		
$(a_3^+(A_1) \times a_3^-(A_1))_{(A_1)}$	$+V_{3,3}^{A_1(A_1)}$	$R^{0(0,0,A_1)}, R^{2(0,0,A_1)}, R^{2(2,0,A_1)},$ $R^{4(0,0,A_1)}, R^{4(2,0,A_1)}, R^{4(4,0,A_1)},$ $R^{4(4,3,A_1)}$
$\nu_3 - \nu_6$ interaction		
$(a_3^+(A_1) \times a_6^-(E))_{(E)}$	$-V_{3,6}^{A_1E(E)}$	$R^{1(1,1,E)}, R^{3(1,1,E)}, R^{3(3,1,E)},$ $R^{3(3,2,E)}$
$(a_3^+(A_1) \times a_6^-(E))_{(E)}$	$+V_{3,6}^{A_1E(E)}$	$R^{2(2,1,E)}, R^{2(2,2,E)}, R^{4(2,1,E)},$ $R^{4(2,2,E)}, R^{4(4,1,E)}, R^{4(4,2,E)},$ $R^{4(4,4,E)}$
$2\nu_3/\nu_3 + \nu_6/2\nu_6$ triad		
$2\nu_3$ band		
$(A_{33}^{+(A_1)} \times A_{33}^{-(A_1)})_{(A_1)}$	$+V_{33,33}^{A_1(A_1)}$	$R^{0(0,0,A_1)}, R^{2(0,0,A_1)}, R^{2(2,0,A_1)}$
$2\nu_3 - \nu_3 + \nu_6$ interaction		
$(A_{33}^{+(A_1)} \times A_{36}^{-(E)})_{(E)}$	$+V_{33,36}^{A_1E(E)}$	$R^{2(2,1,E)}, R^{2(2,2,E)}$
$(A_{33}^{-(A_1)} \times A_{36}^{+(E)})_{(E)}$	$-V_{33,36}^{A_1E(E)}$	$R^{1(1,1,E)}$
$2\nu_3 - 2\nu_6(A_1)$ interaction		
$(A_{33}^{+(A_1)} \times A_{66}^{-(A_1)})_{(A_1)}$	$+V_{33,66}^{A_1(A_1)}$	$R^{0(0,0,A_1)}, R^{2(0,0,A_1)}, R^{2(2,0,A_1)}$
$2\nu_3 - 2\nu_6(E)$ interaction		
$(A_{33}^{+(A_1)} \times A_{66}^{-(E)})_{(E)}$	$+V_{33,66}^{A_1E(E)}$	$R^{2(2,1,E)}, R^{2(2,2,E)}$
$(A_{33}^{-(A_1)} \times A_{66}^{+(E)})_{(E)}$	$-V_{33,66}^{A_1E(E)}$	$R^{1(1,1,E)}$
$\nu_3 + \nu_6$ band		
$(A_{36}^{+(E)} \times A_{36}^{-(E)})_{(A_1)}$	$+V_{36,36}^{EE(A_1)}$	$R^{0(0,0,A_1)}, R^{2(0,0,A_1)}, R^{2(2,0,A_1)}$
$(A_{36}^{+(E)} \times A_{36}^{-(E)})_{(A_2)}$	$-V_{36,36}^{EE(A_2)}$	$R^{1(1,0,A_2)}$
$(A_{36}^{+(E)} \times A_{36}^{-(E)})_{(E)}$	$+V_{36,36}^{EE(E)}$	$R^{2(2,1,E)}, R^{2(2,2,E)}$
$\nu_3 + \nu_6 - 2\nu_6(A_1)$ interaction		
$(A_{36}^{+(E)} \times A_{66}^{-(A_1)})_{(E)}$	$-V_{36,66}^{EA_1(E)}$	$R^{1(1,1,E)}$
$(A_{36}^{-(E)} \times A_{66}^{+(A_1)})_{(E)}$	$+V_{36,66}^{EA_1(E)}$	$R^{2(2,1,E)}, R^{2(2,2,E)}$
$\nu_3 + \nu_6 - 2\nu_6(E)$ interaction		
$(A_{36}^{+(E)} \times A_{66}^{-(E)})_{(A_1)}$	$+V_{36,66}^{EE(A_1)}$	$R^{0(0,0,A_1)}, R^{2(0,0,A_1)}, R^{2(2,0,A_1)}$
$(A_{36}^{+(E)} \times A_{66}^{-(E)})_{(A_2)}$	$-V_{36,66}^{EE(A_2)}$	$R^{1(1,0,A_2)}$
$(A_{36}^{+(E)} \times A_{66}^{-(E)})_{(E)}$	$-V_{36,66}^{EE(E)}$	$R^{1(1,1,E)}$
$(A_{36}^{-(E)} \times A_{66}^{+(E)})_{(E)}$	$+V_{36,66}^{EE(E)}$	$R^{2(2,1,E)}, R^{2(2,2,E)}$

TABLE I. (Continued.)

Basic vibrational coupling	Vibrational operators	Associated rotational operators
$2\nu_6(A_1)$ component		
$(A_{66}^{+(A_1)} \times A_{66}^{(A_1)})^{(A_1)}$	$+V_{66,66}^{A_1(A_1)}$	$R^{0(0,0,A_1)}, R^{2(0,0,A_1)}, R^{2(2,0,A_1)}$
$2\nu_6(A_1) - 2\nu_6(E)$ interaction		
$(A_{66}^{+(A_1)} \times A_{66}^{(E)})^{(E)}$	$+V_{66,66}^{A_1(E)}$	$R^{2(2,1,E)}, R^{2(2,2,E)}$
$(A_{66}^{+(A_1)} \times A_{66}^{(E)})^{(E)}$	$-V_{66,66}^{A_1(E)}$	$R^{1(1,1,E)}$
$2\nu_6(E)$ component		
$(A_{66}^{+(E)} \times A_{66}^{(E)})^{(A_1)}$	$+V_{66,66}^{E(A_1)}$	$R^{0(0,0,A_1)}, R^{2(0,0,A_1)}, R^{2(2,0,A_1)}$
$(A_{66}^{+(E)} \times A_{66}^{(E)})^{(A_2)}$	$-V_{66,66}^{E(A_2)}$	$R^{1(1,0,A_2)}$
$(A_{66}^{+(E)} \times A_{66}^{(E)})^{(E)}$	$+V_{66,66}^{E(E)}$	$R^{2(2,1,E)}, R^{2(2,2,E)}$

$H^{(\text{Triad})}$, involves 99 terms among which 40 are to be determined (not taking into account any ambiguity problem). However, since some of the transformed Hamiltonian can not be determined unequivocally from the experimental energy levels alone, the fit of the same experimental data set to equivalent theoretical models (related by a change of basis) can lead to apparently inconsistent results. This phenomenon has been explored, for the case of spherical-top Hamiltonians, in Refs. 28 and 30, but is even more important in the case of symmetric-top molecules: undeterminable parameters are even more numerous for a given order in the expansion of the Hamiltonian. Possible manifestations of this problem were encountered when studying the ν_3/ν_6 dyad, in the form of very strong correlations between some of the parameters. These parameters are damped to obtain an artificial decorrelation that allows the fit to converge. When faced with this problem, in the present study, we applied a similar expedient. A lower order Hamiltonian, involving only six terms to be determined (the lower-degree parameters mentioned above), was tried first. Experience nevertheless showed that the low- J values were not easily accessible from the spectrum. Further assignments required a higher-order expansion, which is consistent with the isolated-band models we also used.

The values of only two parameters, corresponding to the band centers of $2\nu_3$ and $2\nu_6^{(A_1)}$, have been previously estimated³¹ via force field calculations and correlated with observed values mentioned in Ref. 19 (these values are, respectively, 1988.9 and 2072.9 cm^{-1}). As far as intensities are concerned, we have only considered the lower-degree operators associated with the four bands involved in the upper state of the $2\nu_3/(\nu_3 + \nu_6)/2\nu_6$ triad of CHD₃, i.e., the dipole moment was developed to first order. An expression for the effective dipole moment is then

$$M^{(\text{G.S.,Triad})} = M_{(\text{G.S.},\{\text{Triad}\})}^{(\text{G.S.,Triad})} \quad (3)$$

The relative intensities of the four bands are not known, nor are the four dipolar terms that represent them. As a first set of dipole moment parameters, we have used (on the basis of order-of-magnitude considerations) those involved in the $\nu_1/\nu_3/2\nu_2/(\nu_2 + \nu_4)/2\nu_4$ pentad of ¹²CD₄. The ν_4 band of ¹²CD₄ being associated with the ν_3/ν_6 dyad of ¹²CHD₃ (in terms of vibrational correspondence), the dipole moment parameters

of $2\nu_4$ were used to describe the intensities of the $2\nu_3/(\nu_3 + \nu_6)/2\nu_6$ triad of CHD₃. This is, of course, not very realistic and these parameters need to be adjusted to values properly describing the relative intensities of the combination triad bands.

C. Prediction of the hot-band system

$$\{(\nu_3 = 2/(\nu_3 = \nu_6 = 1)/\nu_6 = 2) - (\nu_3 = 1/\nu_6 = 1)\}$$

At ambient temperature, the hot bands that are *a priori* more intense are those arising from the lower excited states of a molecule, that is, when considering CHD₃, those originating from the $\nu_3 = 1$, $\nu_6 = 1$, and $\nu_5 = 1$ states. We pointed out in Sec. I that the absorption region that is situated around 2000 cm^{-1} involves numerous vibrational bands. We then expect transitions belonging to numerous hot bands to appear in the 1000 cm^{-1} region, associated with "octad- $\nu_3/\nu_6/\nu_3$ difference bands."

The ones in which we are interested are those participating in the $2\nu_3/(\nu_3 + \nu_6)/2\nu_6 - \nu_3/\nu_6$ subsystem, the ν_3 mode and its overtones being excluded for the reasons mentioned previously. The intensity of these bands may be described, to the first order of approximation, by the dipole moment terms relating to the ν_3 and ν_6 fundamentals. This subsystem consists of four hot bands, namely, $2\nu_3 - \nu_3$, $\nu_3 + \nu_6 - \nu_3$, $\nu_3 + \nu_6 - \nu_6$, and $2\nu_6 - \nu_6$. The corresponding dipole moment may then be written

$$M^{(\nu_3/\nu_6, \text{Triad})} = M_{(\text{G.S.},\{\nu_3/\nu_6\})}^{(\nu_3/\nu_6, \text{Triad})} + M_{(\nu_3/\nu_6),\{\text{Triad}\}}^{(\nu_3/\nu_6, \text{Triad})} \quad (4)$$

where Triad stands for $2\nu_3/(\nu_3 + \nu_6)/2\nu_6$.

As we limit ourselves to the first order of approximation, we will consider only the first term in this sum. Under these restrictions, the intensities of the above-mentioned hot bands are described by the same operators and parameters as the ν_3/ν_6 dyad: we estimate them from extrapolation of the dyad analysis. Specific operators are involved in each one of the four hot band intensities, but take part in a higher order expansion of the dipole moment. We will not consider these, the primary goal of this study being assignment of the 1000 and 2000 cm^{-1} spectra.

IV. RESULTS AND DISCUSSION

An early stage of our work was devoted to a quantitative understanding of the $2\nu_3/(\nu_3 + \nu_6)/2\nu_6$ polyad. First using vibrational extrapolation only, and then trying different values of the anharmonicities, we obtained various predictions of the spectrum which we attempted to match with the experimental data.

This process was greatly facilitated by having spectra at two different temperatures (103 and 264 K) displayed in Fig. 1. The lower state energy for a particular transition was calculated from the ratio of the absorbances of the transition at the two temperatures, viz.,

$$\ln\left(\frac{A_{T_1}}{A_{T_2}}\right) = \frac{E}{k_B} \left(\frac{T_1 - T_2}{T_1 T_2} \right) + \ln\left(\frac{l_{T_1} P_{T_1}}{l_{T_2} P_{T_2}}\right) + \ln\left[\frac{Q(T_1)}{Q(T_2)}\right]. \quad (5)$$

In Eq. (5), $A = -\ln(\%T/100)$ is the absorbance of the transition, E is the lower-state energy, k_B is Boltzmann's constant, l is the path length, P is the pressure, and Q is the statistical partition coefficient. The subscripts T_1 and T_2 refer to the spectra recorded at the two temperatures given above. To eliminate the combined effect of experimental uncertainties in the pressure, path length, and temperature measurements, we used assigned transitions in the $^Q P$ branch of the CHD₃ ν_2 fundamental^{18,19} and the well-known values for the CHD₃ ground state²⁵ to fit these parameters in Eq. (5). Ground-state energies for strong, but not saturated, unblended lines were calculated to an accuracy of several wavenumbers from these intensity data.

Ground-state combination differences (G.S.C.D.) were also calculated. The agreement between observed and calculated frequencies being on the order of 0.00014 cm^{-1} for the ground state, we could limit the number of possible partners by requiring them to match a combination difference with a discrepancy not exceeding $|0.0005 \text{ cm}^{-1}|$. The comparison between the intensities in the 103 and 264 K spectra provided an estimate of the corresponding ground state energy, which confirmed or negated the assignments obtained using the G.S.C.D.'s.

Transitions meeting both the ground-state energy and G.S.C.D. criteria were considered reliable and included in the fits. These were mainly transitions with lower state $J \leq 12$, since transitions having $J > 12$ are almost unobservable in the low-temperature spectrum.

A. The overtone region ($2\nu_3/(\nu_3 + \nu_6)/2\nu_6$ bands)

The first step in analyzing the overtone region was to eliminate a number of lines present in this region which do not belong to the $2\nu_3/(\nu_3 + \nu_6)/2\nu_6$ manifold; these are principally ν_2 and ν_4 transitions. The ν_2 transitions are quite intense. They mostly appear as saturated in both the 103 and 264 K spectra. The $1910\text{--}2150 \text{ cm}^{-1}$ region includes most of the P branch, (although it is sometimes difficult to identify transitions having $J \geq 15$ in the 264 K spectrum), all of the Q branch, and the $R(0)$ transition that appears at $2149.1047 \text{ cm}^{-1}$. To identify these various ν_2 features, we carried out a prediction of this band using an isolated band model together with the tensorial translation of the parameters determined

by Jennings and Blass.^{18,24,25} Most lines of ν_2 in the 103 and 264 K spectra were easily identified, despite the fact that a few regions involving this band are obviously strongly perturbed.

Our purpose not being a full reanalysis of this band, we only used our model to identify as many lines of ν_2 as possible so as to eliminate them from the overtone analysis. Previous work¹⁹ has attributed the above-mentioned perturbations to interactions with ν_4 and the overtones of ν_3 , ν_6 , and ν_5 . We assumed, in the present study, that when considering the $2\nu_3/(\nu_3 + \nu_6)/2\nu_6$ triad, the most important perturbations were those arising from interactions within the triad, interactions with other bands (such as ν_2) being weaker. We therefore restricted our model to the triad, but a more comprehensive study should possibly involve interactions among all the nonad levels.

The ν_4 band is also present in the 2000 cm^{-1} region. Nevertheless, a prediction of ν_4 as an isolated band, using parameters determined by Kattenberg and Brodersen,¹⁹ indicates that no line with $J < 13$ should appear in the wave number region studied here. Therefore, we would not expect to see any ν_4 features in the low-temperature (103 K) spectrum. No features attributable to ν_4 were identified in either of our experimental spectra, and this band was not considered further in the analysis.

Let us consider the several components of the triad in turn.

(i) *The $2\nu_3$ band.* The $2\nu_3$ band was assigned up to a J value of 12, but proved difficult to assign further because of intensity limitations. In fact, this band is the least intense of the four we studied. The P branch features are stronger while the $^Q Q$ branch is almost not seen, even for low J values and in the low temperature spectrum. A prediction resulting from the vibrational extrapolation of the ν_3/ν_6 dyad is quite consistent with the experimental spectra, except for the low intensity of the Q branch. This certainly means that additive interactions, not incorporated in the vibrational extrapolation, are responsible for that.

Nevertheless, this band does not seem to be highly perturbed in the sense of predicted transition frequencies. An isolated band model allows us to obtain an r.m.s. agreement of 0.063 cm^{-1} between observed and calculated features (the r.m.s. agreement is 0.048 cm^{-1} if transitions only up to $J = 10$ are included). The fit involved 129 lines from the 103 K spectrum and 123 lines from the 264 K spectrum.

(ii) *The $\nu_3 + \nu_6$ band.* The $l = +1$ Coriolis component of this band was assigned up to $J = 12$, including as many as 224 lines in the 103 K spectrum. The problem here was to assign the other Coriolis component. A crude prediction, together with vibrational extrapolation, tells us that these subbands are overlapping. It appears as if the intensity of the second component is also quite perturbed. We are thus able to assign safely only a very few lines. This prevented us from determining a realistic value for the internal Coriolis parameter of this band, or even to provide a realistic fit for these data. During additional isolated band fits, we simply fixed the internal Coriolis parameter to the value we determined for the one of ν_6 when performing the analysis of the fundamentals.^{24,25} Nevertheless, this did not make the task

TABLE II. Parameter table for the $2\nu_3$ overtone band: Familiar notation. Standard deviation (in parentheses) is in units of the last digit quoted. The corresponding ground state parameters, given in Table III of Ref. 25, are not repeated here.

Parameter	Value (cm ⁻¹)
ν_{33}	1991.295(22)
ΔC_{33}	$2.04(21) \times 10^{-2}$
ΔB_{33}	$-3.985(12) \times 10^{-1}$
ΔD_{33}^J	$-2.56(18) \times 10^{-4}$
ΔD_{33}^{JK}	$6.99(47) \times 10^{-4}$
ΔD_{33}^K	$-3.38(54) \times 10^{-4}$
ΔH_{33}^{JJ}	$8.92(76) \times 10^{-7}$
ΔH_{33}^{JK}	$-2.03(25) \times 10^{-6}$
ΔH_{33}^{KK}	$2.35(42) \times 10^{-6}$
ΔH_{33}^K	$-4.1(4.5) \times 10^{-7}$

easier: parameter values oscillated as before because the labeling of the levels was not correct. As both Coriolis components overlap, it is difficult to distinguish between the energy levels belonging to each component. If we are not able to perform this operation for low J values, the fit simply does not converge as it should and oscillates, preventing us from fitting this band properly. Because of this, we were unable to introduce the interactions between the various bands of the triad.

(iii) *The $2\nu_6^{(A_1)}$ band.* Even if we could not use the full model in the analysis, it nevertheless proved quite useful as an aid in the assignments. For example, the distinctive patterns of the $2\nu_6^{(A_1)}$ band were easily recognized from the vibrational extrapolation of the ν_3/ν_6 dyad. We combined this process with the ground-state energies and the G.S.C.D.'s to obtain 149 assignments in the 103 K spectrum and 253 in the 264 K spectrum, for J values up to 13. A fit of these, using an isolated band model, provided an r.m.s. agreement of 0.088 cm⁻¹ between observed and calculated lines. The two vibrational components of $2\nu_6(A_1$ and $E)$ are the most intense features of the overtone bands we studied.

(iv) *The $2\nu_6^{(E)}$ band.* We were able to assign a substantial number of lines both in the $l = +2$ and $l = -2$ Coriolis components up to $J = 9$. Almost all the energy levels can be identified, despite that fact that the $l = +2$ component exhibits stronger features than the $l = -2$ component.

When these assignments were fit to an isolated band model, the analysis showed that this band is strongly perturbed and that the perturbation increases with J . This is illustrated by the r.m.s. (obs-calc), which is 0.020 cm⁻¹ including J up to 5, increases to 0.060 cm⁻¹ up to $J = 6$, and to 0.140 cm⁻¹ up to $J = 7$. The fit was carried out up to $J = 9$, with an r.m.s. deviation of 0.176 cm⁻¹. A full treatment of this band will require interactions with neighboring levels. A clear indication of this is the apparently large, positive value of ΔB found for this band. If an approximate ΔB is calculated for the $\nu_3 + \nu_6$ ($l = +1$) band from the assignments given in Table S-II,³² a large negative value of ΔB is found. This relationship is a symptom of strong perpendicular Coriolis interactions between these bands. Simple arguments predict perpendicular Coriolis interactions between $\nu_3 + \nu_6$ and $2\nu_6^{(E)}$

TABLE III. Parameter table for the $2\nu_6^{(A_1)}$ overtone band: Familiar notation. Standard deviation (in parentheses) is in units of the last digit quoted. The corresponding ground state parameters, given in Table III of Ref. 25, are not repeated here.

Parameter	Value (cm ⁻¹)
ν_{66_0}	2064.100(28)
ΔC_{66_0}	$-7.12(27) \times 10^{-2}$
ΔB_{66_0}	$8.8(1.4) \times 10^{-3}$
$\Delta D_{66_0}^J$	$4.6(1.8) \times 10^{-5}$
$\Delta D_{66_0}^{JK}$	$-1.89(63) \times 10^{-4}$
$\Delta D_{66_0}^K$	$5.76(63) \times 10^{-4}$
$\Delta H_{66_0}^{JJ}$	$9.2(6.5) \times 10^{-8}$
$\Delta H_{66_0}^{JK}$	$-8.2(3.1) \times 10^{-7}$
$\Delta H_{66_0}^{KK}$	$5.43(58) \times 10^{-6}$
$\Delta H_{66_0}^K$	$-3.52(49) \times 10^{-6}$

to be $\sqrt{2}$ larger than the significant interaction observed in the analysis of the ν_3 and ν_6 fundamentals.^{16,17} Parallel Coriolis interaction may also occur between these bands, but is expected to be smaller than the perpendicular interaction because it requires $\Delta l = 3$ interactions induced by anharmonic mixing.

(v) *Results for the overtone levels.* Tables S-I through S-IV, which have been deposited with the Physics Auxiliary Publication System,³² give assignment tables for the $2\nu_3$, $\nu_3 + \nu_6$, $2\nu_6^{(A_1)}$, and $2\nu_6^{(E)}$ bands, together with the frequency differences (obs-calc) resulting from the preceding analysis. Tables II through IV present the corresponding spectroscopic parameters in their familiar notation. The fits presented in Tables II through IV have been performed using isolated band models. Although all calculations were realized in the tensorial formalism, we only show the parameters in their familiar form for reasons of simplicity. The translation of the Hamiltonian and dipole-moment terms for the hot bands be-

TABLE IV. Parameter table for the $2\nu_6^{(E)}$ overtone band: Familiar notation. Standard deviation (in parentheses) is in units of the last digit quoted. The corresponding ground state parameters, given in Table III of Ref. 25, are not repeated here.

Parameter	Value (cm ⁻¹)
$\nu_6^{(E)}$	2068.26(10)
$(C_6)_{66}$	$-2.85(17) \times 10^{-1}$
ΔC_{66}	$-1.26(18) \times 10^{-1}$
ΔB_{66}	$6.106(44) \times 10^{-1}$
r_{66}	$4.5(7.8) \times 10^{-3}$
q_{66}	$-3.148(23) \times 10^{-1}$
r_{66}^*	$2.3(2.1) \times 10^{-3}$
r_{66}^{\dagger}	$3.7(3.4) \times 10^{-3}$
ΔD_{66}^J	$2.954(54) \times 10^{-3}$
ΔD_{66}^{JK}	$-7.95(41) \times 10^{-3}$
ΔD_{66}^K	$5.18(57) \times 10^{-3}$
$r_{66,66}^{(4,2,EE)EE}$	$-8.3(2.6) \times 10^{-5}$
$f_{66}^{(42)}$	Fixed to zero

*The correspondence between familiar and tensorial parameters is not complete. Nevertheless, the missing links affect only higher order terms, that certainly would not be involved in the existing correspondence relations.

tween tensorial and familiar notations is less straightforward and is omitted here.

B. The hot-band region ($\{\nu_3=2/(\nu_3=\nu_6=1)/\nu_6=2\}$ - $\{\nu_3=1/\nu_6=1\}$)

We have assigned most of the ν_3/ν_6 and ν_3 lines contained in the 1000 cm^{-1} spectrum described in Sec. II A.^{24,25} Nevertheless, a number of weaker features remained unassigned in this absorption region, and many of these are hot-band features. As noted in the Introduction, assignment of these features is crucial to interpretation of the double-resonance experiments on this molecule.¹³

One problem encountered when assigning the hot-band system was the threshold of the peakfinding routine used to identify features and center frequencies in the 1000 cm^{-1} spectrum. For the analysis of the fundamentals, this threshold was set rather high just in order to discriminate against background features belonging to the hot bands. In order to analyze the hot bands, we first eliminated the fundamental transitions from the spectrum, and compared the predictions of our models with the remaining features. For carrying out the fits, we included only the stronger lines for which an accurate center frequency had been established by the peakfinding routine. The assignments were, in many cases, confirmed by the time-dependent behavior of the intensities as seen in the double-resonance measurements, as well as by the nuclear-spin alternation in the intensities. In general, upper-level term values derived independently from the hot-band and overtone line positions agreed to within 0.01 cm^{-1} .

Table S-V³² contains our hot-band assignments for the $2\nu_3-\nu_3$ band. While most of the predicted frequencies match well with features observed in the experimental spectrum, only a fraction of these correspond to measured line centers. In the $2\nu_3-\nu_3$ assignment table (S-VI),³² most of the $^Q Q$ and a number of the $^Q R$ features have been peakfound.

The $2\nu_6-\nu_6$ hot band contains A_1 and E components. Transitions calculated for the $2\nu_6^{(A_1)}-\nu_6$ subband using the vibrational extrapolation model presented in Sec. III also were not numerous, and could not at first be clearly identified with experimental features. In this case, the double-resonance experiment provided the clue to the assignment. We were able to identify a transition with an upper state estimated energy of 2293.902 cm^{-1} and a known lower state $8A_17(K=4, l=+1)$ belonging to ν_6 . From the double-resonance selectivity, we knew that the upper state had to be of A symmetry and was characterized by a J value of 7, 8, or 9. A comparison with the previously assigned overtone transitions showed that the transition could be none other than $2\nu_6^{(A_1)}$, $8A_26(K=3, l=0) \leftarrow \nu_6$, $8A_17(K=4, l=+1)$, that is, a transition of the $^P Q$ subband of $2\nu_6^{(A_1)}-\nu_6$. A systematic calculation of the $^P P$, $^P Q$, and $^P R$ lines of this subband produced a number of predicted transitions, some of which had been identified by the peakfinding routine. These lines were not included in the fit, but are included in Table S-VI³² together with their assignments. We show in Fig. 3 the experimental region near 1028 cm^{-1} associated with most of these assignments, that is, the $^P Q$ branch of $2\nu_6^{(A_1)}-\nu_6$.

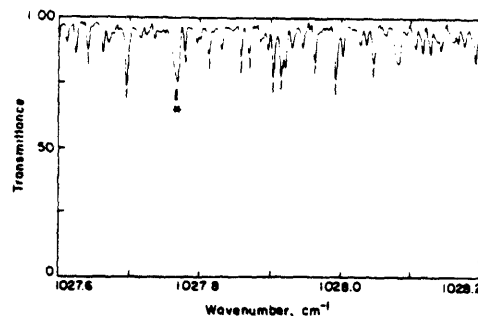


FIG. 3. Portion of CHD_3 spectrum recorded on the FTIR spectrometer at the Laboratoire de Physique Moléculaire et Applications (Paris), showing the $^P Q$ region of the $2\nu_6^{(A_1)}-\nu_6$ hot band near 1028 cm^{-1} . Features due to the fundamental absorption bands have been subtracted before plotting. Vertical strokes indicate identified hot-band transitions (see Table S-IV) (Ref. 32). The starred transition at 1027.768 cm^{-1} is the $^P Q(8)$ line identified by its double-resonance.

Calculations were also carried out for the $2\nu_6^{(E)}-\nu_6$ subbands. One of these, which is predicted to occur at around 1033 cm^{-1} , possesses quite weak features, and very few were identified by the peak finding routine. However, visual inspection of the spectrum recorded in this region provides good qualitative correlation with the predicted features.

C. Conclusions

We have assigned approximately 800 lines belonging to the $2\nu_3(\nu_3+\nu_6)/2\nu_6$ triad of CHD_3 , and an additional 100 lines in the triad- ν_3/ν_6 hot-band system. The lack of identified features in the $\nu_3+\nu_6(l=-1)$ component prevented us from making full use of the tensorial model presented in the theoretical section. We were thus not able to introduce the interaction parameters between the different bands in the fit. We therefore limited the analysis to the determination of isolated band parameters for the three completely assigned vibrational bands, namely, $2\nu_3$, $2\nu_6^{(A_1)}$, and $2\nu_6^{(E)}$. The methods of vibrational extrapolation, together with experimental verifications resulting from time-resolved double-resonance measurements on the system, provided the key to the assignment and analysis of this quite congested and complicated spectrum. Although it was not possible to determine all of the tensorial parameters from the experimental data, the model nevertheless is able to predict most line positions to within $\pm 0.1\text{ cm}^{-1}$ or less. This analysis provided the identifications essential for proper interpretation of the results of the double-resonance experiments, as reported in the companion paper. This, in turn, permitted us to determine rotational energy transfer rates and propensity rules for this system.

ACKNOWLEDGMENTS

The work at M.I.T. is supported by grants from the NASA Upper Atmosphere Research Program (NAGW-1677) and Planetary Atmospheres Program (NAGW-2387). Work in Dijon is supported by the Region Bourgogne and the

C.N.R.S. Y.M. gratefully acknowledges support from Seki Technotron Co. Ltd. for the work in Tokyo. We are pleased to acknowledge the assistance of Dr. M. Spencer and Dr. C. Chackerian, Jr., Atmospheric Physics Research Branch, NASA Ames Research Center with measurement of the FTIR spectra, and also valuable discussions with Dr. G. Tarrago, Laboratoire de Physique Moléculaire et Applications, Université de Paris-Sud.

APPENDIX

This Appendix contains explanations of terms used throughout this paper. In order to get more insight and details concerning the underlying theoretical notions, we recommend the reading of Refs. 23–25 and 27–29.

Transformed Hamiltonian

Determining the contribution of the Hamiltonian terms to the rotation–vibration energies usually deals with perturbative methods. Among these methods, one now in common use is that of the contact transformation, initiated by Van Vleck.³³ It allows us to introduce a new basis of functions where the transformed Hamiltonian \tilde{H} is totally or partially diagonal with respect to the vibrational quantum numbers ν_s , through the application of a unitary transformation to the initial Hamiltonian H

$$\tilde{H} = THT^{-1}, \quad (\text{A1})$$

where $T = e^{iS}$ (S is a Hermitian operator).

The T transformation being a unitary one, both the \tilde{H} and H Hamiltonians are defined on the same rotation–vibration wave function space and possess the same properties (reality, Hermiticity, and invariance when reversing time).

The transformed Hamiltonian \tilde{H} is then the sum of terms related to the different vibrational polyads (that is to say, sets of interacting states) of the molecule, the contributions corresponding to the interaction terms between these different sets of vibrational states being assumed small enough to be accounted for by perturbation. As the T unitary transformations modify the Hamiltonian eigenfunctions it is necessary to apply a corresponding transformation to the dipole moment operator.

A problem arising from use of the contact transformation is that the spectroscopic parameters involved in the transformed Hamiltonian depend on the contact transformation generators. Thus only the combinations of spectroscopic parameters that remain invariant under such transformations can be retrieved. For a given molecule, the number of independent combinations between spectroscopic parameters is a characteristic of the polyad studied but is of course independent of the formalism used to set up the Hamiltonian.

Effective Hamiltonian

Once the contact transformations have been performed, one obtains effective Hamiltonians by projecting the transformed Hamiltonian \tilde{H} on the vibrational spaces under study. The effective Hamiltonian related to a given vibrational set of states $\langle \nu \rangle$ is defined by the relation,

$$\mathcal{H} = P^{(\nu)} \tilde{H} P^{(\nu)}, \quad (\text{A2})$$

where $P^{(\nu)}$ is the projection operator on the Hilbert subspace spanned by the vibrational functions of the $\langle \nu \rangle$ set of states.

These effective Hamiltonians are closely related to the polyad structure of the molecule. If we consider the CHD_3 molecule, its vibrational structure can be pictured by the partially transformed Hamiltonian,

$$\tilde{H} = \tilde{H}_{\{\text{G.S.}\}} + \tilde{H}_{\{\nu_3/\nu_6/\nu_5 \text{ Triad}\}} + \dots \quad (\text{A3})$$

If we build the two first effective Hamiltonians associated with \tilde{H} , we obtain

$$\begin{cases} \mathcal{H}_{\{\text{G.S.}\}}^{(\text{G.S.})} = P_{\{\text{G.S.}\}}^{(\text{G.S.})} \tilde{H} P_{\{\text{G.S.}\}}^{(\text{G.S.})} = \mathcal{H}_{\{\text{G.S.}\}}^{(\text{G.S.})} \\ \mathcal{H}_{\{\text{Triad}\}}^{(\text{Triad})} = \mathcal{H}_{\{\text{G.S.}\}}^{(\text{Triad})} + \mathcal{H}_{\{\text{Triad}\}}^{(\text{Triad})} \end{cases} \quad (\text{A4})$$

An important fact is that all effective $\mathcal{H}_{\{\text{G.S.}\}}$ contain the same set of spectroscopic parameters as well as all $\mathcal{H}_{\{\text{Triad}\}}$ and so on. This corresponds to the ground-state (respectively, Triad) operators contribution to the various effective Hamiltonians. This property allows us to use the so-called vibrational extrapolation scheme.^{27–29}

¹ *Atom–Molecule Collision Theory: A Guide for the Experimentalist*, edited by R. B. Bernstein (Plenum, New York, 1979).

² J. I. Steinfeld and P. L. Houston, in *Laser and Coherence Spectroscopy*, edited by J. I. Steinfeld (Plenum, New York, 1978), pp. 1–123.

³ B. Foy, J. Hetzler, and J. I. Steinfeld, *J. Chem. Phys.* **92**, 7135 (1990).

⁴ J. R. Hetzler and J. I. Steinfeld, *J. Chem. Phys.* **92**, 7135 (1990).

⁵ R. Parson, *J. Chem. Phys.* **93**, 8731 (1990).

⁶ R. Parson, *J. Chem. Phys.* **95**, 8941 (1991).

⁷ W. G. Harter, C. W. Patterson, and F. J. da Paixao, *Rev. Mod. Phys.* **50**, 37 (1978).

⁸ W. G. Harter and C. W. Patterson, *Phys. Rev. A* **19**, 2277 (1979).

⁹ G. Tarrago and J. Dupre-Maquaire, *J. Mol. Spectrosc.* **96**, 170 (1982).

¹⁰ W. L. Meerts and I. Ozier, *J. Chem. Phys.* **75**, 596 (1981), and cited by Dúbal *et al.* (Ref. 11). Dúbal *et al.* calculate an *ab initio* value of $\langle 0|\mu|0 \rangle = 0.013$ D.

¹¹ H.-R. Dúbal, T.-K. Ha, M. Lewerenz, and M. Quack, *J. Chem. Phys.* **91**, 6698 (1989).

¹² F. Menard-Bourcin and L. Doyennette, *J. Chem. Phys.* **88**, 5506 (1988).

¹³ J. J. Klaassen, S. L. Coy, J. I. Steinfeld, and Ch. Roche, *J. Chem. Phys.* **100**, 5519 (1994), following paper.

¹⁴ D. G. Rea and H. W. Thompson, *Trans. Faraday Soc.* **52**, 1304 (1956).

¹⁵ J. K. Winhurst and H. J. Bernstein, *Can. J. Chem.* **35**, 226 (1957).

¹⁶ J. Dupre-Maquaire and G. Tarrago, *J. Mol. Spectrosc.* **96**, 156 (1982).

¹⁷ J. Dupre-Maquaire, Thèse d'état, Orsay, 1986.

¹⁸ D. E. Jennings and W. E. Blass, *J. Mol. Spectrosc.* **55**, 445 (1975).

¹⁹ H. W. Kattenberg and S. Brodersen, *J. Mol. Spectrosc.* **59**, 126 (1976).

²⁰ H. C. Allen, Jr. and E. K. Plyler, *J. Res. Natl. Bur. Stand. A* **63**, 145 (1959).

²¹ M. Lewerenz and M. Quack, *J. Chem. Phys.* **88**, 5408 (1988).

²² A. Campargue, F. Stoessel, M. Chenevier, and H. Ben-Kraïem, *J. Chem. Phys.* **87**, 5598 (1987).

²³ J.-P. Champion, M. Loete, and G. Pierre, in *Spectroscopy of the Earth's Atmosphere and Interstellar Molecules*, edited by K. N. Rao and A. Weber (Academic, New York, 1992), p. 339 ff, and references therein.

²⁴ (a) Ch. Roche, Thèse de Doctorat de l'Université de Bourgogne, Dijon, 1992; (b) Ch. Roche and J.-P. Champion (to be published).

²⁵ Ch. Roche, J.-P. Champion, and A. Valentin, *J. Mol. Spectrosc.* **160**, 517 (1993).

²⁶ L. S. Rothman, R. R. Gamache, R. H. Tipping, C. P. Rinsland, M. A. H. Smith, D. C. Benner, V. M. Devi, J.-M. Flaud, C. Camy-Peyret, A. Perrin, A. Goldman, S. T. Massie, L. R. Brown, and R. A. Toth, *J. Quant. Spectrosc. Radiat. Transfer* **48**, 469 (1992).

²⁷ J.-P. Champion, *Can. J. Phys.* **55**, 1802 (1977).

²⁸ J.-P. Champion and G. Pierre, *J. Mol. Spectrosc.* **79**, 225 (1980).

²⁹V. G. Tyuterev, J.-P. Champion, and G. Pierre, *Mol. Phys.* **71**, 995 (1990).

³⁰N. Husson and G. Poussigue, *J. Phys.* **32**, 859 (1971).

³¹D. L. Gray and G. Robiette, *Mol. Phys.* **37**, 1901 (1979).

³²See AIP document no. PAPS JCPSA-100-5508-23 for 23 pages of tables of assigned overtone and hot-band transitions in CHD_3 . Order by PAPS number and journal reference from American Institute of Physics, Physics

Auxiliary Publication Service, Carolyn Gelbach, 500 Sunnyside Boulevard, Woodbury, New York 11797-2999. The price is \$1.50 for each microfiche (98 pages) or \$5.00 for photocopies of up to 30 pages, and \$0.15 for each additional page over 30 pages. Airmail additional. Make checks payable to the American Institute of Physics.

³³J. H. Van Vleck, *Phys. Rev.* **33**, 467 (1929).

Appendix Three

**"State-to-state rotational energy transfer measurements in methane (CHD_3)
by infrared double resonance with a tunable diode laser"**

J. Chem. Phys. **100**, 5519 (1994).

State-to-state rotational energy transfer measurements in methane (CHD₃) by infrared double resonance with a tunable diode laser

J. J. Klaassen, S. L. Coy, and J. I. Steinfeld

Department of Chemistry, Massachusetts Institute of Technology, Cambridge, Massachusetts 02139

Ch. Roche^{a)}

Laboratoire de Spectronomie Moléculaire et Instrumentation Laser, Université de Bourgogne, Dijon France

(Received 18 October 1993; accepted 4 January 1994)

An infrared double-resonance laser spectroscopic technique is used to study state-resolved rotational energy transfer (RET), vibration-vibration (V-V) transfer, and symmetry-exchanging collisions in asymmetrically deuterated methane (CHD₃). The molecules are prepared in selected rovibrational states of the $\{v_3, v_6\}=1$ dyad using coincidences between CO₂ laser lines and dyad-ground state transitions. Measurements of both the total rate of depopulation by collisions and the rates of transfer into specific rovibrational (v, J, K) levels are carried out using time-resolved tunable diode laser absorption spectroscopy. Total excited-state depopulation and ground-state recovery rates range from 0.5 to 1.0 times the Lennard-Jones collision rate, consistent with relaxation due to short-range forces. V-V ($v_6 \rightarrow v_3$) processes contribute about 10% of the total relaxation rate, and symmetry-changing ($A \leftrightarrow E$) collisions occur at a rate another order of magnitude smaller, viz. $(0.17 \pm 0.02) \mu\text{s}^{-1} \text{Torr}^{-1}$, corresponding to an effective cross section of 0.64 \AA^2 , around $10^{-2} \sigma_{\text{LJ}}$. The symmetry-exchanging collision efficiency for CHD₃ as well as for other systems reported elsewhere (CD₃Cl, CH₃F) can be quantitatively estimated using a simple Förster resonant exchange mechanism. The state-to-state RET rates are modeled using a kinetic master equation. A strong propensity rule, $\Delta K = \pm 3x$ (integer), similar to that found for highly dipolar symmetric tops such as ammonia, applies to CHD₃ as well. We conclude that the flow of energy and angular momentum in molecular relaxation is dominated by the internal level structure of the molecule, rather than by specific details of the intermolecular potential.

I. INTRODUCTION

In a series of measurements on the spherical-top molecules methane (¹³CD₄)¹ and silane,² using the time-resolved infrared double-resonance (TRIRDR) technique, we have established the following propensity rules for collision-induced rotational energy transfer (RET):³

(i) nuclear spin symmetry species do not interconvert on the time scale of the experiments;

(ii) the vector difference $\Delta(\mathbf{J}-\mathbf{R})=0$, where \mathbf{R} is the pure rotational angular momentum and \mathbf{J} is the total angular momentum: in effect, the orientation of the vibrational angular momentum $l=\mathbf{J}-\mathbf{R}$ is conserved in the molecular frame during the collision;

(iii) large changes in angular momentum (up to $\Delta J = \pm 5$) can occur in a single collision;

(iv) in addition to the nuclear-spin and Coriolis sublevel propensity rules [(i) and (ii), respectively], RET is highly selective with respect to the fine-structure designation C^n . This latter selectivity has been eloquently explained by Parson,⁴ drawing on the Harter-Patterson theory of spectral clustering.⁵ The resulting propensity rule can be expressed as

$\Gamma(S_4)$ is unchanged when $\Delta k_R = 0, 4 \dots$ (k_R is the projection of the rotational angular momentum along one of the symmetry axes of the molecule), so that $F_1 \leftrightarrow F_1$ and $F_2 \leftrightarrow F_2$, but $F_1 \not\leftrightarrow F_2$;

$\Gamma(S_4)$ changes when $\Delta k_R = 2, 6 \dots$, which permits $F_1 \leftrightarrow F_2$.

In order to explore the relationship of the molecular symmetry to energy-transfer pathways, we have carried out TRIRDR experiments in trideuteromethane, CHD₃. As noted by Parson,⁴ clustered energy levels⁵ of tetrahedral molecules such as ¹³CD₄ and silane behave effectively as do those of symmetric tops during a collision, since the vibration-rotation interaction distorts the molecule along or perpendicular to one of its symmetry axes. In these levels, during the very short duration of a molecular collision, the rotational angular momentum is localized on one of the equivalent symmetry axes, so that symmetric-top propensity rules may be expected to apply to changes in that angular momentum. CHD₃ already possesses the symmetry (and thus the level structure) assumed by tetrahedral molecules during a collision; it is an oblate symmetric top ($A_0 = B_0 = 3.279 \text{ 18 cm}^{-1}$, $C_0 = 2.628 \text{ 96 cm}^{-1}$).^{6,7} A permanent dipole moment $\mu_0 = 0.006 \text{ D}$ has been measured for CH₃D,⁸ and Dübäl *et al.*⁹ have concluded on the basis of this and related work¹⁰ that μ_0 for CHD₃ should also be close to 0.006 D . The CHD₃-perturber intermolecular potential differs from the CH₄- (or CD₄-)perturber intermolecular potential primarily from effects due to the shift in the center of mass, as discussed further below. CHD₃ thus represents an ideal test case for separating the effects of molecular symmetry (level structure) from those of collision dynamics in inelastic scattering processes.

Previous TRIRDR experiments on CHD₃ (Ref. 11) used

^{a)}Present address: Department of Chemistry, University of Durham, England, U.K.

a c.w. CO₂ laser to probe levels pumped by a pulsed CO₂ laser. While such experiments are unable to interrogate specifically selected rovibrational levels, they did yield a V-V relaxation rate between the ν_3 and ν_6 levels (approximately "gas kinetic"), an apparent relaxation rate between *A* and *E* symmetry levels $[(2.3 \pm 0.2) \times 10^5 \text{ s}^{-1} \text{ Torr}^{-1}]$, presumably due to resonant V-V exchange collisions, and an overall V-(*T,R*) relaxation rate $[(1.16 \pm 0.35) \times 10^3 \text{ s}^{-1} \text{ Torr}^{-1}]$. Use of a tunable diode laser probe, as in our previous experiments on ¹³CD₄ (Ref. 1) and silane,² allows us to determine state-to-state rotational energy transfer pathways and the dependence of the inelastic collision rates on ΔJ and ΔK . We are also able to identify excited-state absorptions to overtone and combination levels from the $\{\nu_3, \nu_6\}$ dyad. This aids in the assignment of the hot-band and overtone spectra, as discussed below.

A further motivation for these studies is the wish to understand pressure broadening in terms of inelastic collision rates. While much of the literature¹² on pressure broadening of infrared transitions in methane reports data for atmospheric collision partners (air, N₂ and/or O₂), self-broadening coefficients are available for several infrared¹³ and Raman bands of CH₄,¹⁴ and CD₄.¹⁵ The (*J,C*[∞])-averaged infrared and Raman broadening coefficients ($\bar{\gamma}/p$) for CH₄ are both around 0.075 cm⁻¹ atm⁻¹, while those for CD₄ are somewhat larger (approximately 0.085 cm⁻¹ atm⁻¹). Pure rotational self-broadening coefficients for CH₃D^{8,16} are in the range 0.06–0.07 cm⁻¹ atm⁻¹, but for the $\nu_6 \leftarrow 0$ band¹⁷ the corresponding values are 0.078–0.088 cm⁻¹ atm⁻¹ (both at 295 K). There are no corresponding data available for CHD₃. We have measured $\bar{\gamma}/p$ for several transitions in the CHD₃ $\nu_3 \leftarrow 0$ band; these are reported and compared with time-domain relaxation measurements in Sec. IV C.

In the rest of this paper, we briefly describe the experimental methods (Sec. II) and provide essential background on aspects of the spectroscopy (Sec. III A) and kinetic modeling (Sec. III B). Experimental results are presented in Sec. IV, and discussed in Sec. V. A brief preliminary account of this work has appeared.¹⁸

II. EXPERIMENT

A. Double-resonance measurements

The TRIRD experiments were carried out using a pulsed TEA CO₂ pump laser and a tunable lead-salt semiconductor diode probe laser as in previous studies of silane² and ammonia.¹⁹ The pump and probe beams are copropagated through the 1.8 m long cell in order to obtain maximum overlap through the sample. Care must be taken, however, to prevent pump laser radiation from reaching either the diode or the detector. This was accomplished by polarizing the two beams perpendicular to each other and utilizing the difference in reflectivity for *s*- and *p*-polarized light. A ZnSe plate is placed in the probe beam plane at an angle of 75°. At this angle the transmission of the probe beam is high (~96%). Approximately 60% of the pump beam, which is *s* polarized with respect to the ZnSe plate, is reflected from the plate. With 20–30 mJ of CO₂ laser pulse energy, the reflected portion of the pump is sufficient to reach 60% saturation of

the CHD₃ transition. The pump and probe beams are separated by a diffraction grating at the end of the cell. The probe is sent through a monochromator, further isolating it from any scattered pump radiation.

The pulsed laser used in these experiments was a Laser Sciences Inc. PRF-150S which has a gain bandwidth of ~1 GHz. In some instances, as discussed in the following section, this would be sufficient to pump more than one line in the CHD₃ fundamental, thereby complicating interpretation of the data. In order to alleviate this problem, a low-pressure gain cell was introduced in the cavity. This reduced the laser bandwidth sufficiently to eliminate the possibility of pumping transitions detuned from the CO₂ laser line by more than a few hundred MHz.

CHD₃ (98 atom % D) obtained from Merck Sharpe and Dohme of Canada was used without further purification. Sample pressures, generally in the range 5 to 500 mTorr, were measured with a capacitance manometer (MKS Baratron, model 227 A). Further experimental details will be given elsewhere.²⁰

B. Self-broadening measurements

Self-broadening coefficients for several lines in the CHD₃ $\nu_3 \leftarrow 0$ band were determined using the experimental arrangement, diode laser sweep-integration technique,²¹ and data reduction procedures previously employed for ozone self-broadening measurements.²² The results are given below in Sec. IV C.

III. ROVIBRATIONAL ENERGY LEVELS OF CD₃H

In order to interpret the TRIRD measurements, we must possess secure assignments for the excited-state absorptions (hot-band transitions) which are probed following pulsed laser excitation. While the spectroscopy of the CHD₃ ground state^{6,7} and vibrational fundamentals^{23–26} is well known, that of the overtone region in the vicinity of 2000 cm⁻¹, and of the hot band system associated with it, was largely unknown when we began this work.

The vibrational level structure of CHD₃ consists of the (ν_3, ν_6) dyad at 1000 cm⁻¹, the ν_5 level near 1300 cm⁻¹, and a polyad situated around 2000 cm⁻¹ which includes the ν_4 and ν_2 fundamentals, the $2\nu_3$, $2\nu_5$, and $2\nu_6$ overtone levels, and the $\nu_3 + \nu_5$, $\nu_3 + \nu_6$, and $\nu_5 + \nu_6$ combination levels. There are relatively few detailed studies in the latter region.^{27–29} and none of these furnished assignments for the interacting $2\{\nu_3, \nu_6\}$ bands. The vibrational spectroscopy^{9,30,31} and dynamics³² of highly excited C–H stretching mode (ν_1) levels have also been analyzed, but these levels are not pertinent to the work described here.

Assignments for the $2\nu_3 \leftarrow 0$ overtone band were made from a high-resolution Fourier transform (FTIR) spectrum of CHD₃ recorded at the National Research Council of Canada in Ottawa. Frequencies for $2\nu_3 \leftarrow \nu_3$ hot-band transitions were then calculated using known rovibrational energies for $\nu_3 = 1$ levels^{25,26} and compared with an experimental FTIR spectrum of the 1000 cm⁻¹ region recorded by Valentin in Paris. In most cases, the calculated line positions were sufficiently accurate to give unambiguous identification of the hot-band

TABLE I Pump and probe transitions in CHD₃($\nu_1, \nu_2 = 1$) levels.

(A) CO ₂ laser-CHD ₃ absorption coincidences			
CO ₂ laser transitions	Frequency (cm ⁻¹) ^a	CHD ₃ level pumped ^b	$\delta\nu$ (cm ⁻¹) ^c
10R(22)	977.214	$\nu_2RP(9,3)A$	-0.011
10R(24)	978.472	$\nu_2QQ(12,7)E$	0.0001
		$\nu_2QQ(11,5)E$	0.033
10R(34)	984.383	$\nu_2QQ(12,9)A$	0.002
		$\nu_2QQ(16,14)E$	-0.010

(B) CHD₃ levels probed (all in $2\nu_2-\nu_3$)(i) Pump $\nu_3=1, J=12, K=9$ (A)

CHD ₃ transition	ν_{calc} (cm ⁻¹) ^d	(obs-calc) ^{e,f} cm ⁻¹ × 10 ⁻³	ΔE cm ⁻¹	ΔJ	ΔK
QR(3,0)	1009.8317	-0.8 ^e	-403.23	-9	-9
QR(3,3)	1009.9409	-1.9 ^e	-405.57	-9	-6
QR(4,0)	1015.0985	-1.1 ^e	-379.60	-8	-9
QR(4,3)	1015.6864	-0.8 ^e	-382.41	-8	-6
QR(5,0)	1019.9388	-0.9 ^e	-349.72	-7	-9
QR(5,3)	1020.8480	-1.0 ^e	-352.91	-7	-6
QR(6,0)	1024.3739	-0.7 ^e	-313.49	-6	-9
QR(6,3)	1025.4684	-0.5 ^e	-316.99	-6	-6
QR(6,6)	1027.3683	1.6 ^e	-325.64	-6	-3
QR(7,0)	1028.4618	-0.8 ^e	-270.88	-5	-9
QR(7,6)	1032.6163	-1.1 ^e	-284.73	-5	-3
QR(8,0)	1032.2692	-0.7 ^e	-221.85	-4	-9
QR(8,6)	1036.3984	-0.5 ^e	-236.91	-4	-3
QR(9,3)	1037.0455	0.9 ^e	-170.51	-3	-6
QR(9,6)	1040.6021	-1.5 ^e	-182.35	-3	-3
QR(9,9)	1044.7155	-2.2 ^e	-198.28	-3	0
QR(10,0)	1039.2726	0.4 ^e	-104.45	-2	-9
QR(10,6)	1043.9536	-2.1 ^e	-121.15	-2	-3
QR(10,9)	1049.4076	-0.6 ^e	-139.54	-2	0
QR(11,3) ^g	1043.6626	-0.3 ^e	-40.47	-1	-6
QR(11,6)	1047.0845	-1.6 ^e	-53.35	-1	-3
QR(11,9)	1052.8571	-2.4 ^e	-73.28	-1	0
QR(12,6)	1050.0734	-4.1 ^e	21.00	0	-3
QR(12,9)	1055.7759	-1.6 ^e	0.00	0	0
QR(12,12)	1061.9841	2.5 ^e	-23.67	0	+3
QR(13,9) ^h			80.07	+1	0

(ii) Pump $\nu_3=1, J=12, K=7$ (E)

CHD ₃ transition	ν_{calc} (cm ⁻¹) ^d	(obs-calc) ^{e,f} cm ⁻¹ × 10 ⁻³	ΔE cm ⁻¹	ΔJ	ΔK
QR(3,1)	1009.8767	-0.8 ^e	-418.28	-9	-6
QR(3,2)	1009.9686	-1.2 ^e	-419.11	-9	-5
QR(4,1)	1015.1829	5.7 ^e	-394.70	-8	-6
QR(4,2)	1015.4107	-1.0 ^e	-395.67	-8	-5
QR(4,4)	1015.7613	-1.1 ^e	-398.97	-8	-3
QR(5,1)	1020.0498	-1.0 ^e	-364.85	-7	-6
QR(5,2)	1020.3697	-1.3 ^e	-365.93	-7	-5
QR(6,1)	1024.5003	-1.0 ^e	-328.66	-6	-6
QR(6,2)	1024.8731	-0.6 ^e	-329.84	-6	-5
QR(6,4)	1026.2266	-0.6 ^e	-334.32	-6	-3
QR(6,5)	1026.9976	-0.1 ^e	-337.34	-6	-2
QR(7,1)	1028.5950	-1.0 ^e	-286.07	-5	-6
QR(7,4)	1030.5245	-1.4 ^e	-292.21	-5	-3
QR(8,1)	1032.4035	-1.0 ^e	-237.06	-4	-6
QR(8,4)	1034.4012	-1.2 ^e	-243.58	-4	-3
QR(8,5)	1035.5640	-2.6 ^e	-247.32	-4	-2
QR(8,7)	1038.2214	-0.4 ^e	-256.36	-4	0
QR(8,8)	1038.9410	-2.0 ^e	-260.76	-4	+1
QR(9,1)	1035.9884	-0.8 ^e	-181.60	-3	-6
QR(9,4)	1037.9764	-0.8 ^e	-188.43	-3	-3
QR(9,5)	1039.1676	-1.0 ^e	-192.41	-3	-2
QR(9,7)	1042.2179	-0.8 ^e	-202.40	-3	0
QR(9,8)	1043.8175	-1.0 ^e	-207.96	-3	+1
QR(10,2)	1039.7845	-0.8 ^e	-121.12	-2	-5
QR(10,4)	1041.3364	-2.1 ^e	-126.78	-2	-3

TABLE I. (Continued.)

CHD ₃ transition	ν_{calc} (cm ⁻¹) ^d	(obs-calc) ^{e,f} cm ⁻¹ × 10 ⁻³	ΔE cm ⁻¹	ΔJ	ΔK
QR(10,7)	1045.6477	-3.1 ^e	-141.61	-2	0
QR(10,8)	1047.5357	-0.5 ^e	-147.85	-2	+1
QR(11,4)	1044.5413	-1.2 ^e	-58.62	-1	-3
QR(11,5)	1045.6782	-4.6 ^e	-62.93	-1	-2
QR(11,7)	1048.7636	2.4 ^e	-74.12	-1	0
QR(11,8)	1050.7051	-2.7 ^e	-80.82	-1	+1
QR(11,10)	1054.9935	-1.4 ^e	-95.39	-1	+3
QR(11,11)	1056.2383	-5.3 ^e	-101.88	-1	+4
QR(12,7)	1051.6969	-1.9 ^e	0.00	0	0
QR(12,8)	1053.6000	-5.5 ^e	-7.03	0	+1
QR(12,10)	1058.1985	2.0 ^e	-23.00	0	+3

^aCO₂ transition frequencies from Ref. 33.^bCHD₃ assignments from Ref. 25.^cCHD₃ transition frequencies from an FTIR spectrum recorded by A. Valentin (Refs. 35 and 37).^dSee Ref. 37.^eThe measured $2\nu_2-\nu_3$ transition frequencies were obtained from either the Valentin FTIR spectrum (Refs. 35 and 37), designated by e, or from our diode-laser absorption scans, designated by f. The experimental precision of these data are $\pm 4 \times 10^{-4}$ cm⁻¹ for e and $\pm 5 \times 10^{-3}$ for f.^fSee footnote e.^gQR(11,3) is A₁-A₂ resolved. The component at 1043.6626 cm⁻¹ was used in the energy transfer measurements. The amplitude of the double resonance signal was multiplied by two to compensate for the reduction of degeneracy due to resolution of A₁-A₂. The other component of QR(11,3) is at 1043.6729 cm⁻¹.^hQR(13,9) was identified by double resonance at 1058.460 cm⁻¹.

transitions used in the TRIRDR experiments. Population in the $\nu_6=1, J=8, K=4, l=1$ level pumped by the CO₂ 10R(22) laser line was monitored via a hot-band line at 1027.768 cm⁻¹ which has been identified as a ^PQ transition to the $\nu_6=2$ (A₁ or A₂), $J=8, K=3, l=0$ level.

Table I gives a list of the CHD₃ levels pumped by the CO₂ laser,³³ along with a list of the $2\nu_2-\nu_3$ transitions probed in the TRIRDR experiments. Both the ν_3 ^QQ(12,7)E and the ν_3 ^QQ(11,5)E transitions are pumped by the CO₂ 10R(24) laser transition. Even though the ^QQ(11,5)E transition is ~ 0.03 cm⁻¹ off-resonance, enough population would be moved by the broadband laser to cause difficulties in interpreting state-to-state RET data.^{2(b)} To alleviate this problem, a low-pressure intracavity gain cell was employed as described above. This narrowed the laser bandwidth sufficiently to reduce direct pumping of the ($\nu_3=1, J=11, K=5, E$) level to an undetectable level. In the case of the CO₂ 10R(34) laser line, both the ν_3 ^QQ(12,9)A and the ν_3 ^QQ(16,14)E transitions are efficiently pumped. However, the A and E levels are only slowly interconnected by collisions on the time scale of the RET measurements [propensity rule (i), noted in Sec. I; indeed, the slow relaxation between nuclear-spin symmetry states was exploited in previous studies on silane,² in which independent measurements could be made on A, E, and F symmetry levels, all pumped by the same CO₂ laser line]. The fastest process which can interconvert the A and E symmetry species is a resonant V-V exchange process, which proceeds at a rate which is only 1% or 2% of the total relaxation rate.¹¹ Therefore, no attempt was made to narrow the 10R(34) laser output, since this slow

TABLE II. Ground and excited-state total relaxation rates in CHD₃. (A) Ground-state recovery in self-collisions. (B) Excited-state depopulation.

(A)	Depopulated level	$(p\tau)^{-1}$ $\mu\text{s}^{-1}\text{Torr}^{-1}$	k_{eff} $\text{cm}^3\text{molecule}^{-1}\text{s}^{-1}$	σ_{eff} cm^2		
	(9,3)	8.4 ± 1.0	2.59×10^{-10}	32×10^{-16}		
	(12,7)	8.7 ± 0.3	2.68	33		
	(16,14)	11.9 ± 0.6	3.67	45		
	(12,9)	9.4 ± 0.6	2.90	36		
(B)	Pumped level	Collision partner	$(p\tau)^{-1}$ $\mu\text{s}^{-1}\text{Torr}^{-1}$	k_{rel} $\text{cm}^3\text{molecule}^{-1}\text{s}^{-1}$	σ_{rel} cm^2	σ_{LJ}^a cm^2
	$\nu_3(12,9)$	CHD ₃	12.7 ± 0.04	3.9×10^{-10}	48×10^{-16}	54×10^{-16}
		He	7.7 ± 0.2	2.4	13	28
		Ar	8.1 ± 0.1	2.5	36	47
		H ₂	10.4 ± 0.1	3.2	17	35
		CH ₄	14.0 ± 0.1	4.3	51	54
	$\nu_3(12,7)$	CHD ₃	13.6 ± 0.2	4.2	51	54
		CH ₃ F	13.9 ± 0.1	4.3	66	64
	$\nu_6(8,4,l=1)$	CHD ₃	13.3 ± 1.0	4.1	50	54
		H ₂	12.1 ± 2.0	3.8	20	35
		NH ₃	15.1 ± 2.0	4.7	54	

*See Ref. 40.

process would not interfere with measurement on the much faster RET process.

A full analysis of the 2000 cm⁻¹ region of CHD₃ has been carried out using the spherical tensor model developed by Moret-Bailly, Champion, and their co-workers,³⁴ which has recently been extended to lower-symmetry cases, specifically symmetric-top molecules whose equilibrium configuration belongs to the C_{3v} point group.^{7,35,36} The details of this work are published elsewhere.³⁷

IV. RESULTS

A. Total depopulation rates

Total depopulation rates for individually pumped levels were determined by measuring relaxation times of three-level TRIRDR signals. A single exponential was fit to the decaying portion of the signal. For measuring ground-state recovery rates, we used $\nu_3 \leftarrow 0$ probe transitions³⁸ in order to avoid complications arising from population arriving in the upper level of the probe transition; the ν_3 level lies ~ 300 cm⁻¹ higher than the pumped $\{\nu_3/\nu_6\}$ dyad, and V-V transfer into ν_3 is negligible. Since the $\nu_3 \leftarrow 0$ band occurs near 1300 cm⁻¹, a MgF₂ filter was sufficient for separating the pump and probe beams. The results of the measurements are given in Table II, Part A.

Total depopulation rates for $\{\nu_3/\nu_6\}$ dyad levels were measured by following the decay of excited-state absorption (3-level) signals arising from the directly pumped level, using the $2\nu_3 \leftarrow \nu_3$ transitions listed in Table I(B) and the $2\nu_6 \leftarrow \nu_6$ transition identified in Sec. III A. These results are given in Table II, Part B. The rates for both ground-state recovery and excited-state depopulation show no strong dependence on J, K and nuclear-spin symmetry species. While there is also no significant variation in relaxation rate between the ν_3 and ν_6 levels, the rates appear to be larger in the vibrationally excited state than in the ground state. Similar behavior was noted³⁹ in the experiments on ¹³CD₄. It should

be noted, however, that ground-state recovery involves equilibration among a large number of thermally populated levels, while excited-state relaxation is essentially a pure depopulation process. The exponential decay parameter obtained in the former case should therefore be regarded as the lowest eigenvalue of the rate matrix, rather than a direct relaxation rate.

The measured relaxation rates (inverse relaxation times) have been converted to effective cross sections in Table II for convenient comparison with Lennard-Jones cross sections,⁴⁰ using the standard relationship $\sigma = k/(8k_B T/\pi\mu_{AB})^{1/2}$. For the monoatomic collision partners He and Ar, as well as for H₂, the rotationally inelastic cross sections are one-half to \sim two-thirds Lennard-Jones, while for polyatomic collision partners (CHD₃, CH₄, CHF₃) the cross section is very nearly equal to the Lennard-Jones.⁴⁰ In particular, highly dipolar collision partners (CHF₃, NH₃) are not markedly more efficient than nonpolar species. This is consistent with RET due to short-range forces, as discussed in Sec. V.

B. V-V Transfer and symmetry-changing excitation transfer

Two possible types of vibrational exchange processes were investigated for this system, viz., equilibration between the ν_3 and ν_6 components of the dyad,



and a resonant vibrational exchange process which appears to interconnect nuclear-spin symmetries,



In Eq. (2), the asterisk denotes vibrational excitation in the ν_3 mode.

The V-V exchange rate k_{36} for process (1) was measured by pumping the $\nu_6=1, J=8, K=4, l=1$ level ($K-l=3$, thus A symmetry) and monitoring several (J, K) levels

TABLE III. V-V transfer rates from $\nu_3=1, J=8, K=4, l=1$. Collision partner is CHD₃ at 295 K.

Final level	k_{36} ($\mu\text{s}^{-1} \text{Torr}^{-1}$)
$\nu_3(11,9)$	1.2 ± 0.6
$\nu_3(8,3)$	0.78 ± 0.06
$\nu_3(4,0)$	0.83 ± 0.03

in $\nu_3=1$, also of A symmetry, by $2\nu_3-\nu_3$ transient absorption. The resulting signals were fit to the three-level model (ν_3, ν_6 g.s.) used in previous analyses^{1(b),2(c)} of V-V relaxation by TRIRDR, which gives

$$n_6(t) = C_6 \exp(-\lambda_+ t), \quad (3)$$

$$n_3(t) = C_3 [\exp(-\lambda_- t) - \exp(-\lambda_+ t)], \quad (4)$$

where

$$\lambda_+ = k_{36}(1 + \xi) \quad (5)$$

and

$$\lambda_- = (k_{06} + k_{03})/(1 + \xi) \quad (6)$$

with

$$\xi = (g_6/g_3) \exp[-(E_6 - E_3)/kT], \quad (7)$$

where $(g_6/g_3)=2$ and $(E_6 - E_3)=31.3 \text{ cm}^{-1}$.⁶ The λ_+ eigenvalues were determined from a range of CHD₃ pressures, and the resulting values for k_{36} are given in Table III. The rates are about an order of magnitude smaller than the pure RET rate, and are essentially independent of the ν_3 rotational state which is monitored. Similar results were found^{1(b)} for the ($\nu_2 \rightarrow \nu_4$) V-V rates in ¹³CD₄.

The resonant vibrational exchange process (2) was determined by monitoring an A-symmetry level ($\nu_3=1, J=11, K=9$) after pumping E-symmetry levels in $\nu_3=1$ ($J=12, K=7$ plus a small amount of $J=11, K=5$) with the CO₂ 10P(24) line. The analysis was carried out in terms of a three-level model similar to that used for V-V transfer, so that equations of the form (3)-(6) are obtained with $\lambda_+ = k_{A-E}(1 + \xi)$ and $\xi = (g_A/g_E) \exp(-E^*/k_B T)$.⁴¹ The value obtained for k_{A-E} in self-collisions, $(0.17 \pm 0.02) \mu\text{s}^{-1} \text{Torr}^{-1}$, is in reasonable agreement with Doyenette's value,¹¹ $(0.23 \pm 0.02) \mu\text{s}^{-1} \text{Torr}^{-1}$, and justifies the assertion made in Sec. III A, and used below, that the A- and E-symmetry levels pumped by the CO₂ 10R(34) line are only weakly coupled by collisions and can be considered to relax independently of each other.

C. Pressure broadening and inelastic collisions

Before turning to the state-to-state structure of the RET rates, we consider the question raised earlier, namely, whether the collision-broadening coefficient γ/p is wholly accounted for by the RET rates in the upper and lower levels of the spectroscopic transition. Since there were no other measurements of infrared linewidths for CHD₃, we measured γ/p for several transitions in the $\nu_3=0$ band as described in Sec. II B. The results are given in Table IV, along with values of γ/p estimated from the generally accepted relation⁴²

$$\gamma/p (\text{MHz/Torr}) = (1/2\pi)(k_u + k_l)/2. \quad (8)$$

The inelastic collision contributions appear to underestimate the broadening coefficient by about 30%-40%; even if one takes into account that k_l is a lower limit on the true ground-state recovery rate, and sets $k_l = k_u$ in Eq. (8), the predicted value of γ/p is not larger than 2.1 MHz/Torr, still less than the measured values. This can be understood if we interpret the discrepancy as the contribution of elastic collisions to the pressure broadened width. Our time resolved measurements are sensitive only to population changes, whereas frequency domain measurements are sensitive to both inelastic and elastic collisions. Similar discrepancies have been noted in previous studies of methane,⁵ ammonia,¹⁹ and ozone,⁴³ and also in recent TRIRDR experiments on methane (CH₄) carried out in this laboratory.

D. State-to-state rotational energy transfer

Four-level TRIRDR signals were recorded for all accessible $2\nu_3-\nu_3$ transitions in CHD₃ following pumping either A-symmetry ($\nu_3=1, J=12, K=9$) or E-symmetry ($\nu_3=1, J=12, K=7$) levels with the pulsed CO₂ laser. In the latter case, the intracavity gain cell was used in the laser to suppress interference from the ($J=11, K=5$) level. A list of probe transitions has been given in Table I.

The time-dependent absorption signals were fit using a kinetic master equation model. The objective when modeling the double resonance signals is to obtain a set of state-to-state rotational energy transfer rates from the parent level populated by the CO₂ laser pump to all other rotational levels that could be probed in the experiment. This set of rates provides the most detailed information about those properties of the molecule which most strongly affect the RET process. This set of rates can be epitomized as a few propensity rules which apply for CHD₃. By comparing these propensity rules with those that we already know for spherical-top molecules

TABLE IV. Self-broadening and self-relaxation for CHD₃ rovibrational levels.

Transition	Measured γ/p (MHz/Torr)	CHD ₃ lower level	CHD ₃ upper level	k_l		γ/p calculated from Eq. (i) MHz/Torr
				$(\mu\text{s Torr})^{-1}$		
$\nu_3^Q(18,15)$	2.57 ± 0.15	(9,3)	$\nu_3(8,4)$	8.4	13.3	1.73
$\nu_3^Q(4,3)$	3.07 ± 0.12	(12,7)	$\nu_3(12,7)$	8.7	13.4	1.76
		(12,9)	$\nu_3(12,9)$	9.4	12.7	1.76

possessing full tetrahedral symmetry, such as methane¹ and silane,² and for other symmetric tops such as ammonia,¹⁹ we can ascertain the roles and relative importance of intermolecular forces and molecular symmetry in the energy transfer process.

In order to obtain a set of state-to-state RET rates, we need an appropriate model with which to reduce our experimental measurements. Under the conditions of our experiment, a particular level may obtain population in a single collision directly from the parent level or by a sequence of multiple collisions through a series of intermediate levels. This leads to difficulties in obtaining rates for the direct process of RET from the parent level to the probed level, since two or more highly probable consecutive collisions can give rise to the same sort of temporal behavior as a low probability direct process. We deal with the ambiguities caused by multiple collision processes by using a master equation model. We let \mathbf{N} be a column vector representing the populations of all the rotational levels included in the model and \mathbf{K} the matrix containing the individual state-to-state rates that link these levels. The time evolution of \mathbf{N} is given by

$$\dot{\mathbf{N}} = \mathbf{K}\mathbf{N}. \quad (9)$$

The time evolution of the populations, $\mathbf{N}(t)$, can be found either by calculating the eigenvalues⁴⁴ of \mathbf{K} , or as we do here, by numerical solution of the set of coupled first order differential equations

$$\frac{dN_i}{dt} = \sum_{(i \neq j)} k_{ij}N_j + k_{ii}N_i. \quad (10)$$

Here k_{ij} is the direct state-to-state rate from level j to level i . The reverse rate for going from level i to level j , k_{ji} , is related to k_{ij} by detailed balance,

$$k_{ji} = k_{ij}(g_j/g_i)e^{-(E_j - E_i)/kT}. \quad (11)$$

Here g_i and g_j are the degeneracies of levels i and j , respectively, and E_i and E_j are the energies of these levels. k_{ii} is the total depopulation rate from level i which is related to the k_{ij} 's by

$$k_{ii} = - \sum_{(i \neq j)} k_{ji}. \quad (12)$$

Three additional modifications to this general description of the master equation must be included to adequately model the experimental data. First, a time dependent term must be added to the pumped level to account for the population of this level by the CO₂ laser pulse

$$\frac{dN_p}{dt} = \sum_{(\text{all } j)} k_{pj}N_j + \alpha I(t). \quad (13)$$

$I(t)$ is the temporal profile of the CO₂ laser pulse and α is an adjustable parameter in the model used to scale the calculated $N_i(t)$ to the experimentally measured curves. Second, the relatively fast vibrational energy transfer between the CHD₃ ν_3 and ν_6 Coriolis-coupled vibrational modes must be accounted for in the analysis of the RET rates. This V-V rate has been measured in other experiments to be $\sim 1.0 \mu\text{s}^{-1} \text{Torr}^{-1}$ (see Sec. IV B and Ref. 11), slightly less than 10% of the total depopulation rate. We model this process by

treating the ν_6 vibrational mode in a way analogous to that employed by Coy *et al.*⁴⁵ in their treatment of rotational relaxation in formaldehyde, namely, as a set of "basin" levels among which reversible energy transfer may occur. By contrast, "bath" levels are those to which population flows irreversibly and does not return (to any appreciable extent) to either basin or parent levels. The ν_6 level is thus treated as a single additional level in the master equation to which all of the rotational levels in ν_3 are connected by the same rate, $k_{\nu_6 - \nu_3} = 1.4 \mu\text{s}^{-1} \text{Torr}^{-1}$, which is found from the measured rate for $k_{\nu_3 - \nu_6}$ ($0.8 \mu\text{s}^{-1} \text{Torr}^{-1}$) by detailed balance [Eq. (11)]. The population that accumulates in ν_6 is allowed to feed back into each rotational level of ν_3 at the latter rate. The third modification is to include a small total loss rate, k_{loss} , to account for all the additional processes, such as V-T relaxation and vibrational swap [Eq. (2)], which couple the population of a particular level to the bath and also for the overall loss due to beam flyout. This term is subtracted from the diagonal elements, k_{ii} , of \mathbf{K} so that the k_{ii} are given by

$$k_{ii} = - \sum_{(i \neq j)} k_{ji} - k_{\text{loss}}. \quad (14)$$

We have two independent sets of rotational energy transfer measurements for CHD₃, one for the A-type symmetry levels and another for the E-type symmetry levels. As noted earlier, these two different nuclear spin states do not interconvert efficiently by collisions. The fastest process which can cause apparent interconversion, the vibrational swap process [Eq. (2)], occurs on a much slower time scale than that for rotational energy transfer. For the purposes of modeling RET, we treat the A- and E-type symmetry species as separate modifications of CHD₃. Master equation modeling of the A-type symmetry species contains only levels of A-type symmetry, having K values equal to 0, 3, 6, 9, ... Similarly, for the E-type levels, only E-symmetry species are considered, with K values equal to 1, 2, 4, 5, 7, ...

This segregation of rotational levels by symmetry species helps reduce the number of coupled differential equations which must be included in the master equation analysis, but still the number of levels is quite large. For both sets of data we include all levels which are lower in energy than the parent level and all levels that are less than $\sim 2kT$ greater than the parent. J values up to and including $J=13$ were retained for both sets; the value of J_{max} was varied in some runs but this had little effect on the calculated results. This gives us 58 levels for the A symmetry set and 96 levels for the E symmetry set. In the rate matrix \mathbf{K} , there are $N(N-1)/2$ independent state-to-state rates, the remainder being determined by detailed balance [Eq. (11)]. Herein arises one of the fundamental difficulties in studying rotational energy transfer in polyatomics: The number of independent parameters in the model greatly outnumbers the experimental measurements that can reasonably be made on the system.

In order to circumvent this shortcoming, the experimenter is forced to assume some relationship between the state-to-state rates. Empirical fitting laws based on the change in energy or the change in angular momentum are often used in modeling rotational energy transfer. But this is precisely the question we want to address, namely, what type

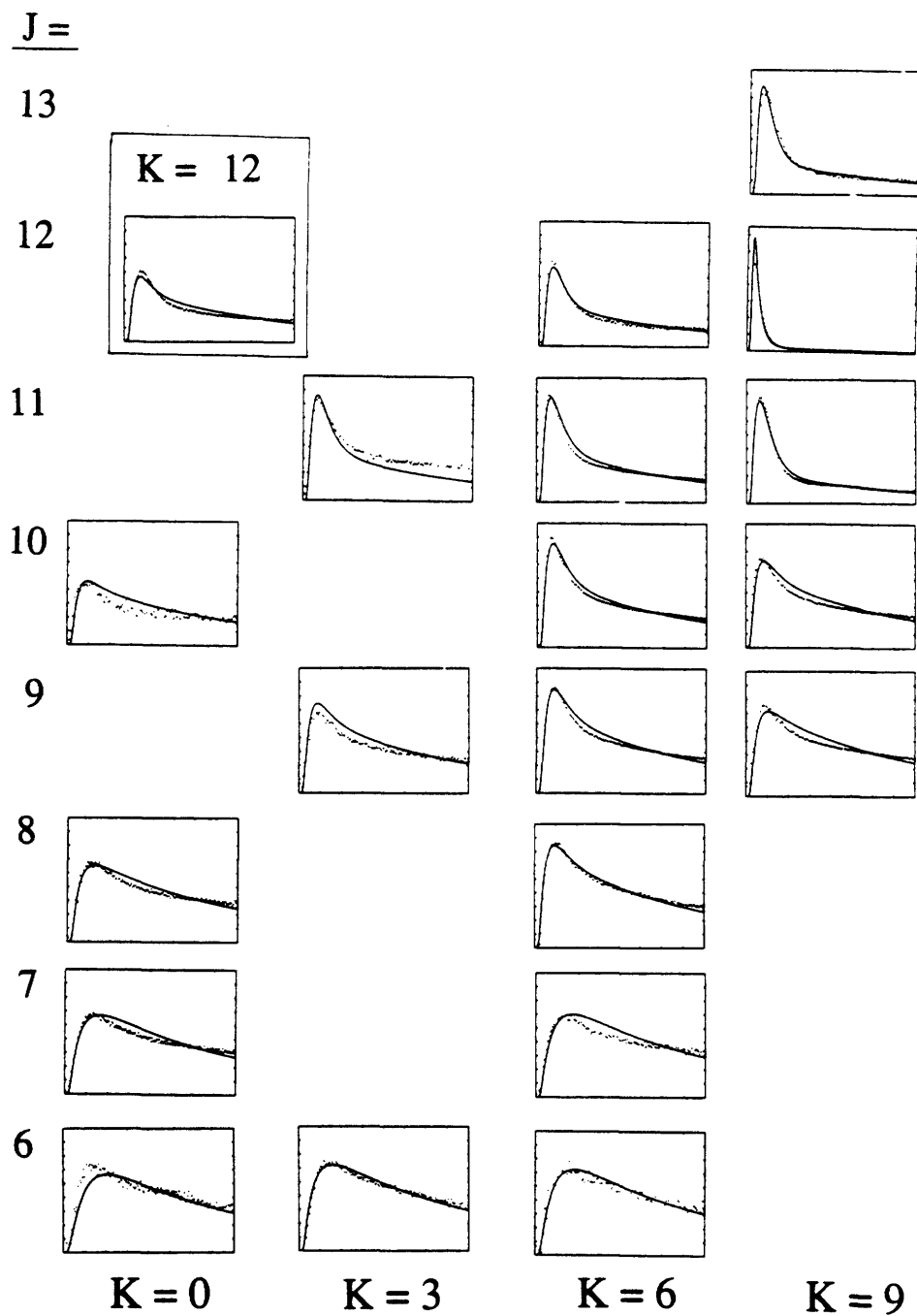


FIG. 1. Experimental TRIRD signals and model simulations for *A*-symmetry levels. *K*=0, 3, 6, and 9 levels are shown, for *J* values between 6 and 13 (the *J*=12, *K*=12 signal is shown in the upper left corner). The time scale is 0–16 μs in all cases and the vertical $\Delta I/I$ scale is 0 to 0.09 absorbance units, except for the parent (*J*=12, *K*=9) signal for which the vertical scale is 0 to 1.5 absorbance units and the *J*=11, *K*=9 ($\Delta J = -1$, $\Delta K = 0$) signal for which the vertical scale is 0 to 0.18 absorbance units. The *J*=3, 4, and 5 (*K*=0 and 3) signals are not displayed; they look very much like the corresponding *J*=6 and 7 signals.

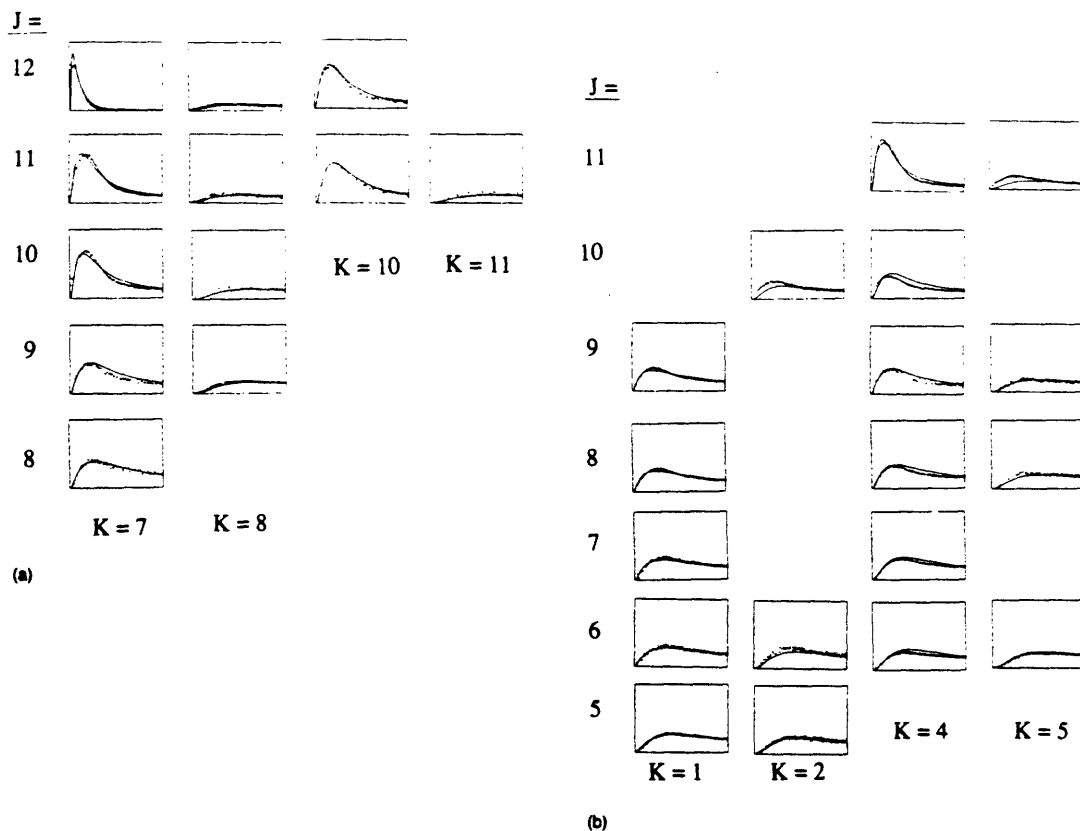


FIG. 2. Experimental TRIRDR signals and model simulations for E -symmetry levels. $K=1, 2, 4, 5, 7, 8, 10,$ and 11 levels are shown, for J values between 5 and 12. The time scale is $0\text{--}10\ \mu\text{s}$ in all cases and the vertical $\Delta I/I$ scale is 0 to 0.05 absorbance units, except for the parent ($J=12, K=7$) signal for which the vertical scale is 0 to 0.75 absorbance units. The $J=3$ and 4 ($K=1, 2,$ and 4) signals are not displayed; they look very much like the corresponding $J=5$ and 6 signals.

of propensity rules govern the RET process in CHD₃. By adopting a fitting law *a priori*, we forfeit answering that question because the fitting law itself necessarily dictates the relationship between the state-to-state rates. Even so, it is useful to begin with two simple scaling laws^{42(a),46} as starting points for a more detailed analysis of the RET rates. Terms in the rate matrix are then individually varied from these initial values to obtain the best fit to the experimental data, as described below.

A widely used form is the exponential gap law (EGL),⁴⁷

$$k_{f \rightarrow i} = (2J_f + 1)k_0 \exp[-C(E_f - E_i)/kT], \quad (15)$$

where C is a fitting parameter and k_0 scales the overall magnitude of the set of rates. Angular momentum based scaling laws⁴⁸ are generally based on the infinite-order sudden (IOS) or energy-corrected sudden (ECS) approximations of inelastic scattering theory.^{49,50} Rather than use the full IOS or ECS expressions, we have employed a simplified transferred angular momentum power-gap law,⁵¹

$$k_R = k_0 [C_1 / (|\Delta I|^2 + C_2^2)] \quad (16)$$

where C_1 and C_2 are fitting parameters and

$$|\Delta I| = \{(K_f - K_i)^2 + [(J_f^2 - K_f^2)^{1/2} - (J_i^2 - K_i^2)^{1/2}]^2\}^{1/2} \quad (17)$$

is the classical angular momentum transferred in the inelastic collision.⁵² For both types of fitting laws, the rates for endothermic processes are calculated from the appropriate expression and those for the exothermic processes are found by detailed balance [Eq. (11)].

The setup of the master equation rate matrix K and the numerical integration of the coupled differential equations [Eq. (10)] were carried out using the MATLAB software package. The numerical integration routine used in MATLAB is based on the automatic step size, fourth and fifth order Runge-Kutta algorithm.

Using the simple two-parameter scaling laws described above and a least squares minimization, we have determined the best global agreement between the calculated transients

TABLE V. State-to-state rotational energy transfer in CHD₃ self-collisions. (A) Transfer from ($\nu_3=1, J=12, K=9, A$). (B) Transfer from ($\nu_3=1, J=12, K=7, E$).

(A)	Probe level	Rate $\mu\text{s}^{-1}\text{Torr}^{-1}$	ΔE cm^{-1}	ΔJ	ΔK
	$\nu_3(12,12)$	0.35(0.07)	-23.67	0	+3
	$\nu_3(13,9)$	1.20(0.13)	80.07	+1	0
	$\nu_3(11,9)$	1.87(0.20)	-73.28	-1	0
	$\nu_3(10,9)$	0.40(0.13)	-139.54	-2	0
	$\nu_3(9,9)$	0.38(0.07)	-198.28	-3	0
	$\nu_3(12,6)$	0.73(0.10)	21.00	0	-3
	$\nu_3(11,6)$	0.87(0.10)	-53.35	-1	-3
	$\nu_3(10,6)$	0.73(0.07)	-121.15	-2	-3
	$\nu_3(9,6)$	0.63(0.07)	-182.35	-3	-3
	$\nu_3(8,6)$	0.57(0.10)	-236.91	-4	-3
	$\nu_3(7,6)$	0.20(0.10)	-284.73	-5	-3
	$\nu_3(6,6)$	0.25(0.07)	-325.64	-6	-3
	$\nu_3(11,3)$	0.80(0.25)	-40.47	-1	-6
	$\nu_3(9,3)$	0.47(0.10)	-170.51	-3	-6
	$\nu_3(6,3)$	0.25(0.07)	-316.99	-6	-6
	$\nu_3(5,3)$	0.19(0.03)	-352.91	-7	-6
	$\nu_3(4,3)$	0.17(0.03)	-382.40	-8	-6
	$\nu_3(3,3)$	0.10(0.05)	-405.57	-9	-6
	$\nu_3(10,0)$	0.37(0.07)	-104.45	-2	-9
	$\nu_3(8,0)$	0.37(0.07)	-221.85	-4	-9
	$\nu_3(7,0)$	0.25(0.03)	-270.88	-5	-9
	$\nu_3(6,0)$	0.29(0.03)	-313.49	-6	-9
	$\nu_3(5,0)$	0.11(0.05)	-349.72	-7	-9
	$\nu_3(4,0)$	0.16(0.05)	-379.60	-8	-9
	$\nu_3(3,0)$	0.11(0.05)	-403.23	-9	-9
(B)	Probe level	Rate $\mu\text{s}^{-1}\text{Torr}^{-1}$	ΔE cm^{-1}	ΔJ	ΔK
	$\nu_3(12,10)$	0.72(0.09)	-23.00	0	+3
	$\nu_3(11,7)$	1.14(0.15)	-74.12	-1	0
	$\nu_3(10,7)$	0.96(0.13)	-141.61	-2	0
	$\nu_3(9,7)$	0.34(0.09)	-202.40	-3	0
	$\nu_3(8,7)$	0.29(0.08)	-256.36	-4	0
	$\nu_3(11,4)$	1.43(0.15)	-58.62	-1	-3
	$\nu_3(10,4)$	0.17(0.15)	-126.78	-2	-3
	$\nu_3(9,4)$	0.24(0.10)	-188.43	-3	-3
	$\nu_3(8,4)$	0.25(0.06)	-243.58	-4	-3
	$\nu_3(7,4)$	0.10(0.03)	-292.21	-5	-3
	$\nu_3(6,4)$	0.05(0.04)	-334.32	-6	-3
	$\nu_3(4,4)$	0.12(0.08)	-398.97	-8	-3
	$\nu_3(9,1)$	0.35(0.07)	-181.60	-3	-6
	$\nu_3(8,1)$	0.32(0.10)	-237.06	-4	-6
	$\nu_3(7,1)$	0.27(0.13)	-286.07	-5	-6
	$\nu_3(6,1)$	0.20(0.18)	-328.66	-6	-6
	$\nu_3(5,1)$	0.12(0.08)	-364.85	-7	-6
	$\nu_3(4,1)$	0.08(0.06)	-394.70	-8	-6
	$\nu_3(3,1)$	0.08(0.07)	-418.28	-9	-6

and the experimental measurements. χ^2 was calculated as the sum of the squares of the differences between the calculated and measured population curves compared at 50 evenly spaced time intervals between 0 and 15 μs . For two-parameter scaling laws, the two parameters are not independent of each other, but are constrained to values such that the sum of all rates from the parent level is the same as that

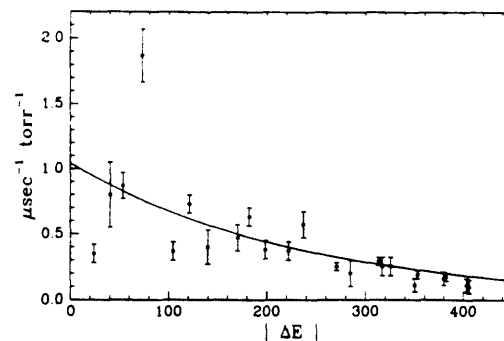


FIG. 3. Rotationally inelastic rates (in units of $\mu\text{s}^{-1}\text{Torr}^{-1}$) for CHD₃ $\nu_3(12,9)$ A-symmetry levels vs energy gap. The upper and lower bounds on each rate coefficient are determined from a sensitivity analysis based on the χ^2 goodness of fit, as described in Sec. IV D. The solid curve is a fit to the exponential energy-gap law, Eq. (15).

determined in the independent measurement of the total depopulation rate (Sec. IV A). This relationship between the k_0 and C parameters in Eqs. (15) and (16) reduces the global χ^2 minimization to a simple one-dimensional minimization.

χ^2 minimization determines the best possible agreement obtainable between experiment and a particular model calculation, but to describe the success or failure of a fit, it is useful to define a quality of fit function which rates how well a particular model comes to perfectly describing the experimental data. We define a quality of fit parameter Q as the ratio of χ^2 determined from drawing a smooth curve through each experimental transient to χ^2 determined in the fit. A value of $Q=1$ implies that the model fits the data to within the experimental noise. As the value of Q decreases, so does the quality of the fit. A Q parameter greater than 0.1 indicates a reasonable fit.

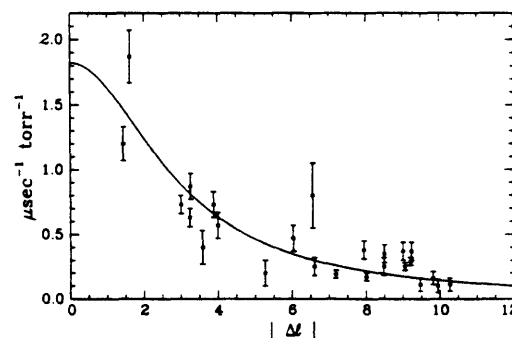


FIG. 4. Rotationally inelastic rates (in units of $\mu\text{s}^{-1}\text{Torr}^{-1}$) for CHD₃ $\nu_3(12,9)$ A-symmetry levels vs angular momentum change parameter $|l|$, defined in Eq. (17). The two largest rates correspond to the dipolar ($\Delta J = \pm 1, \Delta K = 0$) channels. The upper and lower bounds on each rate coefficient are determined from a sensitivity analysis based on the χ^2 goodness of fit, as described in Sec. IV D. The solid curve is a fit to the angular momentum power-gap law, Eq. (16).

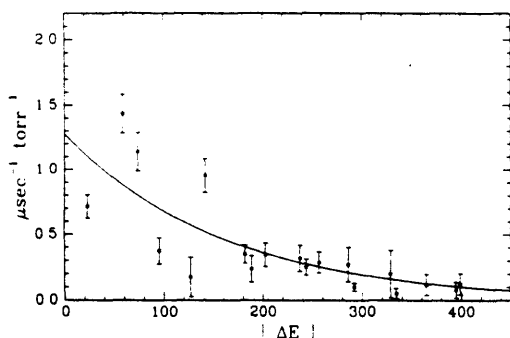


FIG. 5. Rotationally inelastic rates (in units of $\mu\text{s}^{-1}\text{Torr}^{-1}$) for CHD₃ $\nu_3(12,7)$ E -symmetry levels vs energy gap. The upper and lower bounds on each rate coefficient are determined from a sensitivity analysis based on the χ^2 goodness of fit, as described in Sec. IV D. The solid curve is a fit to the exponential energy-gap law, Eq. (15).

For the A -symmetry levels the best fits to the energy gap [Eq. (15)] and angular momentum [Eq. (16)] scaling laws give Q 's of 0.05 to 0.08. Visual comparison of the calculated and experimental curves show some qualitatively correct behavior, particularly for remote levels. The angular momentum scaling law fares better with levels near the parent. However, neither scaling law provides a truly acceptable fit to the experimental measurements.

To determine a set of rates that best describes the data, we use the rate matrices determined by the global χ^2 minimization as a starting point. We assume that the discrepancy between the calculated and measured transients arises predominantly from an incorrect rate in the matrix element connecting the initially pumped level to a probed level. We individually vary the matrix elements between the pumped and probed levels to find the minimum χ^2 for the probed level.

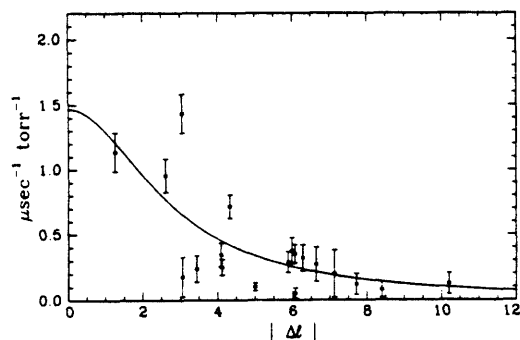


FIG. 6. Rotationally inelastic rates (in units of $\mu\text{s}^{-1}\text{Torr}^{-1}$) for CHD₃ $\nu_3(12,7)$ E -symmetry levels vs angular momentum change parameter $|\Delta J|$, defined in Eq. (17). The three largest rates correspond to the channels ($\Delta J = \pm 1$, $\Delta K = 0$) and ($\Delta J = -1$, $\Delta K = -3$). The upper and lower bounds on each rate coefficient are determined from a sensitivity analysis based on the χ^2 goodness of fit, as described in Sec. IV D. The solid curve is a fit to the angular momentum power-gap law, Eq. (16).

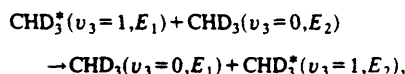
The rate at χ_{\min}^2 is taken as the most appropriate rate for the process of going from the initially populated level to the level being probed. The square root of the inverse of the second derivative of χ^2 is used as a measure of the error associated with that rate.

Because the experimental measurements presented here show effects from multiple collisions, the direct rates determined by minimizing χ^2 between the parent and probed levels of course depend on the structure of the entire rate matrix. In the course of modeling the data, we have tried many different ways of setting up the rate matrix. For all reasonable descriptions of the rate matrix, the rates we report for the direct processes between the parent and probed levels fall within the experimental error limits given here. These rates represent the best set of values we can obtain from a limited number of measurements on a very complex physical system. The Q parameter for the final fit to the A -symmetry levels presented here is 0.24, an improvement over the fits using simple scaling laws by a factor of 4 or 5. The Q value for the corresponding best fit to the set of E -symmetry levels is 0.71.

A selection of experimental signals and model simulations for A -symmetry levels is shown in Fig. 1, and those for the E -symmetry levels in Fig. 2. The set of fitted rates ($k_i \rightarrow k_f$) is given in Table V, along with the associated changes in energy and angular momentum. In the case of the E -symmetry levels, an inspection of the time-dependent signals in Fig. 2 shows a clear alternation of amplitudes and rise times with the K quantum number of the final state reached in the collision: E_1 levels [those with $K(\text{modulo } 3)=1$, i.e., $K=1,4,7,10$] are populated much more efficiently than E_2 levels ($K=2,5,8,11$). Since the initially populated level is E_1 , this evidently reflects a propensity rule $\Delta K = \pm 3n$ (n integer) such as is found in symmetric tops possessing a three-fold symmetry axis.⁵³ The E_2 levels are receiving population, however, and nonzero rates connecting them with E_1 levels must be included in the master equation to obtain satisfactory agreement between the model calculations and the experimental data.

Several mechanisms were considered to account for the $E_1 \leftrightarrow E_2$ processes. A succession of V-V exchanges, in which the ν_3 manifold acts as a basin of states,⁴⁵ would transfer population into the E_2 levels, but agreement with experimental data could be obtained only by using a value for the effective V-V rate four times larger than that measured directly [Sec. IV B]; this was therefore considered unrealistic. A "strong-collision" model, in which all final levels could receive population from any initial level with a rate independent of J and K , was also tested: moderately good agreement between model calculations and experiment could be obtained using a value of $0.048 \mu\text{s}^{-1}\text{Torr}^{-1}$ for the strong-collision rate coefficient. Much better agreement, however, resulted from recognizing⁵³ that the $\Delta K = \pm 3n$ propensity rule applies to the signed value of K , i.e., $\Delta k = \pm 3n$ where $K = |k|$. This permits population to flow from $k=1$ levels to $k=-2$ levels, thus effectively coupling the E_1 and E_2 manifolds. The final set of rates, given in Table V(B), includes $\Delta k = 0, -3$, and -6 [$\Delta k = +3$ and $+6$ are found using detailed balance, Eq. (11)] with ΔJ up to $+8$. The overall fit

was improved by retaining small strong-collision terms, with individual state-to-state rates set to a uniform value of $0.01 \mu\text{s}^{-1} \text{Torr}^{-1}$. Summed over final states, this gives a total $E_1 \rightarrow E_2$ ($\Delta k/3$ non-integer) rate coefficient $\approx 0.6 \mu\text{s}^{-1} \text{Torr}^{-1}$. As discussed below, this can be accounted for by an excitation-transfer process



being responsible for the non-integer $\Delta k/3$ processes.

V. DISCUSSION

With state-to-state RET rate data for CHD₃ now in our possession, we may address the question raised at the outset, namely, whether the inelastic processes are governed by the intermolecular potential or by the details of the level structure intrinsic to the molecule. In addition, we can test the various proposed energy-gap and angular-momentum scaling laws^{46,48,54} to see which gives the best representation of the data.

The data of Table V are plotted against energy gap ΔE and angular-momentum change parameter $|\Delta l|$, defined in Eq. (17), in Figs. 3 and 5 and Figs. 4 and 6, respectively. The RET rates show a broad distribution over ΔE (up to 400 cm^{-1} inelasticity) and angular momentum (ΔJ and ΔK up to nine units occur with nonzero probability), reminiscent of the rate distribution in ¹³CD₄ and silane. The curves in Figs. 3–6 are fitted exponential energy-gap or angular momentum power-gap laws [Eqs. (15) and (16), respectively]. These one or two-parameter fits give good representations of the distribution of state-to-state rates, at least for the larger changes in energy or angular momentum, and do not differ significantly between *A*- and *E*-symmetry levels. In addition, however, we discern some distinctly faster rates, corresponding to the dipolar channels $\Delta J = \pm 1$, $\Delta K = 0$, superimposed on these distributions. The interaction potential between two CHD₃ molecules certainly does not possess a dominant dipole-dipole term, so the appearance of these leading rates presumably reflects a propensity rule dictated by the symmetric-top level structure of the molecule.

In order to make a systematic comparison between RET in ¹³CD₄ and the lower-symmetry CHD₃, we make use of the correspondence between spherical- and symmetric-top systems recently developed in Refs. 35–37. The ν_3 band of CHD₃ studied in this work is part of an interacting ν_2/ν_6 dyad, which corresponds to the ν_4 mode of CD₄. The $\nu_4 = 1$, $l = 1$ state of CD₄ is split by Coriolis interaction into three sublevels that can be characterized by a pure rotational angular momentum $R = J - l$, l being the vibrational angular momentum. These three Coriolis components are denoted F^+ (associated with $R = J + 1$), F^0 ($R = J$), and F^- ($R = J - 1$). Although R is not a good quantum number, it accounts reasonably well for the Coriolis structure of the ν_4 band of CD₄.

In order to extend the formal description of tetrahedral molecules to those whose equilibrium configuration belongs to C_{3v} , such as CHD₃, we operate the reduction of the triply degenerate energy levels of CD₄ into the corresponding sin-

gly (*A*) and doubly (*E*) degenerate levels of CHD₃, and then sort the symmetric top levels thus obtained according to increasing energy. This was carried out for J values between 2 and 13, thus obtaining the tetrahedral assignments corresponding to the ν_3 levels of CHD₃ listed in Tables I and V. The following observations may be noted:

(i) The ν_3 band of CHD₃ corresponds almost exclusively to the F^- component of the ν_4 band of CD₄. Thus all the fast relaxation channels in CHD₃ follow an $F^- \leftarrow F^-$ propensity rule, and the condition $\Delta(J - R) = 0$ is satisfied automatically by the spectroscopic structure of the molecule.

(ii) The $J = 12$, $K = 7$ (*E*) initial level in CHD₃ corresponds to $12 E 2$ ($R = 11$) in tetrahedral notation, and relaxation from this level will be among the set of *E* levels. The $J = 12$, $K = 9$ (*A*) initial level in CHD₃ corresponds to $12 F_{1,2} 2$ ($R = 11$) in tetrahedral notation, and relaxation from this level will also remain in the *F*-symmetry manifold. This corresponds exactly to the $\Delta K = \pm 3n$ (n integer) propensity rule described by Oka⁵³ for symmetric tops possessing a threefold axis; the nuclear-spin-symmetry conservation rule is thus also automatically satisfied, except for the effects of resonant excitation-exchange collisions discussed below.

(iii) In addition to requiring that the symmetry species and Coriolis coupling be preserved in a collision, experimental results for the spherical-top systems^{1,2} revealed the presence of additional restrictions on state-changing collisions expressed in the coupled parity/ Δk_R propensity rule found by Parson.⁴ In order to investigate whether this propensity rule holds for the lower-symmetry species as well, we have calculated Δk_R for each of the pumped and final states listed in Table V. The cluster quantum number k_R was determined by using the simple procedure described by Parson.^{4(a)} The energy levels were first sorted by increasing energy. The patterns thus obtained were then searched for on the "symmetry wheels" published by Harter and Patterson,⁵⁵ after interconverting the parity subscripts. The m value associated with k_R ($k_R = R - m$) was then read out (modulo 4) on the circumference of the wheels.

The result of this analysis is that, while the RET processes in CHD₃ corresponding to Δk_R -allowed channels in the tetrahedral description all correspond to allowed processes with reasonably fast rates (subject to energy-gap constraints), many allowed channels in CHD₃ do *not* satisfy the Δk_R propensity rule. RET in spherically symmetric (*viz.*, tetrahedral) molecules appears to be considerably more restricted than that taking place in the lower-symmetry (C_{3v}) system.

We therefore conclude that the symmetry, or equivalently the internal level structure of the target molecule, plays a dominant role in establishing inelastic collision propensity rules. The CHD₃-perturber intermolecular potential differs from the CH₄- (or CD₄-)perturber intermolecular potential primarily from the effects due to the shift in the center of mass. Although CHD₃ does have a permanent dipole moment of 0.006 D, the dipole-dipole interaction energy in self-collisions at a distance of 2 Å is on the order of 0.02 cm^{-1} , and thus is negligible. Effects of the center of mass shift may be qualitatively evaluated by expanding an approximate CH₄/CHD₃ potential in spherical harmonics about the two

center of mass positions.⁵⁶ Using a point-charge bond-dipole approximation to the potential yields a multipole expansion for CH₄ that begins with the octupole term. It is a general property of multipole expansions that shifting the center of mass makes no change in the values of the lowest order nonzero multipole. The values of all higher order terms may change, however.

When one of the C-H bonds is used as the symmetry axis, the multipole expansion for CH₄ contains nonzero terms for multipole moments, Q_M^L , of order $L=3$ or higher (excepting order 5) for M a multiple of 3. Using the S_4 axis for CH₄ reduces the number of nonzero terms, but does not allow direct comparison with CHD₃. For CHD₃, the octupole terms are identical to those of CH₄, but all higher order terms differ significantly, including additional nonzero terms for $L=5$. Nonetheless, only terms with $M=3n$ are nonzero. The multipole expansions for CH₄ and CHD₃ indicate that the basic selection rules should be essentially identical, since the same terms ($L \geq 3, M=3n$) have nonzero values. Because the values of all terms beyond the octupole are significantly different, individual state-to-state rates may vary significantly.

Finally, we consider the small but nonzero rate ($0.17 \mu\text{s}^{-1} \text{Torr}^{-1}$, corresponding to a cross section of 0.64 \AA^2) for transfer between the A - and E -symmetry manifolds, and the comparably small rate ($\approx 0.6 \mu\text{s}^{-1} \text{Torr}^{-1}$) for direct transfer between E_1 and E_2 levels. Symmetry-changing state-transfer processes have also been observed in other symmetric top systems, such as CD₃Cl ($0.61 \mu\text{s}^{-1} \text{Torr}^{-1}$, 3.9 \AA^2)⁵⁷ and CH₃F ($6.6 \mu\text{s}^{-1} \text{Torr}^{-1}$, 33 \AA^2).⁵⁸ Processes of this type, which appear to violate either rigorous nuclear-spin symmetry restrictions or strong propensity rules such as $\Delta K/3 = \text{integer}$, are generally attributed to resonant exchange of the vibrational excitation between molecules in different symmetry states as a result of a Förster exchange process.⁵⁹ We can test the hypothesized mechanism for the exchange process by calculating the cross sections using a simple model developed by Melton⁶⁰ and Gordon and Chiu⁶¹ to describe excitation transfer processes between ground-state and electronically excited NO molecules.⁶² The treatment is similar to that given by Sharma and Brau⁶³ for the specific case of near-resonant V-V energy transfer, but Gordon and Chiu give a simpler formulation^{60,61} than the full Sharma-Brau theory which, as we shall see, is in tolerably good accord with experiment.

If the excited and ground-state molecules interact via a dipole-dipole potential,⁶⁴

$$V(R) = \frac{\mu_1 \cdot \mu_2}{R^3} - \frac{3(\mu_1 \cdot \mathbf{R})(\mu_2 \cdot \mathbf{R})}{R^5}, \quad (18)$$

where μ_1 and μ_2 are the dipole moments for the spectroscopic transition, then an approximate expression for the resonant transfer cross-section is found⁶⁰ as

$$\sigma_{\text{ex}} = \frac{2E_i}{E_i + E_f} \pi(b^*)^2, \quad (19)$$

where the critical impact parameter b^* is obtained from the condition

$$P(b^*) = \frac{4\mu_1^2\mu_2^2}{9\hbar\bar{v}^2(b^*)^4} \cdot \frac{E_f}{E_i + E_f}. \quad (20)$$

In Eqs. (19) and (20), E_i and E_f are the initial and final kinetic energies of the collision pair, \bar{v} is the average thermal velocity $(8k_B T/\pi\mu_{12})^{1/2}$, and the scalar $\mu_n = |\langle \mu_{0n} \rangle|$ for the $n=0$ vibrational band. We assume that the resonant exchange occurs with nearly zero energy defect $\Delta E = E_f - E_i$ (or at any rate $\Delta E \ll E_i$), so that Eqs. (19) and (20) simplify to

$$\sigma_{\text{ex}} = \pi(b^*)^2$$

and

$$P(b^*) = \frac{8.1 \times 10^{13} [\mu_n/\text{Debye}]^4}{\bar{v}^2 [b^*/\text{Å}]^4} = 0.5$$

We calculated σ_{ex} for CHD₃, CD₃Cl, and CH₃F using the preceding expressions. The required transition dipole moments are $\mu_3 = 0.023$ D for CHD₃,⁶⁵⁻⁶⁷ $\mu_2 = 0.047$ D for CD₃Cl,^{67,68} and $\mu_3 = 0.283$ D for CH₃F.⁶⁹ The calculated results are $\sigma_{\text{ex}} = 0.26 \text{ \AA}^2$ for CHD₃ (experimental 0.64 \AA^2 , see Sec. IV B), $\sigma_{\text{ex}} = 1.8 \text{ \AA}^2$ for CD₃Cl (experimental 3.9 \AA^2),⁵⁷ and $\sigma_{\text{ex}} = 53 \text{ \AA}^2$ for CH₃F (experimental 33 \AA^2).⁵⁸ This is remarkably good agreement, over a range of 2 orders of magnitude, for such an approximate model. It seems that the cross section for resonant exchange can be readily calculated from Eqs. (19) and (20), knowing only the magnitude of the vibrational transition moment for the relevant mode.

There are few calculations of inelastic collision rates for CHD₃ in the literature. Bosanac⁷⁰ has used a line-of-centers model and a simplified hard-core potential to compute classical energy transfer for He-CH₄, He-CH₃D, and He-CHD₃ systems at low relative kinetic energy ($10 \text{ meV} \approx 120 \text{ K}$). Total inelastic cross sections were estimated from the differential cross section plots in Bosanac's paper. The calculated ($\Delta J = +1, \Delta K = 0$) cross section for CHD₃-He, 7.8 \AA^2 , actually agrees rather well with our measured ($12.9-11.9$) value (7.1 \AA^2), and that for the ($\Delta J = +3, \Delta K = +3$) channel also agrees with the measured ($12.9-9.6$) value (calc. 2.4 \AA^2 ; expt. 2.4 \AA^2); but the computed inelastic cross section^{70(b)} for ($\Delta J = 3, \Delta K = 0$), viz., 13.2 \AA^2 , is an order of magnitude larger than our measured $\sigma(12.9-9.9) = 1.4 \text{ \AA}^2$. The close agreement of two pairs of calculated and measured values, while largely fortuitous, does suggest that a hard-core, short-range interaction is an appropriate description for the potential function. Further calculations based on this model, using a more realistic molecular geometry and potential function, may yield quantitative agreement with experiment.

VI. SUMMARY AND CONCLUSIONS

We have undertaken this study of energy transfer processes in CHD₃ to examine the effect of a change in molecular symmetry on these processes. We wished to investigate whether a lower-symmetry isotopomer of methane exhibited the same highly selective energy transfer pathways that were found in the spherically symmetric isotopomer. The answer to this question offers a perspective on the relative importance of the internal structure of a molecule and its intermo-

lecular potential on controlling energy-transfer propensity rules. We have found that CHD₃ shows a selectivity in its energy-transfer pathways which is quite distinct from that in ¹³CD₄. Most notably, the symmetric-top propensity rule $\Delta K = \pm 3n$ (n integer) governs RET in CHD₃, even when K states differing by a non-integer multiple of three are not excluded by nuclear-spin symmetry restrictions. The relaxation process is dominated by state-specific channels following the dipolar propensity rule $\Delta J = \pm 1$, $\Delta K = 0$, but there is a significant contribution from $\Delta J = -1$, $\Delta K = -3$ (indeed, this is the largest single term for the E -symmetry levels). In this specific regard, the behavior of CHD₃ differs from dipolar symmetric tops such as CH₃F,⁵⁸ CH₃Cl,⁷¹ and ammonia,¹⁹ in which $\Delta K = -3$ processes proceed an order of magnitude more slowly than those with $\Delta K = 0$, and the latter account for up to 50% of the total relaxation rate. The remaining terms contributing to rotational relaxation in CHD₃ result in a very broad distribution of final states, which is indeed reminiscent of what is seen in ¹³CD₄, except that in CHD₃ the distribution is more uniform: there are no uniquely preferred final states other than those dictated by molecular symmetry. In its rotational relaxation processes, CHD₃ behaves much more like a symmetric-top molecule such as NH₃ than a spherical top molecule. It is the unique internal structure of a spherical top that accounts for the unusual and highly selective pathways observed, e.g., with ¹³CD₄, and not simply the short-range forces which make up the intermolecular potential.

ACKNOWLEDGMENTS

We are pleased to thank Professor Yoshihiro Mizugai (Sophia University, Tokyo, Japan) for assistance with preliminary experiments on this system and Professor R. W. Field for useful suggestions and references concerning the Förster transfer mechanism. This work was supported by grants from NASA Upper Atmosphere Research Program (NAGW-1667) and Planetary Atmospheres Program (NAGW-2387)

- Smith, and C. P. Rinsland, *J. Mol. Spectrosc.* **157**, 95 (1993); (c) D. C. Benner, V. M. Devi, M. A. H. Smith, and C. P. Rinsland, *J. Quant. Spectrosc. Radiat. Transfer* **50**, 65 (1993).
- ¹³ A. S. Pine, *J. Chem. Phys.* **97**, 773 (1992).
- ¹⁴ G. Millot, B. Lavorel, and J. I. Steinfeld, *J. Chem. Phys.* **95**, 7938 (1991).
- ¹⁵ G. Millot, B. Lavorel, and J. I. Steinfeld, *J. Quant. Spectrosc. Radiat. Transfer* **47**, 81 (1992).
- ¹⁶ G. D. T. Tejwani and K. Fox, *J. Chem. Phys.* **61**, 759 (1974).
- ¹⁷ P. Varanasi and S. Chudamani, *Opt. Lett.* **28**, 2119 (1989).
- ¹⁸ Y. Mizugai, J. J. Klaassen, C. Roche, and J. I. Steinfeld, *Int. Symp. on Advanced Infrared Spectroscopy*, Tokyo, Japan, March 1993; *Appl. Spectrosc.* **47**, 2058 (1993).
- ¹⁹ B. Abel, S. L. Coy, J. J. Klaassen, and J. I. Steinfeld, *J. Chem. Phys.* **96**, 8236 (1992).
- ²⁰ J. J. Klaassen, Thesis, Massachusetts Institute of Technology, 1994.
- ²¹ (a) D. E. Jennings, *Appl. Opt.* **19**, 265 (1980); (b) **23**, 1299 (1984).
- ²² C. Flannery, J. J. Klaassen, M. Gojer, J. I. Steinfeld, M. Spencer, and C. Chackerian, Jr., *J. Quant. Spectrosc. Radiat. Transfer* **46**, 73 (1991).
- ²³ D. G. Rea and H. W. Thompson, *Trans. Faraday Soc.* **52**, 1304 (1956).
- ²⁴ J. K. Winhurst and H. J. Bernstein, *Can. J. Chem.* **35**, 226 (1957).
- ²⁵ J. Dupre-Maquaire and G. Tarrago, *J. Mol. Spectrosc.* **96**, 156 (1982).
- ²⁶ J. Dupre-Maquaire, Thèse d'Etat, Orsay, 1986.
- ²⁷ D. E. Jennings and W. E. Blass, *J. Mol. Spectrosc.* **55**, 445 (1975).
- ²⁸ H. W. Kattenberg and S. Brodersen, *J. Mol. Spectrosc.* **59**, 126 (1976).
- ²⁹ H. C. Allen, Jr. and E. K. Plyler, *J. Res. Natl. Bur. Stand. A* **63**, 145 (1959).
- ³⁰ M. Lewerenz and M. Quack, *J. Chem. Phys.* **88**, 5408 (1988).
- ³¹ A. Campargue, F. Stoeckel, M. Chenevier, and H. Ben-Kraïem, *J. Chem. Phys.* **87**, 5598 (1987).
- ³² C. Iung and C. Leforestier, *J. Chem. Phys.* **97**, 2481 (1992).
- ³³ G. Guelachvili and K. N. Rao, *Handbook of Infrared Standards* (Academic, Orlando, 1986), pp. xxvi-xxix.
- ³⁴ J.-P. Champion, M. Loëte, and G. Pierre, in *Spectroscopy of the Earth's Atmosphere and Interstellar Molecules*, edited by K. N. Rao and A. Weber (Academic, New York, 1992), p. 339 ff and references therein.
- ³⁵ C. Roche, Thèse Doctorat de l'Université de Bourgogne, Dijon, 1992.
- ³⁶ C. Roche and J.-P. Champion (to be published).
- ³⁷ C. Roche, J. P. Champion, S. L. Coy, J. J. Klaassen, J. I. Steinfeld, A. Valentin, Y. Mizugai, and J. W. C. Johns, *J. Chem. Phys.* **100**, 5508 (1994), preceding paper.
- ³⁸ J. Dupre-Maquaire, J. Dupre, and G. Tarrago, *J. Mol. Spectrosc.* **90**, 63 (1981).
- ³⁹ B. Foy, L. Laux, S. Kable, and J. I. Steinfeld, *Chem. Phys. Lett.* **118**, 564 (1985).
- ⁴⁰ Lennard-Jones ϵ_s and σ_s parameters were taken from tabulations in J. O. Hirschfelder, C. F. Curtiss, and R. B. Bird, *Molecular Theory of Gases and Liquids* (Wiley, New York, 1954). ϵ_M and σ_M for CHD₃ were assumed to be identical to the values for methane. The Lennard-Jones collision cross section was calculated as $\sigma_{LJ} = (\pi/4)(\sigma_s + \sigma_M)^2 \Omega^{(2,2)*} \times (kT/\sqrt{\epsilon_A \epsilon_M})$, where $\Omega^{(2,2)*}$ is the tabulated collision integral. The cross section for methane-CHF₃ was estimated by interpolation between those for methane-CH₂F₂ (63 Å²) and methane-CF₄ (67 Å²).
- ⁴¹ Since A_1 and A_2 components are not resolved, $g_A/g_E = 22/16 = 11/8$. The value of $(1+\xi)$ is approximately 1.01, so in this case $\lambda_{-} = k_{A-E}$.
- ⁴² (a) A. E. DePristo and H. Rabitz, *J. Chem. Phys.* **69**, 902 (1978); (b) A. E. DePristo and H. Rabitz, *J. Quant. Spectrosc. Radiat. Transfer* **22**, 65 (1979); (c) L. L. Strow and R. M. Gentry, *J. Chem. Phys.* **84**, 1149 (1986); (d) B. Gentry and L. L. Strow, *ibid.* **86**, 5722 (1987).
- ⁴³ C. C. Flannery and J. I. Steinfeld, *J. Chem. Phys.* **96**, 8157 (1992).
- ⁴⁴ (a) J. I. Steinfeld, J. S. Francisco, and W. L. Hase, *Chemical Kinetics and Dynamics* (Prentice-Hall, Englewood Cliffs, 1989), Chap. 14; (b) W. D. Lawrence, A. E. W. Knight, R. G. Gilbert, and K. D. King, *Chem. Phys.* **56**, 343 (1981).
- ⁴⁵ S. L. Coy, S. D. Halle, J. L. Kinsey, and R. W. Field, *J. Mol. Spectrosc.* **153**, 340 (1992).
- ⁴⁶ J. I. Steinfeld, P. Ruttenberg, G. Millot, G. Fanjoux, and B. Lavorel, *J. Phys. Chem.* **95**, 9638 (1991), and references therein.
- ⁴⁷ The EGL may readily be derived from the entropy maximization principle of information theory, as discussed by I. Procaccia and R. D. Levine, *J. Chem. Phys.* **63**, 4261 (1975) and R. D. Levine, *Annu. Rev. Phys. Chem.* **29**, 59 (1978).
- ⁴⁸ A. J. McCaffery, Z. T. Alwahabi, M. A. Osborne, and C. J. Williams, *J. Chem. Phys.* **98**, 4586 (1993).

- ⁴⁹(a) A. E. DePristo, A. D. Augustin, R. Ramaswamy, and H. Rabitz, *J. Chem. Phys.* **71**, 850 (1979); (b) A. E. DePristo, *ibid.* **74**, 5037 (1981).
- ⁵⁰(a) P. J. Agg and D. C. Clary, *J. Chem. Phys.* **95**, 1037 (1991); (b) S. L. Davis, *ibid.* **95**, 7219 (1991).
- ⁵¹D. A. Greenhalgh and L. A. Rahn, *J. Raman Spectrosc.* **21**, 847 (1990).
- ⁵²Z. T. Al-Wahabi, C. G. Harkin, A. J. McCaffery, and B. J. Whitaker, *J. Chem. Soc. Faraday Trans. 2* **85**, 1003 (1989).
- ⁵³T. Oka, *Adv. At. Mol. Phys.* **9**, 127 (1973).
- ⁵⁴H. Odashima, H. Ikeda, T. Minowa, and T. Shimizu, *J. Chem. Phys.* **99**, 169 (1993).
- ⁵⁵W. G. Harter and C. W. Patterson, *J. Chem. Phys.* **66**, 4872 (1977).
- ⁵⁶W. Miller, *Adv. Chem. Phys.* **25**, 69 (1974); H. Kreek and R. J. LeRoy, *J. Chem. Phys.* **63**, 338 (1975).
- ⁵⁷L. Doyennette and F. Menard-Bourcin, *J. Chem. Phys.* **89**, 5578 (1988).
- ⁵⁸H. O. Everitt and F. C. DeLucia, *J. Chem. Phys.* **90**, 3520 (1989).
- ⁵⁹Th. Förster, *Ann. Phys.* **2**, 55 (1948); Th. Förster, *Z. Naturforsch. Teil A* **4**, 321 (1949); Th. Förster, *Discuss. Faraday Soc.* **27**, 7 (1959); Th. Förster, *Mod. Quantum Chem.* **3**, 93 (1965).
- ⁶⁰L. A. Melton, Ph.D. thesis, Harvard University, 1972.
- ⁶¹R. D. Gordon and Y. N. Chiu, *J. Chem. Phys.* **55**, 1469 (1971).
- ⁶²L. A. Melton and W. Klemperer, *J. Chem. Phys.* **55**, 1468 (1971); **59**, 1099 (1973).
- ⁶³R. D. Sharma and C. A. Brau, *J. Chem. Phys.* **50**, 924 (1969).
- ⁶⁴H. Margenau and N. R. Kestner, *Theory of Intermolecular Forces* (Pergamon, Oxford, 1969).
- ⁶⁵The transition moment for the ν_1 band of CHD₃ was estimated from the band strength $S_1 = (24 \pm 5) \text{ cm}^{-2} \text{ atm}^{-1}$ given by Dupre-Maquire and Tarago (Ref. 25), which was in turn based on the overall band strength $S_1 + S_6 = (62 \pm 5) \text{ cm}^{-2} \text{ atm}^{-1}$ reported by Hiller and Straley (Ref. 66), using the relationship between band strength and transition moment given by Smith *et al.* in Ref. 67.
- ⁶⁶R. E. Hiller, Jr. and J. W. Straley, *J. Mol. Spectrosc.* **5**, 24 (1960).
- ⁶⁷M. A. H. Smith, C. P. Rinsland, B. Fridovich, and K. N. Rao, in *Molecular Spectroscopy: Modern Research*, edited by K. N. Rao and A. Weber (Academic, New York, 1988), Vol. 3, p. 111ff.
- ⁶⁸The transition moment for the ν_2 band of CD₃Cl was estimated from the band strength $\Gamma_2 = 1046 \text{ cm}^2 \text{ mol}^{-1}$ [$S_2 = 44 \text{ cm}^{-2} \text{ atm}^{-1}$] given by J. W. Russell, C. D. Needham, and J. Overend [*J. Chem. Phys.* **45**, 3383 (1966)], using the relations given by Smith *et al.* in Ref. 67.
- ⁶⁹The transition moment for the ν_3 band of CH₃F was found to be $\mu_3 = 0.283 \text{ D}$ by direct measurement using laser Stark spectroscopy [G. Duxbury, S. M. Freund, and J. W. C. Johns, *J. Mol. Spectrosc.* **62**, 99 (1976)].
- ⁷⁰(a) S. D. Bosanac, *Phys. Rev. A* **43**, 3427 (1991); (b) S. D. Bosanac (private communication).
- ⁷¹T. W. Pape, F. C. DeLucia, and D. D. Skatrud, *J. Chem. Phys.* **100**, 5666 (1994).

Appendix Four

"Program for converting LeCroy "*.tra" files to ASCII files"

All of the time-resolved data presented in this thesis were taken on the LeCroy 9400A oscilloscope. The MASP storage program provided by LeCroy was used to transfer these files to a PC. Unfortunately, the MASP program does not provide the option of storing data files in an ASCII format. The ".tra" files created by the MASP program are binary files which contain both the data and information about the front panel setup of the oscilloscope written in a not easily interpreted format. The C code provided in this Appendix will crunch through a ".tra" file to extract the oscilloscope trace which is then written as an ASCII file with the same name as the ".tra" file but with the extension ".dat", and will also append to the file DATALIST the file comments and information about the trace. Hopefully, this program will be of use to future users of this oscilloscope.

```

/* this program takes the signal stored by the Lecroy oscilloscope and
   converts it into a ASCII file */
/* last modified 13 DEC 1991 */

#include <stdlib.h>
#include <stdio.h>
#include <dos.h>
#include <graph.h>
#include <math.h>
#include <float.h>

struct videoconfig config;

float
time_code[29]={0,0,0,0,.002,.005,.01,.02,.05,.1,.2,.5,1,2,5,10,
               20,50,100,200,500,1000,2000,5000,10000,20000,50000,
               100000,200000};

float gain_code[10]={5,10,20,50,100,200,500,1000,2000,5000};

float time_per_point_code[21]={.01,.02,.04,.08,.2,.4,.8,2.0,4.0,
                               8.0,20.0,40.0,80.0,200.0,400.0,800.0,
                               2000.0,4000.0,8000.0,20000.0,40000.0};

main()
{
FILE *fp, *fi;
char filename[15], fileroot[15];
char comment1[80];
char comment2[80];
char comment3[80];
char comment4[80];
char time_and_date[20];
int desc_offset, data_offset, time_offset;
int number_of_points;
float time_per_division, time_per_point, trig_delay, gain,
      variable_gain, offset;
float data[5001];
long int x1,y1;
int i,j,x,y,z,m,n;
unsigned int high, low;
char ch, lett;
float mark, zeropoint;

extern struct config;

```

```

void drawaxis(), tcls();

/* setup screen */
/*      _setvideomode(_HRESBW);
_getvideoconfig(&config); */

/* open file */
    printf("Enter filename sans extension\n");
    scanf("%s",fileroot);
    strcpy(filename,fileroot);
    strcat(filename, ".TRA");
    fp = fopen(filename, "rb");

/* get offsets for desc, data, and time */
    fseek(fp, 884, 0);
        ch=getc(fp);
        x=ch;
        if (x<0)
            x = 256 + x;
        ch=getc(fp);
        y=ch;
        y=256*y;
        desc_offset = x + y;

    fseek(fp, 888, 0);
        ch=getc(fp);
        x=ch;
        if (x<0)
            x = 256 + x;
        ch=getc(fp);
        y=ch;
        y=256*y;
        data_offset = x + y;

    fseek(fp, 892, 0);
        ch=getc(fp);
        x=ch;
        if (x<0)
            x = 256 + x;
        ch=getc(fp);
        y=ch;
        y=256*y;
        time_offset = x + y;

```

```

/* get time and date */
    fseek(fp,864,0);
    for (i=0;i<20;i++)
        time_and_date[i]=getc(fp);
    printf("time= %s\n",time_and_date);

/* get comments */
    fseek(fp,84,0);
    for (i=0;i<80;i++)
        comment1[i]=getc(fp);
    printf("comment1= %s\n",comment1);
    fseek(fp,155,0);
    for (i=0;i<80;i++)
        comment2[i]=getc(fp);
    printf("comment2= %s\n",comment2);
    fseek(fp,226,0);
    for (i=0;i<80;i++)
        comment3[i]=getc(fp);
    printf("comment3= %s\n",comment3);
    fseek(fp,297,0);
    for (i=0;i<80;i++)
        comment4[i]=getc(fp);
    printf("comment4= %s\n",comment4);

/* get vertical gain */
    fseek(fp,desc_offset+8,0);
    ch=getc(fp);
    x=ch;
    gain = gain_code[x-22];
    printf("mv/div = %f\n",gain);

/* get variable vertical gain */
    fseek(fp,desc_offset+9,0);
    ch=getc(fp);
    x=ch;
    variable_gain =0.005*x+0.4;
    printf("variable gain = %f\n",variable_gain);

/* get vertical offset */
    fseek(fp,desc_offset+12,0);
    ch=getc(fp);
    x=ch;
    if (x<0)
        x = 256 + x;
    ch=getc(fp);

```

```

        y=ch;
        if(y<0)
            y = 256 + y;
        offset = 0.08*gain*((x*256 + y)/2)-100);
        printf("offset = %f\n",offset);

/* get time per division */
        fseek(fp,desc_offset+17,0);
        ch=getc(fp);
        x=ch;
        time_per_division = time_code[x];
        printf("time per division = %f\n",time_per_division);

/* get number of points */
        fseek(fp,data_offset+6,0);
        ch=getc(fp);
        x=ch;
        if (x<0)
            x = 256 + x;
        ch=getc(fp);
        y=ch;
        if(y<0)
            y = 256 + y;
        number_of_points = (x*256 + y)/2;
        printf("number of points = %d\n",number_of_points);

/* get time per point */
        fseek(fp,desc_offset+18,0);
        ch=getc(fp);
        x=ch;
        time_per_point = time_per_point_code[x-16];
        x=.5+(10*time_per_division/time_per_point)/number_of_points;
        time_per_point=x*time_per_point;
        printf("time per point = %f\n",time_per_point);

/* get trigger delay */
        /* trig delay is a percent delay */

        fseek(fp,desc_offset+29,0);
        ch=getc(fp);
        x1 = ch;
        if(x1<0)
            x1=256+x1;
        trig_delay=x1*0.02*time_per_division;
        printf("trig delay = %f\n",trig_delay);

```

```

/* get data */
    fseek(fp,data_offset+8,0);
    for(i=0;i<number_of_points;i++)
    {
        high = getc(fp);
        low = getc(fp);
        data[i]=(gain*((256*high+low-32768.0)/8192.0)-offset)
            *variable_gain;
    }

fclose(fp);

/* write information to .dat file */

    strcpy(filename,fileroot);
    strcat(filename, ".dat");
    fp=fopen(filename, "w");

    for(i=0;i<number_of_points;i++)
    {
        mark=i*time_per_point-trig_delay;
        fprintf(fp, "%8.4f %11.5f\n",mark,data[i]);
    }

    fclose(fp);

/* write information to reference file */

    fp=fopen("datalist", "a");
    fprintf(fp, "%s\n", fileroot);
    fprintf(fp, "    %s\n", fileroot);
    fprintf(fp, "    %s\n", comment1);
    fprintf(fp, "    %s\n", comment2);
    fprintf(fp, "    %s\n", comment3);
    fprintf(fp, "    %s\n", comment4);

    zeropoint=trig_delay*100+1;
    fprintf(fp, "    zeropoint = %f\n", zeropoint);
    fprintf(fp, "    number of points= %d\n", number_of_points);

fprintf(fp, "*****\n");

```

```
fprintf(fp, "\n");  
    fclose(fp);
```

```
}
```

Appendix Five

"Timing circuit for synchronization of Continuum NY61-20 Nd:YAG laser and Lambda Physik LPX-200 Excimer laser"

This appendix provides a description of the operation of a homemade triggering circuit which was built to externally trigger the Continuum NY61-20 Nd:YAG laser and the Lambda Physik LPX-200 Excimer laser at 20 Hz. This trigger box was also used to provide a 500 Hz synchronous square wave for use in frequency modulating the Laser Photonics diode laser in sync with the NY61-20 YAG. This device is basically a 10 MHz clock and three variable delay circuits. The front panel layout of the circuit is shown in Figure A5.1

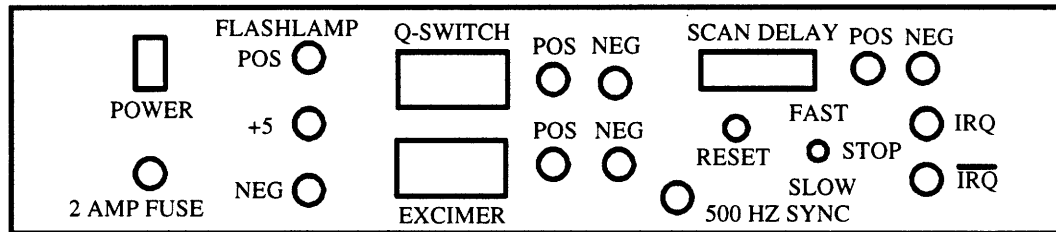


Figure A5.1

Front panel of homebuilt trigger box

The circuit box provides four different output pulses: Flashlamp, Q-switch, Scan Delay, and IRQ. All of these provide both positive and negative going TTL level pulses $\sim 7.5 \mu\text{sec}$ long at a repetition rate of 20 Hz. The Flashlamp pulse begins the pulse sequence. As its name suggests, it is used to trigger the NY61-20's flashlamp. Both the Q-switch and Excimer pulses can be delayed with respect to the Flashlamp pulse through the frontpanel thumbwheel switches. These pulses can be adjusted in $0.1 \mu\text{sec}$ increments up to $999.9 \mu\text{sec}$. The Q-switch pulse is used to trigger the NY61-20's Q-switch and the Excimer pulse is used as an external trigger for the LPX-200. The Scan Delay feature was designed to scan the time delay between the firing of the NY61-20 and the LPX-200. This feature is useful in time-resolved energy transfer measurements. The final output pulse is the interrupt request, IRQ, which can be used to trigger an A/D board for shot-to-shot measurements.

Afterword

"Since Nature is an open book, for anyone to read who has the wit to understand, it must be concluded that the slowness of scientific progress is at least partly, if not wholly, explained by human stupidity."

William F. Meggers
National Bureau of Standards (Washington, D.C.)
Spectrochimica Acta, Vol. III, No. 1, p. 5, 1947.